NASA CR- 132413

1

TP- 3720318

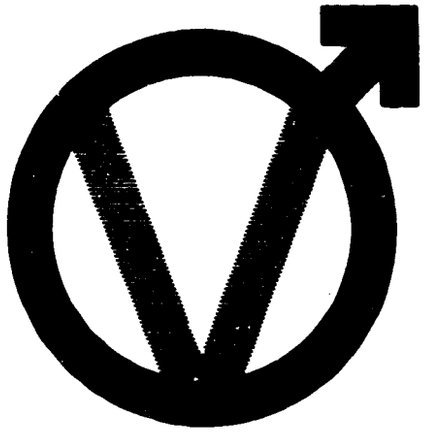

Viking'75 Project

HEAT TRANSFER AND PRESSURE DISTRIBUTION AT M=8 ON 0.029 SCALE MODELS OF THE VIKING ENTRY VEHICLE

(NASA-CR-132413) HEAT TRANSFER AND PRESSURE DISTRIBUTIONS AT M EQUALS 8 ON 0.029 SCALE MODELS OF THE VIKING ENTRY VEHICLE (Martin Marietta Corp.) 156 p HC $11.00 CSCL 22B G3/31

N74-17568

Unclas 30201

1974

NAS1-9000

MARTIN MARIETTA

NASA CR- 132413

TP-3720318

July 1972

DRL Line Item No.: N3-T022

HEAT TRANSFER AND PRESSURE DISTRIBUTIONS AT M = 8 ON 0.029 SCALE MODELS OF THE VIKING ENTRY VEHICLE

Prepared by

R. Faye-Petersen
D. Sarver
H. Carroll

Approved by

Robert J. Polutchko
Project Engineer
Viking Vehicle Engineering

Prepared under Contract NAS1-9000 by
Martin Marietta Corporation
Denver Division

CONTENTS

	Page
LIST OF TABLES	iv
LIST OF ILLUSTRATIONS	v
SUMMARY	x
I. INTRODUCTION	1
II. DEFINITIONS	3
A. Symbols and Nomenclature	3
B. Abbreviations and Acronyms	5
III. TEST DESCRIPTION	7
A. Test Facility	7
B. Model and Instrumentation	7
1. Pressure Test Model	8
2. Heat Transfer Model	8
3. Heat Transfer Sphere	9
C. Test Procedure	10
1. Pressure Tests	10
2. Heat Transfer Test	11
3. Heat Transfer Reference Hemisphere Test	12
IV. DATA REDUCTION AND PRESENTATION	13
A. Pressure Test Data	13
B. Heat Transfer Data	14
1. Aeroshell	14
2. Reference Hemisphere	15
C. Base Cover	15

TABLE OF CONTENTS (CONTINUED)

		Page
V.	DISCUSSION OF RESULTS	16
	A. Pressure Distribution	16
	1. Aeroshell Basic Data	16
	2. Base Cover Basic Data	17
	3. Pressure Data Interpolation	17
	B. Heat Transfer Distribution	18
	1. Aeroshell	18
	2. Base Cover Frustum	21
VI.	CONCLUSIONS	23
VII.	REFERENCES	24
VIII.	APPENDIX	A-1
	A. Heat Conduction Corrections	A-1
	B. Surface Roughness	A-3

LIST OF TABLES

Table	Title	Page
I	2.9 Percent Model Pressure Test Run Program	25
II	2.9 Percent Model Heat Transfer Test Run Program	26
III	Reference Hemisphere Probe Run Program	28
IV	Composition of 17-4 PH Stainless Steel	29

LIST OF ILLUSTRATIONS

Figure No.	Title	Page
1	Langley Mach 8 Variable-Density Hypersonic Tunnel Description	30
2	Pressure Model Installed in Tunnel Injection Mechanism	31
3	Mercury Manometer Board	32
4	Langley Mach-8 Variable-Density Hypersonic Tunnel Calibration	33
5	Pressure Model Drawing	34
6	Heat Transfer Model Thermocouple Gauge Location	35
7	Heat Transfer Model Parts	36
8	Four-Inch Stagnation Heat Transfer Reference Hemisphere	37
9	Thermocouple Installation in Heat Transfer Calibration Model	38
10	VLC Model Wall Temperature Time History for Station 0	39
11	Schlieren Photographs of VLC Model Tested in the LRC Mach-8 Variable-Density Hypersonic Wind Tunnel	40
12	Schlieren Photographs of Reference Hemisphere Tested in the LRC Mach-8 Variable Density Hypersonic Wind Tunnel	41
13	Aeroshell Pressure Distribution Along Meridian Plane ($\phi = 0$), $R_e \approx 3.4 \times 10^6$ (a) α = 0.1 deg (b) α = -3.8 and +5.2 deg (c) α = -8.2 and +8.0 deg (d) α = -11.0, +10,8, and +12.0 deg (e) α = -1.65 and 15.1 deg (f) α = -19.8 and 20.0 deg	42
14	Aeroshell Pressure Distribution Along Meridian Plane ($\phi = 0$) $R_e \approx 2.8 \times 10^6$ α = 0 deg	48

Figure No.	Title	Page
15	Aeroshell Pressure Distribution Along Meridian Plane ($\phi = 0$) $R_e \approx 1.5 \times 10^6$ (a) $\alpha = 0$ deg. (b) $\alpha = -12.2$ and 9.7 deg (c) $\alpha = -30.3$ deg	49
16	Variation of Aeroshell Pressure Distribution with Angle of Attack along the Radial Plane, $R_e = 3.3 \times 10^6$ (a) $\phi = 0$ and 180 deg (b) $\phi = 90$ and 270 deg (c) $\phi = 330$ deg (d) $\phi = 300$ deg (e) $\phi = 30$ deg (f) $\phi = 60$ deg	52
17	Aeroshell Isobar Contours at -11.2 deg Angle of Attack, $R_e = 3.4 \times 10^6$	58
18	Aeroshell Pressure Distribution at -30.3 deg Angle of Attack, $R_e = 1.5 \times 10^6$	59
19	Aeroshell Isobar Contours at -11.2 deg Angle of Attack, $R_e = 3.3 \times 10^6$	60
20	Variation in Base Pressure along the Meridian Plane ($\phi = 0$, 180 deg.) at several Angles of Attack, $R \approx 3.3 \times 10^6$.	61
21	Reynolds Number Effect on Base Pressure Variation along the Meridian Plane ($\phi = 0$, 180 deg) at 0 and $\pm$ 12 deg. Angle of Attack	62
22	Variation of Base Pressure along $R = 0.7016\ R_B$	63
23	Base Pressure Distribution at -30.3 deg Angle of Attack	64
24	Specific Heat of 17-4 PH Stainless Steel.	65
25	Variation of Aeroshell Heating Rate Distribution Along Meridian Plane ($\phi = 0$) with Variation in Reynolds Number (a) $\alpha \approx 0$ deg (b) $\alpha \approx \pm 4$ deg (c) $\alpha \approx \pm 8$ deg (d) $\alpha \approx \pm 12$ deg (e) $\alpha \approx \pm 16$ deg (f) $\alpha \approx \pm 20$ deg	66

Figure No.	Title	Page
26	Aeroshell Heating Rate Distribution Along Meridian Plane (ϕ = 0) for Angle of Attack α = -30.3 deg and $R_e = 1.7 \times 10^6$	72
27	Aeroshell Heating Rate Distribution in the Test High Reynolds Number Range (a) α = -.4 deg (b) α = -4.0 and +4.2 deg (c) α = -8.3 and +7.7 deg (d) α = -10.4 and +11.2 deg (e) α = -16.4 and +15.0 deg (f) α = -20.0 and +22.2 deg	73
28	Aeroshell Heating Rate Distribution in the Test Mean Reynolds Number Range (a) α = -.8 deg (b) α = -4.5 and +3.4 deg (c) α = -8.2 and +7.0 deg (d) α = -11.5 and +10.6 deg (e) α = -16.4 and +15.0 deg (f) α = -20.2 and +18.5 deg	79
29	Aeroshell Heating Rate Distribution in the Test Low Reynolds Number Range (a) α = -1.0 deg (b) α = -4.5 and +3.4 deg (c) α = -8.1 and +7.8 deg (d) α = -11.7 and +10.0 deg (e) α = -16.4 and +14.9 deg (f) α = -20.2 and +18.1 deg	85
30	Local Heating Rates as Functions of Angles of Attack (a) ϕ = 0 outer points, (b) ϕ = 0 mid points, (c) ϕ = 0 inner points, (d) ϕ = 180 deg (e) ϕ = 0 and 270 deg (f) ϕ = 90 and 270 deg (g) ϕ = 60 and 90 deg (h) ϕ = 30, 60 and 300 deg (i) ϕ = 300 deg (j) ϕ = 300, 330 and 354 deg (k) ϕ = 330 deg (l) ϕ = 354 deg	91
31	Heating Rate Distribution at Zero Angle of Attack for Low, Mean, and High Test Reynolds Numbers	103

Figure No.	Title	Page
32	Heating Rate Distribution at α Angle of Attack in the Test High Reynolds Number Range (b) α = 4 deg (c) α = 8 (d) α = 12 (e) α = 16 (f) α = 20	104
33	Heating Rate Distribution at α Angle of Attack in the Test Mean Reynolds Number Range (b) α = 4 deg (c) α = 8 (d) α = 12 (e) α = 16 (f) α = 20	109
34	Heating Rate Distribution at α Angle of Attack in the Test Low Reynolds Number Range (b) α = 4 deg (c) α = 8 (d) α = 12 (e) α = 16 (f) α = 20	114
35	Comparison of Radial Shifts in Pressure Stagnation Point and Point of Maximum Heat Transfer Rate for Equivalent Variation in α	119
36	Aeroshell Constant Heat Transfer Rate Contours at α Angle of Attack in the Test High Reynolds Number Range (b) α = 4 deg (c) α = 8 (d) α = 12 (e) α = 16 (f) α = 20	120
37	Comparison of Trip Runs and Non-Trip Runs at the Test High Reynolds Number Range	125
38	Base Heating Rates Along the Meridian Plane (ϕ = 0) with Variation in Angles of Attack between Zero and 20 Deg (a) High (b) Mean (c) Low	126
39	Base Heating Rates Along the Meridian Plane (ϕ = 0) at Model Tested at Two Angles of Attack, 0 and 11 deg over the Reynolds Number range from High to Low.	129

Figure No.	Title	Page
40	Base Heating Rates Along the Circle R = 0.61 R_B with Variation in Angles of Attack between Zero and 20 deg (a) High (b) Mean and Low	130
41	Base Heating Rate Distribution, Angle of Attack α = -30.5 deg	132

SUMMARY

An investigation in the Langley Research Center Mach-8 Variable Density Hypersonic Tunnel was made of the pressure distributions and heat transfer rate distributions on two 0.029 scale Viking Entry Vehicle models. Comparable ranges of test Reynolds number (R_e) were exercised for the two tests between high R_e run conditions around 4×10^6 and low R_e conditions of about 1.6×10^6.

At angles of attack less than 20 degrees the pressure ratio distribution (PRD) referended to stagnation pressure P_{t_2} appeared invariant with R_e. Increasing α results in a flatter distribution of both the windward and leeward pressure distributions; in addition, the stagnation point shifted into the windward plane.

Base pressures were uniform for the higher R_e test conditions and were of the same magnitude as the ambient static pressure, P_∞.

Model $\dot{q}$ measurements obtained from 53 sensors were normalized by the stagnation heat transfer rate $\dot{q}_s$ based on a separate reference hemisphere model test. Interpolated plots of Aeroshell distributions of heat transfer rate ratios, $\dot{q}/\dot{q}_s$, presented as a function of α illustrate the gradual shift in the region of maximum heating rates ($\dot{q}_{max} \approx 0.63$) toward the model windward region and the reduction in heating rates on the leeward side with increases in α up to 16 degrees.

A subsequent rise in the heating rate profile on the leeward side with further increase in α is attributed to boundary layer natural transition to turbulent flow.

Schlieren photographs were taken for flow field visualization and to correct model angle of attack.

Forced transition of the leeward boundary layer resulted in a measurable increase in heat rate over the pitch plane mid-cone surface. At $\alpha < 22$ degrees however, the increase in heat rate reduces near the cone edge. At $\alpha > 22$ deg the heat-rate increase resulting from natural transition prevails along the pitch plane leeward surface throughout.

I. INTRODUCTION

To verify the analytical predictions for the heating environment of the Viking Lander Capsule (VLC) Martian entry phase, it is necessary to determine experimentally the convective heat transfer rates to the VLC aeroshell and base cover surfaces. The present investigation provides pressure distributions and heat transfer distributions over the VLC at representative flight conditions.

On the basis of the common assumption of heat transfer rate ratio $(\dot{q}_i/\dot{q}_s)$ invariance with hypersonic Mach number, a wind tunnel investigation was implemented in the NASA/LRC Mach-8 Variable Density Tunnel (M-8 VDHT) for the measurement of the convective heat transfer over the VLC A S and BC surfaces.

In addition to the heat transfer model, an identical scale pressure model was provided to obtain pressure distributions at test conditions comparable to those of the heat transfer tests.

An additional test objective was to obtain near-wake temperature measurements for use in communication attenuation/blackout analyses. This portion of the investigation was completed during July 1972. The wake temperature data will be added as an Appendix subsequent to release of this document.

This investigation provides data under equilibrium flow conditions in air of specific heat ratio γ equal 1.4; a later investigation using these models is planned in the NASA/LRC Hypersonic Freon (CF_4) Tunnel to establish the equivalent heat transfer and pressure data in a test medium more nearly simulating the Martin CO_2 real gas environment.

The magnitude of the heating rate depends on the boundary layer state (laminar or turbulent). An assessment of the A/S boundary layer characteristics was made through boundary layer tripping surveys over the model leeward regions as can be seen from heating rate data.

The Mach-8 test Reynolds number (R_e) conditions for the pressure and heat-transfer tests are 3.5×10^6 and 4×10^6 (High), 2.8×10^6 and 2.8×10^6 (Mean) and 1.5×10^6 and 1.7×10^6 (Low) respectively.

These VLC pressure/heat-transfer tests were performed during the period of February 18 - March 2, 1972 and all the data obtained during this period are presented in this report.

II. DEFINITIONS

A. Symbols and Nomenclature

A	Reference area $\frac{\pi}{4} d^2$, .08735 ft^2.
a	Speed of sound, $a = 49.01 \sqrt{T\ (^oR)}$ (ft/sec) for air
C_p	Specific heat at constant pressure, C_p = .24 Btu/lb-^oR
C_v	Specific heat at constant volume, C_v = .17 Btu/lb-^oR
C_D	Drag force coefficient
d	Model diameter = 4.002 in = .333 ft
g	Acceleration of gravity, 32.17 ft/sec^2
h	Enthalpy (Btu/lb); heat transfer coefficient, or "film" coefficient defined as: $\frac{C_p \cdot (\omega) \frac{\partial T}{\partial t}}{T_{ad} - T_w}$
^oR	Degrees Rankine
M	Free stream Mach number, defined in tunnel by: $\frac{-b}{2c} + \left[\frac{b^2}{4c^2} - \left(\frac{a - \log_{10} P_o\ (psi)}{c}\right)\right]^{\frac{1}{2}}$ where: a = 69.731, b = -20.290, c = 1.494
P	Pressure (psi)
Pa	Barometric Pressure (psi)
Pr	Prandtl number $\frac{C_p \mu}{k}$
q	Dynamic pressure ($\rho V^2/2$)
$\dot{q}$	Heat transfer rate (Btu/ft^2-sec)
$\dot{Q}$	Heat transfer rate (Btu/sec)
Q	Total heat load (Btu/ft^2)

R_e	Reynolds number ($\rho Vd/\mu$)
R_{e_θ}	Reynolds number based on boundary layer momentum thickness. $\frac{\rho_e V_e \theta}{\mu_e}$
s	Curvilinear coordinate, surface length (in)
T	Temperature, (degrees Rankine)
t	Time, (sec)
V,u	Velocity (ft/sec)
X	Distance measured along longitudinal axis, (in)
Y	Distance measured along Y axis
Z	Distance measured along Z axis
α	Angle of attack (deg)
β	Angle of bow shock; angle of sideslip (deg)
γ	Ratio of specific heats, Cp/Cv
γ_E	Entry flight path angle, (deg)
δ	Boundary layer thickness, (in)
δ_L	Laminar boundary layer thickness, (in)
δ_T	Turbulent boundary layer thickness, (in)
δ^*	Boundary layer displacement thickness, (in)
ϵ	Density ratio, ρ_1/ρ_2
θ	Boundary layer momentum thickness, (in)
k	Total thermal conductivity, (Btu/sec-ft)
μ	Coefficient of viscosity (lb-sec/ft^2)
ρ	Density (slugs/ft^3)
ϕ	Roll angle (deg), denoting positioning of pressure/temperature sensors
η	Recovery factor, defined on page 15.
ℓ	Assumed width of A/S peripheral flange.

Subscripts

B	Base
E	Inertial entry conditions
e	Edge of boundary layer
i	Integer denoting pressure pickup or thermocouple
L	Local conditions
max	Maximum
N	Normal to surface
P	Parallel to surface
S	Stagnation conditions
t	Total conditions, time
w	Wall conditions
θ	Based on boundary layer momentum thickness
1	Ahead of shock wave
2	Behind shock wave
∞	Free stream conditions, static

B. Abbreviations and Acronyms

in	Inches
dia	Diameter
VLC	Viking Lander Capsule
α	Angle of Attack
A/S	Aeroshell
BC	Base cover
id	Inside diameter
od	Outer diameter

em	Electromagnetic
deg	Degrees in angular sense or degrees Rankine
Sta(s)	Station(s)
$\equiv$	Nominally equal to or "defined as"
$\dot{q}D$	Heat Transfer distribution
sec	Seconds
Hg	Mercury
BLIMPC	Boundary layer integral matrix procedure - Version C
PD	Pressure distribution
PRD	Pressure ratio distribution
$\dot{q}$	Heat transfer rate
$\dot{q}_{max}$	Maximum heat transfer rate
$\dot{q}_i/\dot{q}_s$	Heat transfer ratio, "heating rate", "heat rate"
EV	Entry vehicle
pos	Positive
neg	Negative

III. TEST DESCRIPTION

A. Test Facility

Pictorial views and operating description of the M-8 VDHT Test facility are given in Figures 1, 2 and 3.

The tunnel is supplied with tank stored air delivering a range in tunnel total pressure P_{t_1} from about 350 to 2800 psia at a constant Mach number of 8. The tunnel flow exhausts into the atmosphere when P_{t_1} exceeds 2300 psia. For P_{t_1} below this value the tunnel exhausts into a vacuum tank. The axisymmetric contoured nozzle test section measures 18 inches diameter, but the test core diameter ranges between 4 to 14 inches depending on the total pressure level. As stated in Figure 1, the tunnel air flow is heated electrically to provide the required test temperature environment to prevent air liquefaction.

The 4 inch diameter VLC model (Figure 2) is sting mounted on an injection mechanism which operates from an enclosure or housing below the test section. Model α - settings are approximated on the sting-mounted bracket adaptor where allowance is made for finite deflection occurring in the injection system caused by model airloads.

Post-test cooling of the model is accomplished by air cooling jets activated to impinge on the model retracted to the housing.

Figure 4 illustrates the operation envelope of the LRC M-8 VDHT.

B. Model and Instrumentation

Separate VLC pressure and heat-transfer stainless steel models of 0.029 scale were fabricated for the test program.

1. Pressure Test Model

A geometrically scaled pressure model (Figure 2) was assembled as shown in Figure 5.

The capsule attachment to the 0.75-inch-diameter sting is located in the lower region of the base cover away from pressure orifice locations. A small air gap is made to provide pressure equilibrium inside the model and to minimize both heat conduction from the A/S and model thermal warpage. The pressure model A/S surface thickness is about 0.09 inch.

The model pressure tubing installation is described in Reference 1. The fifty steel pressure tubes channeled from the model through the hollow sting were mated with a pinch-bar mechanism incorporated within the injection system housing. The pinch-bar mechanism permits holding an existing pressure level at the time the test run is terminated. The run can then be repeated as many times as required to eliminate pressure lag in the system. Flexible tubing completed in the pressure connection to the manometer board and the barocells.

Schlieren coverage of the model was monitored prior to and during each run. The schlieren photographs provide the means of determining the test angles-of-attack, α_T, within 0.1 - 0.2 deg accuracy.

2. Heat Transfer Model

The 2.9 percent scale heat transfer model of the VLC was fabricated for convective $\dot{q}$ measurements at tunnel operating conditions nearly similar to those employed in the pressure test. A drawing of the test article is presented in Figure 6 and a photograph of the model components is shown in Figure 7. The $\dot{q}$ model is of the thin skin type and equipped with 46 30-gage chromel/alumel thermocouples spot-welded to the inside

model surface at locations duplicating those defined for the pressure orifices of the pressure model. The model skin thicknesses measured at each thermocouple are listed in Figure 6. For the BC $\dot{q}$ measurements, special sensors are used to meet the requirement for high sensitivity: two Hy Cal calorimeters, responsive to $\dot{q}$-rates less than one Btu/ft^2-sec, were installed on the 40 and 62-deg frustums.

Further inboard on the 62-deg frustum and oriented at radial planes of ϕ = 30, 60, and 90 deg several thermocouple-type sensors (thin isolated discs) are installed that are similarly capable of sensitive measurements of low $\dot{q}$ values.

All $\dot{q}$-sensor wires were channeled through the sting support to the control room data system. While some of the BC $\dot{q}$ data were monitored as control-room real-time observables all the A/S and BC temperature data were transmitted directly to the remote Beckman digitizer system. A few A/S thermocouple readings were monitored in real time on strip chart displays.

To accomodate the A/S thermal expansion and to minimize heat conduction to the BC during test, a semi-elastic bond was devised between the A/S and BC. An A/S sleeve-extension was seated and retained in a RTV-filled circular groove machined into the base. Again, model α-settings were approximated on the sting mounting fixture prior to each run and then accurately determined by measurements on Schlieren pictures of the on-line model attitude.

3. Heat Transfer Sphere

A four-inch diameter stagnation heat transfer reference hemisphere was assembled as shown in Figures 8 and 9. This .35 inch thick polished hemisphere was instrumented with thermocouples on the inside

surface axisymmetrically about the stagnation point. The thermocouple locations include one at the central stagnation point and four on the X-Y axes at spherical-coordinate equi-angular marks of β = 9.5 deg. The skin thickness was measured at thermocouple locations and these data are listed in Figure 9.

The output of the five thermocouples was directed to the remote Beckman recording and digitizing system and also displayed as real-time curve plots in the control room.

C. Test Procedure

Run programs of the PD and $\dot{q}D$ tests are given in Tables I, II and III. The arrangement of instrumentation locations on the upper pitch plane necessiates running the model at numerically equal positive and negative α-settings to determine complete A/S data distributions over the representative flight α-range. The numerically equal (or approximately equal) positive and negative model α-settings are referred to as conjugate α-settings.

1. Pressure Test

Nominal conjugate α-settings at 4-degree intervals from α = 0 to $\pm$ 20 degrees (plus one additional run at α = -30 deg) were approximated for the High and Low R_e conditions. At zero-α one additional run was made at a Mean R_e. The duration of each run was governed by the tunnel operational constraints and by the model capacity to withstand the heat buildup. The model could remain in the test section 50-60 sec depending on the operating R_e. Since this operating time limitation conflicted with the equilibrium lag time inherent in the pressure system, it was necessary to repeat "accumulative" pressure runs. The model

pressure system pinch-bar mechanism was actuated to hold the existing Hg pressure columns level while tunnel shut down procedures, including cooling of the model, were followed. When the model was re-injected in the test section the pinch-bar mechanism was released allowing a new iterative pressure profile to appear on the manometer board. This entire procedure was repeated until the columns described a non-changing profile tantamount to pressure system equilibrium.

The manometer board levels were monitored on TV and also photographed prior to each sequential shut-down. For each on-line test condition the tunnel parameters were recorded and processed through the LRC Beckman/CDC digitizer/computer. The tunnel parameters were P_1, Pt_1, P_∞, T_{ad}, T_t, T_∞, V_∞, M_∞, R_e, q_∞, and P_a.

2. Heat Transfer Test

Table II defines the operating R_e conditions as High, Mean and Low. For each R_e the conjugate pairs of α_T-settings ranged from 0 to $\pm$20 degrees, at 4-degree intervals. One additional low-R_e run at α = -30.5 deg was included and one "extra low" (X-Low) R_e condition of 0.4×10^6 was attempted for $\alpha_T \approx 0$. The temperature time history on the model was monitored with a strip chart connected to several A/S thermocouples. Starting with model injection, the thermocouple typical temperature history develops as illustrated in Figure 10. The transient temperature data were also recorded on magnetic tape. As was the case during the pressure test, the effective model α_T's were measured approximations of the nominal αs specified for the test.

Special High-R_e $\dot{q}$ runs were made with the model containing a boundary layer trip (.005 in diameter wire) placed on the model leeward surface. Two additional high-α conditions, (α_T equal 22.2 and 26.2 deg) were also

tested in an attempt to induce natural transition in accordance with data in Reference 4. Schlieren photos taken prior to and during test conditions were used to define α_T accurately.

Representative schlieren views of the model at negative α's are presented in Figure 11.

3. Heat Transfer Reference Hemisphere Test

As listed in Table III, the stagnation $\dot{q}$ reference hemisphere was injected in the tunnel at four different R_e test conditions, X-Low, Low, Mean, and High.

The temperature time-histories recorded for the "shoulder" thermocouples provided heat transfer rates. These data, when combined with BLIMPC computer solutions of blunt-body $\dot{q}$-distribution, provided semi-empirical solutions of reference stagnation heat transfer rates $\dot{q}_s$.

Schlieren pictures of the hemisphere are presented in Figure 12.

IV. DATA REDUCTION AND PRESENTATION

The wind tunnel test parameters P_t, T_t, P_∞, P_a, were recorded vs time on magnetic tape for subsequent use in data reduction.

A. Pressure Test Data

When the pressure system equilibrium was reached the on-line condition was marked by simultaneous actuation of both the schlieren and manometer board cameras. The manometer photographs were scanned by a film reader to a resolution of 0.02 in Hg ($\approx$ .01 psi). Each pressure readout, P_i, was non-dimensionalized by the stagnation pressure, P_{t_2}. For each pair of conjugate runs from which the diametrical pressure distribution was determined, P_{t_2} is the stagnation pressure derived from interpolation of the windward pitch-plane peak pressures.

VLC base-pressures and pressures around the A/S corner were obtained with barocells and recorded at about three-second intervals for inclusion in the LRC Beckman/CDC data processing routine. Similarly, the tunnel static pressure was also recorded by the Barocell Beckman data link.

Schlieren views of the VLC operating at neg α_T's (pos α_T's not shown) are illustrated in Figure 11. The basic pressure data are plotted in Figures 13, 14 and 15.

Because of the discrepancies occurring between conjugate α_T-settings, the data were entered on a three-dimensional plot of radial (or surface-dimensional) PRD's with variation in α_T. Figure 16 introduces different data symbols which denote pressure-tap locations along A/S intersections of radial planes (through VLC body-axis of symmetry) identified by the ϕ-coordinates 0 and 180 deg, 90 and 270, 330, 300, 30 and 60 deg.

Figures 17 and 18 are quasi-isometric illustrations of A/S PDs for α = -11.2 and -30.3 deg. Also, an isobar plot has been prepared for α = -11.2 deg in Figure 19.

Radial and angular variations in base pressures are shown from basic in Figure 20 for α = -11.2 deg.

B. Heat Transfer Data

1. Aeroshell

The general equation (Reference 6) describing the transient heat-transfer process for the VLC blunt cone having a thin wall, $\Delta\sigma$, is:

$$\dot{q}_{\text{total (per unit area)}} = \dot{q}_{\text{convection}} + \dot{q}_{\text{conduction in skin}} + \dot{q}_{\text{radiation}} + \dot{q}_{\text{conduction to inside model}} \quad (1)$$

or

$$\rho C_p \Delta\sigma \frac{\partial T_w}{\partial t} = \left[h\,(T_{ad} - T_w)\right] + \left[k\Delta\sigma\left(\frac{\partial^2 T_w}{\partial X^2} \pm \frac{1}{X}\,\frac{\partial T_w}{\partial X}\right)\right] + \dot{q}_{\text{radiation}} + \dot{q}_{\text{conduction to inside of model}} \quad (2)$$

Justifications for neglecting the small radiation and conduction terms are given in Reference 5. Calculations of the radial conduction are given in the Appendix. Although generally negligible, the conduction terms do apply to areas of high temperature gradient such as the BC corner area. For α = 0 the heat conduction around the A/S corner from front to back is equivalent to a negative heating rate correction, $\Delta(\dot{q}_i/\dot{q}_s)$, pertaining to the BC peripheral thermocouple Station #15.

The basic data expression for local heat transfer coefficient, h, is defined as:

$$h = \frac{\rho C_p \Delta\sigma \dfrac{\partial T_{w_i}}{\partial T}}{(T_{ad} - T_{w_i})} = \frac{\dot{q}_i}{T_{ad} - T_{w_i}}$$

where the wall temperature rate of change was evaluated from data. The adiabatic wall temperature, T_{ad}, was acquired from the expression $T_{ad} = T_t \eta$; where η is the recovery factor (η = 0.90 for laminar and 0.99 for turbulent boundary layers). Figure 24 describes the temperature-dependent coefficient for specific heat, C_p, for the model material 17-4 PH stainless steel alloy composition listed in Table IV.

2. Reference Hemisphere

Stagnation $\dot{q}_s$ reference data are based on reference hemisphere thermocouple data and on BLIMPC computer runs of $\dot{q}$Ds over a sphere.

These sphere-test $\dot{q}_s$ quantities, corrected for the ratio of the VLC model nose radius to the reference sphere radius, were adjusted to reflect the explicit turnel operating P_t and T_t conditions (Table II) corresponding to each set of $\dot{q}_i/\dot{q}_s$ solutions.

The latter computations were made with reference to the Fay & Riddell expression for $\dot{q}_s$, reference 7.

C. Base Cover

The BC heating rates, detected by calorimeters and by thermocouple sensors, are evaluated independently in accordance with their respective calibrations. The two types of sensors were calibrated jointly in the laboratory to ensure compatibility in the low BC $\dot{q}$ environment.

V. DISCUSSION OF RESULTS

A portion of the figures presented in this report deals with the manual interpolation of the basic data. The different symbols relating the High, Mean and Low R_e run conditions are consistently maintained throughout the plotted data.

A. Pressure Distribution

The on-line tunnel condition coinciding with the attainment of model pressure system equilibrium are listed in Table I.

1. Aeroshell Basic Data

A/S radial PDs obtained from the $\phi = 0$, 180 deg pitch (meridian) plane pressure orifices are plotted for all test conditions in Figures 13, 14 and 15.

A radial shift in the windward pitch plane is seen in the stagnation-pressure region from the apex to $s/R_B = -.25$ with variation in α_T from 0 to -11.2 deg. At $\alpha = -20$ deg the stagnation point is observed at $s/R_B = -0.46$. Also, with increasing neg α a flattening trend is seen of the windward PDs along with a pressure decrease on the leeward side. Typical of the high-α leeward PD decrease is the appearance of the shallow bucket profile which is attributable to flow overexpansion occurring in the nose-cone tangency region.

The A/S PDs obtained for High, Mean and Low test conditions at $\alpha = 0$ were essentially congruent. Moreover, at A/S flight attitude ($\alpha = -11.2$ deg) the meridian-plane basic data PDs appear invariant with R_e.

2. Base Cover Basic Data

Radial BC PDs are shown in Figures 20 and 21. The significant point to be made about the BC PDs is that they are rather uniform and that they measure approximately 1 to 1½ percent of the stagnation pressure. In close agreement with earlier VLC Mach-8 BC pressure studies (Reference 6), the base pressures are very similar to the freestream static pressure, P_∞, which is superimposed (dashed lines) on all the BC pressure data.

For zero-α test condition, the pressure near the half-radius (R/R_B = .5) location shows a rise with increase in R_e. However, for α_t = -11.2 deg the test data do not suggest a similar R_e-dependency. Conversely, a slight amount of base-pressure α- dependency appears unaffected by variation in R_e.

Figures 22 and 23 present additional pressure data plotted at constant base radius. The near constant pressures maintained with variation in ϕ is almost independent of model α- variation.

3. Pressure Data Interpolation

The difficulty in aligning the model at nominal even alphas at 4-deg intervals was discussed in Section III. Although the basic data were obtained at attitudes which differed from the even-α settings, they were interpolated by the three-dimensional views of pressure profiles plotted against α_T as shown in Figures 16a-f. The interception of pressure-lines at even alphas is easily seen on these plots. The three-dimensional plot clearly shows that the pressure had not reached equilibrium for the run at α_T = +15.1 deg. Figure 17 clearly shows the flattening of the windward pressure distribution and the leeward pressure reduction with increase in

negative α. Also observed at high α is the local drop in pressure at the leeward hemisphere-nose/cone-body tangency intersection.

Minor discrepancies in conjugate data-sets may be traced to tunnel core-flow variations encountered with model installation changes. Figure 16b illustrates the pressures obtained diametrically across the A/S for ϕ-planes of 90 and 270 deg. These lateral pressure taps exhibit, at zero α, the characteristic pressure bump at the nose and the sloping off of pressure profile toward the cone edge. With increase in α, the lateral pressures decrease and assume a flatter profile. Ideally, the interpolated pressures should measure the same for conjugate pairs, but differences in flow fields with model positional variation in a nonuniform core give rise to data anomalies.

When used together, the interpolation plots are instrumental in developing Figures 17 and 18 which are idealized three-dimensional PRDs over the A/S operating at α = -11.2 deg at High R_e. The contrast between the windward and leeward flow regimes is evident in Figure 19 which represents a plan view of isobars contoured about a windward stagnation region at $R/R_B \approx 0.35$.

B. Heat Transfer Distribution

1. Aeroshell

Basic data obtained for the A/S ϕ = 0, 180 deg pitch plane are presented in Figure 25a-f . Each figure, listed consecutively by increasing α_T, depicts the conjugate sets of windward and leeward heat rate ratios obtained throughout the R_e-range.

At low α, the heating rate distribution ($\dot{q}D$) is nearly independent of R_e. Figure 26 shows the basic $\dot{q}D$ for the Low R_e run at α_T = -30.3 deg.

Complete A/S basic data are presented in Figures 27 through 29. Each figure represents an α_T condition and describes the radial ϕ-plane $\dot{q}Ds$ including, for comparison, the ϕ= 0 180 deg pitch plane solid-symbol data set.

Heating rates are plotted versus α for each thermocouple in Figures 30a-l.

A certain pattern of data fluctuation, or scatter, appears for these plots, particularly with positive α-settings, that has to do with the nonuniformity of the test core enthalpy profile.

A synthesis of all $\dot{q}$ data have been performed to develop the interpolated heating-rate plots for α = 0, $\pm$ 4, $\pm$ 8, $\pm$ 12, $\pm$ 16 and $\pm$ 20 deg as shown in Figures 31 through 34: for small α the windward $\dot{q}D$ tapers off from $\dot{q}/\dot{q}_s$ = 0.65 near the nose to about 0.4 at s/R_B = 0.8. Toward the cone edge the heating rate rises to 0.45 + before dropping to about 0.2 at the extreme edge. As α is increased, a flatter $\dot{q}D$ is seen to develop over both the windward and leeward pitch plane cone surfaces.

The pressure stagnation point and the point of $\dot{q}_{max}$ are seen to shift in the windward direction with variation in α.

For equivalent variations in α, however, the shift in $\dot{q}_{max}$ is very gradual when compared to the noticeable shift in pressure stagnation point (Figure 35). This may be due to a flow field velocity gradient build-up over the nose surface curvature. Conceptually, the $\sqrt{\partial w/\partial s}$ term constitutes the driving member of the equilibrium boundary layer $\dot{q}_s$-equation given by Fay & Riddell (Reference 7).

From examination of all $\dot{q}$ test data obtained for Stations #9 and #10 (s/R_B approximately equal 0.6 and 0.73 respectively), it is concluded that the heating rates are low relative to a faired distribution obtained when by-passing these test points. The sleeve, or flange, machined as an integral part of the A/S, and used as expansion point between the A/S and model base, acts as a heat sink. This results in losses in $\dot{q}$s at thermocouple Stations #9 and #10 located close to the sleeve.

The following observations are made of the A/S leeward heat transfer data. At low α the heating rate reduces from a 0.63 max value at or near the nose to a 0.4+ level along the cone. At greater values of s/R_B the level rises to 0.48. At higher α's (< 11.2 deg) the leeward mid-cone and edge heating rates rise to about 0.45 and 0.6 respectively. A further increase in α to $\pm$ 20 deg reverses the trend by lowering the leeward heating rate profile along the cone. Toward the A/S edge, however, a R_e-dependent rise in $\dot{q}/\dot{q}_s$ values appears which suggests the onset of boundary layer transition.

The $\dot{q}$ interpolation plots were used to estimate the planform plots of constant $\dot{q}/\dot{q}_s$ lines - iso- $\dot{q}/\dot{q}_s$ lines - as presented in Figure 36.

These idealized plots are symmetrical about the pitch plane and show the shift in stagnation region with increase in negative α. At α = -12 deg the region of $\dot{q}_{max}$ is recognized at $s/R_B \approx .06$. Less α-dependent is a belt-like pattern of iso-$\dot{q}/\dot{q}_s$ lines equal 0.5 seen to prevail around the peripheral region at $\alpha > 20$ deg.

Additional High-R_e, high-α runs with and without the wire boundary-layer forced-transition device are shown in sequence in Figure 37. Without the boundary layer trip the heating rate profile is being reduced with increase in α_T from 11.2 to 22.2 deg. At α = 26.2 deg a pronounced

increase in heating rate is seen attributable to the onset of transition to a turbulent boundary layer. With the wire trip placed in the vicinity of the nose-cone tangency region a pronounced increase in $\dot{q}$ appears over the mid-cone surface region. However, at α_T of 9.3 and (possibly) 15.1 deg the rise in $\dot{q}$ subsides to lower levels near the edge, possibly indicating a reversal to the laminar boundary layer state.

At α_T = 19.7 deg and 26.2 deg however, the trip-induced $\dot{q}$-increase persists in a strong transitional - or possibly turbulent - boundary layer state throughout.

2. Base Cover Frustums

For simplicity, the afterbody heating characteristics can be categorized into the following regions: the 40 deg frustum, the 62 deg frustum, or the outer separation regions, and the inner (flat) base or inner separation region.

The VLC base flow heating characteristics are shown in Figures 38 through 41. The BC $\dot{q}$ results were plotted in sets of three R_e and two α_T (0 and -11.2 deg.) conditions. The outer and inner thermocouple readings (Stas #15 and #18 respectively) are combined with the readings of the two calorimeters (Stas #16 and #17) located in between to form a characteristic $\dot{q}$ profile which prevailed throughout the test. The innermost base thermocouple on the 62-deg frustum exhibits higher heating rates than do the calorimeters located further out on the 62 and 40 deg frustum. In fact, the low values measured by the Hy Cals would imply that a low-temperature, low-density flow expansion about the 40 deg frustum occurs over a local region too remote to be affected by the thermally elevated base-recirculation flow fields. By contrast, the inboard Station 18 thermocouple is more accessible and hence more influenced by the base recirculation flow regime.

By the same reasoning, the pos-α runs result in the higher $\dot{q}$ profile in each conjugate set. Simple measurements of the differences between the heating rates for negative and positive α runs suggest that the R_e effect on the BC $\dot{q}$ is indirect in nature: the base-recirculation heating is relatively more pronounced at higher R_e.

In addition to Sta #18 thermocouple located at $\phi = 0$ on the 62 deg frustum, three similar sensors were installed at constant base radii at ϕ- angles of 30, 60 and 90 deg as measured from the pitch plane. The $\dot{q}$ results from these sensors appear in Figures 40 and 41. Heating rates $(\dot{q}/\dot{q}_s)$ less than 0.01 were obtained with neg-α runs whereas higher rates as high as 0.04 were measured for the positive -α runs.

The three sets of runs at nominal α's of 11.2, 16 and 20 deg performed with and without A/S boundary layer wire tripping devices were compared for base heat-transfer rates as shown in Figure 38a.

The BC heat transfer values denoting the tripped flow runs appeared slightly lower than the equivalent no-trip data. Speculations that this negative difference, although slight, be attributed to the trip run flow energy losses to the A/S may be countered by the argument of data uncertainty normally associated with heat transfer tunnel tests.

In Section III, the convective heat transfer rate was identified by equation 3 which assumes a very thin model skin. Sample calculations based upon this assumption appear in Appendix A. For the A/S corner region (Stas #13 and #15) showing the highest temperature gradient, the thermal conduction correction term $\Delta(\dot{q}_i/\dot{q}_s)$ may come to 0.044. In terms of heating rates measured for Sta #15, on the order of 0.08, the conduction correction provides a 50 percent reduction to the measured value.

VI. CONCLUSIONS

A/S and BC pressure and heat-transfer distribution measurements were obtained for two 0.029 VLC models tested in the LRC M-8 VDHT at αs between 0 and $\pm$ 20 deg. The ranges in R_e are between 3.5×10^6 and 1.5×10^6 for the pressure test and between 4.3×10^6 and 1.7×10^6 for the heat transfer test.

Results of the study led to the following conclusions:

1) A/S PRDs are nearly independent of variations in R_e.

2) Windward and leeward PDs vary in profiles with increase in α from the one diametrical/symmetrical profile at $\alpha = 0$ to the two flatter PD profiles appearing at $\alpha = 20$ deg.

3) BC PDs with High-R_e conditions are nearly uniform and match very closely the ambient free stream static pressure P_∞.

4) A/S radial plots at $\alpha = 0$ of heating rate ratios $\dot{q}_l/\dot{q}_s$, vary from about 0.63 at $s/R_B = 0$ to a low of 0.4 at $s/R_B = 0.5$. Variations in α result in flatter $\dot{q}$Ds over both the windward and leeward pitch plane surfaces. While the low-α $\dot{q}$D is unaffected by changes in R_e, the high-α $\dot{q}$D levels appear to rise slightly with increase in R_e.

5) BC heating rates are less than a few percent of the reference stagnation heat transfer rates. Radial distributions are characterized by an elevated $\dot{q}$ value for the inboard sensor which can be correlated with a thermally elevated near-wake circulation flow pattern.

VII. REFERENCES

1. Viking Aerophysics Data Book, VER-18 (TR-3720003), Martin Marietta Corporation, Denver Division, December 1971 (Revision E, May 1972).

2. Mars Engineering Model (M75-125-1), Langley Research Center, 08 December 1970.

3. R. Faye-Petersen, T. Surline, and S. Steinberg: "Pre-test Report for Entry Vehicle Model Convective Heat Transfer and Pressure Tests," TR-372031, Martin Marietta Corporation, January 1972.

4. R. A. Jones: Wind-Tunnel Measurements of Transition on the Face of a Blunt Entry Capsule at Angle of Attack, AIAA Journal, Vol. 6, No. 3, March 1968.

5. John R. Jack and N. S. Diacrnis: NASA Technical Note 3776, "Heat-Transfer Measurements on Two Bodies of Revolution at Mach Number of 3.12," NASA Lewis Flight Propulsion Laboratory, Cleveland, Ohio, October 1956.

6. W. Blake: MMC TR-3720106, "Experimental Aerodynamic Characteristics of the Viking Entry Vehicle Over the Mach Range 1.5 - 10.0," Martin Marietta, Denver Division, April 1971.

7. W. H. Dorrance, "Viscous Hypersonic Flow", McGraw-Hill Book Company, Inc., 1962.

8. Max Jacob: Heat Transfer, Vol. 1, John Wiley & Sons, Inc., New York, 1949.

TABLE I

2.9% MODEL PRESSURE TEST RUN PROGRAM

RUN NO.	MACH NO.	α (deg)	T_t (^oR)	P_{t_1} (psia)	P_{t_2} (psia)	P (psia)	$R_e \times 10^{-6}$ Based on Model Dia.	KNUDSEN NO. $\times 10^6$ Based on Model Dia.
5	7.94	.2	1404.6	1100.0	9.76	.114	1.5	7.8
8	8.07	.3	1472.2	2082.2	17.02	.224	2.8	4.3
11	7.99	.1	1459.9	2496.9	21.25	.225	3.3	3.6
14	8.01	-11.0	1462.6	2490.0	20.99	.260	3.3	3.6
17	7.93	-12.2	1425.6	1111.0	9.81	.116	1.7	6.9
19	7.98	-8.2	1469.5	2493.0	21.40	.253	3.3	3.6
21	8.00	-3.8	1466.6	2495.7	21.30	.253	3.3	3.6
22	7.99	-16.5	1470.6	2470.2	21.18	.254	3.3	3.6
23	7.95	-19.8	1464.2	2473.6	21.25	.256	3.3	3.6
26	7.91	-30.3	1446.2	1085.5	9.69	.115	1.5	7.8
27	7.99	5.2	1488.1	2484.0	21.22	.260	3.6	3.3
28	7.98	8.0	1467.7	2485.7	21.34	.255	3.5	3.4
29	8.01	12.0	1479.0	2483.0	20.93	.254	3.7	3.2
30	8.01	10.8	1489.6	2482.0	20.92	.255	3.4	3.5
32	7.93	9.7	1450.1	1084.9	9.59	.115	1.5	7.8
33	7.99	15.1	1476.6	2470.0	21.18	.262	3.5	3.4
35	7.97	20.0	1472.8	2469.0	21.21	.262	3.5	2.3

TABLE II

2.9% MODEL HEAT TRANSFER TEST RUN PROGRAM

RUN NO.	α (deg)	P_{t_1} (psia)	MACH NO.	P_{t_2} (atm)	$\dot{q}_s$ - $\frac{Btu}{Ft^2\text{-sec}}$	Re x 10^{-6} Based on Model Dia.	T_{t_1} ($^\circ$R)
1	+ 9.3	216.	7.797	.1397	10.36	0.4	1295
2	+ 10.0	1110.	8.011	.6373	26.2	1.6	1395
3	+ 10.6	2141.	8.087	1.1783	37.8	2.8	1475
4	+ 11.2	2843.	8.119	1.535	39.55	4.2	1360
5	+ 7.8	1108.	8.011	.6361	25.8	1.7	1380
6	+ 7.0	2107.	8.085	1.1596	36.62	2.9	1415
7	+ 7.7	2830.	8.118	1.528	39.02	4.1	1370
8	+ 3.4	1103.	8.011	.6332	26.75	1.5	1450
9	+ 3.4	2101.	8.085	1.1563	37.5	2.9	1425
10	+ 4.2	2823.	8.118	1.5258	40.1	4.0	1390
11	+ 14.9	1087.	8.009	.6251	25.3	1.9	1395
12	+ 15.0	2108.	8.085	1.160	38.6	2.8	1470
13	+ 15.0	2799.	8.117	1.5156	40.2	4.1	1370
14	+ 18.1	1130.	8.013	.6126	25.68	1.7	1395
15	+ 18.5	2110.	8.086	1.1612	37.81	2.9	1440
25	- 8.1	1102.	8.010	.6327	25.8	1.6	1395
26	- 8.2	2114.	8.086	1.1634	36.67	2.9	1435
27	- 8.3	2722.	8.114	1.470	38.1	3.8	1410
28	- 1.0	1092.	8.009	.6269	24.38	1.8	1335
29	- 0.8	2121.	8.086	1.1672	37.8	2.7	1480
30	- 0.4	2805.	8.117	1.515	40.0	4.0	1385
31	- 12.5	208.	7.792	.1345	9.55	0.3	1270
32	- 11.7	1090.	8.009	.6265	23.83	1.8	1335
33	- 11.5	2154.	8.088	1.185	36.25	3.0	1410
34	- 10.4	2756.	8.115	1.488	39.0	4.1	1355
35	- 16.4	1082.	8.008	.6212	24.4	1.8	1345
36	- 16.4	2115.	8.086	1.163	37.9	2.8	1470
37	- 16.4	2721.	8.114	1.473	40.7	3.8	1410

TABLE II (Continued)

RUN NO.	α (deg)	P_{t_1} (psia)	MACH NO.	P_{t_2} (atm)	$\dot{q}_s$ - $\frac{Btu}{t_t^2\text{-sec}}$	$R_e \times 10^{-6}$ Based on Model Dia.	T_{t_1} ($^\circ$R)
38	- 4.5	1094.	8.011	.628	25.7	1.7	1380
39	- 4.5	2107.	8.085	1.159	37.07	2.8	1445
40	- 4.0	2829.	8.118	1.532	41.80	3.8	1425
41	- 20.2	1101.	8.010	.6321	25.86	1.7	1375
42	- 20.2	2100.	8.085	1.156	36.2	2.8	1470
43	- 20.0	2822.	8.118	1.528	39.1	4.2	1360
44	- 30.5	1104.	8.011	.6338	26.36	1.6	1405
45	+ 9.5	2824.	8.118	1.529	39.57	4.2	1360
46	+ 15.6	2817.	8.118	1.525	40.60	3.9	1405
47	+ 15.1	2802.	8.117	1.517	40.1	4.0	1390
48	+ 19.7	2816.	8.118	1.524	39.62	4.1	1365
49	+ 22.2	2808.	8.117	1.520	39.96	4.0	1390
50	+ 26.2	2830	8.118	1.532	40.4	4.0	1405

TABLE III

REFERENCE HEMISPHERE PROBE RUN PROGRAM

Sphere dia. = 4 in

RUN NO.	MACH NO.	T_t (^oR)	P_{t_1} (psia)	P_{t_2} (atm)	P_{∞} (psia)	$\dot{q}_s$ (Btu/ft^2-sec)	R_e	
1	7.794	1244.5	210.9	.1372		6.173	.4 x 10^6	X-Low
2	8.01	1413.9	1104.6	.6355		16.110	1.7 x 10^6	Low
3	8.085	1484.1	2106.8	1.1621		23.13	2.8 x 10^6	Mean
4	8.116	1422.9	2765.9	1.4998		23.45	3.9 x 10^6	High

TABLE IV

COMPOSITION OF 17-4 PH STAINLESS STEEL

COMPOSITION OF 17-4 PH		
MATERIAL	SYM.	COMPOSITION, PERCENT
Carbon	C	.043
Manganese	MN	.24
Phosphorus	P	.017
Sulfur	S	.017
Silicon	SI	.52
Chromium	CR	15.59
Nickel	NI	4.40
Copper	CU	3.47
Columbium	CB	.22
Tantalum	TA	.01

LANGLEY MACH 8 VARIABLE-DENSITY HYPERSONIC TUNNEL

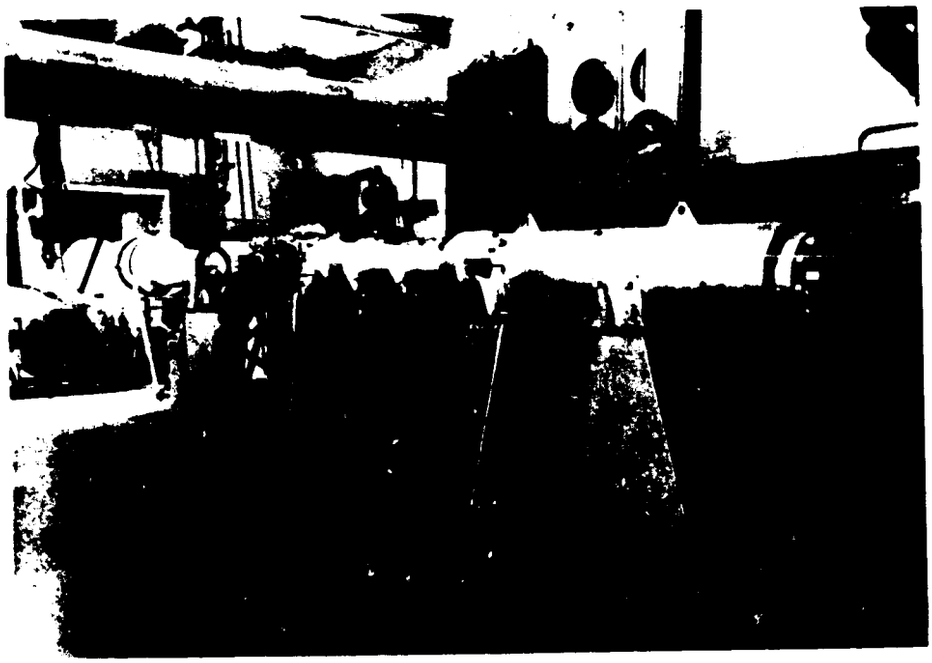

L-61-2866

The Langley Mach 8 variable-density hypersonic tunnel is located in Building 1247D and is under the direction of the Aero-Physics Division. This tunnel is used for fundamental aerodynamic and fluid dynamic investigations over large Reynolds number ranges using pressure and heat-transfer measurements. The test medium is air and is heated by a combination of Dowtherm and electrical resistance. Model mounting consists of sting mount with injection mechanism. The tunnel has an axially symmetric contoured nozzle. The test-section diameter is 18 inches, and the test core size is 4 inches to 14 inches depending on pressure. It exhausts into a vacuum tank or atmosphere. Examples of operating conditions are as follows:

Stagnation pressure, psia	15 to 2930
Stagnation temperature, ^{o}R	1160 to 1510
Mach number	7.5 to 8.0
Reynolds number per foot	0.1×10^6 to 12.0×10^6
Running time, sec, for -	
Exhausting into vacuum tank	90
Exhausting into atmosphere	600

Repeatability
@2500 psi repeatability $\simeq$ 30 psi/run to run
@ 200 psi repeatability $\simeq$ 5 psi/run to run

Total Temperatures for given Total Pressures

P_{t_1} = 304 psi	T_t = 1236 ^{o}R
= 1100 psi	= 1390 ^{o}R
= 1864 psi	= 1396 ^{o}R
= 2500 psi	= 1415 ^{o}R

Insertion G Force $\simeq$ 50 g

Figure 1 Langley Mach 8 Variable-Density Hypersonic Tunnel Description

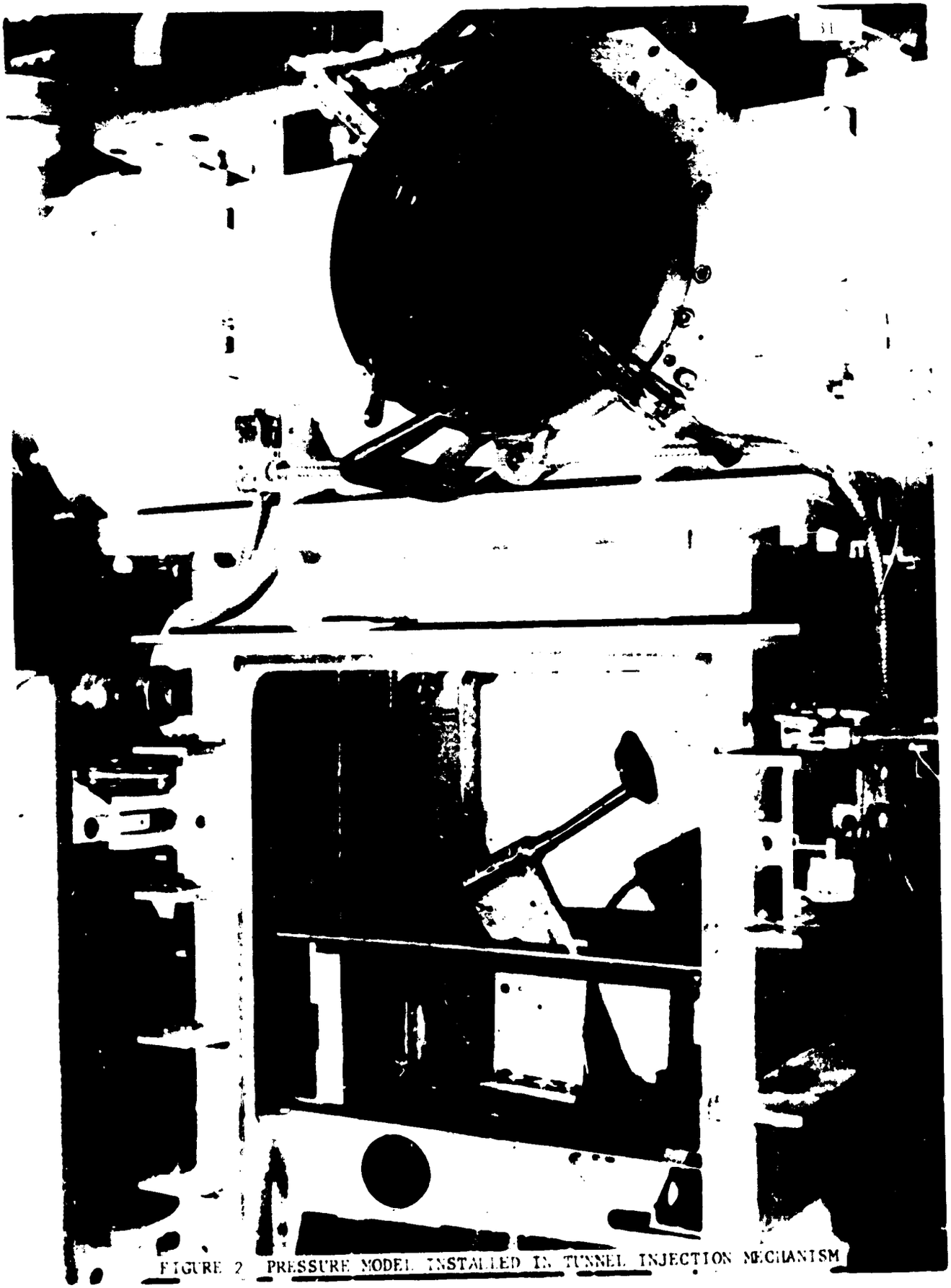

FIGURE 2 PRESSURE MODEL INSTALLED IN TUNNEL INJECTION MECHANISM

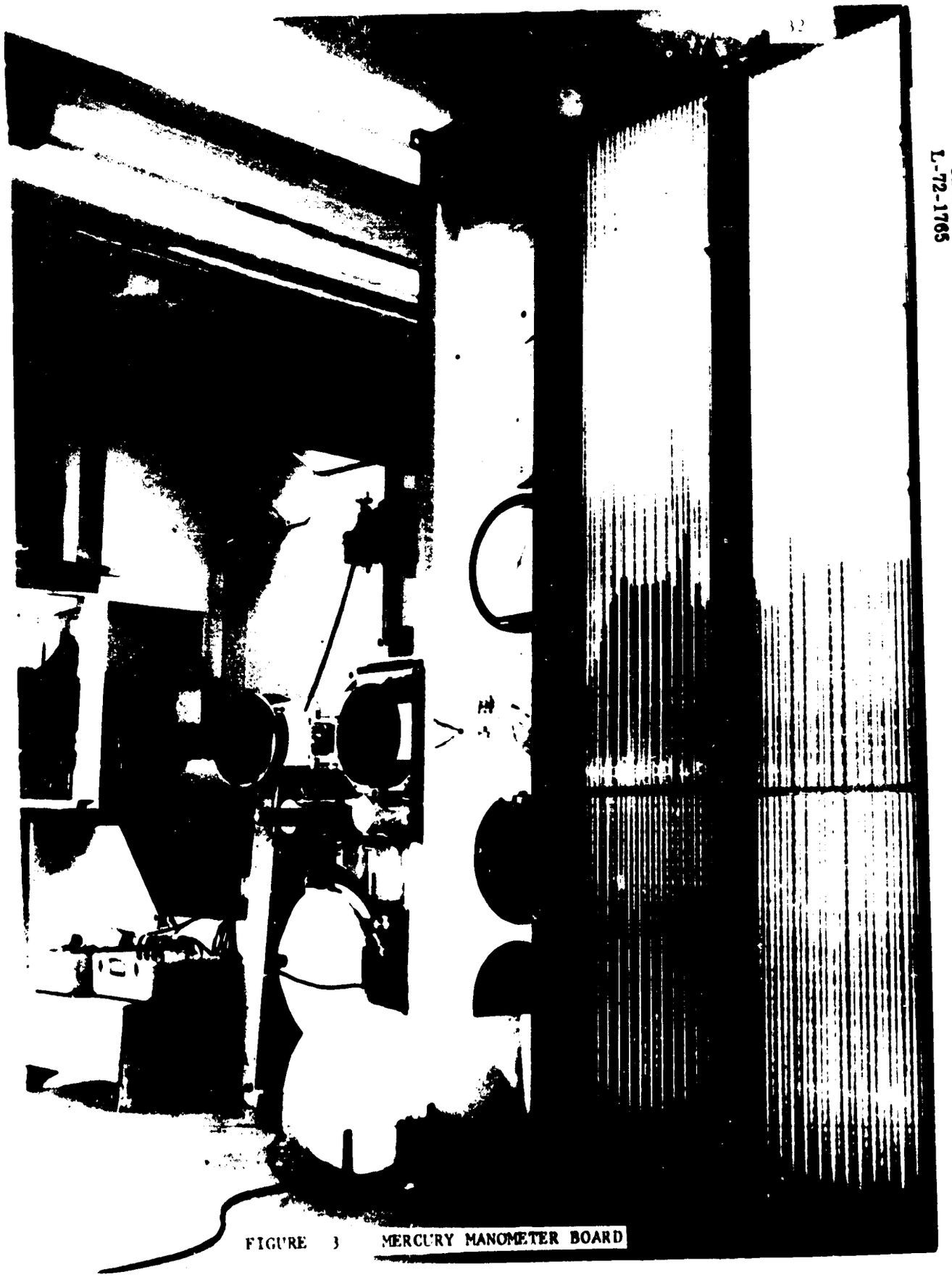

NASA
L-72-1765

FIGURE 3 MERCURY MANOMETER BOARD

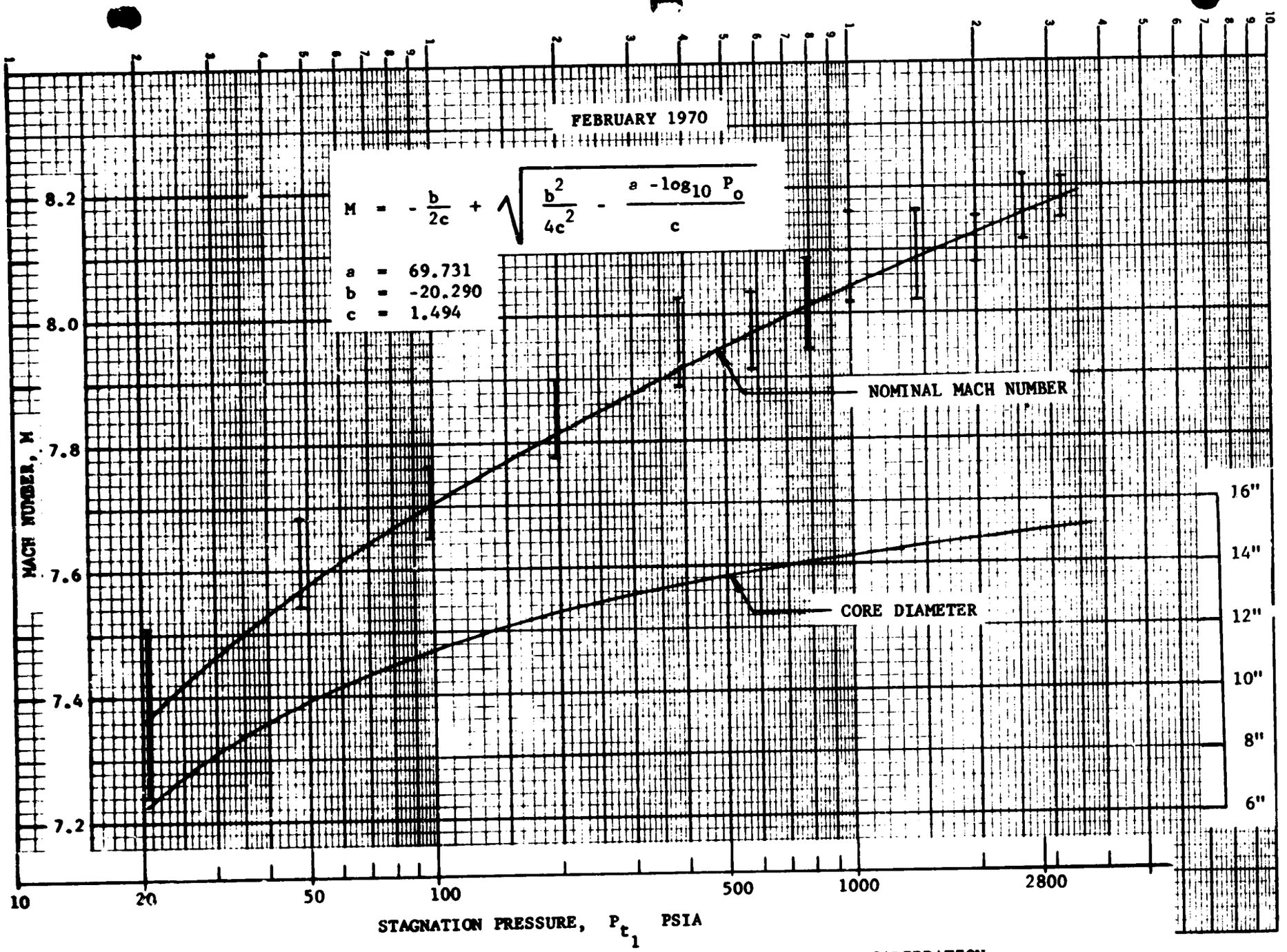

FIGURE 4 LANGLEY MACH 8 VARIABLE-DENSITY HYPERSONIC TUNNEL CALIBRATION

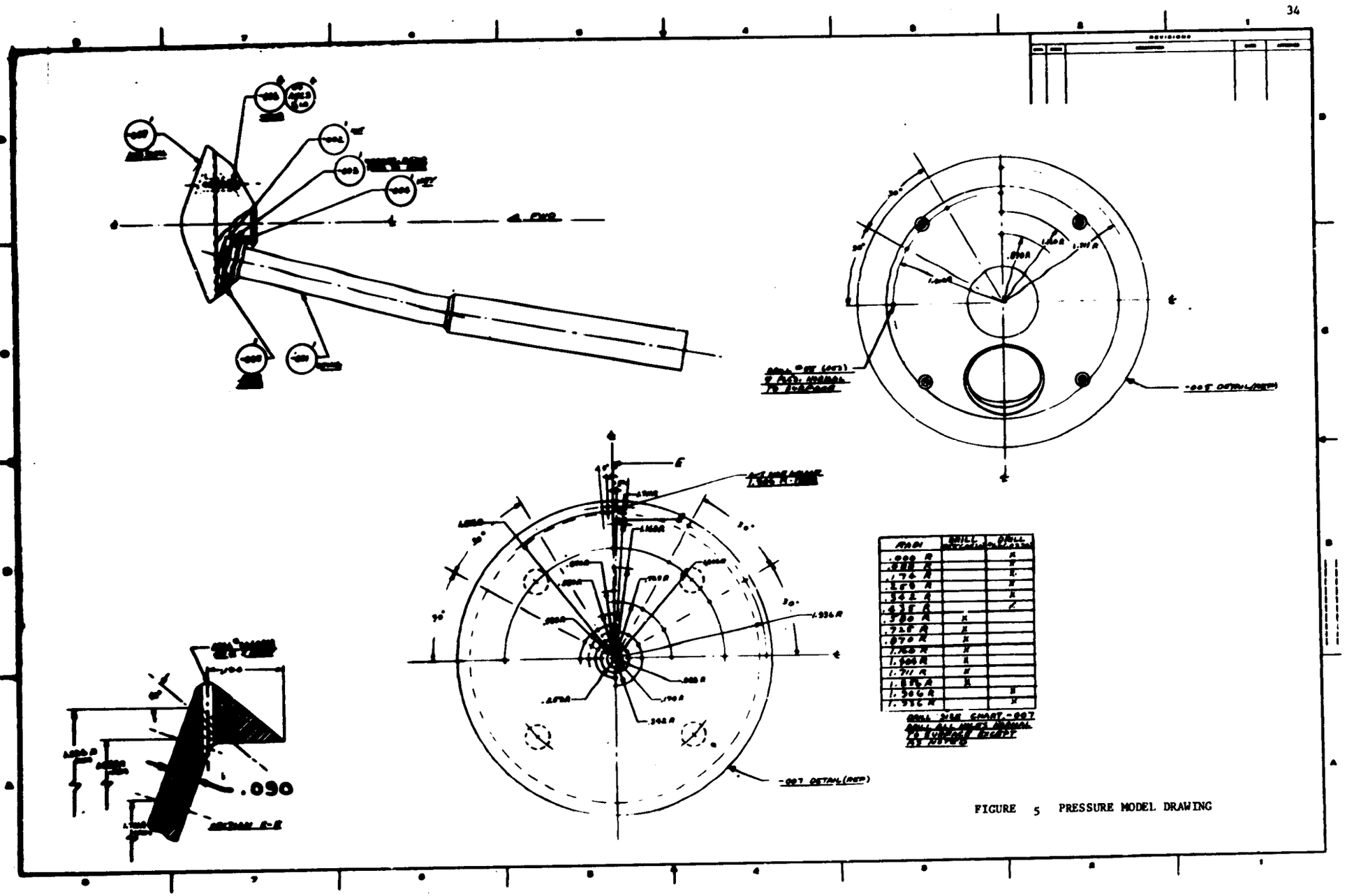

FIGURE 5 PRESSURE MODEL DRAWING

FOLDOUT FRAME

STATION NUMBER	RADIAL LOCATION DEGREES	CHORD LENGTH INCHES	WALL THICKNESS INCHES
0	0°	0.000	.0358
1		.088	.0358
2		.174	.0353
3		.259	.0336
4		.342	.0330
5		.435	.0330
6		.580	.0331
7		.725	.0325
8		.870	.0318
9		1.160	.0310
10		1.404	.0300
11		1.711	.0300
12	0°	1.856	.0300
13	354°	1.936	.0175
14	354°	1.986	.0170
15	0°	1.906	.0165
16		1.711	*
17		1.404	*
18	0°	1.160	.0240
19	270°	1.871	.0300
20	30°	.259	.0348
21	30°	.435	.0338
22	60°	.259	.0356
23	60°	.435	.0333
24	90°	.259	.0350
25		.342	.0333
26		.435	.0332
27	90°	1.404	.0290
28	180°	.088	.0358
29		.174	.0353
30		.259	.0356
31	180°	.342	.0331
32	270°	.174	.0350
33		.342	.0332
34		.725	.0331
35		1.404	.0287
36	270°	1.936	.0170
37	300°	.174	.0353
38		.342	.0332
39		.725	.0316
40		1.404	.0286
41	300°	1.936	.0170
42	330°	.174	.0340
43		.342	.0347
44		.725	.0346
45		1.404	.0296
46	330°	1.936	.0170
47	270°	1.404	.0240
48	300°	1.404	.0240
49	330°	1.404	.0240
50	300°	1.871	.0300
51	330°	1.871	.0300

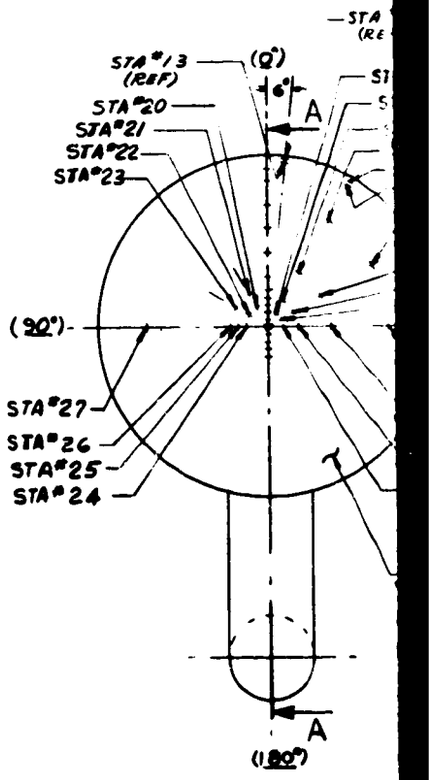

* HY-CAL CALORIMETERS LOCATED AT STATIONS #13 & #17. THEIR CALIBRATION DATA POINTS ARE IDENTIFIED IN THE COLUMN ABOVE BY AN ASTERISK (*) ARE 0.488 & 0.465 MICRO VOLTS/B.T.U. RESPECTIVELY.

FOLDOUT FRAME

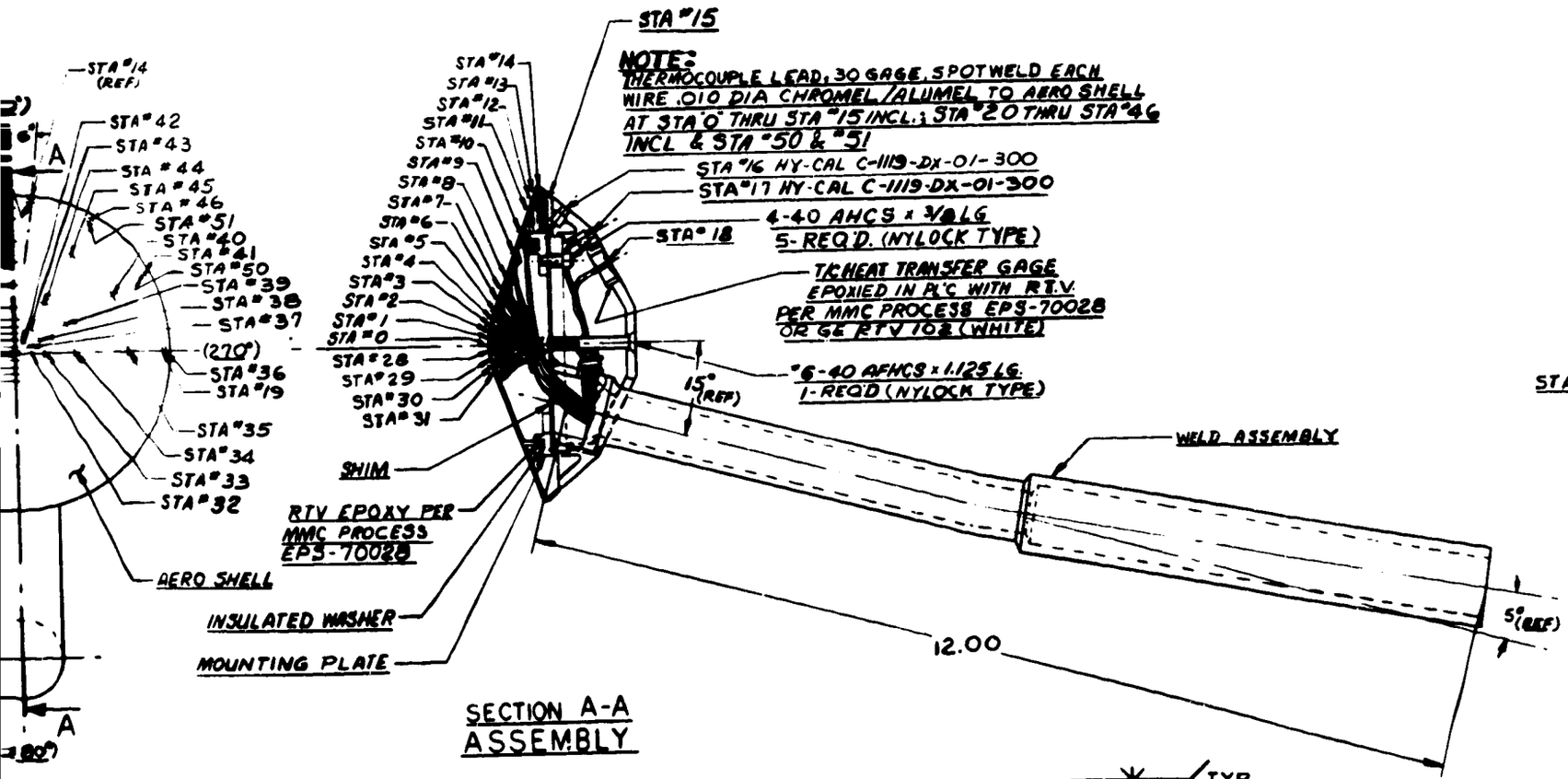

SECTION A-A
ASSEMBLY

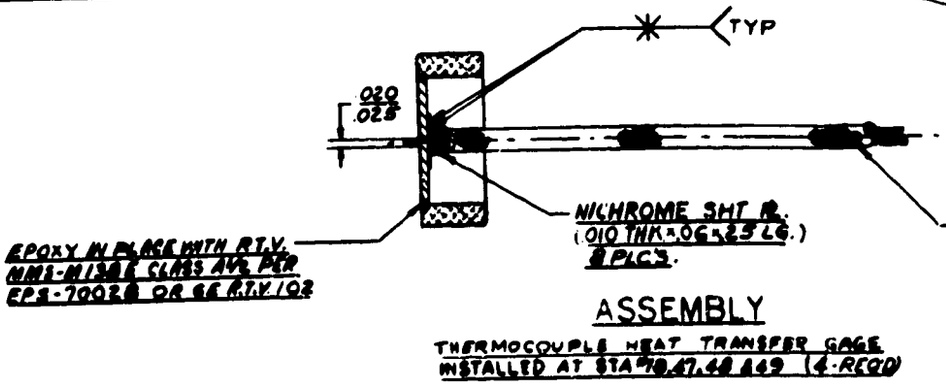

ASSEMBLY

THERMOCOUPLE HEAT TRANSFER GAGE INSTALLED AT STA "0, 47, 48 & 49 (4-REQD)

FOLDOUT FRAME

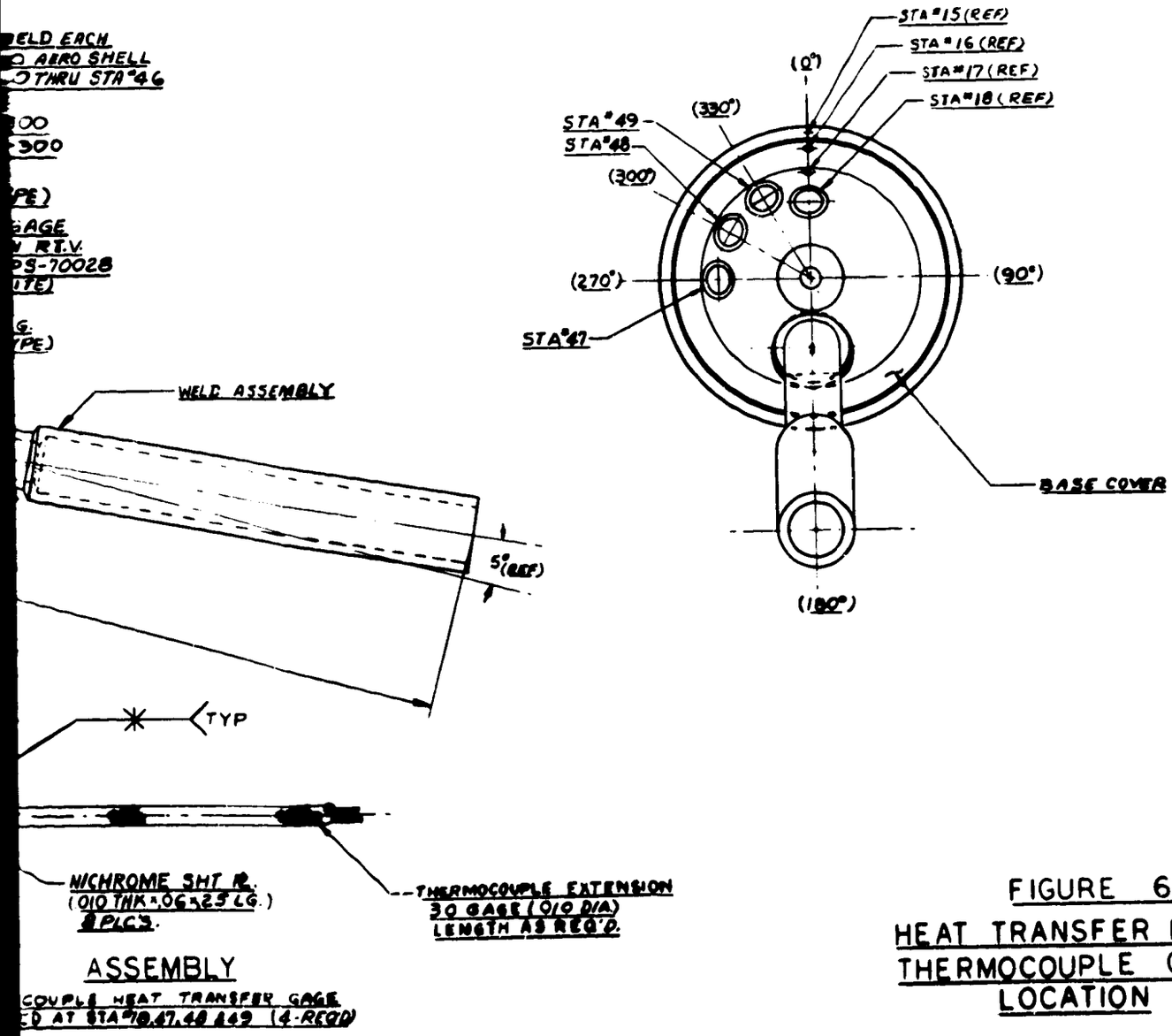

FIGURE 6

HEAT TRANSFER MODEL THERMOCOUPLE GAUGE LOCATION

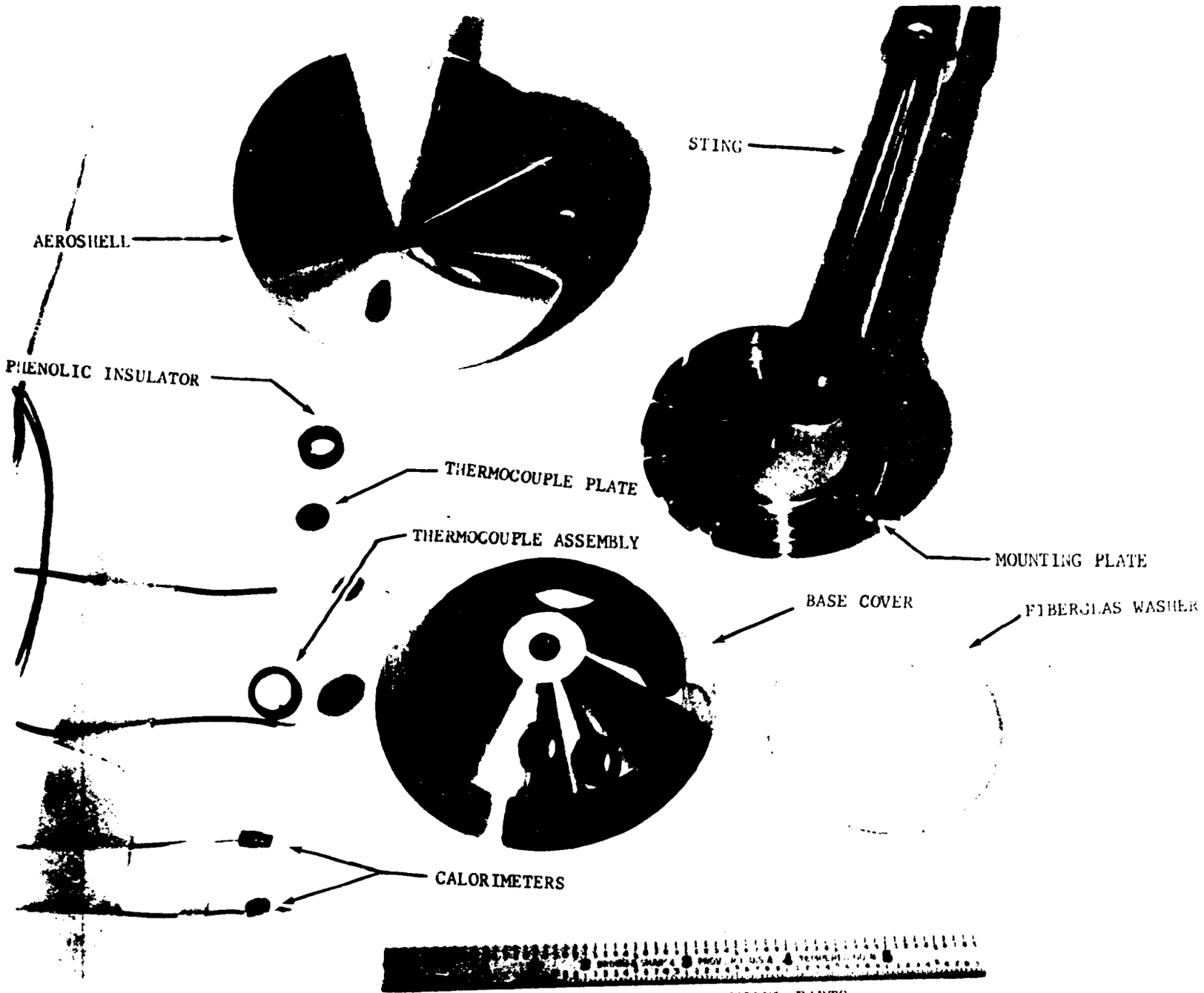

FIGURE 7 HEAT TRANSFER MODEL PARTS

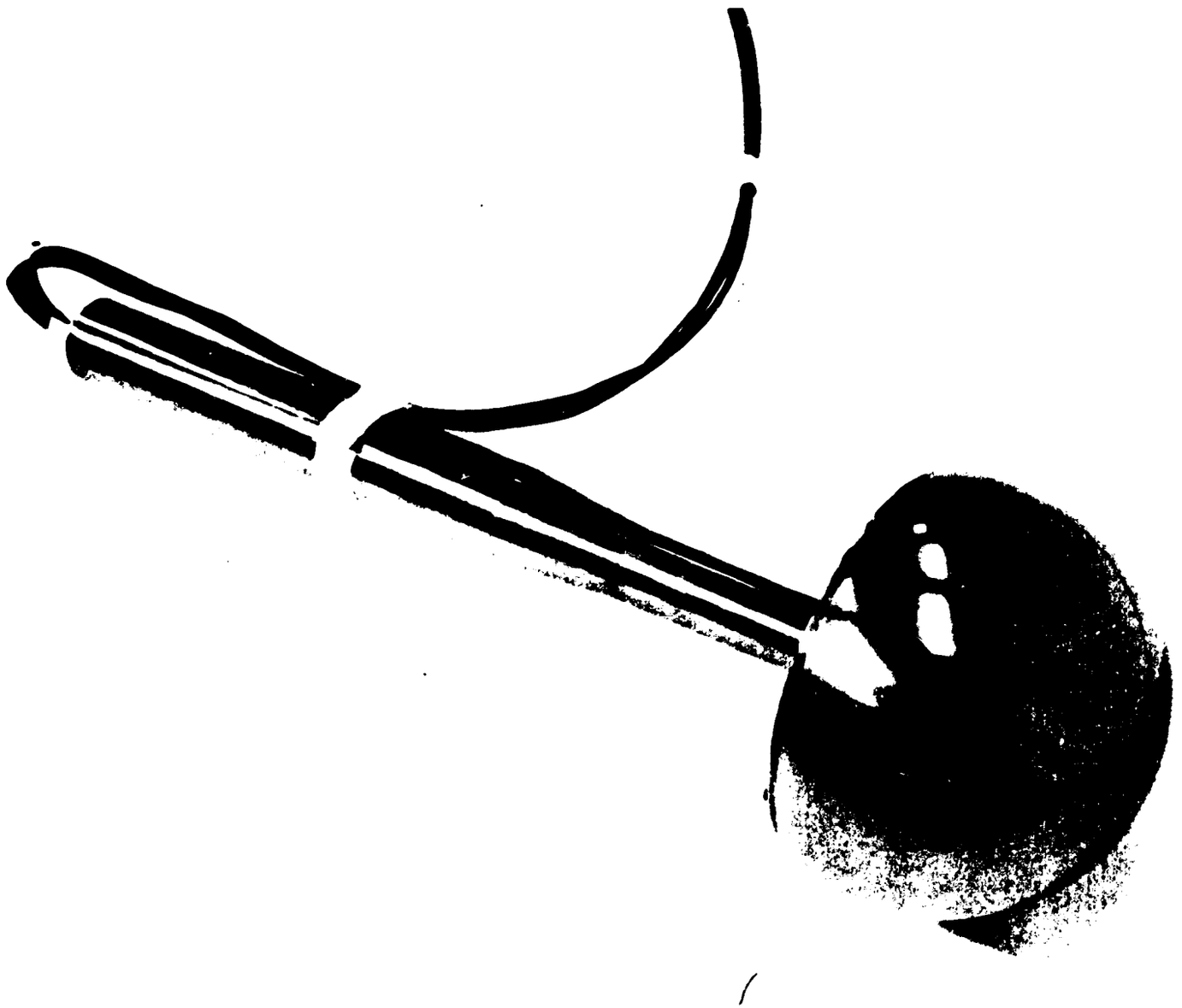

FIGURE 8 FOUR-INCH STAGNATION HEAT TRANSFER CALIBRATION HEMISPHERE

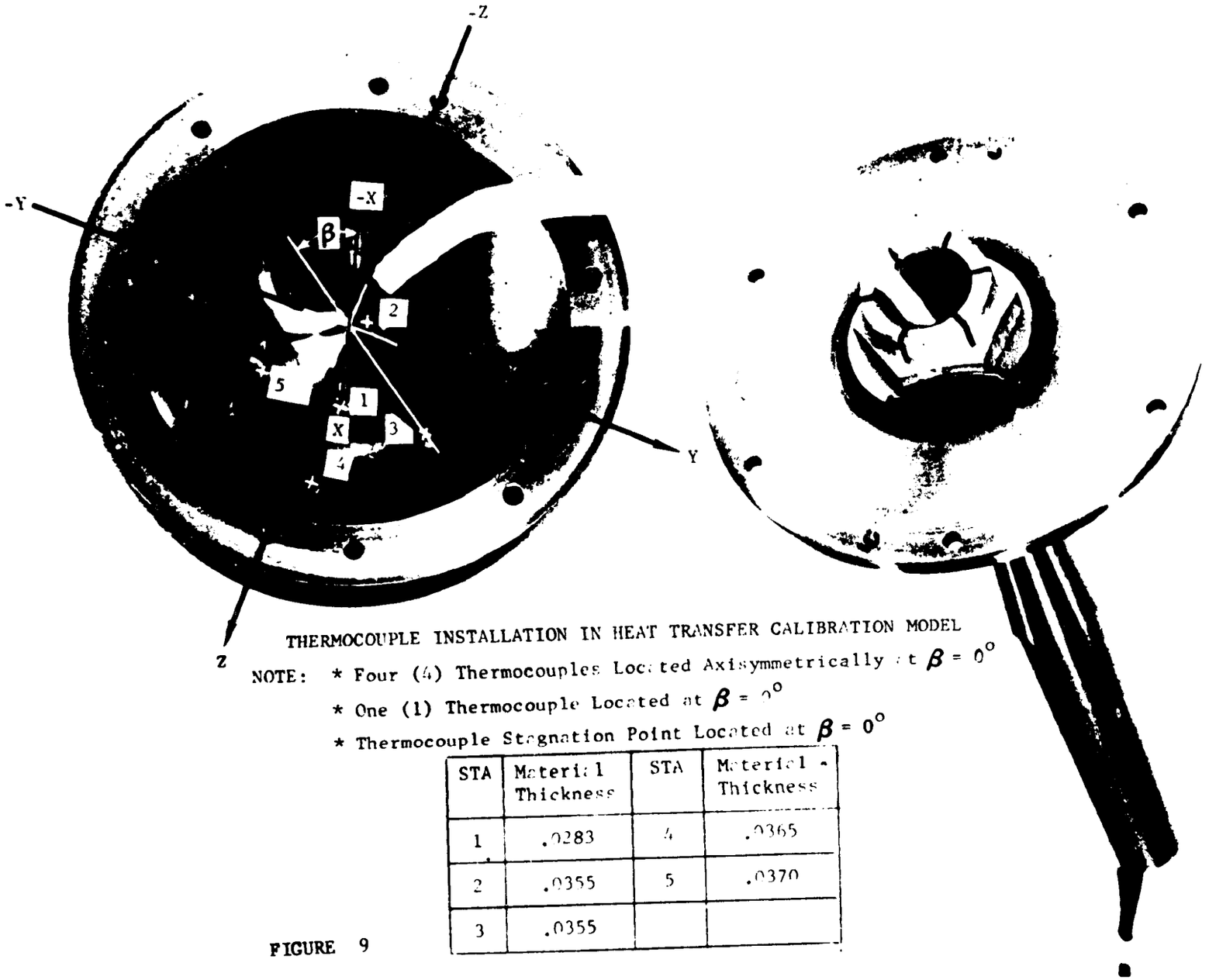

THERMOCOUPLE INSTALLATION IN HEAT TRANSFER CALIBRATION MODEL

NOTE: * Four (4) Thermocouples Located Axisymmetrically at $\beta = 0^{\circ}$

* One (1) Thermocouple Located at $\beta = 0^{\circ}$

* Thermocouple Stagnation Point Located at $\beta = 0^{\circ}$

STA	Material Thickness	STA	Material Thickness
1	.0283	4	.0365
2	.0355	5	.0370
3	.0355		

FIGURE 9

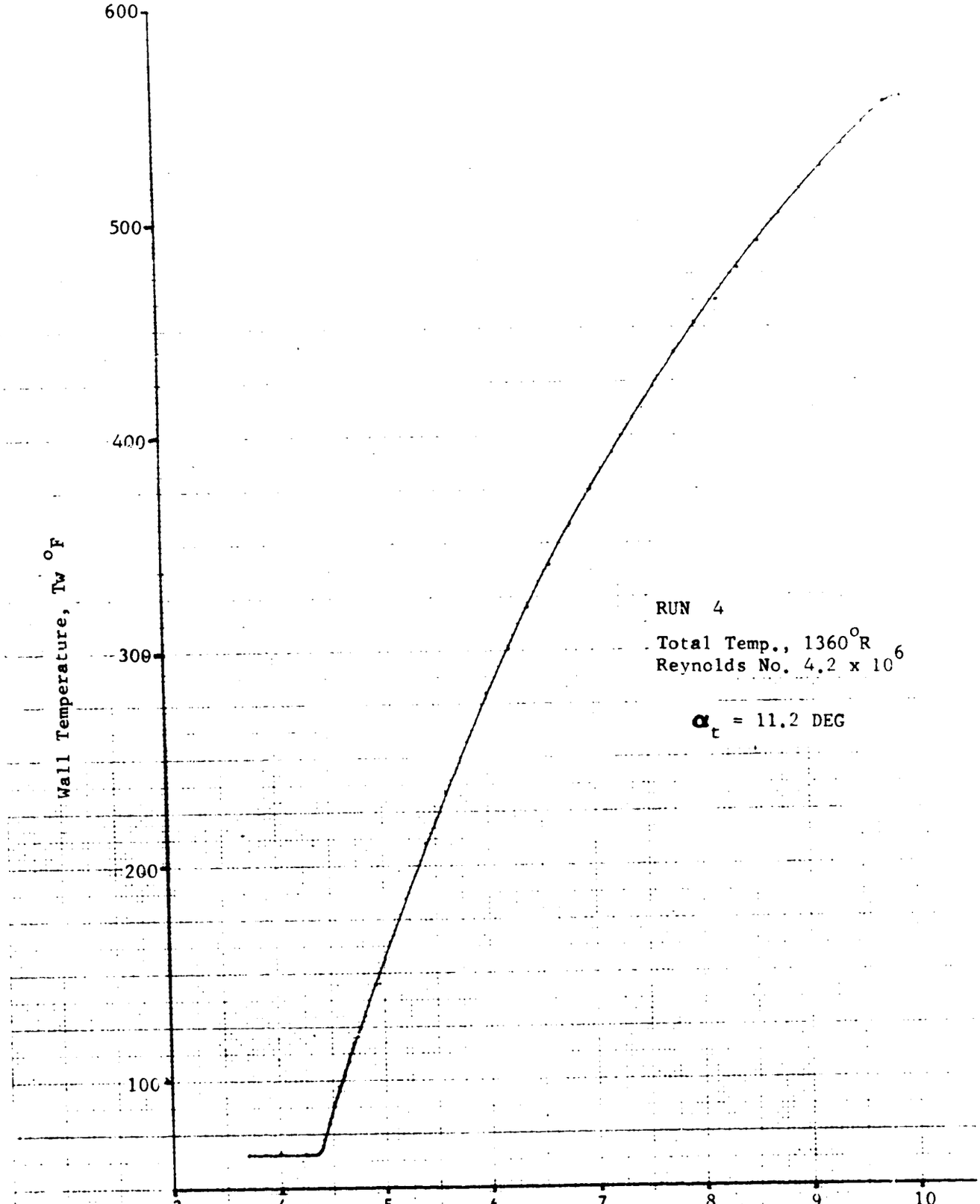

Figure 10 VLC Model Wall Temperature Time History for Station 0.

FOLDOUT FRAME

FOLDOUT

$R_e = 3.5 \times 10^6$

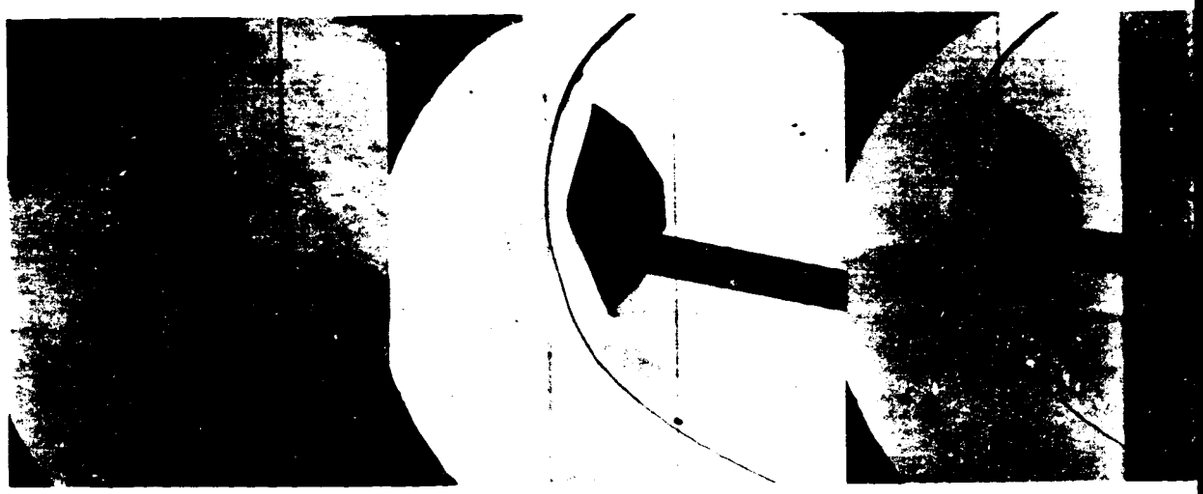

α = .1 deg -3.8 deg -8.2 deg

$R_e = 1.5 \times 10^6$

α = 0 deg

FIGURE 11 SCHLIEREN PHO

FOLDOUT FRAME

-8.2 deg -11 deg -16.5 deg -?.8 deg

-12.2 DEG.

URE 11 SCHLIEREN PHOTOGRAPHS OF THE VLC MODEL TESTED IN THE LRC MACH-8 VARIABLE DENSITY HYPERSONIC WIND TUNNEL

FOLDOUT FRAME 3

-19. 8 deg

-30. 3 deg

FOLDOUT FRAME

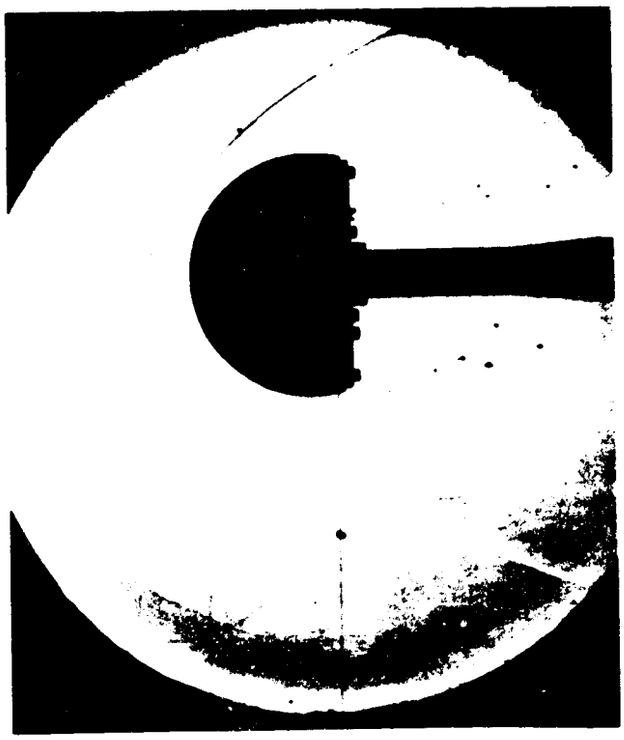

M = 7.8

$R_e = 0.4 \times 10^6$

M = 8

$R_e = 1.7 \times 10^6$

FIGURE 12 SCHLIEREN PHOTOGRAPHS OF REFERENCE HEMISP
VARIABLE DENSITY HYPERSONIC WIND TUNNEL

BOILERPLATE FRAME

M = 8.1

$R_e = 2.9 \times 10^6$

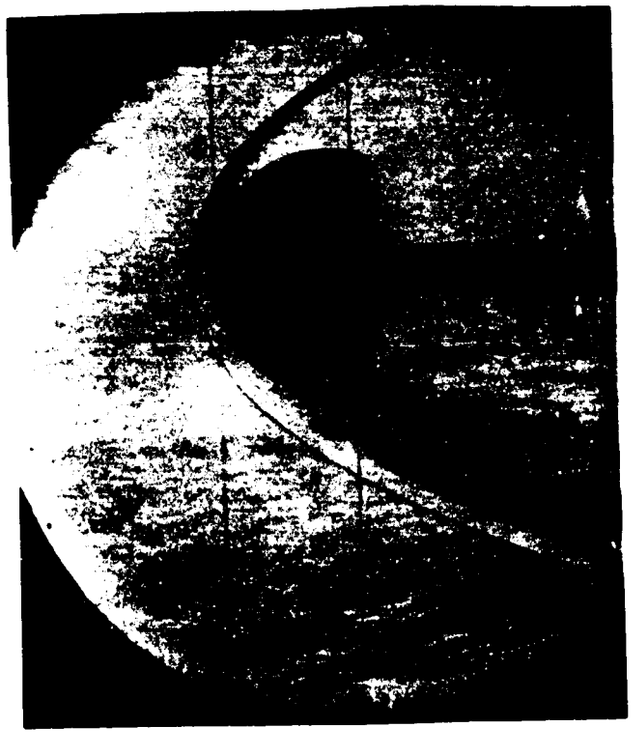

M = 8.1

$R_e = 3.9 \times 10^6$

HEMISPHERE TESTED IN THE LRC MACH-8 TUNNEL

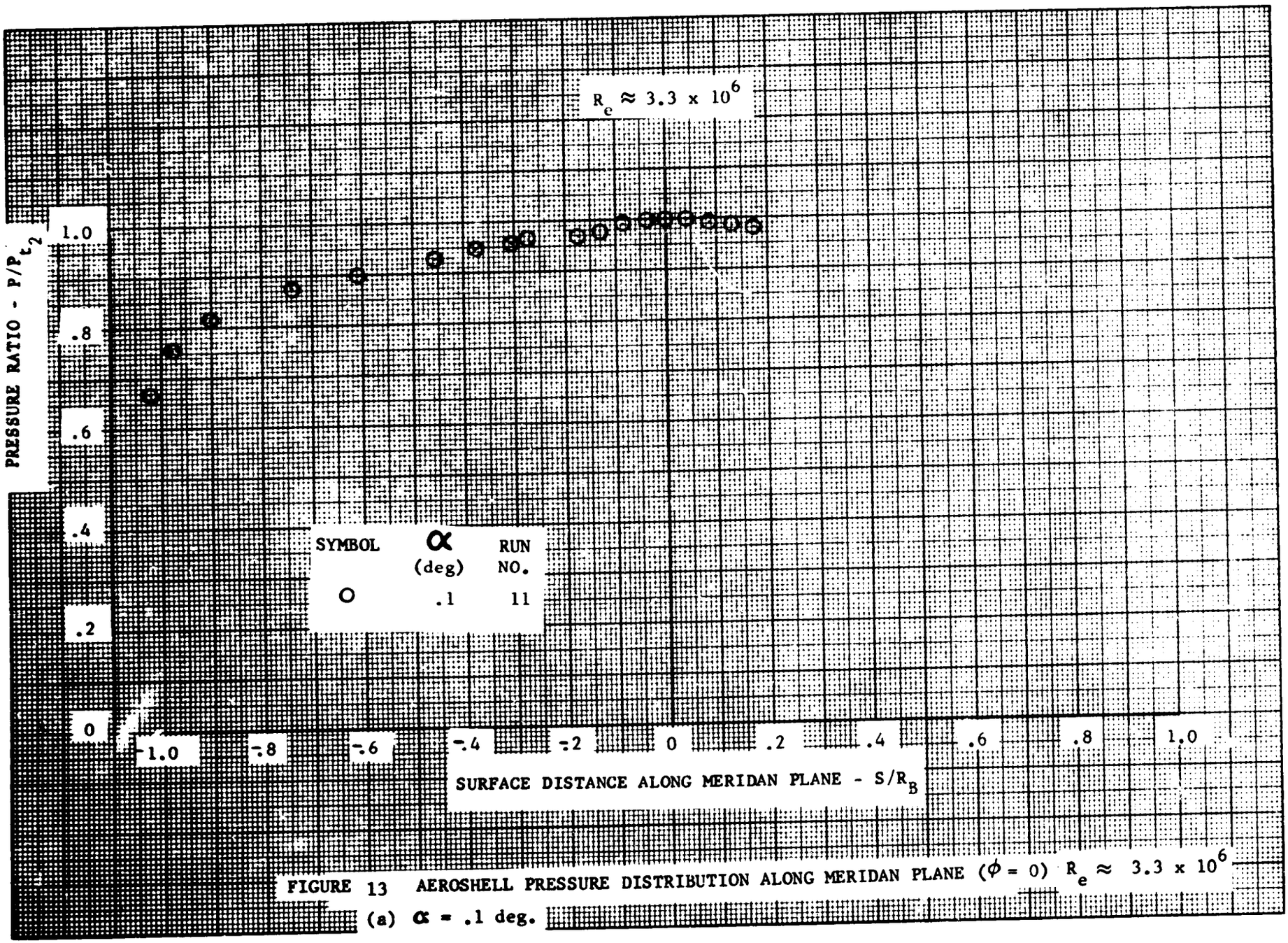

FIGURE 13 AEROSHELL PRESSURE DISTRIBUTION ALONG MERIDAN PLANE ($\phi = 0$) $R_e \approx 3.3 \times 10^6$

(a) $\alpha = .1$ deg.

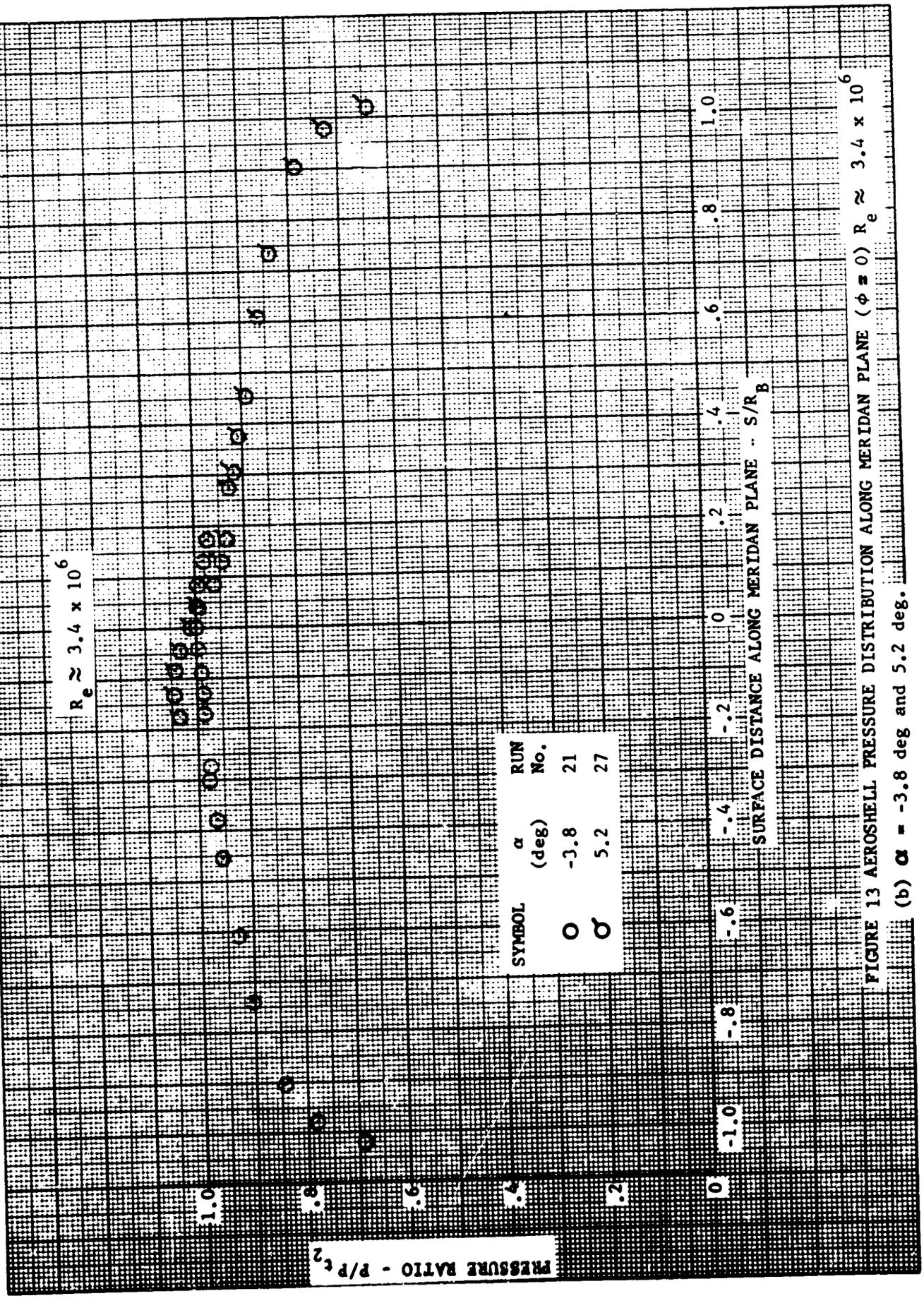

FIGURE 13 AEROSHELL PRESSURE DISTRIBUTION ALONG MERIDAN PLANE ($\phi = 0$) $R_e \approx 3.4 \times 10^6$

(b) α = -3.8 deg and 5.2 deg.

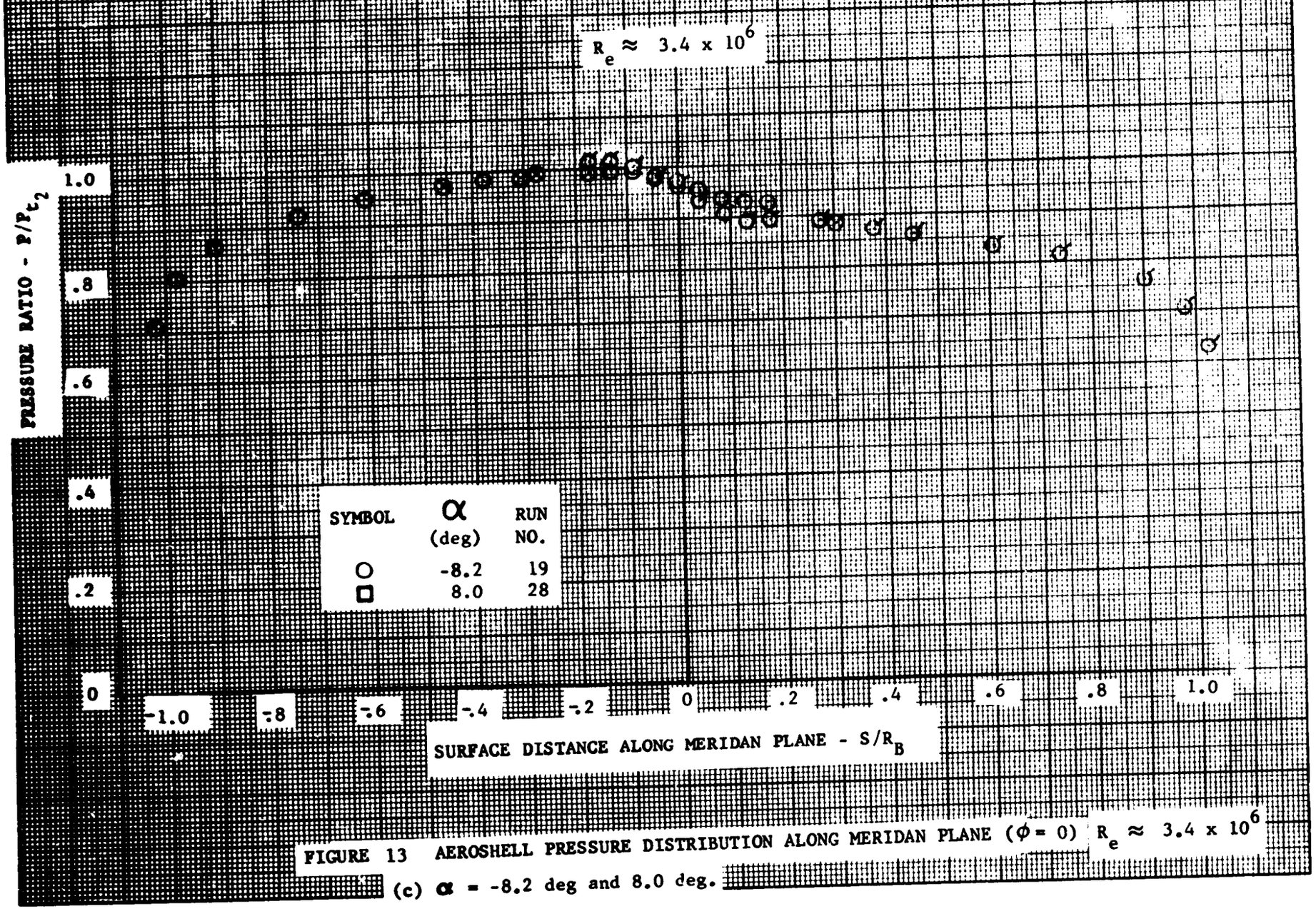

FIGURE 13 AEROSHELL PRESSURE DISTRIBUTION ALONG MERIDAN PLANE ($\phi = 0$) $R_e \approx 3.4 \times 10^6$

(c) α = -8.2 deg and 8.0 deg.

K•E 10 X 10 TO THE CENTIMETER 46 1517
18 X 25 CM • ALBANENE®
KEUFFEL & ESSER CO.

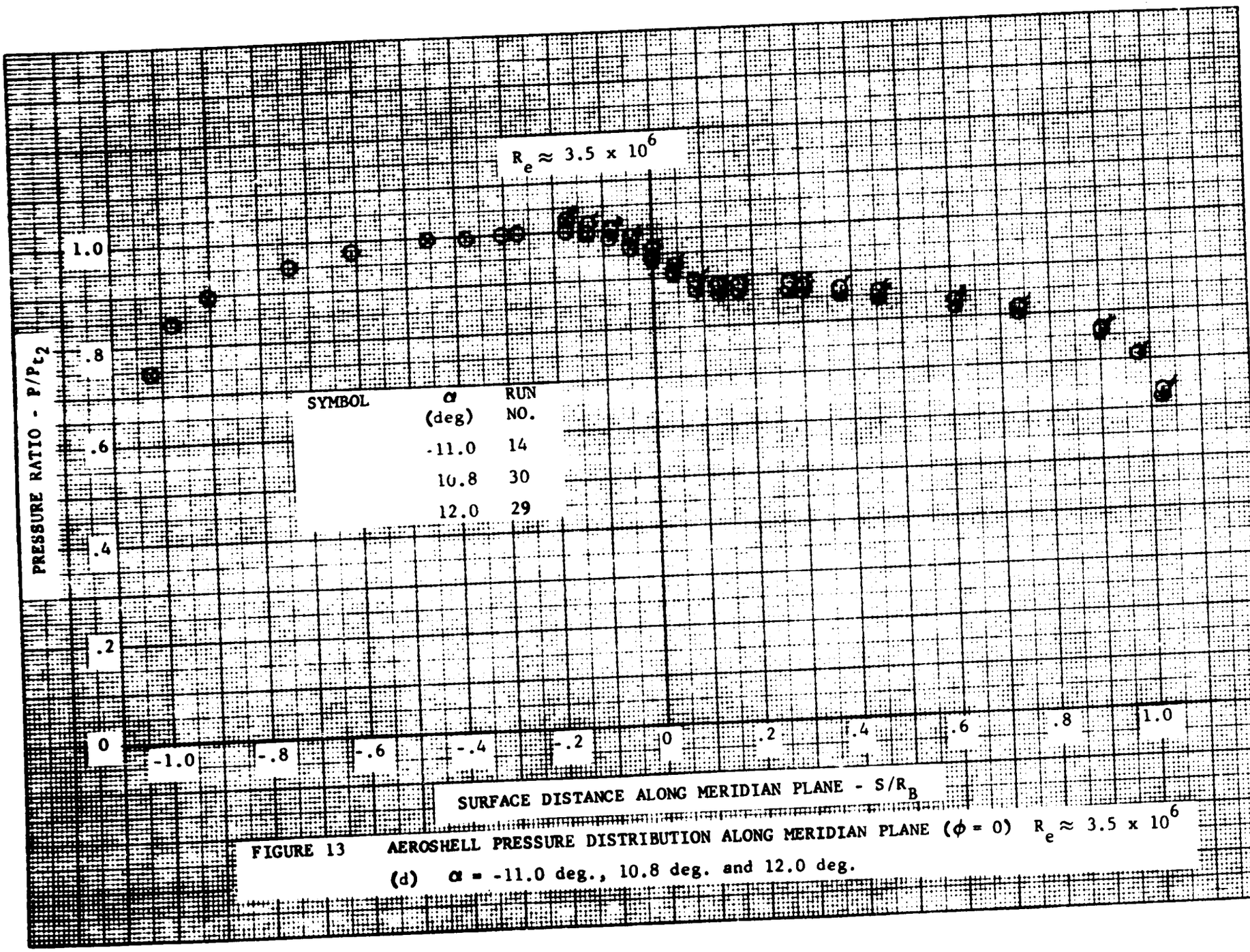

FIGURE 13 AEROSHELL PRESSURE DISTRIBUTION ALONG MERIDIAN PLANE ($\phi = 0$) $R_e \approx 3.5 \times 10^6$

(d) α = -11.0 deg., 10.8 deg. and 12.0 deg.

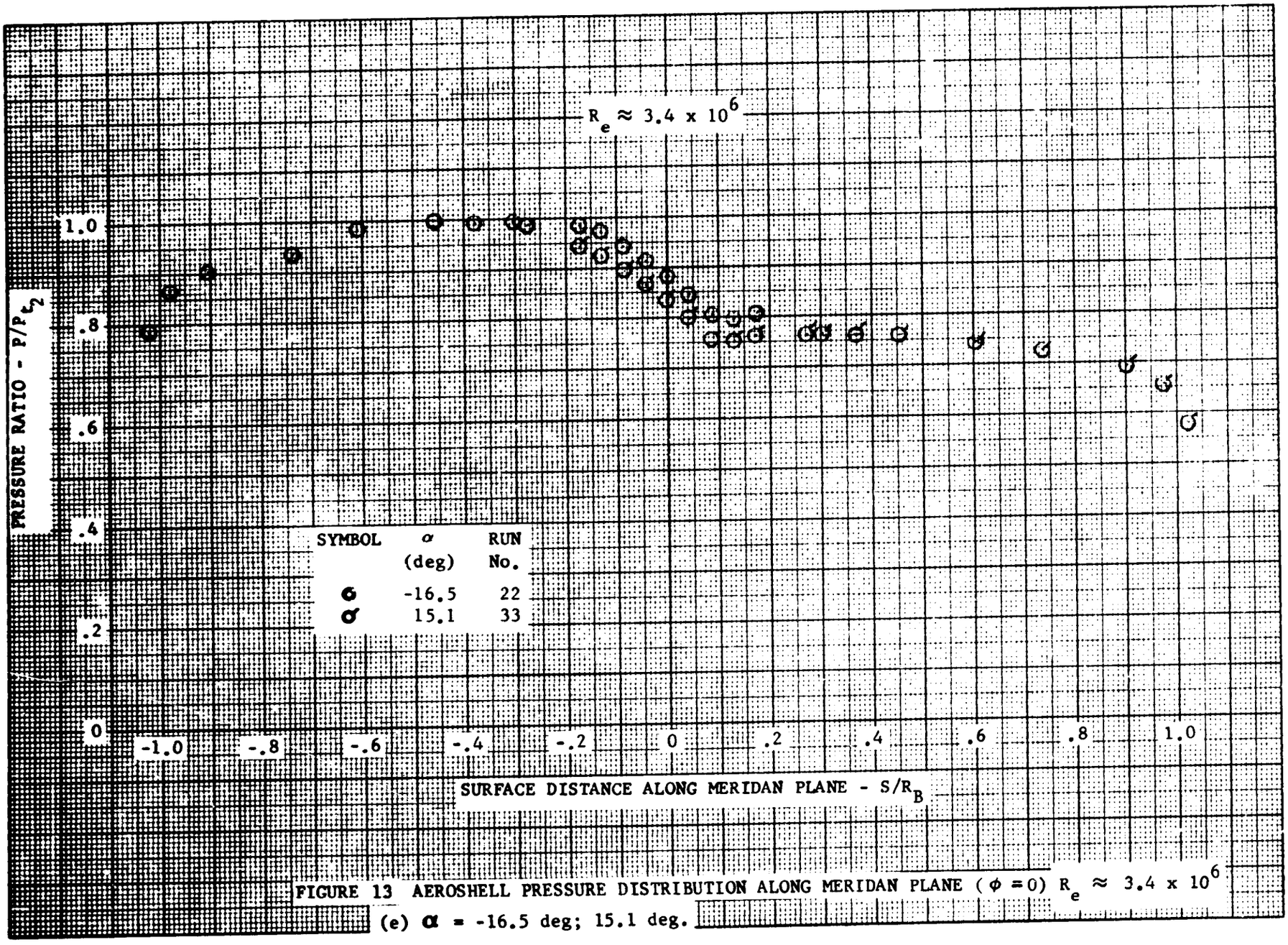

FIGURE 13 AEROSHELL PRESSURE DISTRIBUTION ALONG MERIDAN PLANE ($\phi = 0$) $R_e \approx 3.4 \times 10^6$

(e) α = -16.5 deg; 15.1 deg.

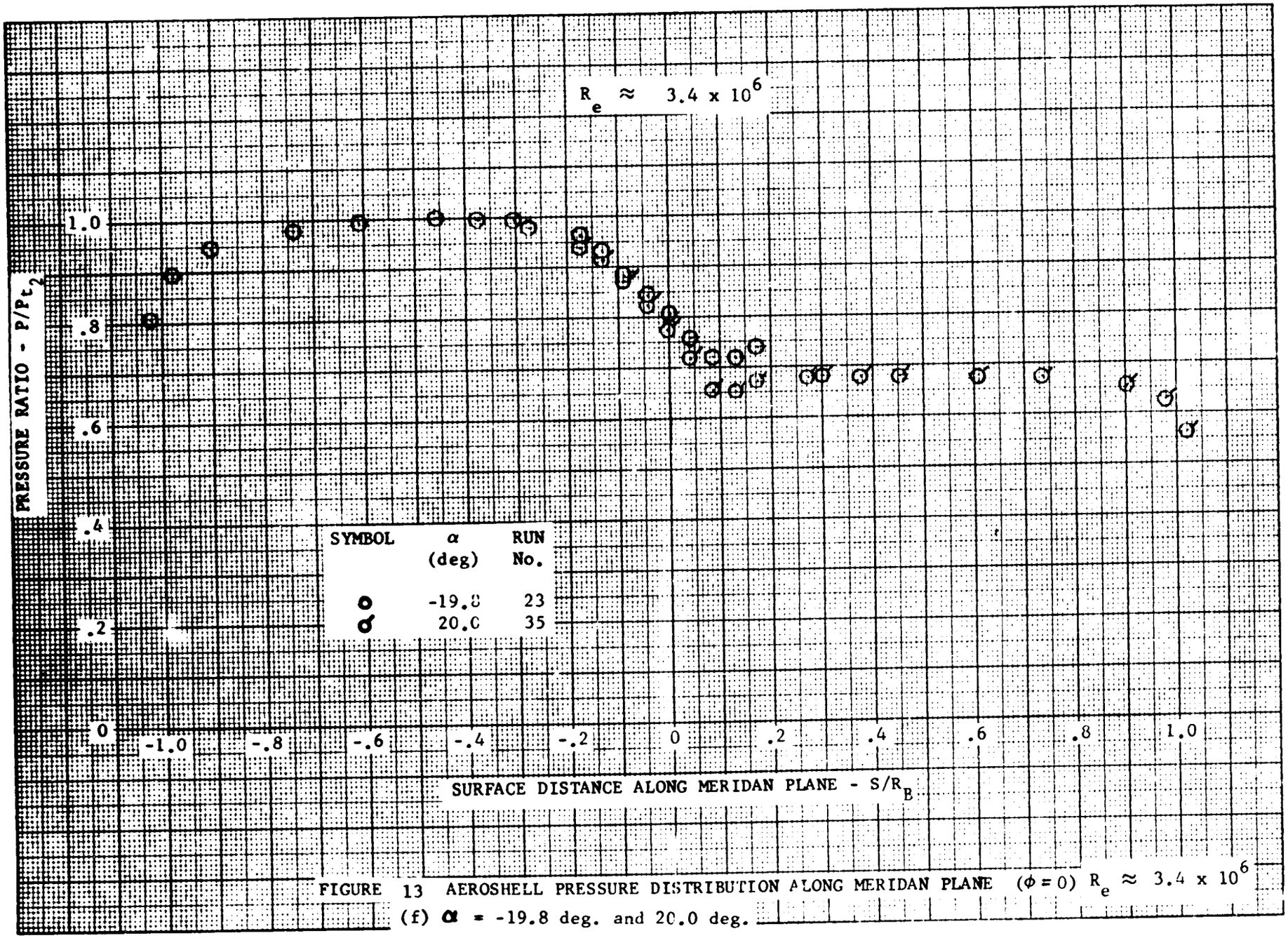

FIGURE 13 AEROSHELL PRESSURE DISTRIBUTION ALONG MERIDAN PLANE ($\phi = 0$) $R_e \approx 3.4 \times 10^6$

(f) α = -19.8 deg. and 20.0 deg.

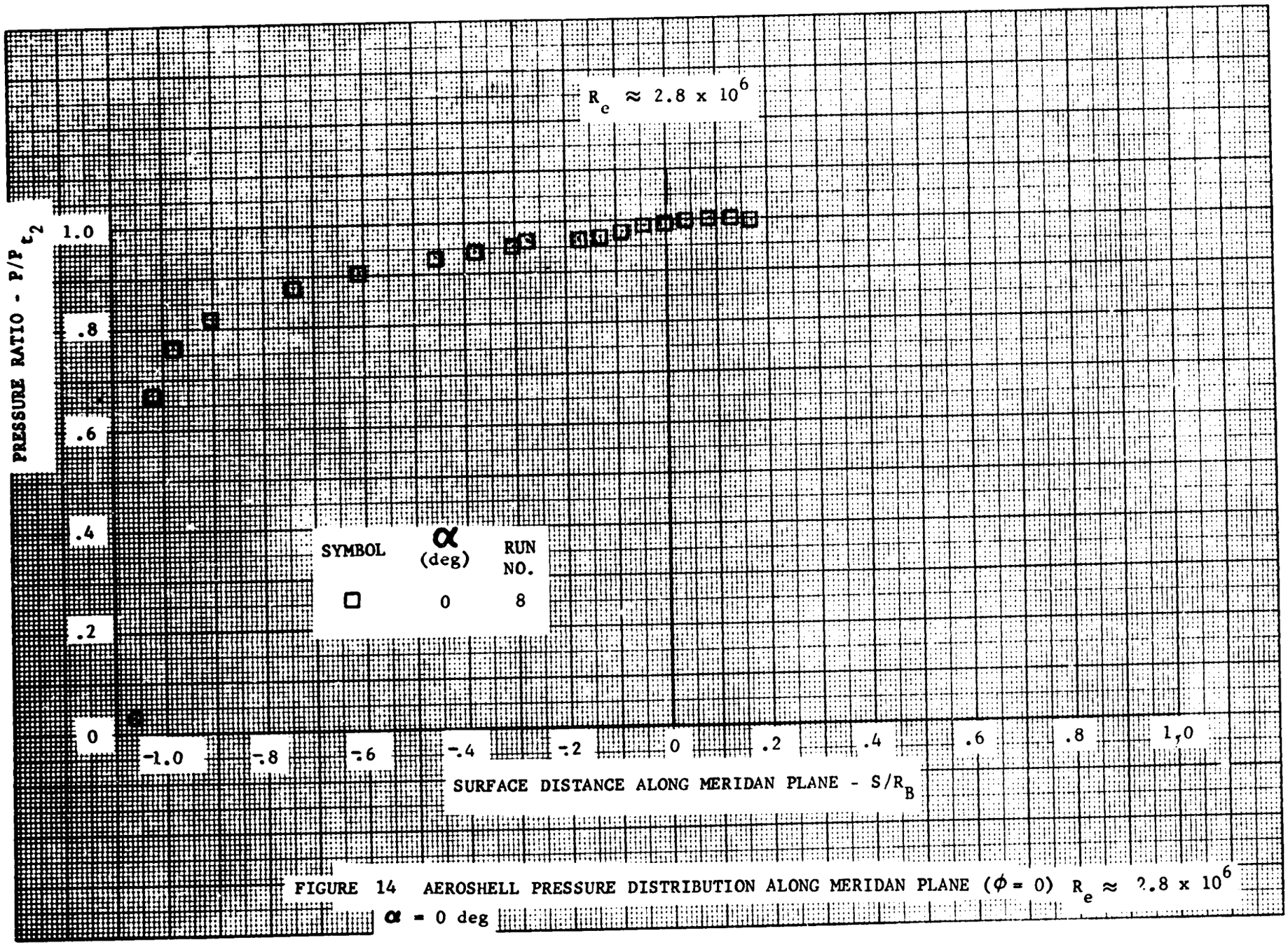

FIGURE 14 AEROSHELL PRESSURE DISTRIBUTION ALONG MERIDAN PLANE ($\phi = 0$) $R_e \approx 2.8 \times 10^6$
α = 0 deg

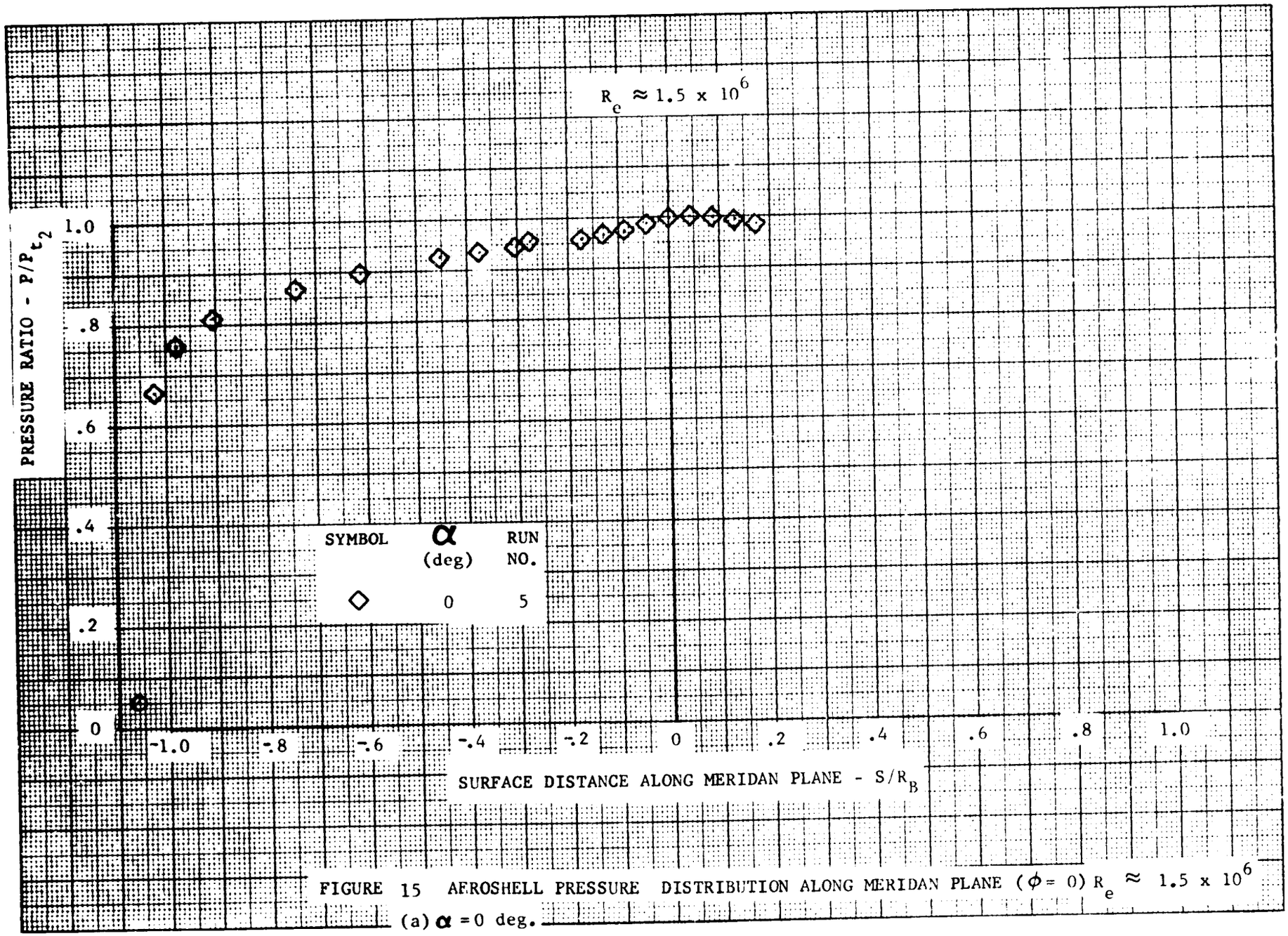

FIGURE 15 AEROSHELL PRESSURE DISTRIBUTION ALONG MERIDAN PLANE ($\phi = 0$) $R_e \approx 1.5 \times 10^6$

(a) $\alpha = 0$ deg.

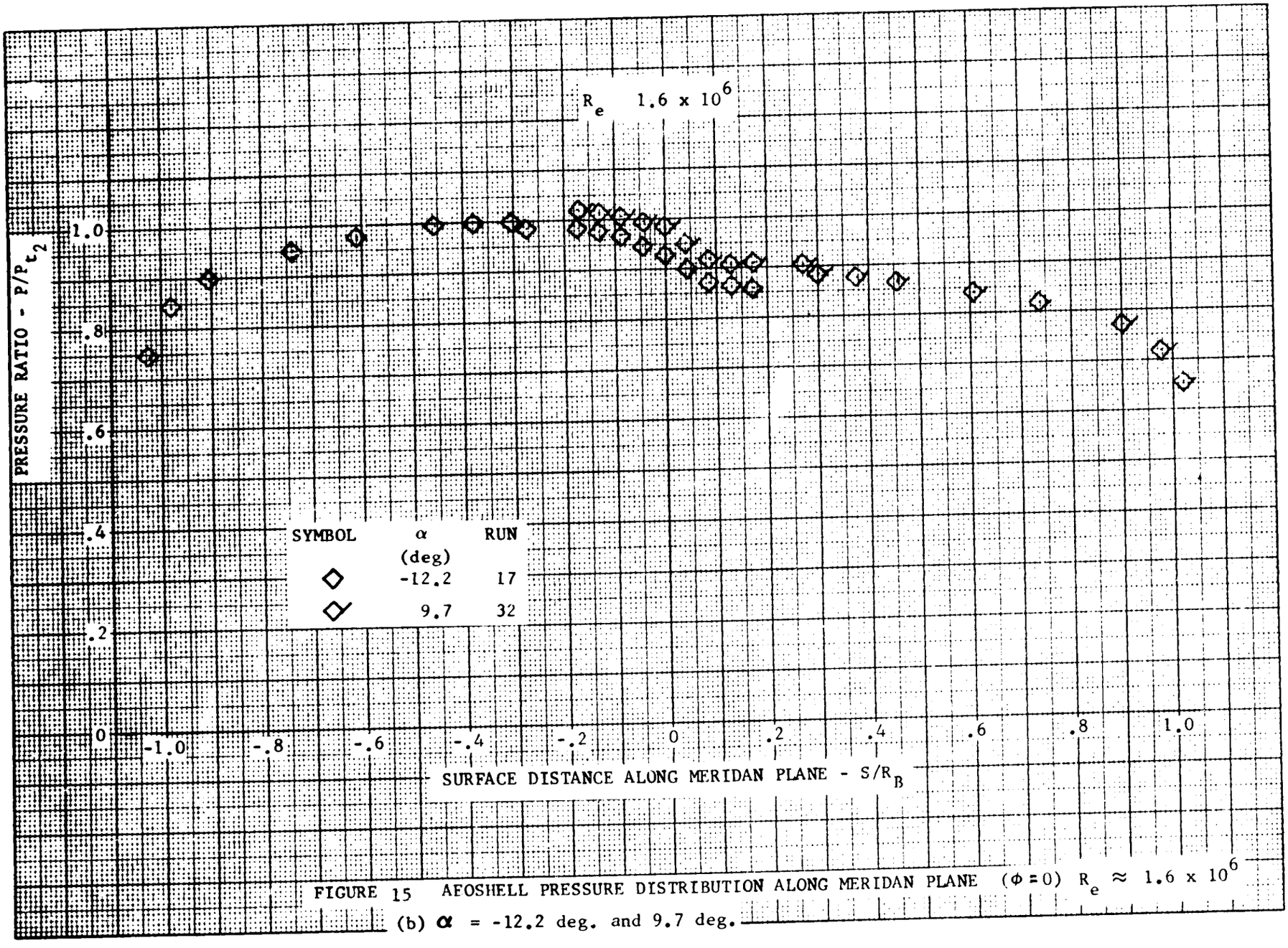

FIGURE 15 AEOSHELL PRESSURE DISTRIBUTION ALONG MERIDAN PLANE ($\Phi = 0$) $R_e \approx 1.6 \times 10^6$

(b) α = -12.2 deg. and 9.7 deg.

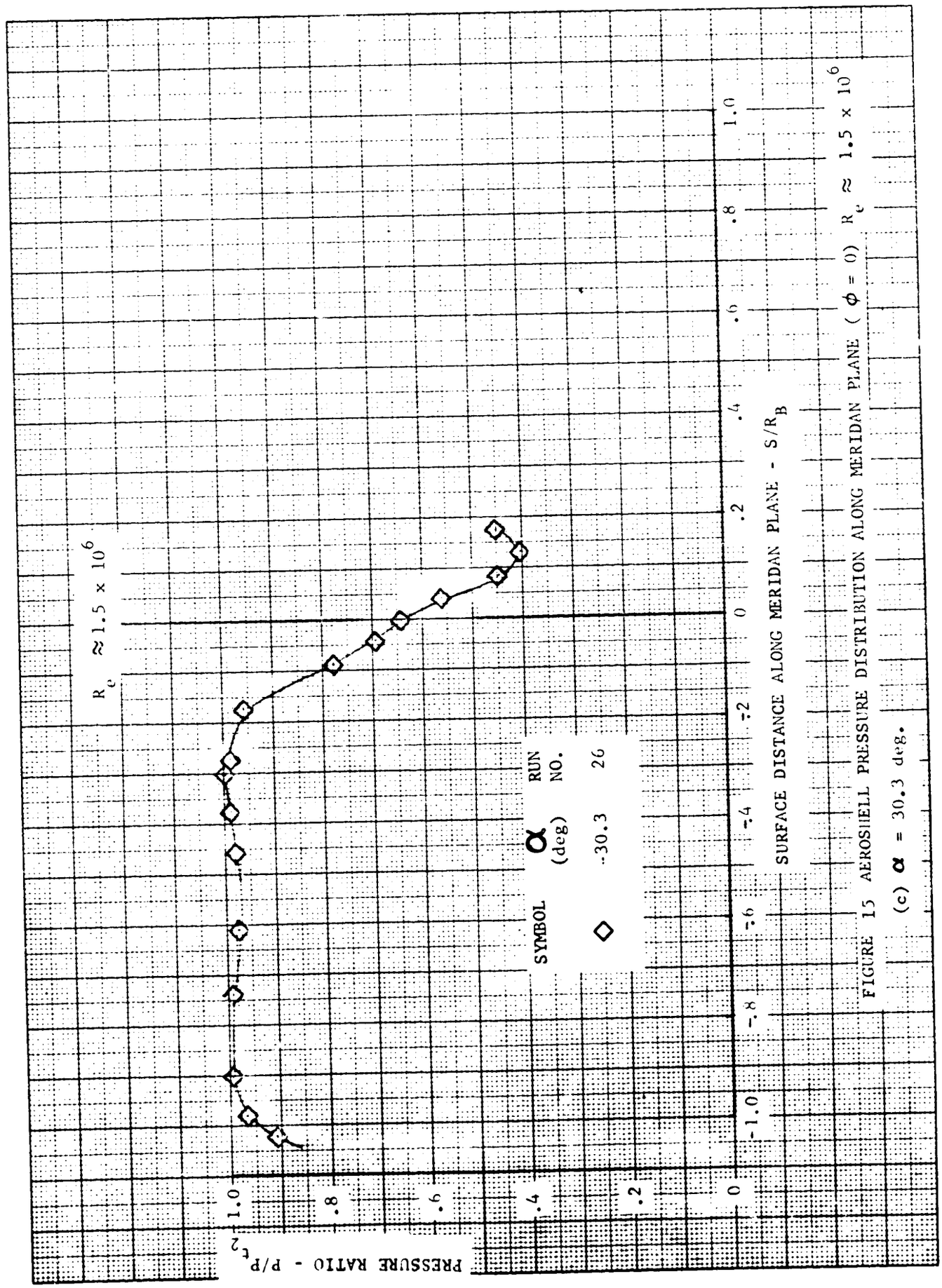

FIGURE 15 AEROSHELL PRESSURE DISTRIBUTION ALONG MERIDAN PLANE ($\phi = 0$) $R_e \approx 1.5 \times 10^6$

(c) α = 30.3 deg.

FOLDOUT FRAME

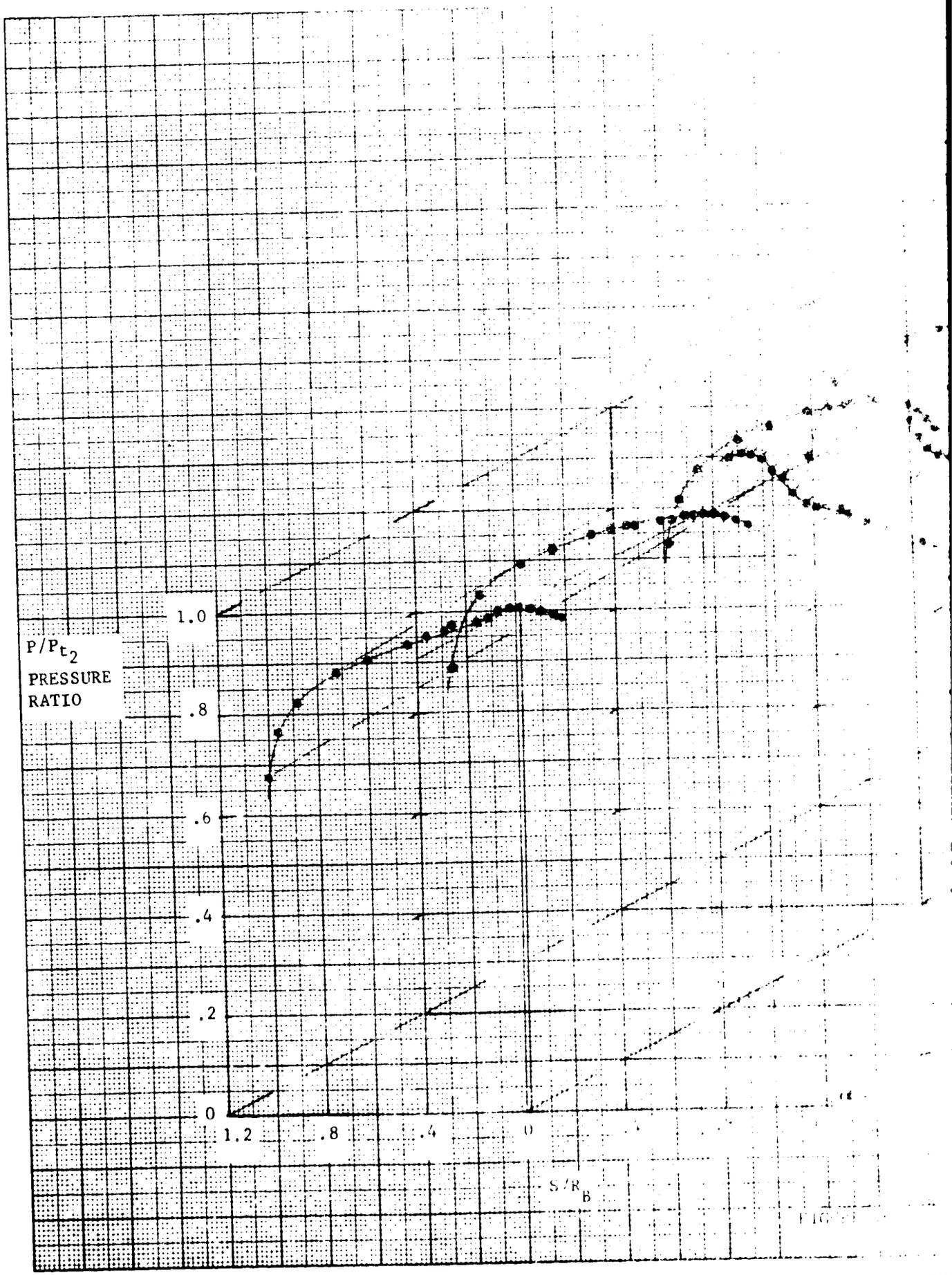

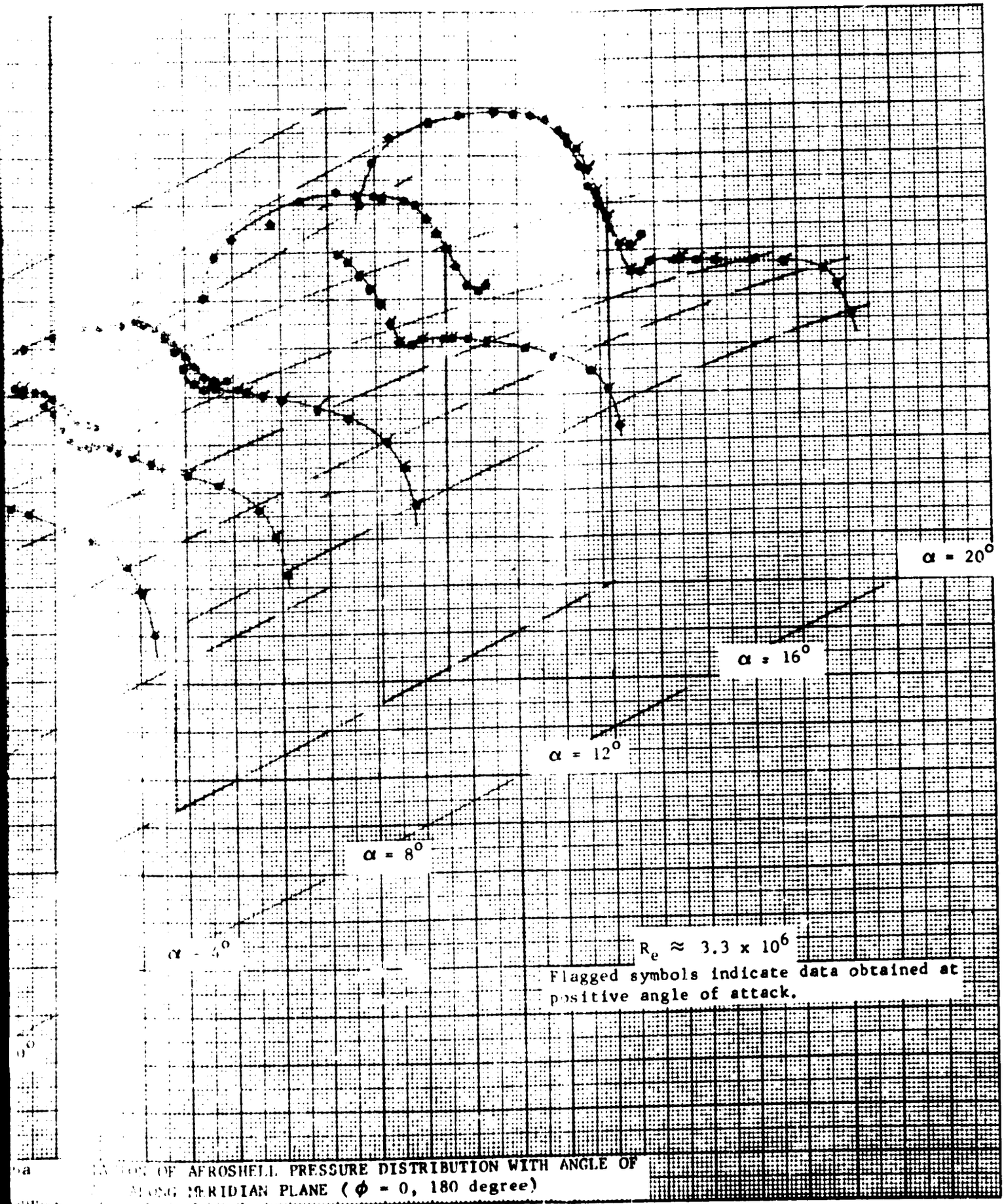

...a ...OF AEROSHELL PRESSURE DISTRIBUTION WITH ANGLE OF ...ONG MERIDIAN PLANE (ϕ = 0, 180 degree)

FOLDOUT FRAME

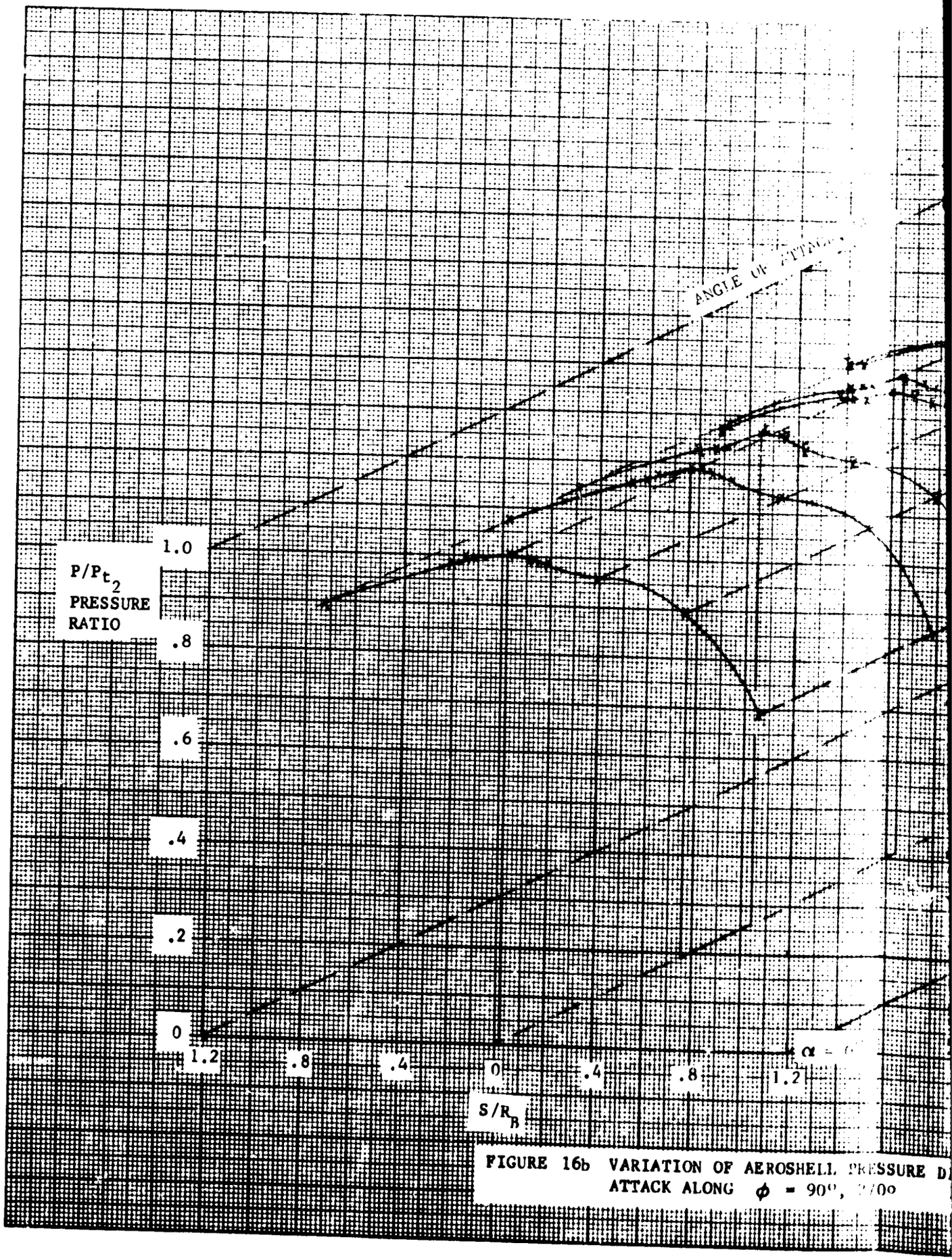

FIGURE 16b VARIATION OF AEROSHELL PRESSURE D
ATTACK ALONG ϕ = 90°, 270°

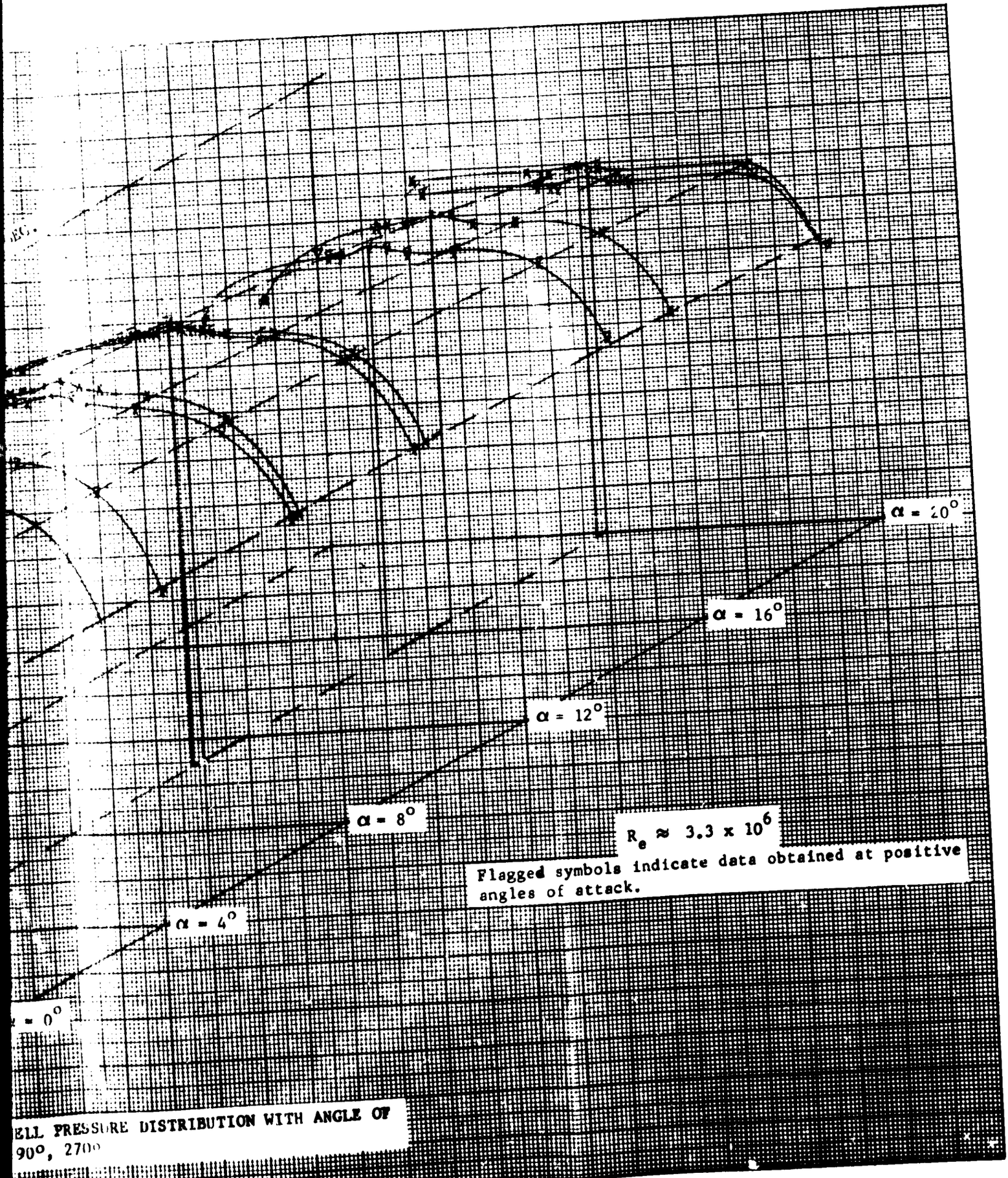

ELL PRESSURE DISTRIBUTION WITH ANGLE OF
90°, 270°

FOLDOUT FRAME

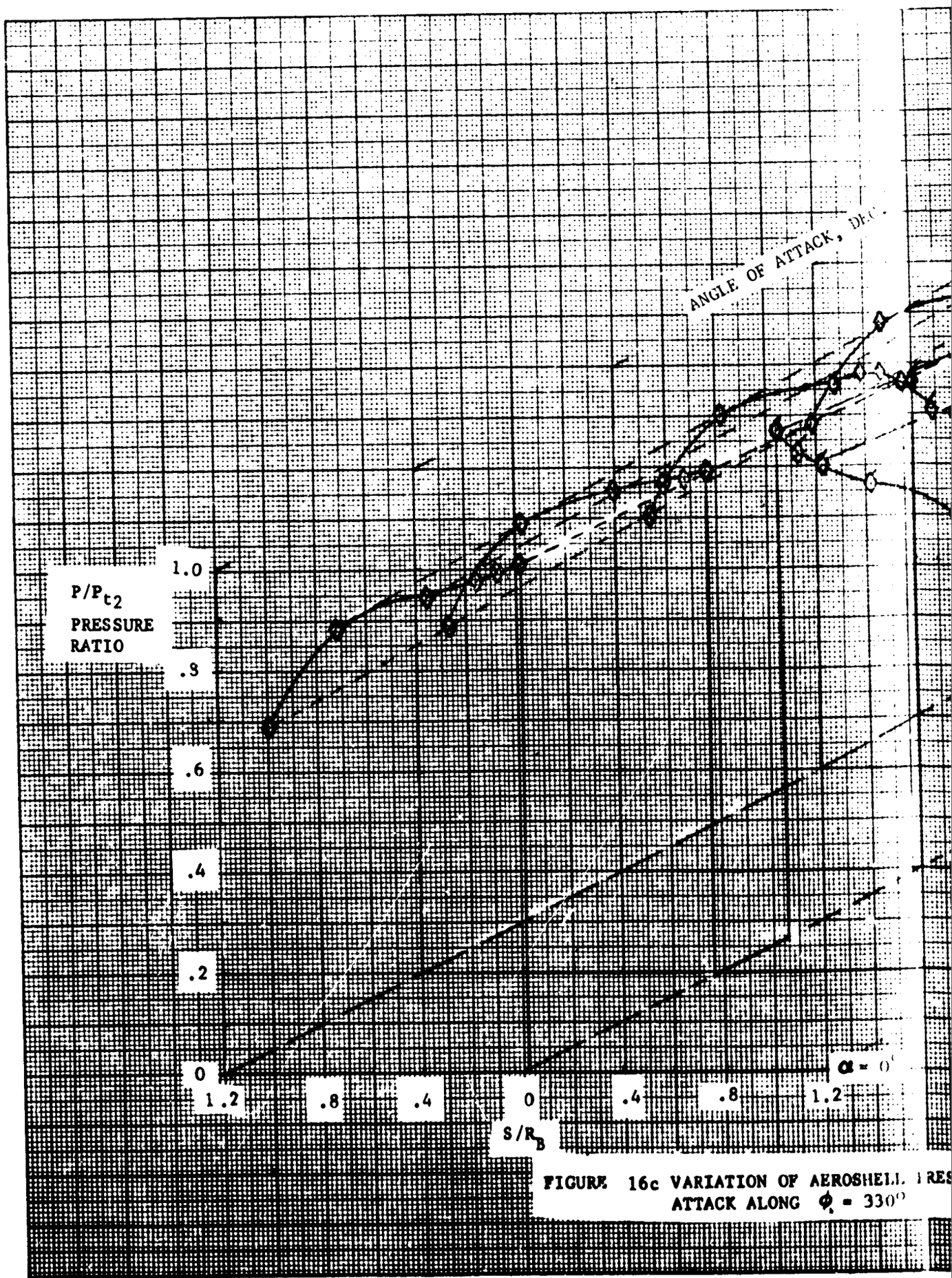

FIGURE 16c VARIATION OF AEROSHELL PRES
ATTACK ALONG ϕ_s = 330°

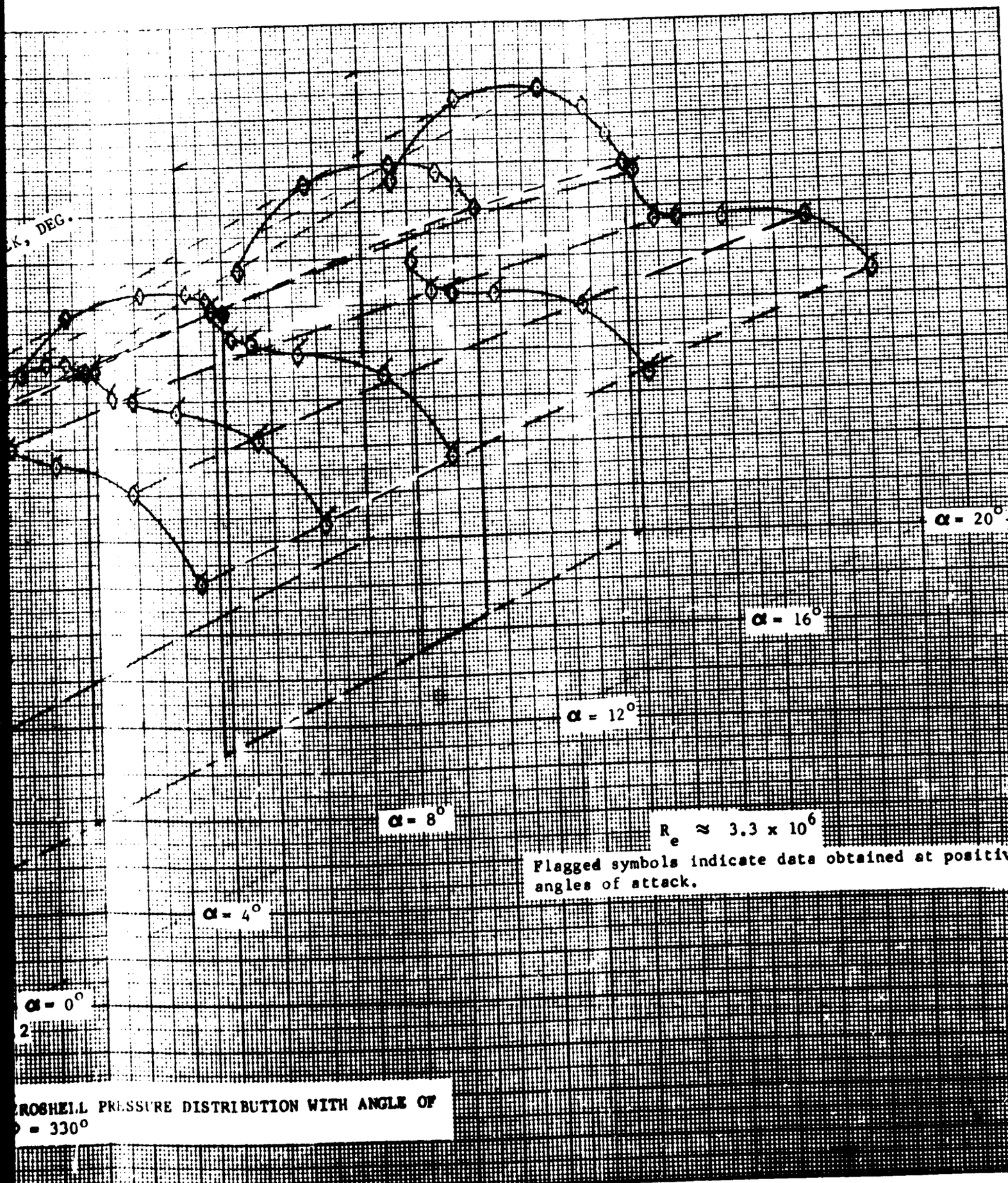

$R_e \approx 3.3 \times 10^6$

Flagged symbols indicate data obtained at positive angles of attack.

ROSHELL PRESSURE DISTRIBUTION WITH ANGLE OF
= 330°

FOLDOUT FRAME

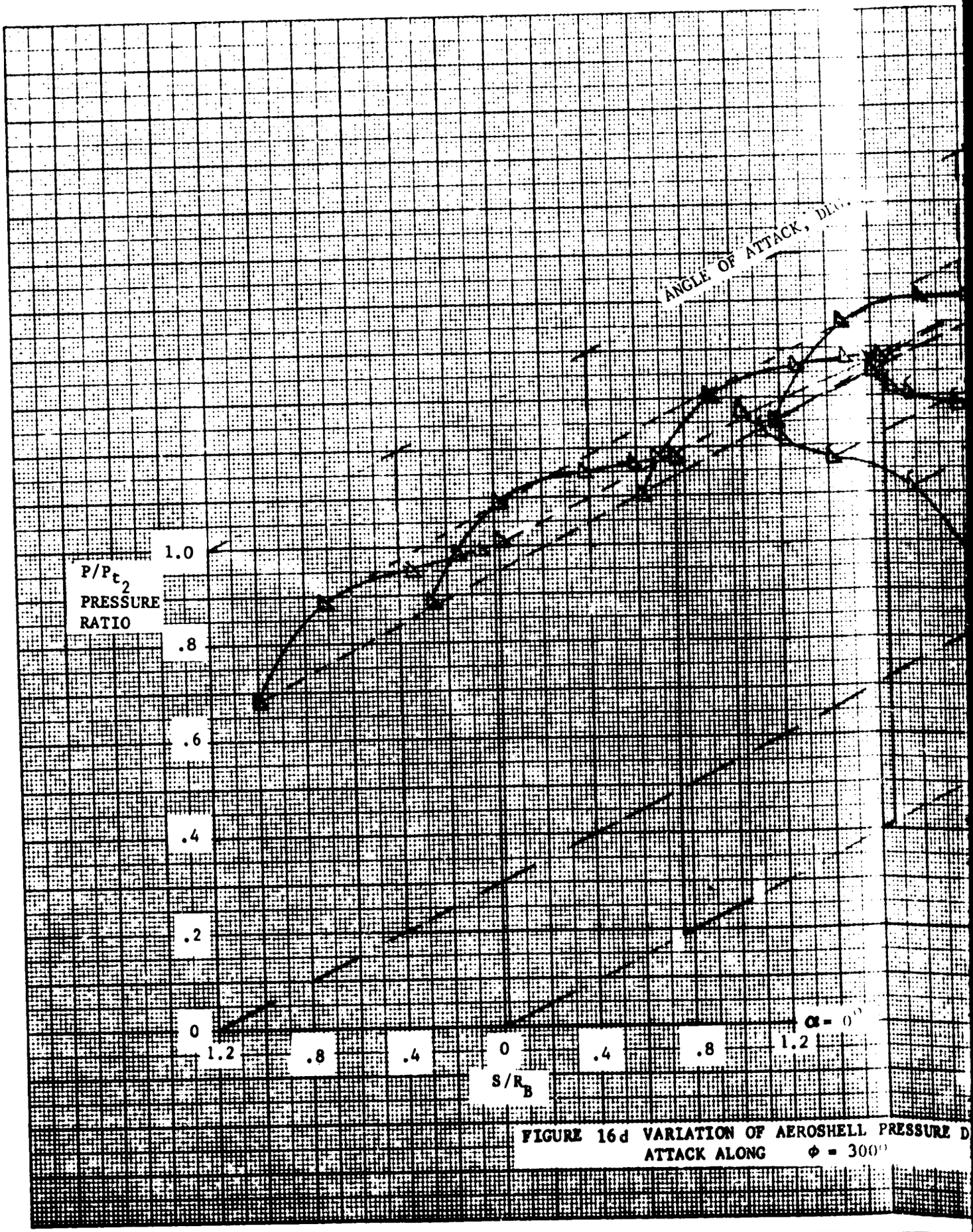

FIGURE 16d VARIATION OF AEROSHELL PRESSURE D
ATTACK ALONG $\phi = 300$

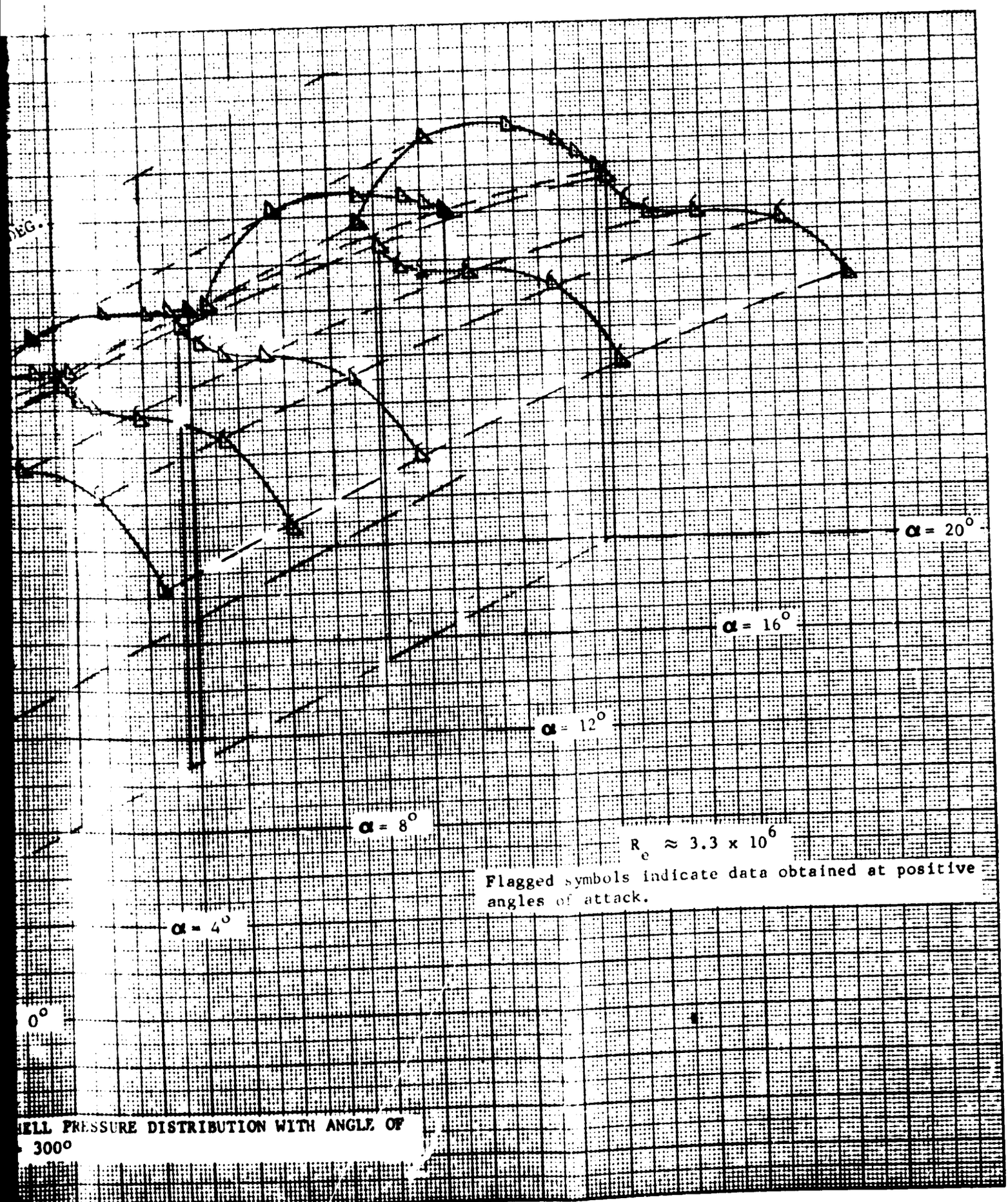

$R_e \approx 3.3 \times 10^6$

Flagged symbols indicate data obtained at positive angles of attack.

ELL PRESSURE DISTRIBUTION WITH ANGLE OF
300°

FOLDOUT FRAME

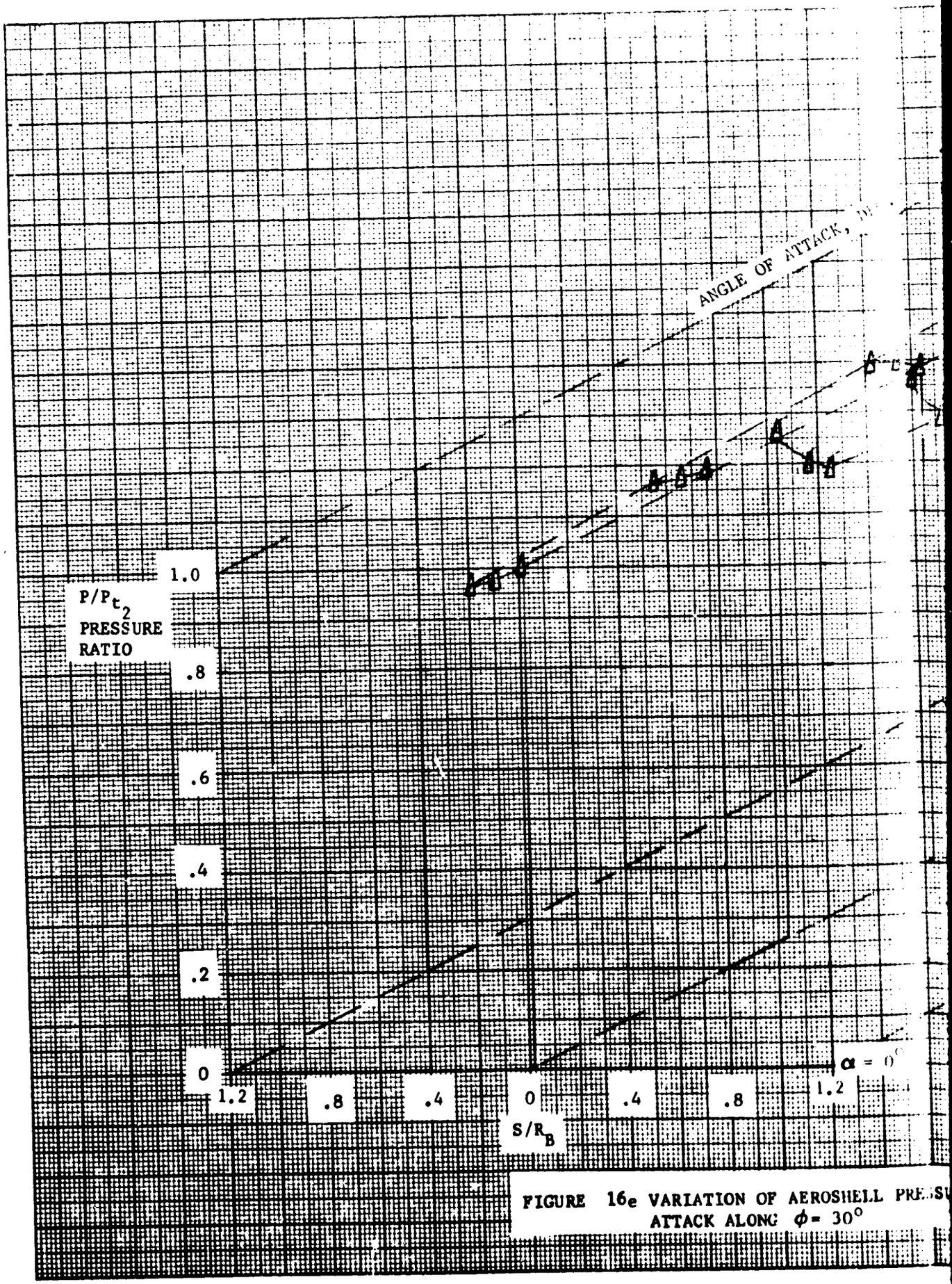

FIGURE 16e VARIATION OF AEROSHELL PRESSU
ATTACK ALONG $\phi = 30^\circ$

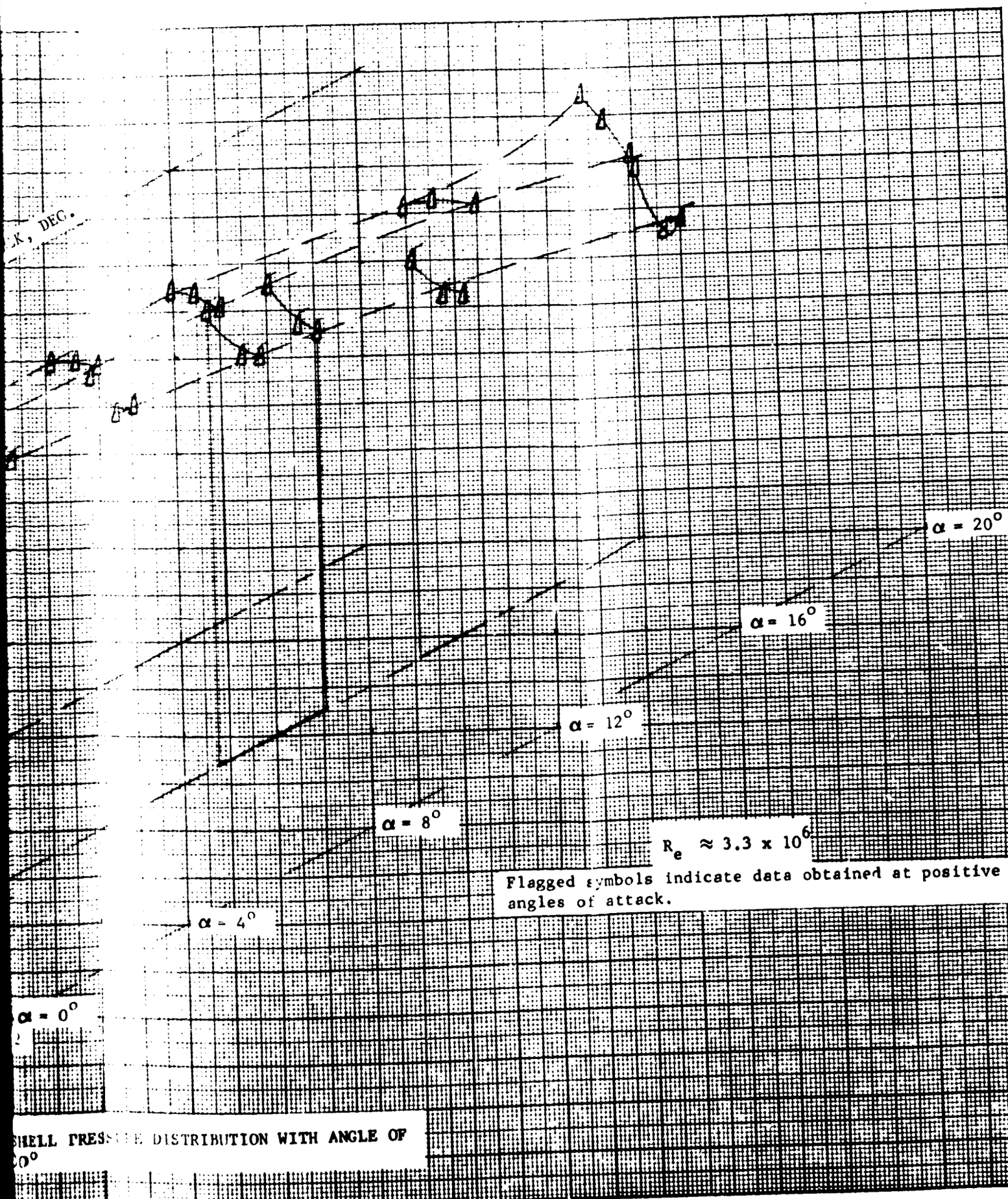

HELL PRESSURE DISTRIBUTION WITH ANGLE OF
O°

FOLDOUT FRAME

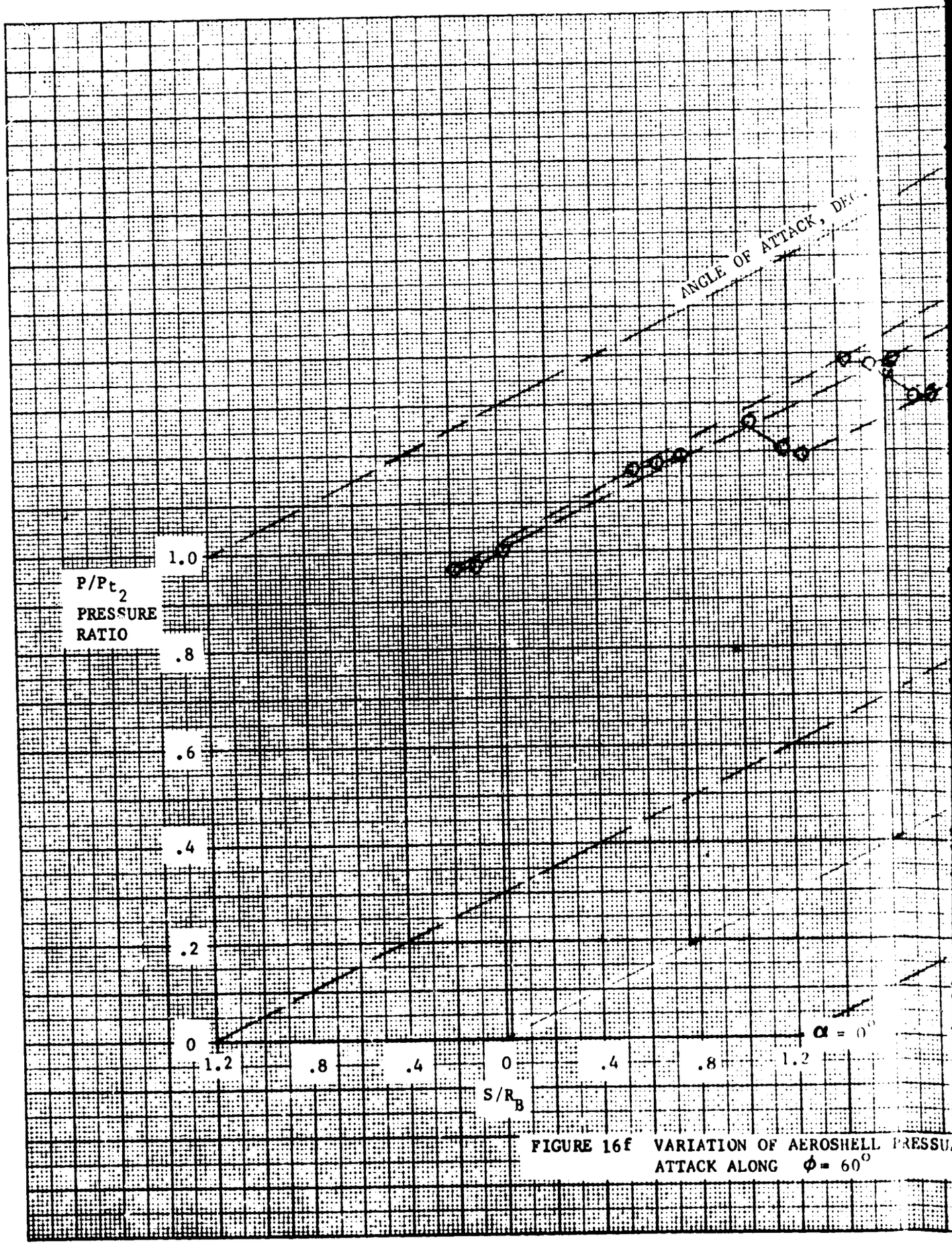

FIGURE 16f VARIATION OF AEROSHELL PRESSU
ATTACK ALONG $\phi = 60^\circ$

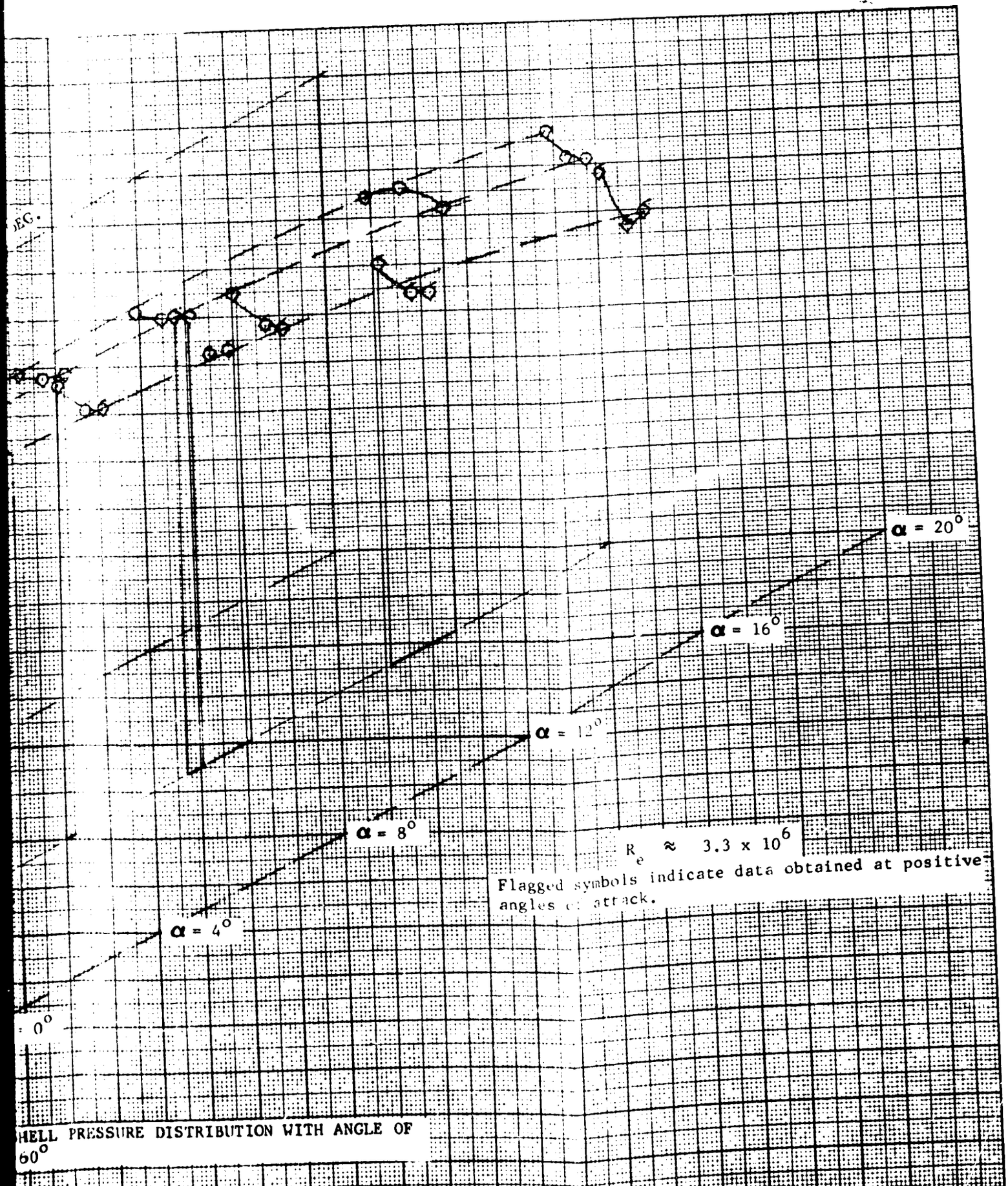

Flagged symbols indicate data obtained at positive angles of attack.

HELL PRESSURE DISTRIBUTION WITH ANGLE OF 60°

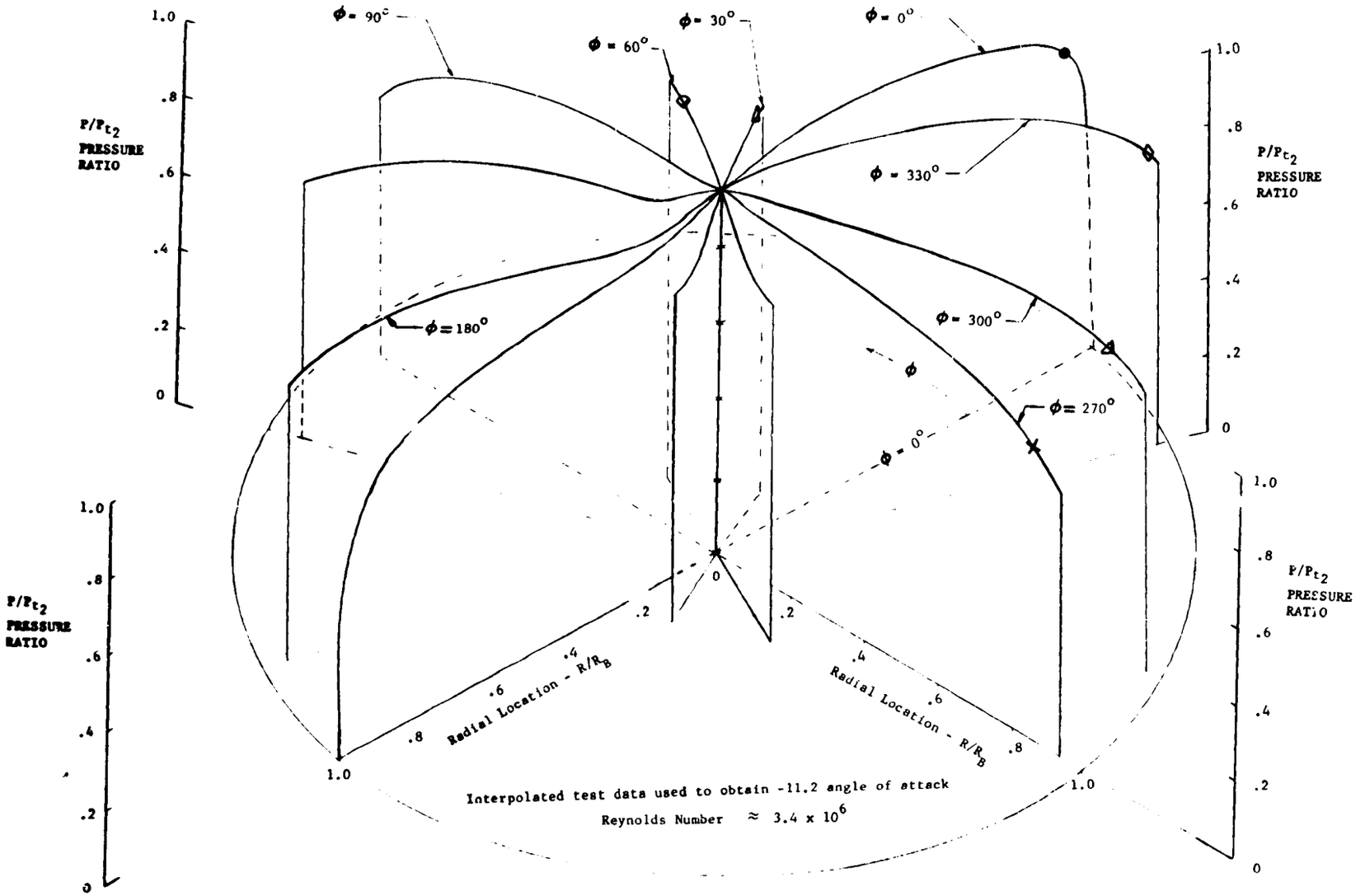

FIGURE 17 AEROSHELL PRESSURE DISTRIBUTION AT -11.2° ANGLE OF ATTACK

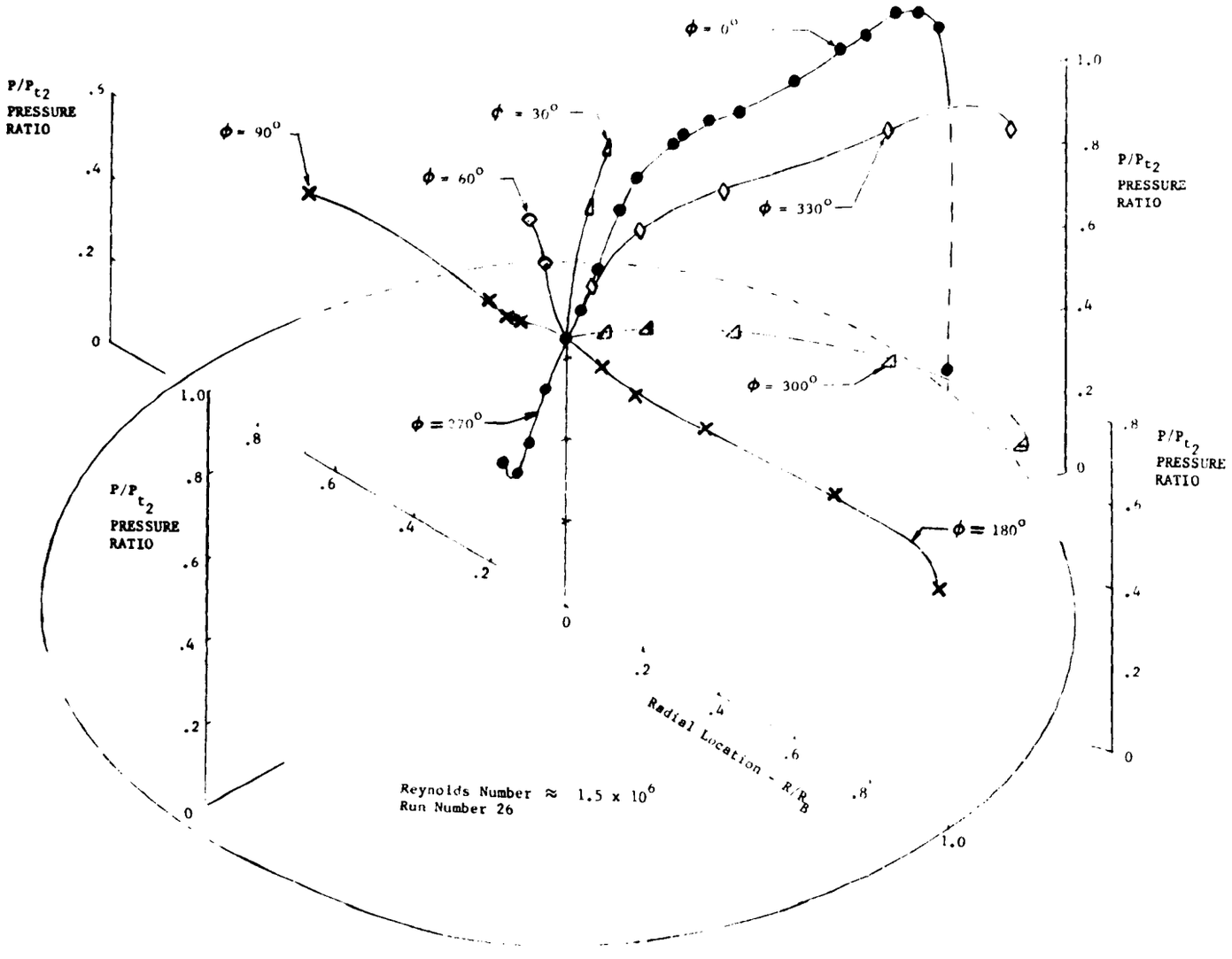

FIGURE 18 AEROSHELL PRESSURE DISTRIBUTION AT -30.3° ANGLE OF ATTACK

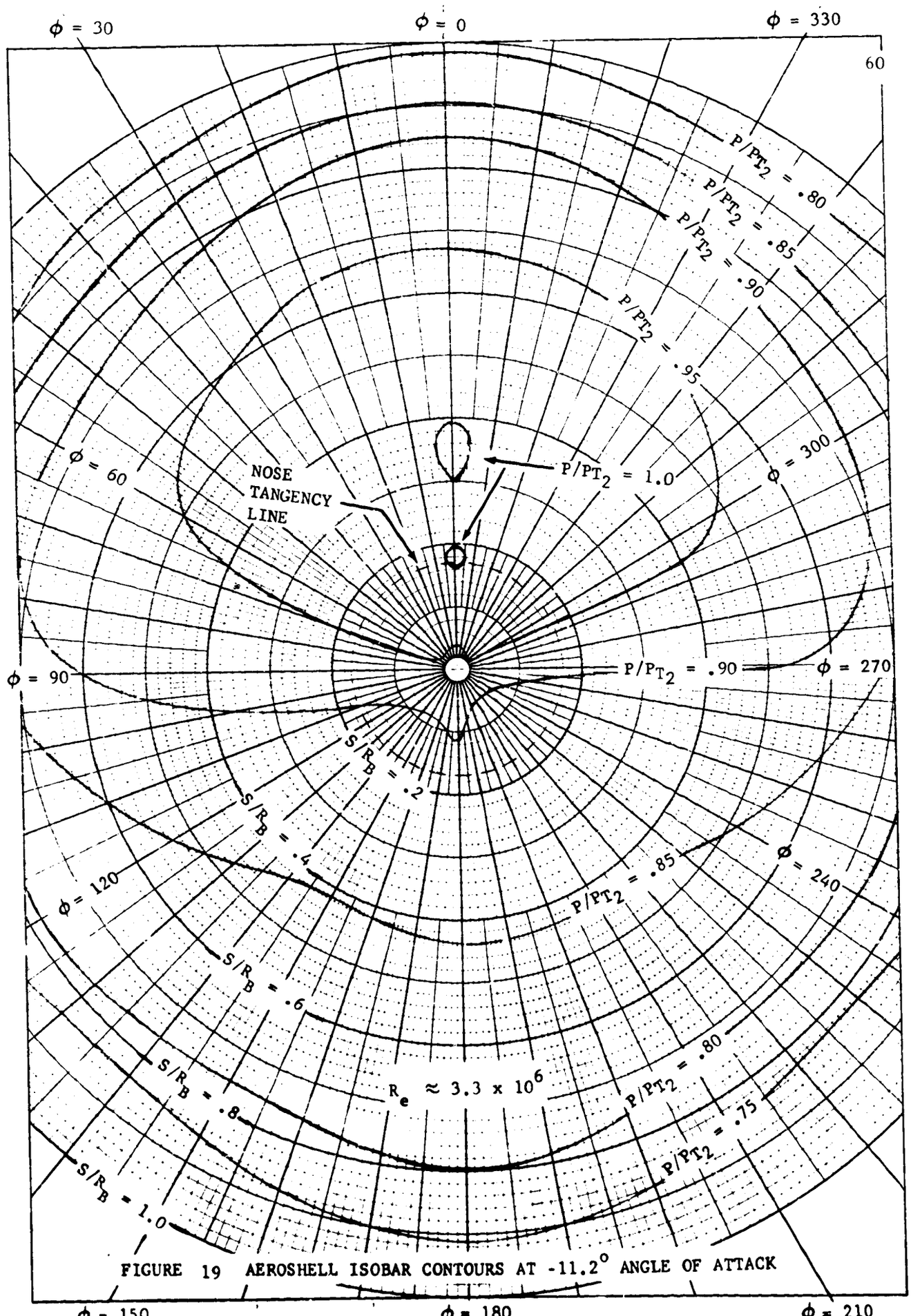

FIGURE 19 AEROSHELL ISOBAR CONTOURS AT -11.2° ANGLE OF ATTACK

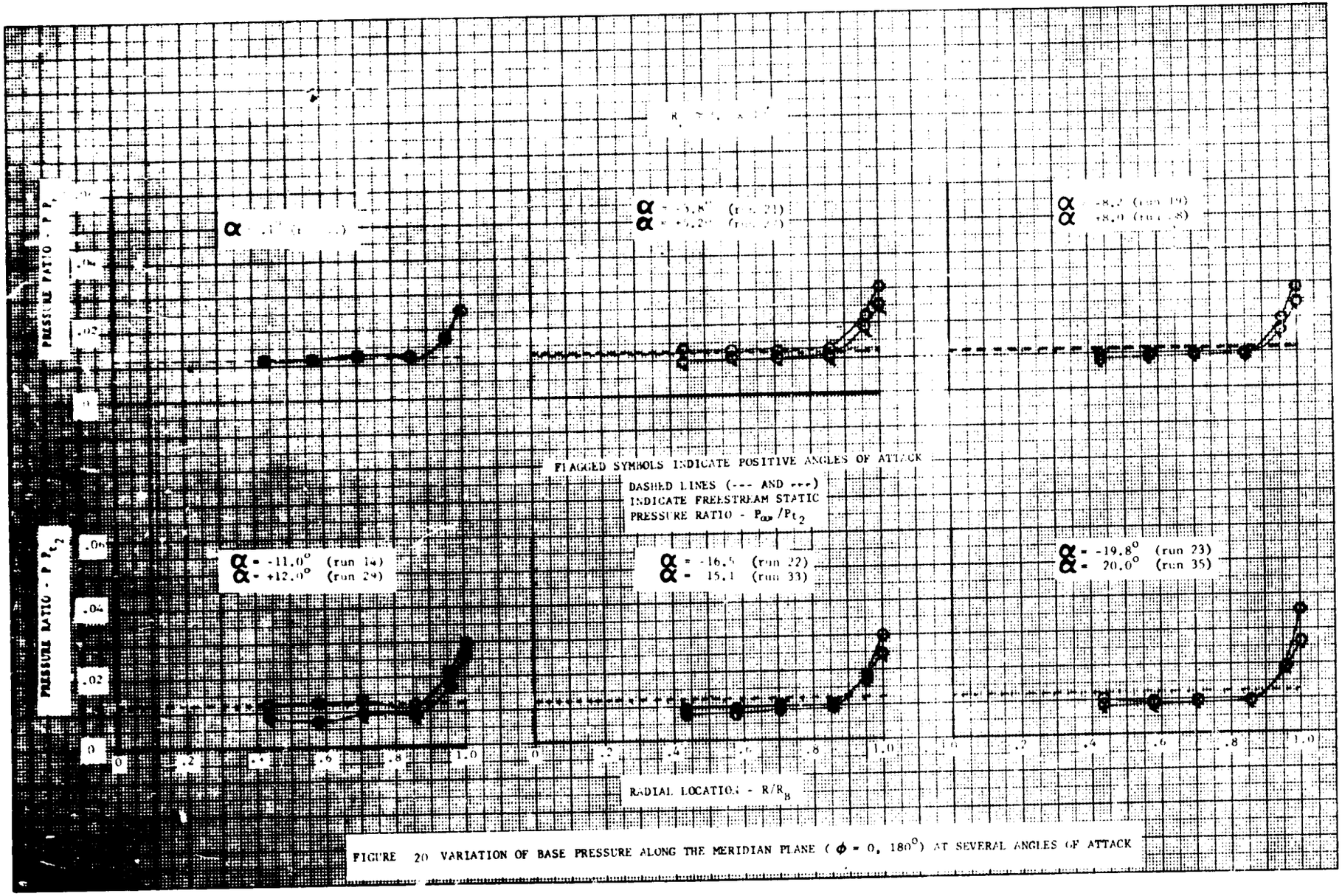

FIGURE 20 VARIATION OF BASE PRESSURE ALONG THE MERIDIAN PLANE (ϕ = 0, 180°) AT SEVERAL ANGLES OF ATTACK

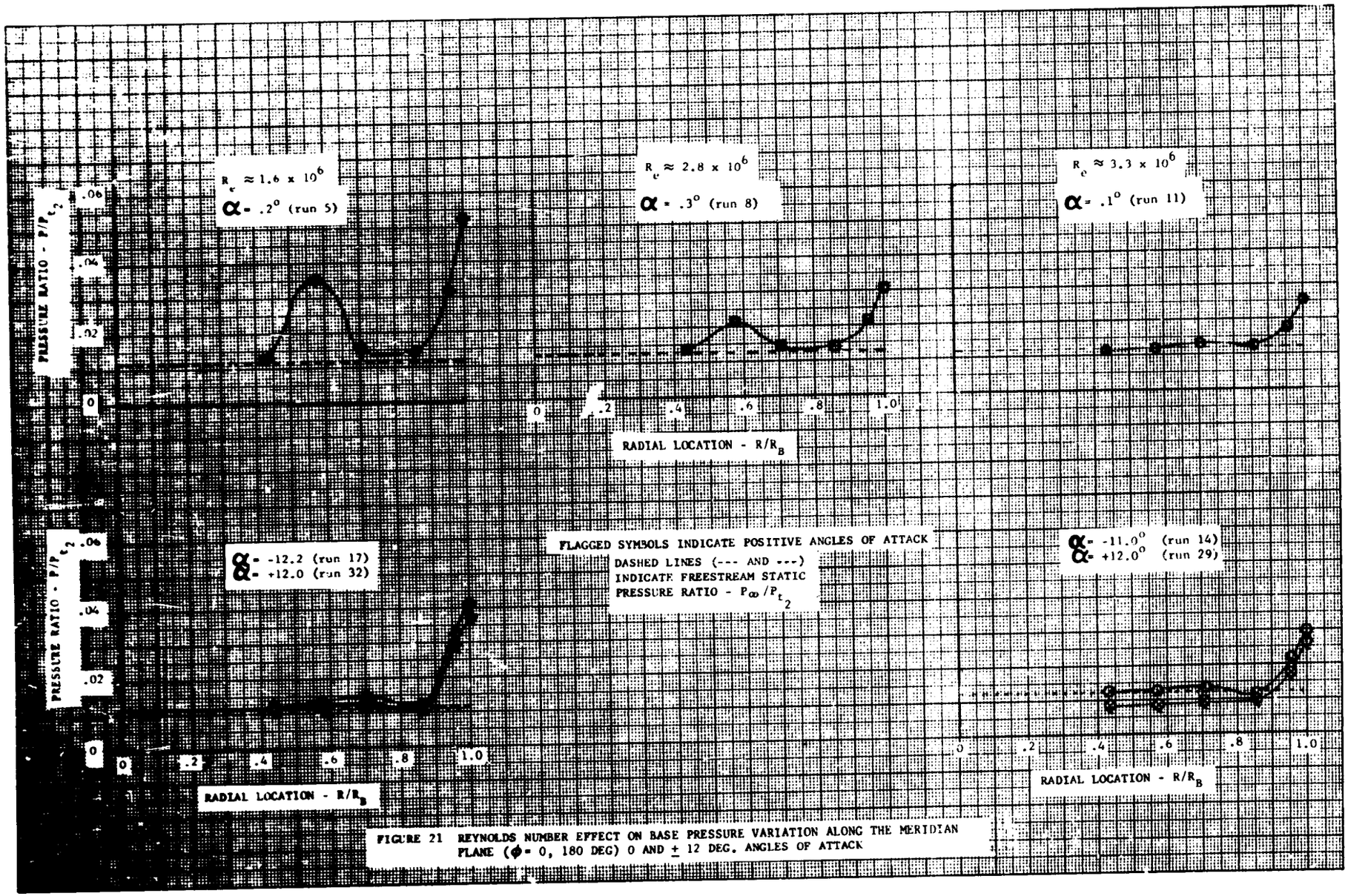

FIGURE 21 REYNOLDS NUMBER EFFECT ON BASE PRESSURE VARIATION ALONG THE MERIDIAN PLANE (ϕ = 0, 180 DEG) 0 AND ± 12 DEG. ANGLES OF ATTACK

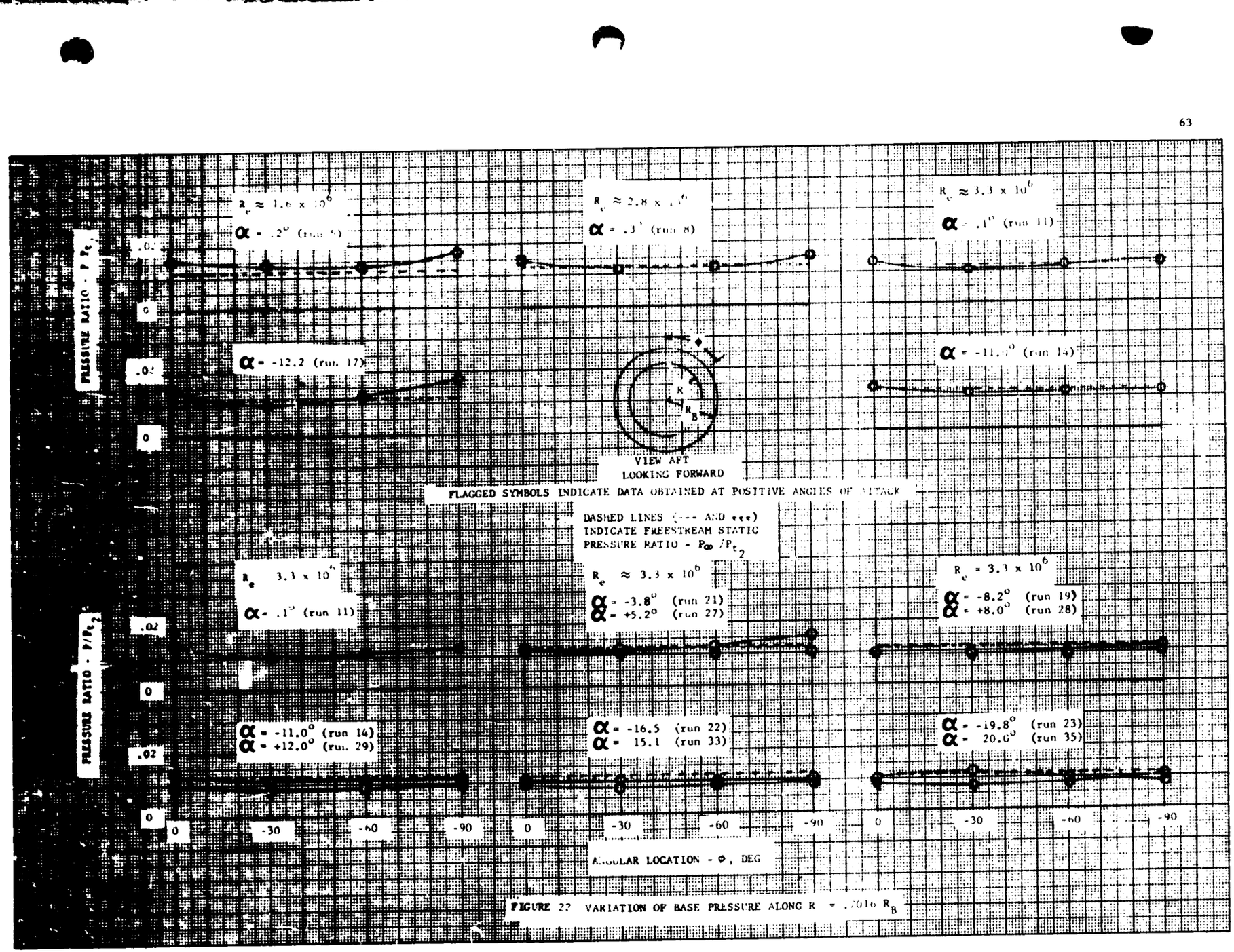

FIGURE 22 VARIATION OF BASE PRESSURE ALONG R = .7016 R_B

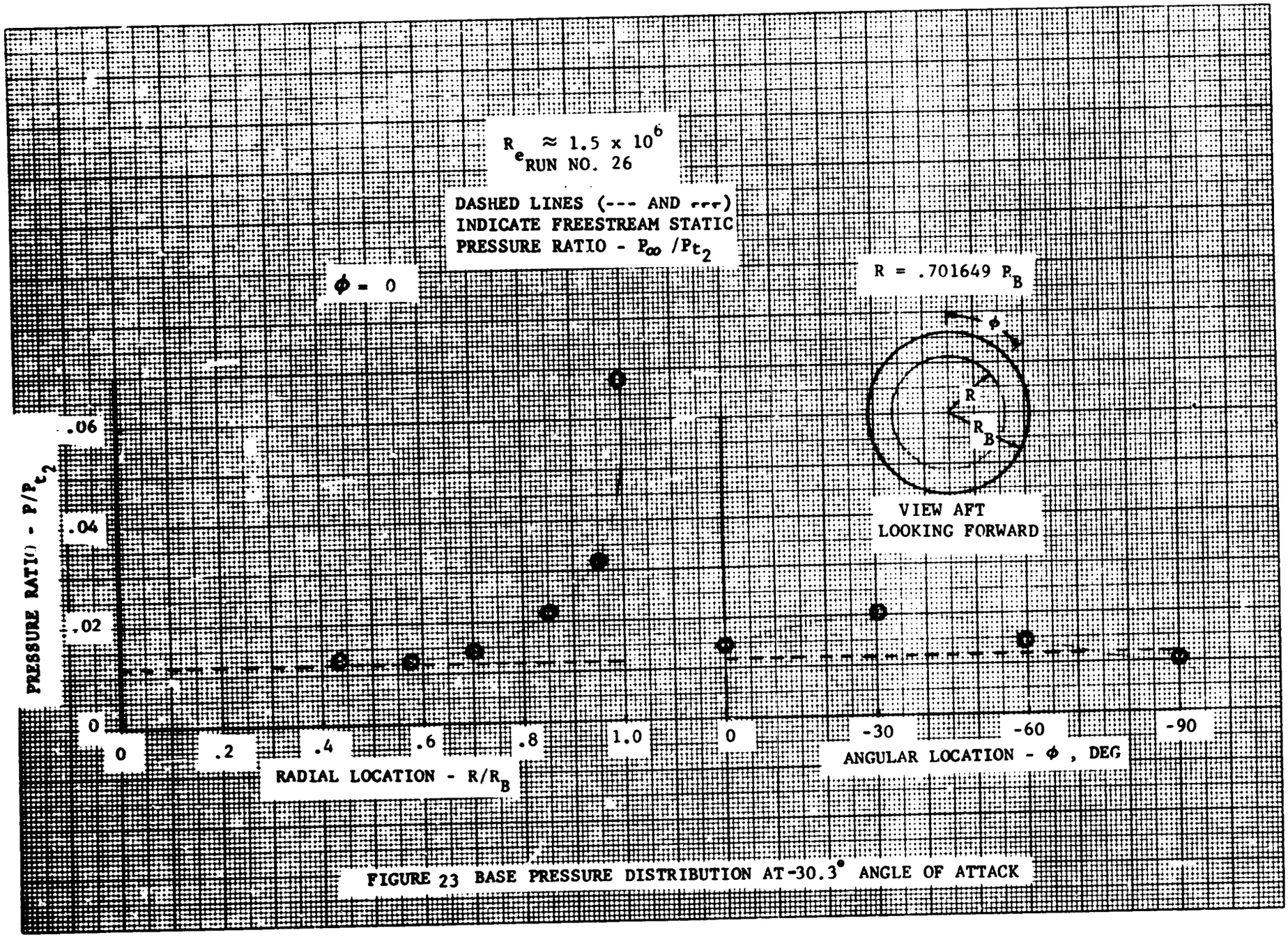

FIGURE 23 BASE PRESSURE DISTRIBUTION AT -30.3° ANGLE OF ATTACK

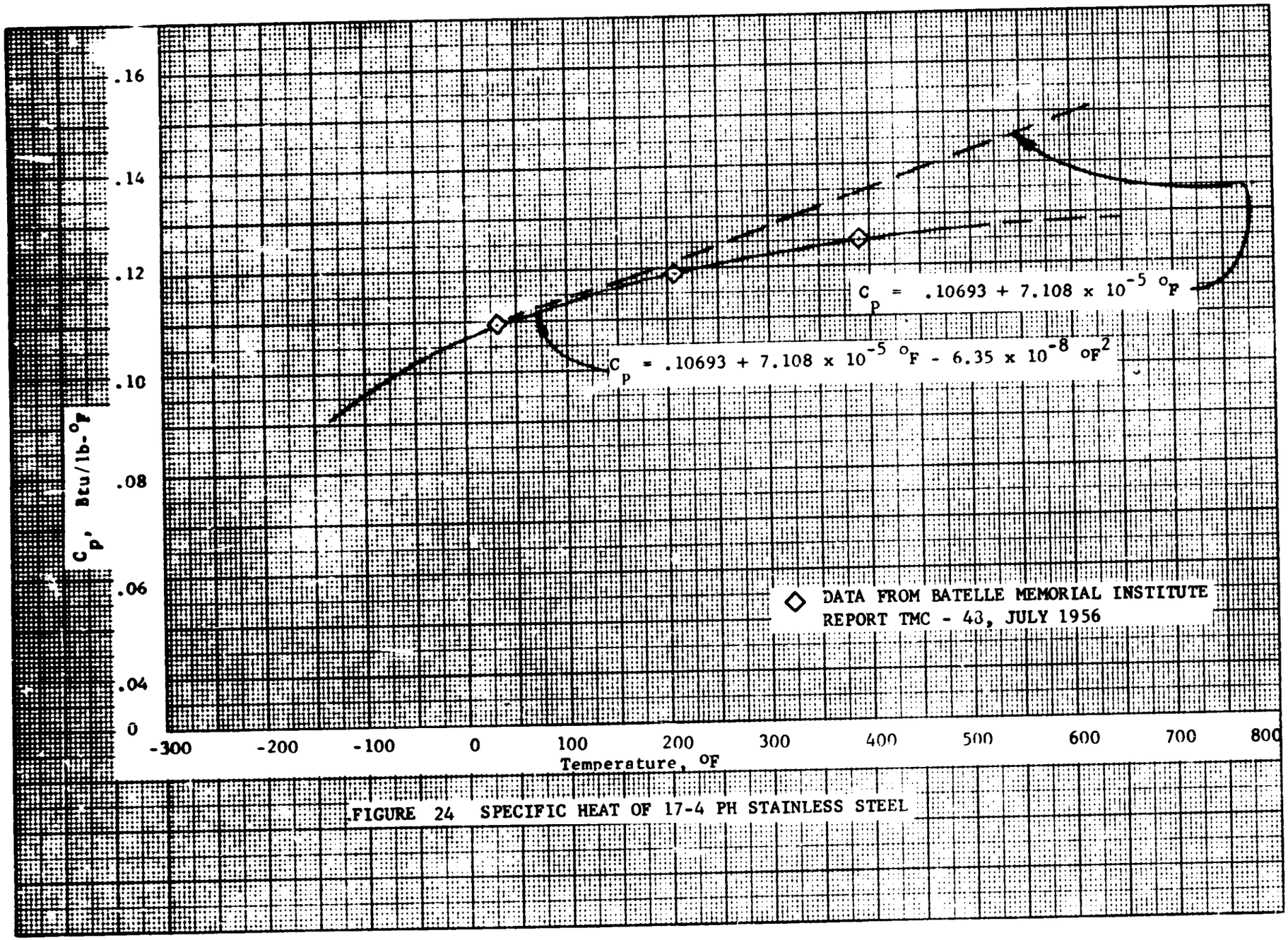

FIGURE 24 SPECIFIC HEAT OF 17-4 PH STAINLESS STEEL

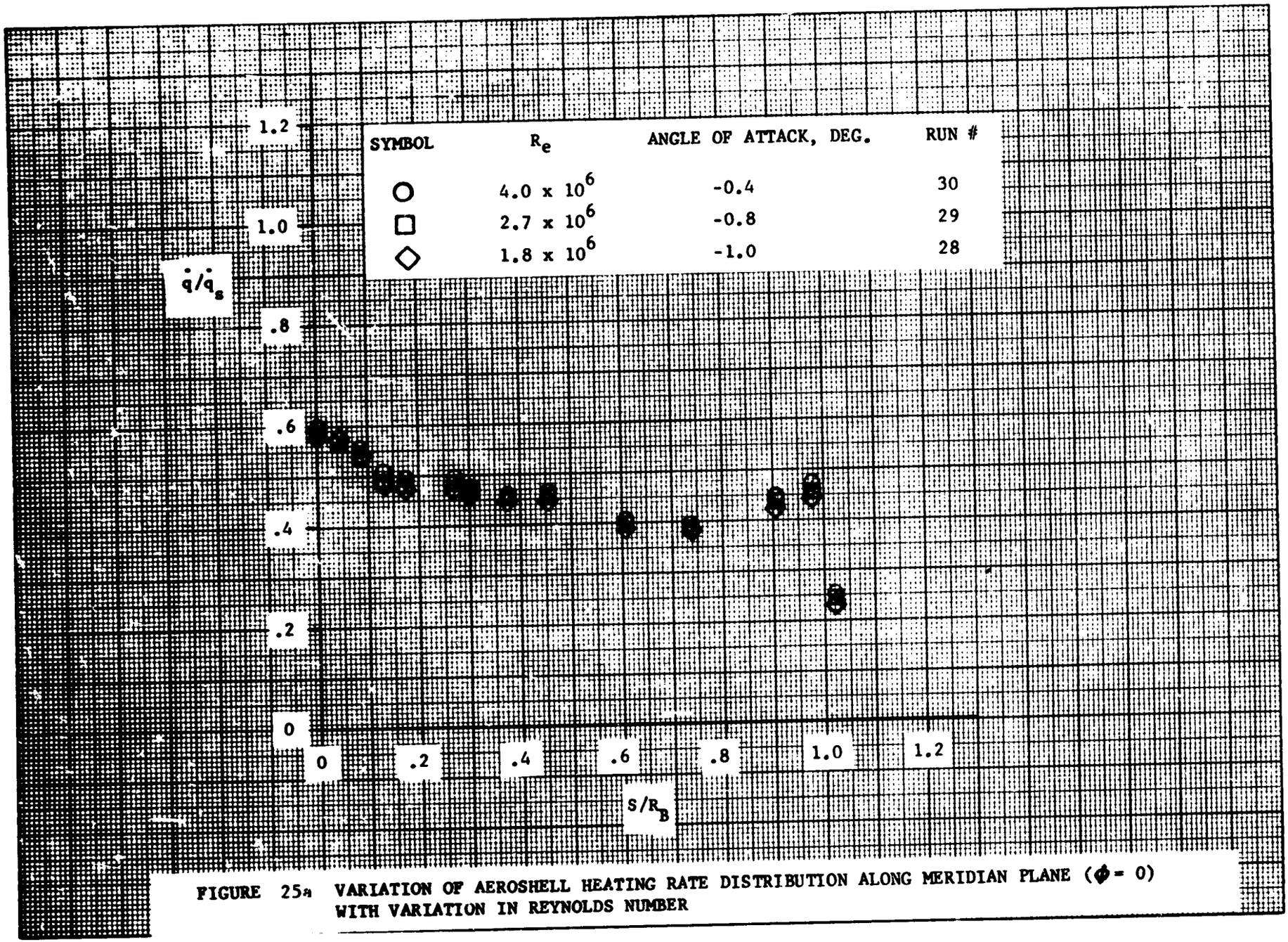

FIGURE 25a VARIATION OF AEROSHELL HEATING RATE DISTRIBUTION ALONG MERIDIAN PLANE (ϕ = 0) WITH VARIATION IN REYNOLDS NUMBER

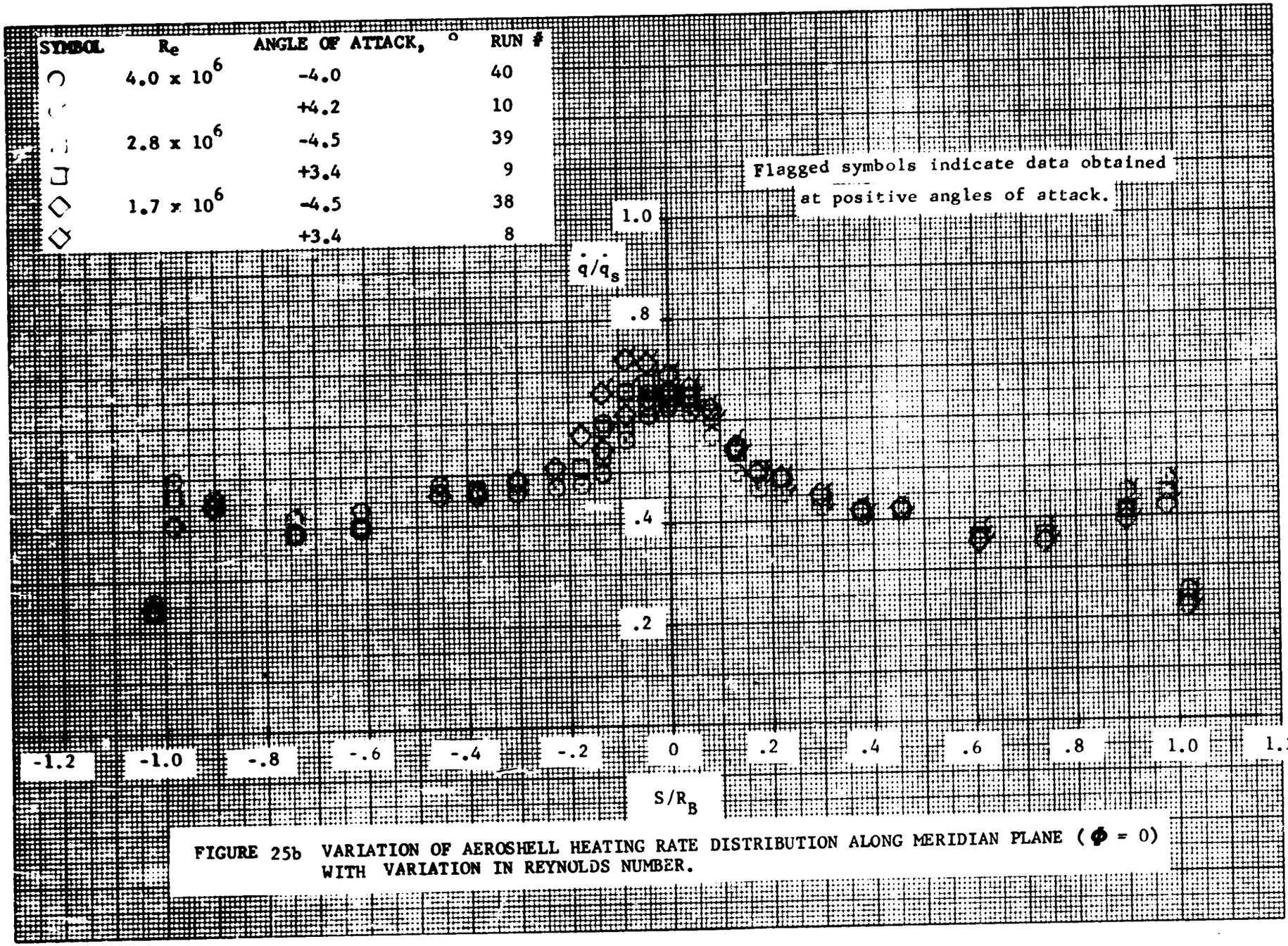

FIGURE 25b VARIATION OF AEROSHELL HEATING RATE DISTRIBUTION ALONG MERIDIAN PLANE (ϕ = 0) WITH VARIATION IN REYNOLDS NUMBER.

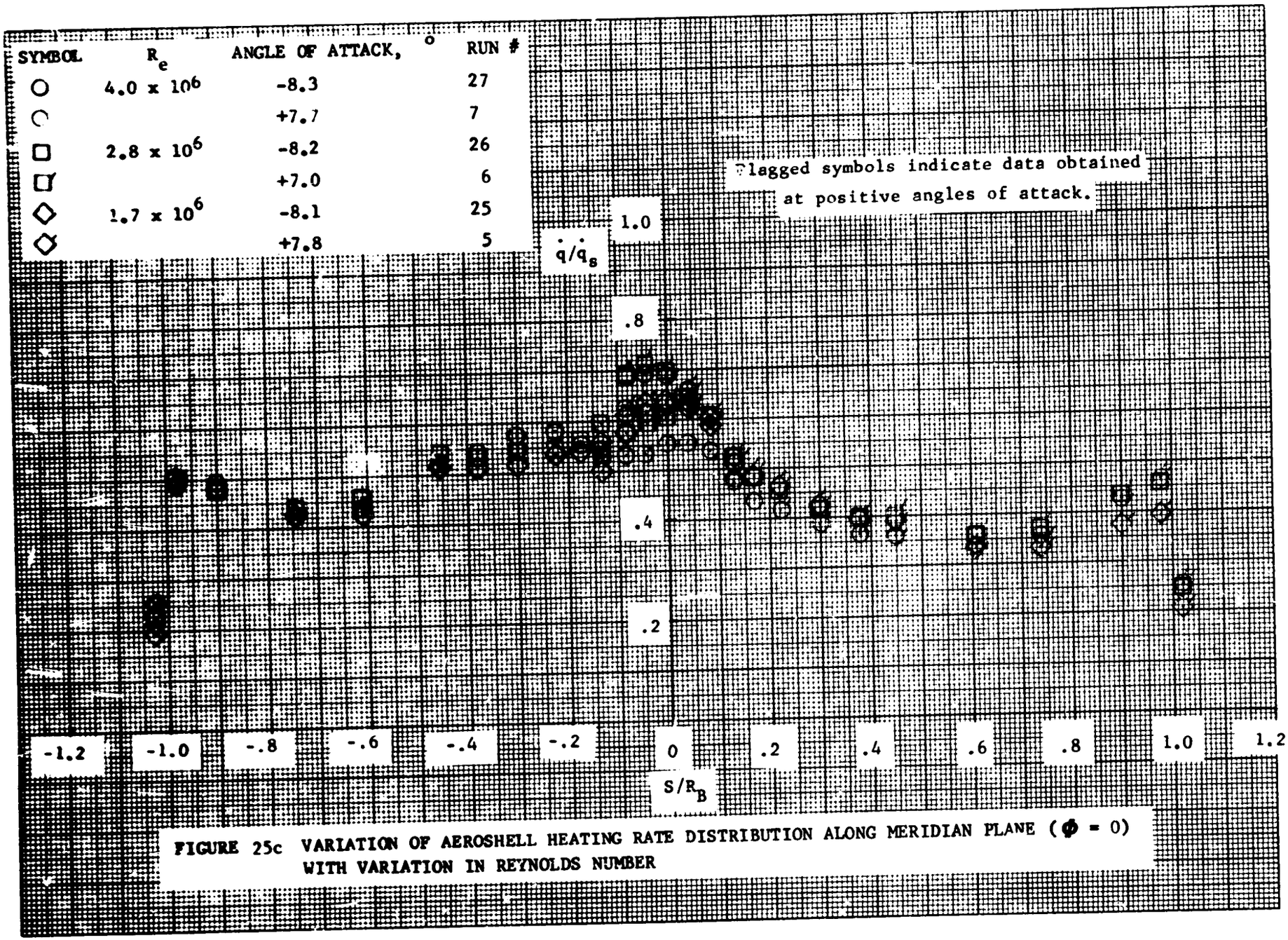

FIGURE 25c VARIATION OF AEROSHELL HEATING RATE DISTRIBUTION ALONG MERIDIAN PLANE (ϕ = 0) WITH VARIATION IN REYNOLDS NUMBER

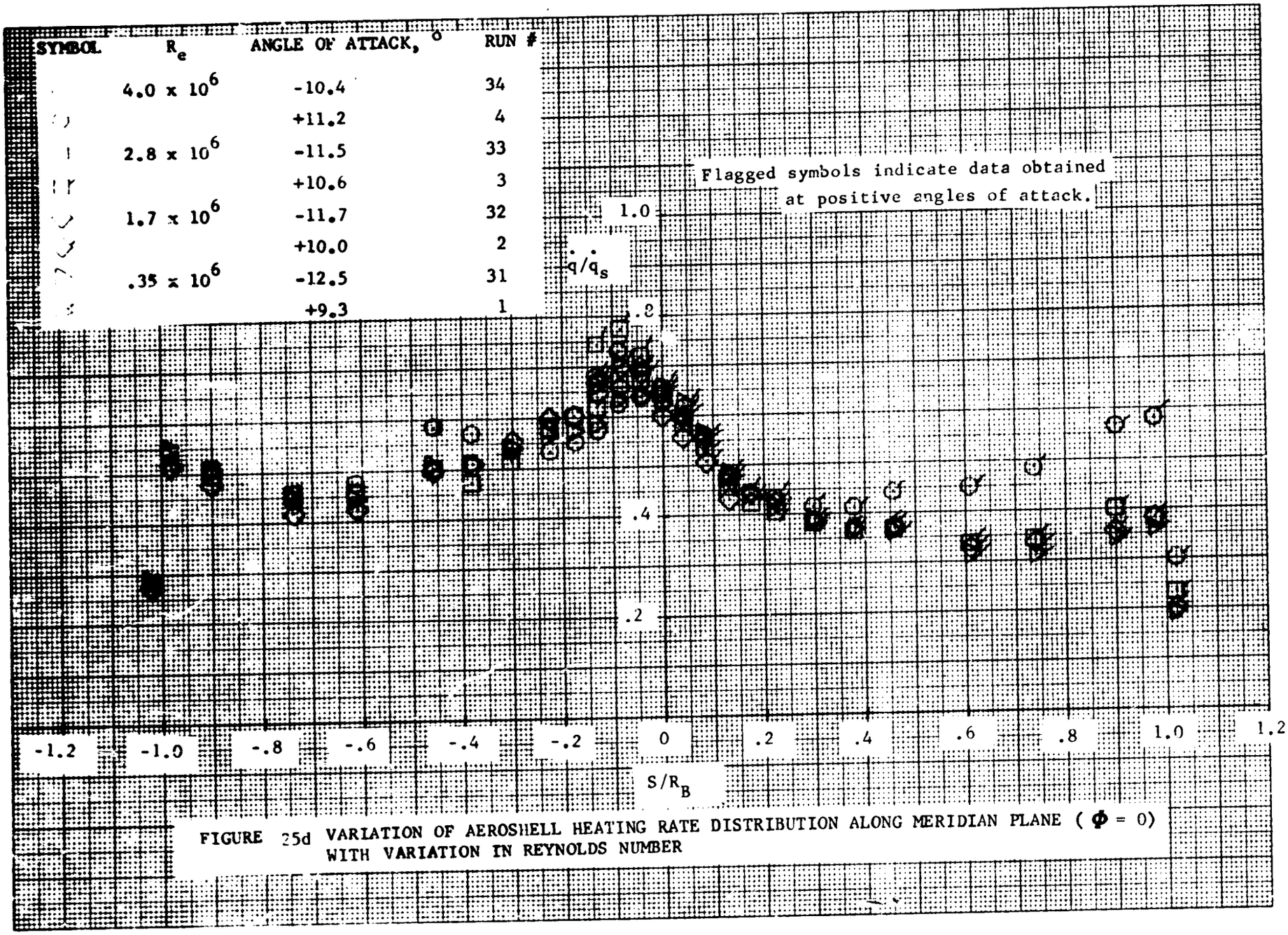

FIGURE 25d VARIATION OF AEROSHELL HEATING RATE DISTRIBUTION ALONG MERIDIAN PLANE (Φ = 0) WITH VARIATION IN REYNOLDS NUMBER

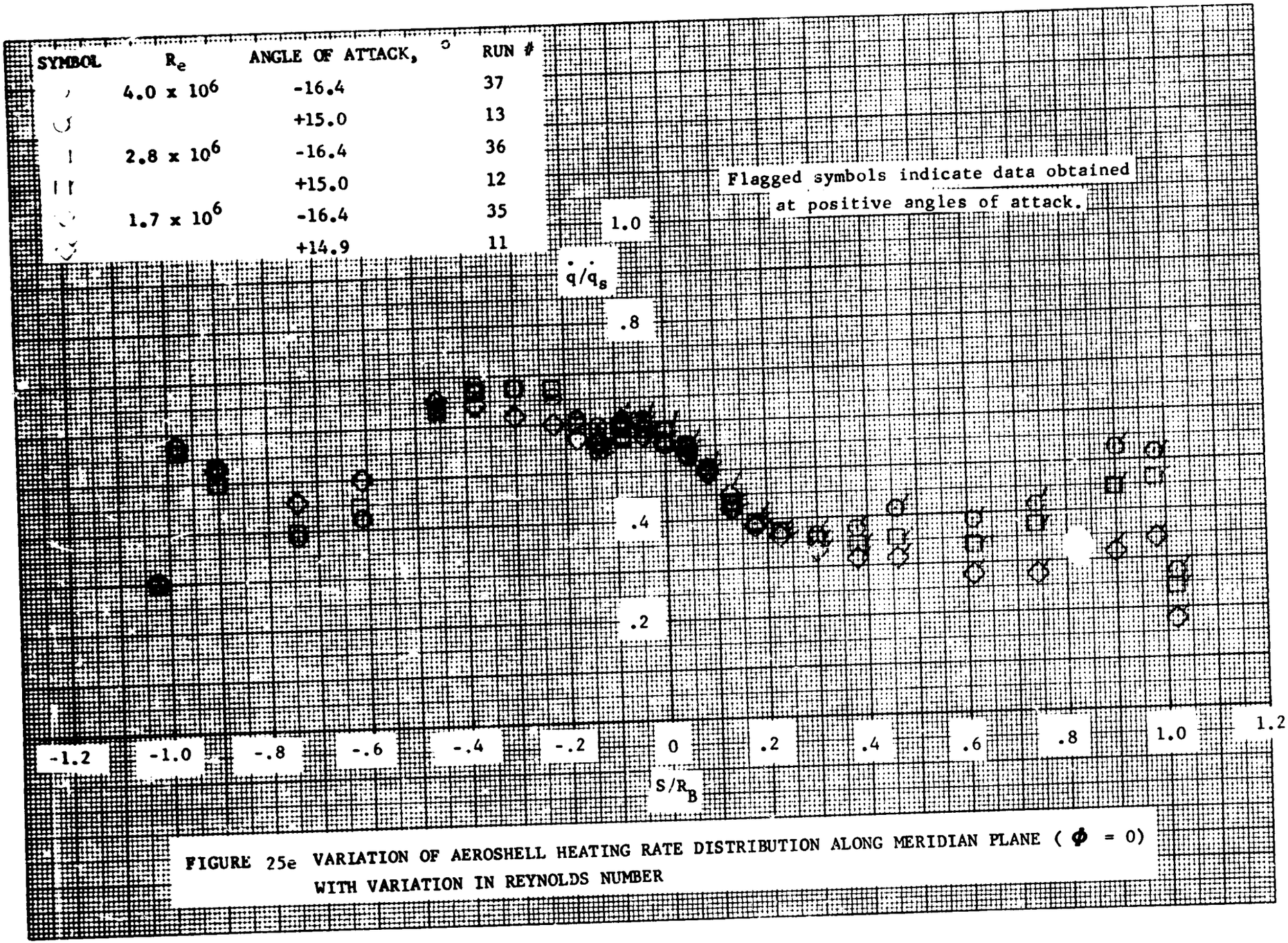

FIGURE 25e VARIATION OF AEROSHELL HEATING RATE DISTRIBUTION ALONG MERIDIAN PLANE (ϕ = 0) WITH VARIATION IN REYNOLDS NUMBER

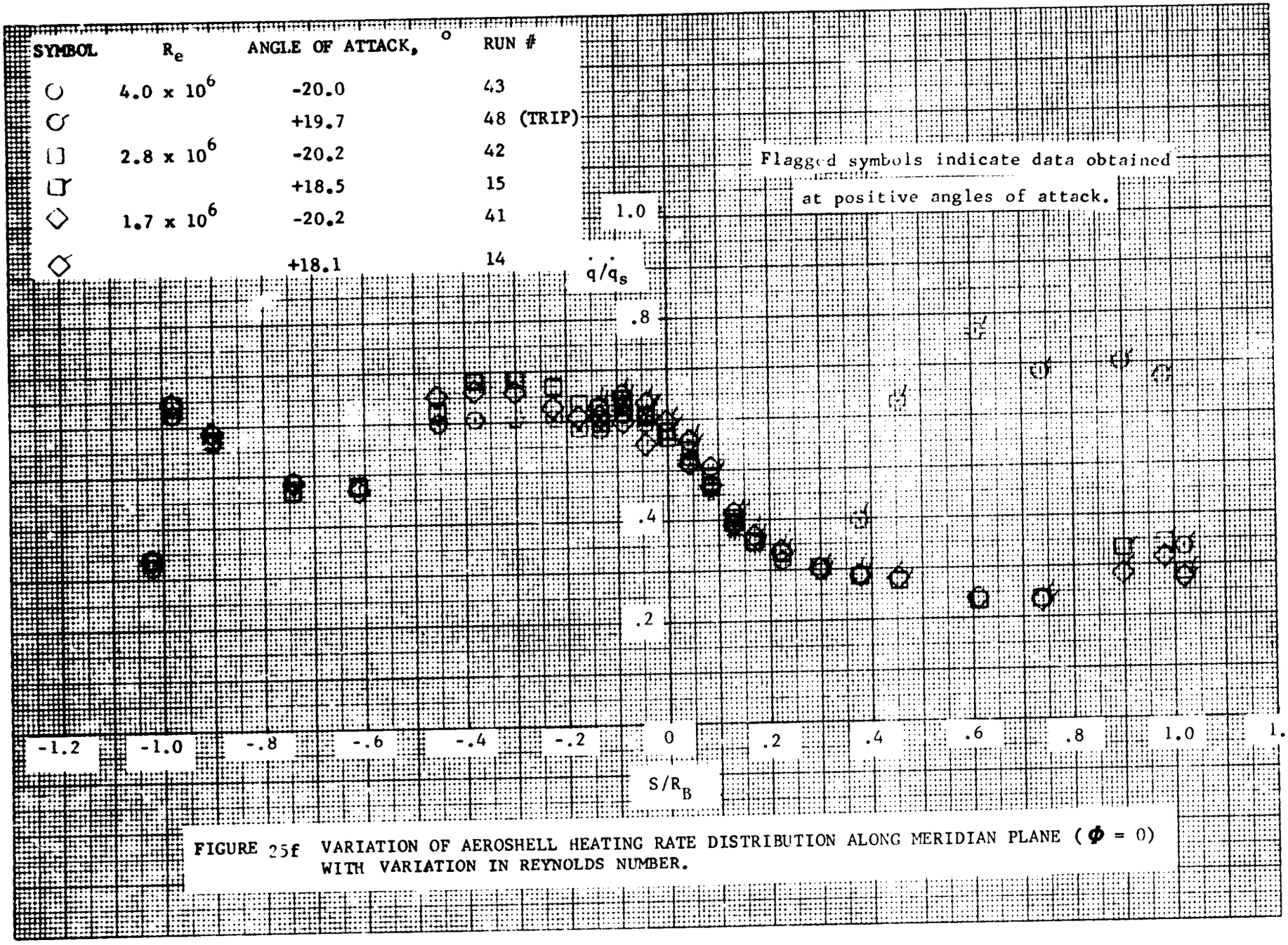

FIGURE 25f VARIATION OF AEROSHELL HEATING RATE DISTRIBUTION ALONG MERIDIAN PLANE (Φ = 0) WITH VARIATION IN REYNOLDS NUMBER.

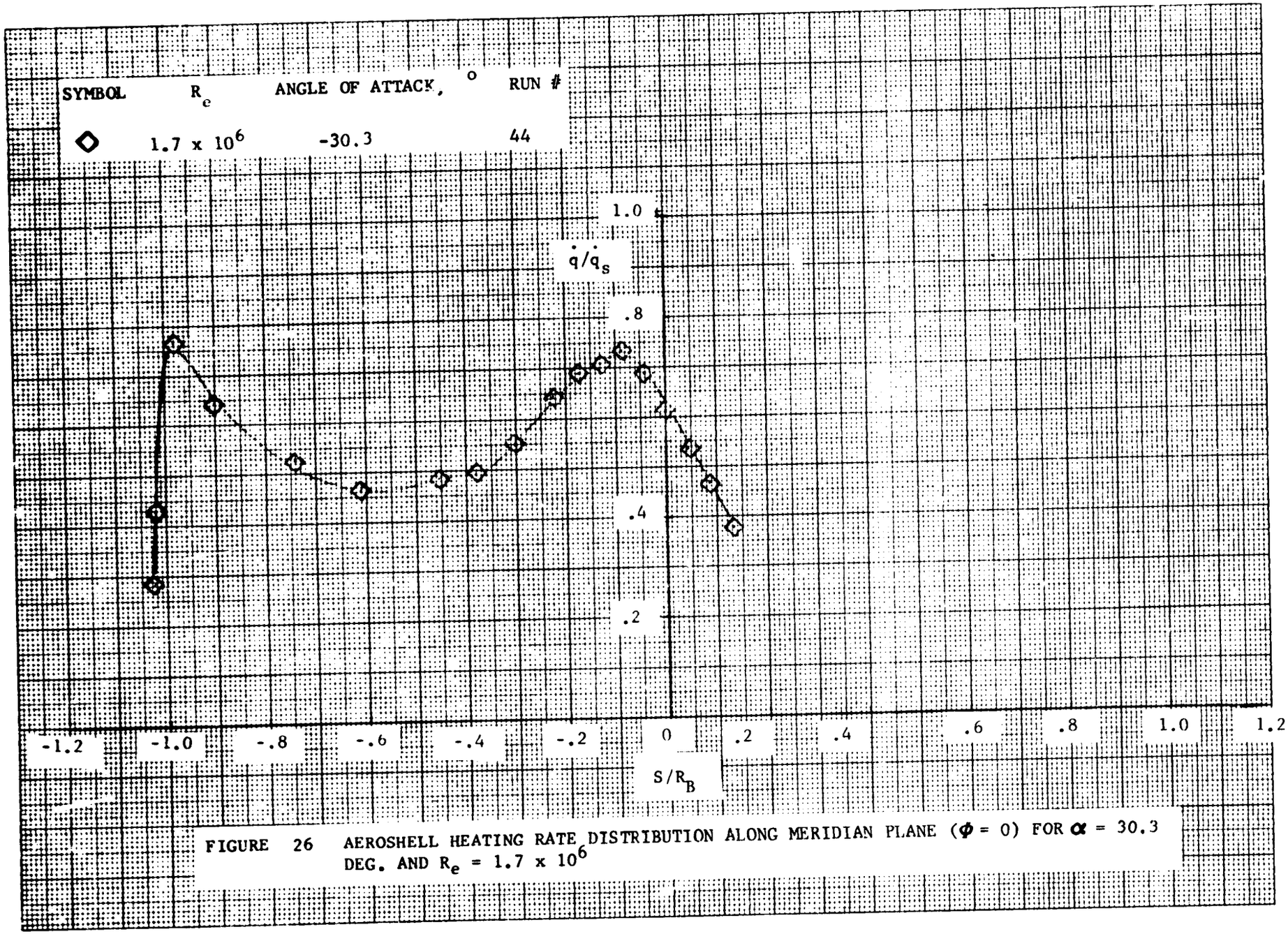

FIGURE 26 AEROSHELL HEATING RATE DISTRIBUTION ALONG MERIDIAN PLANE (ϕ = 0) FOR α = 30.3 DEG. AND R_e = 1.7 x 10^6

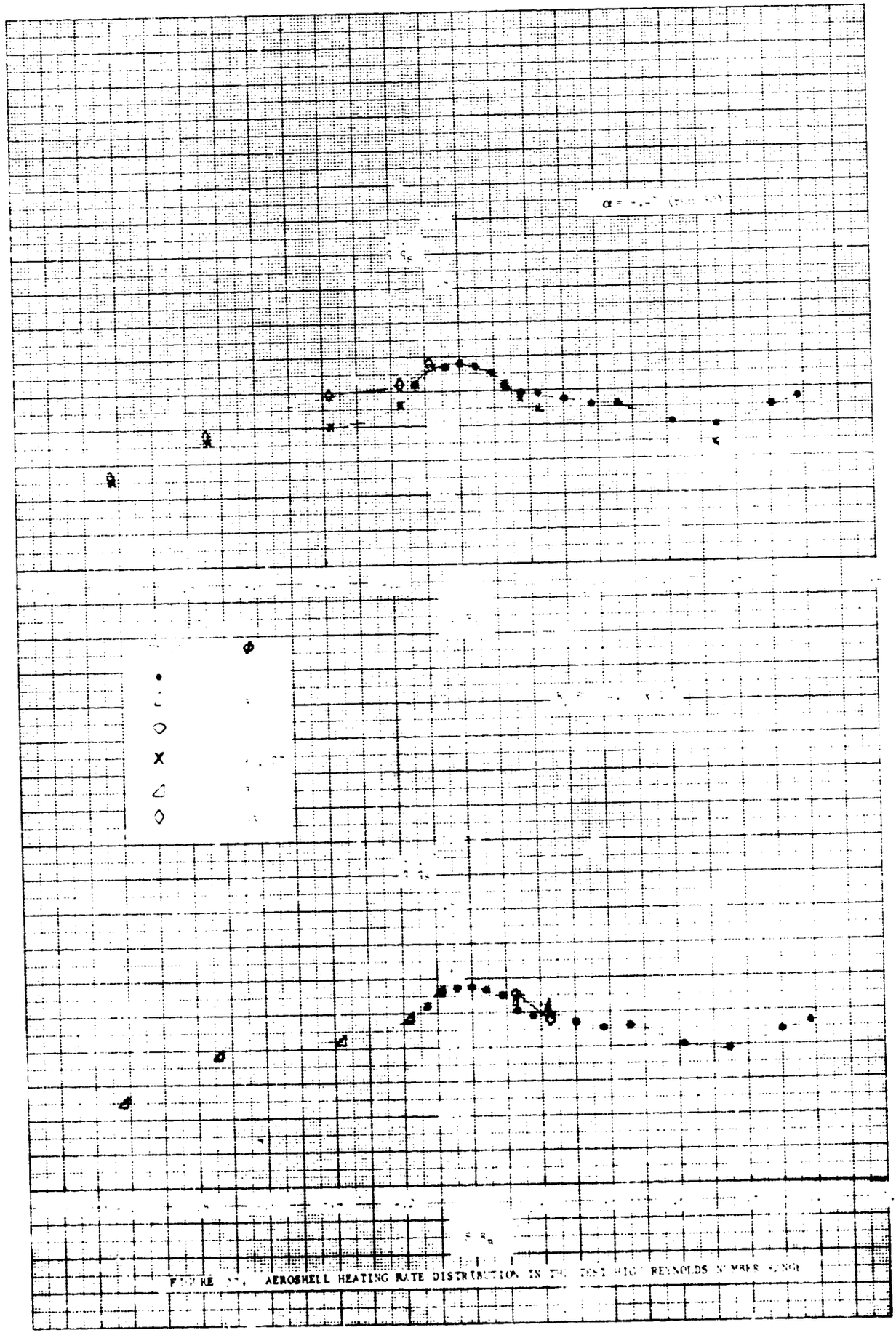

FIGURE [illegible], AEROSHELL HEATING RATE DISTRIBUTION IN THE [illegible] REYNOLDS NUMBER RANGE

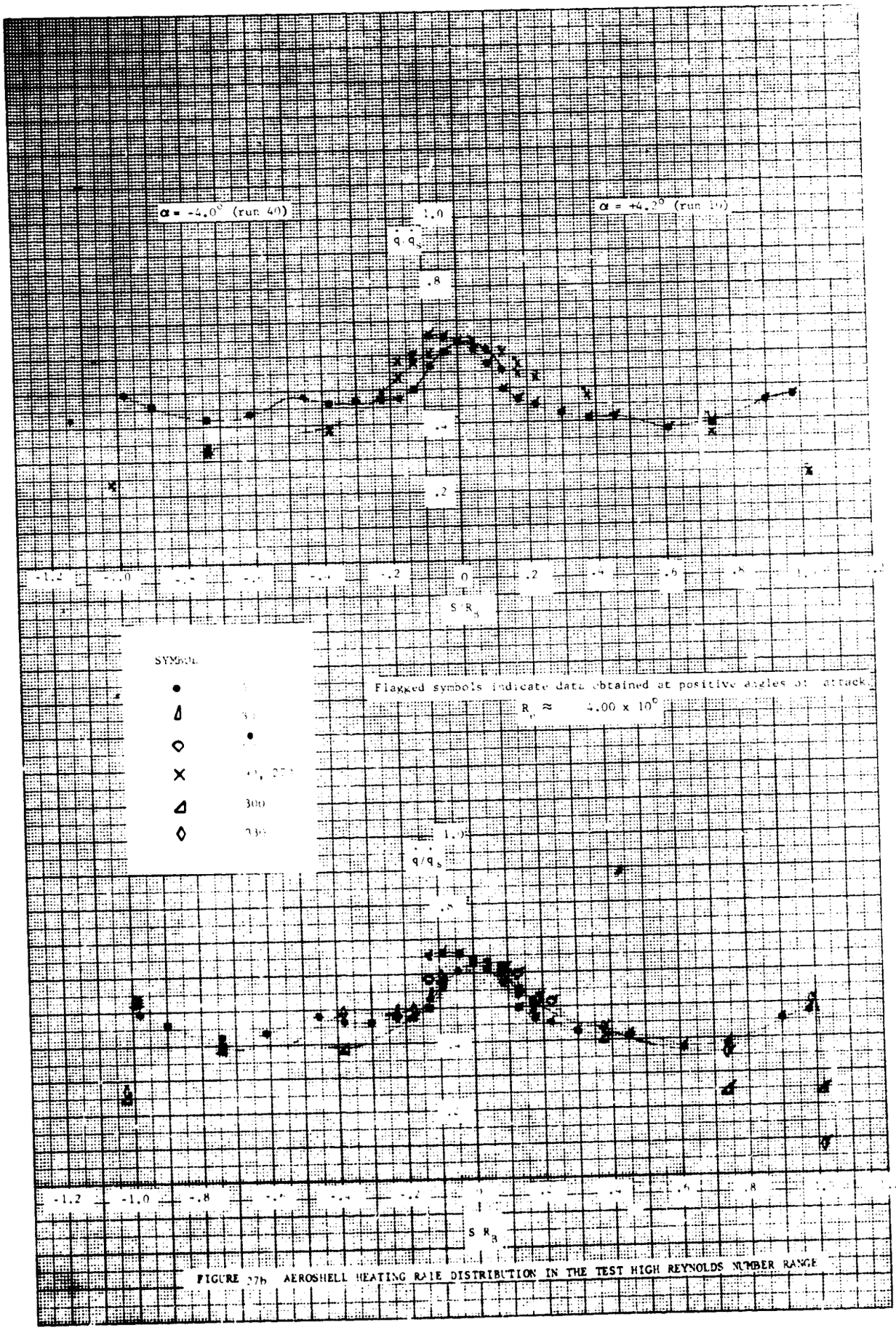

FIGURE 27b AEROSHELL HEATING RATE DISTRIBUTION IN THE TEST HIGH REYNOLDS NUMBER RANGE

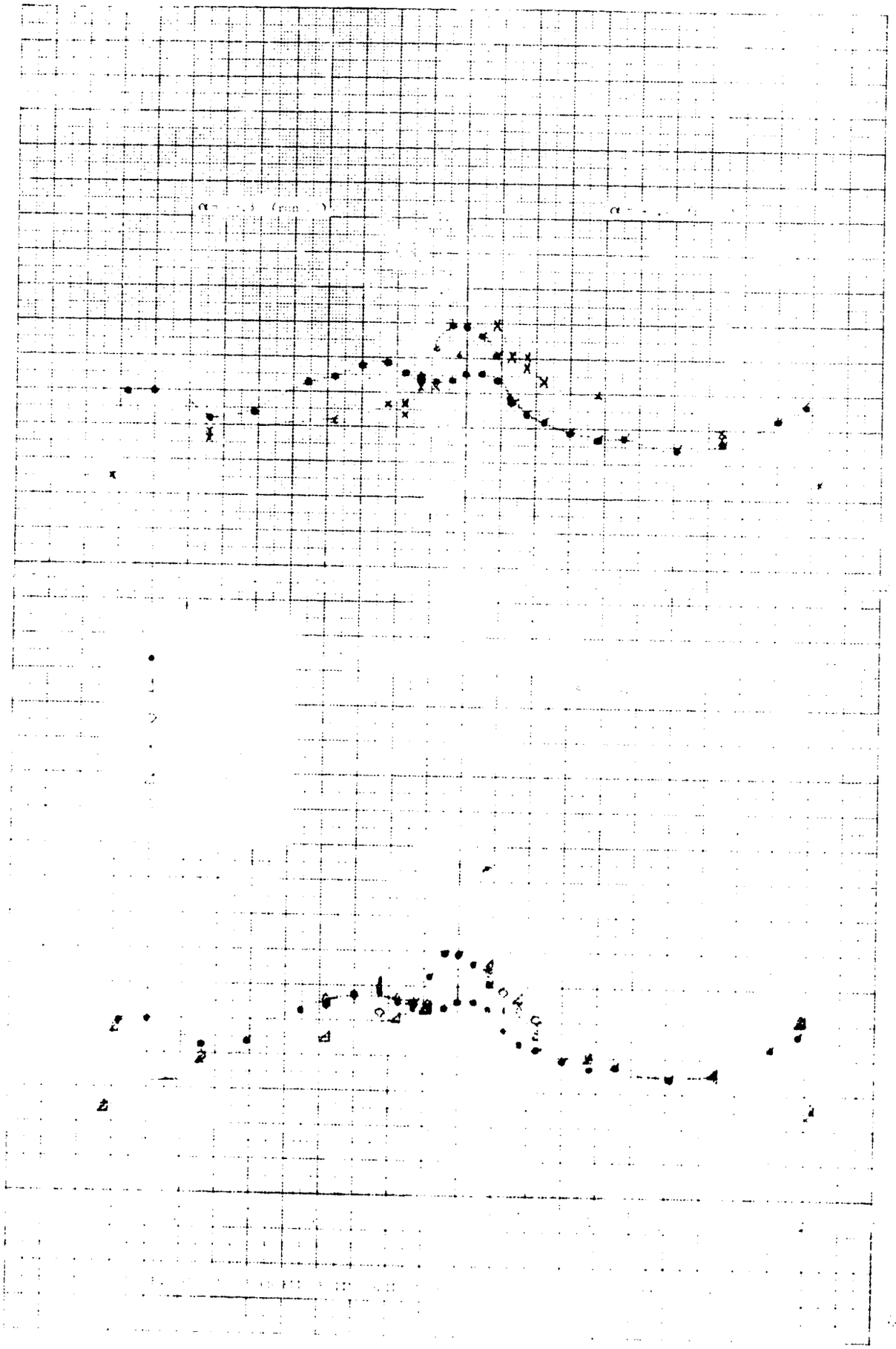

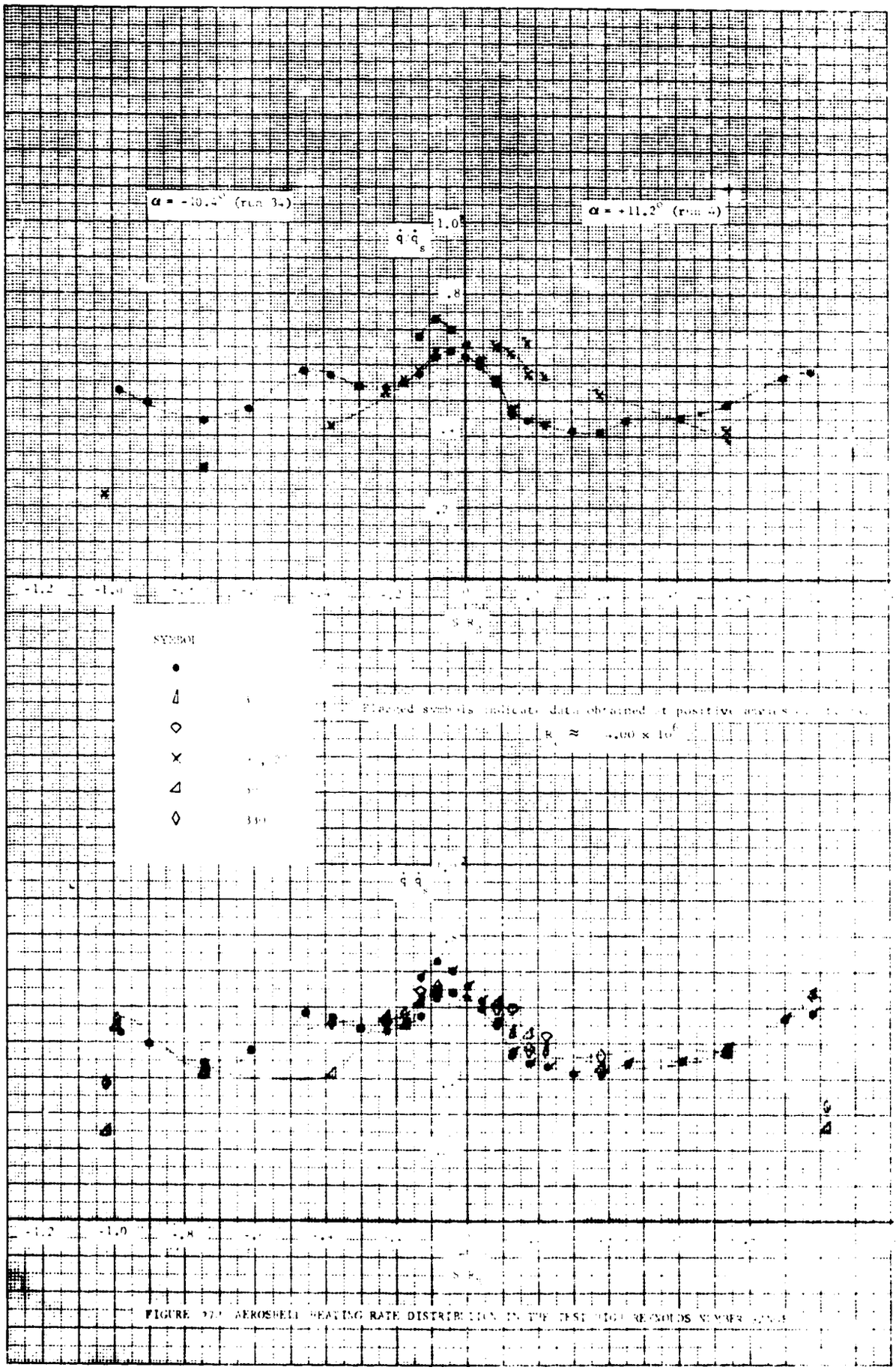

FIGURE 22. AEROSHELL HEATING RATE DISTRIBUTION IN THE TEST FLOW REYNOLDS NUMBER

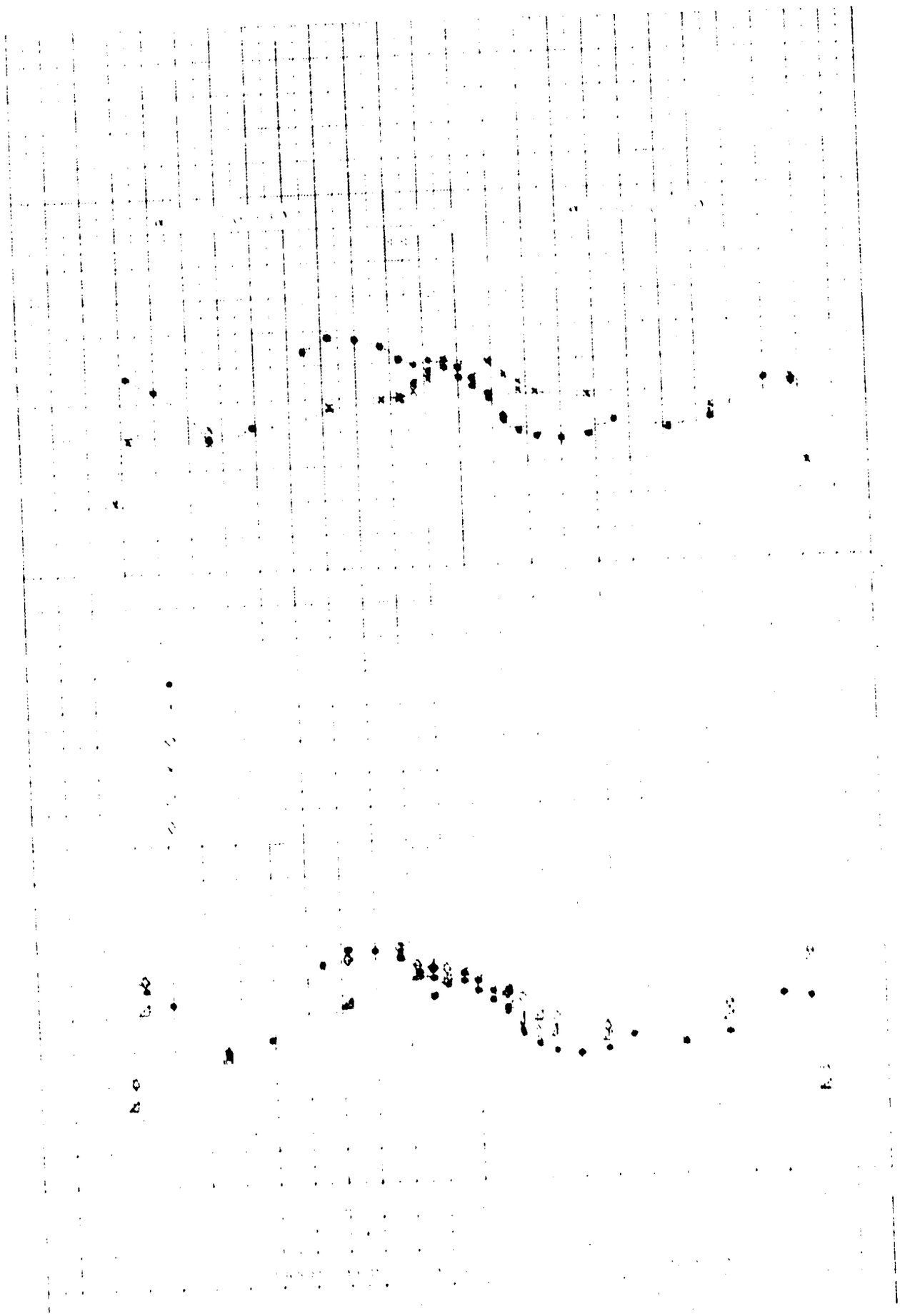

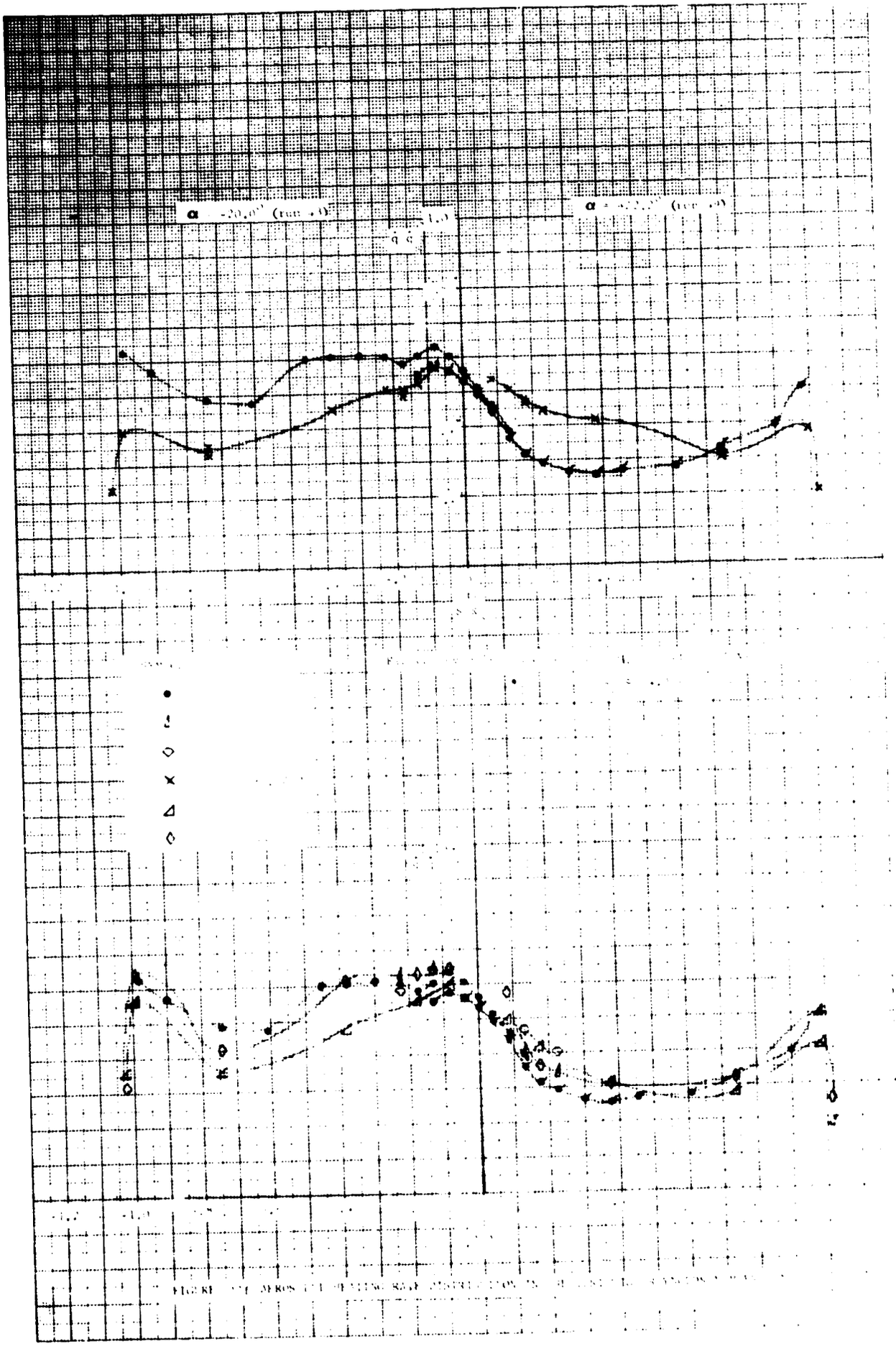

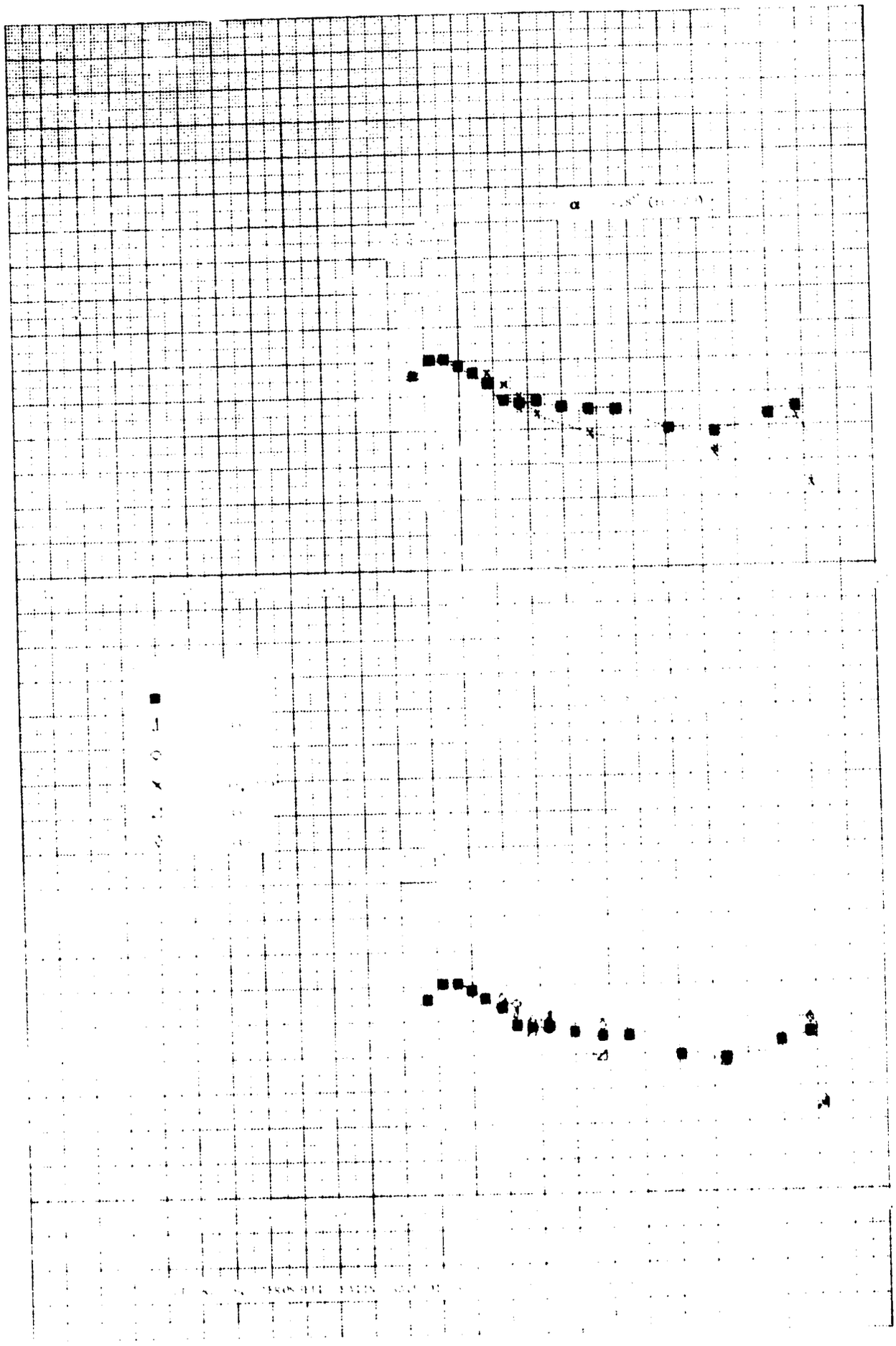

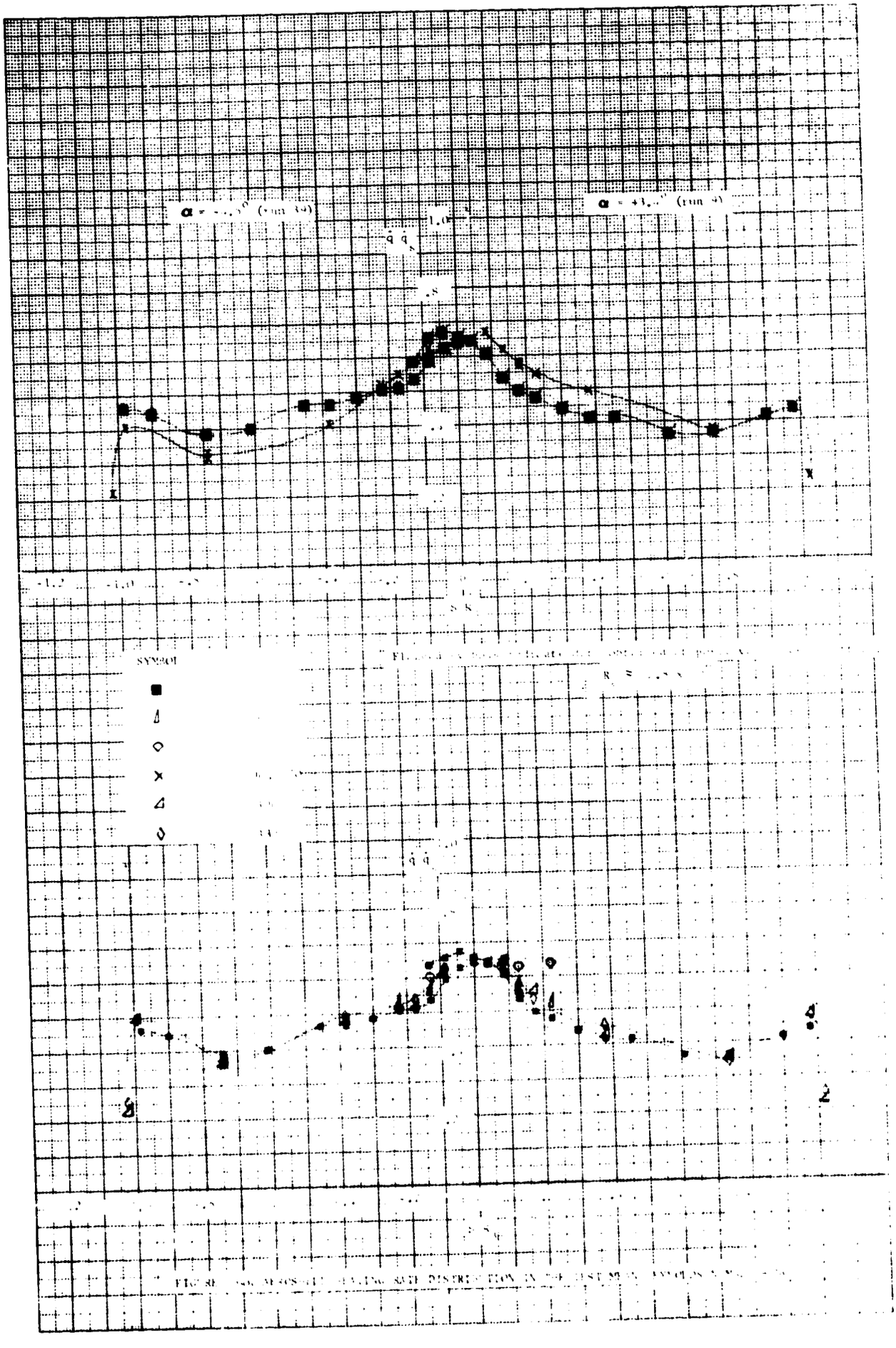

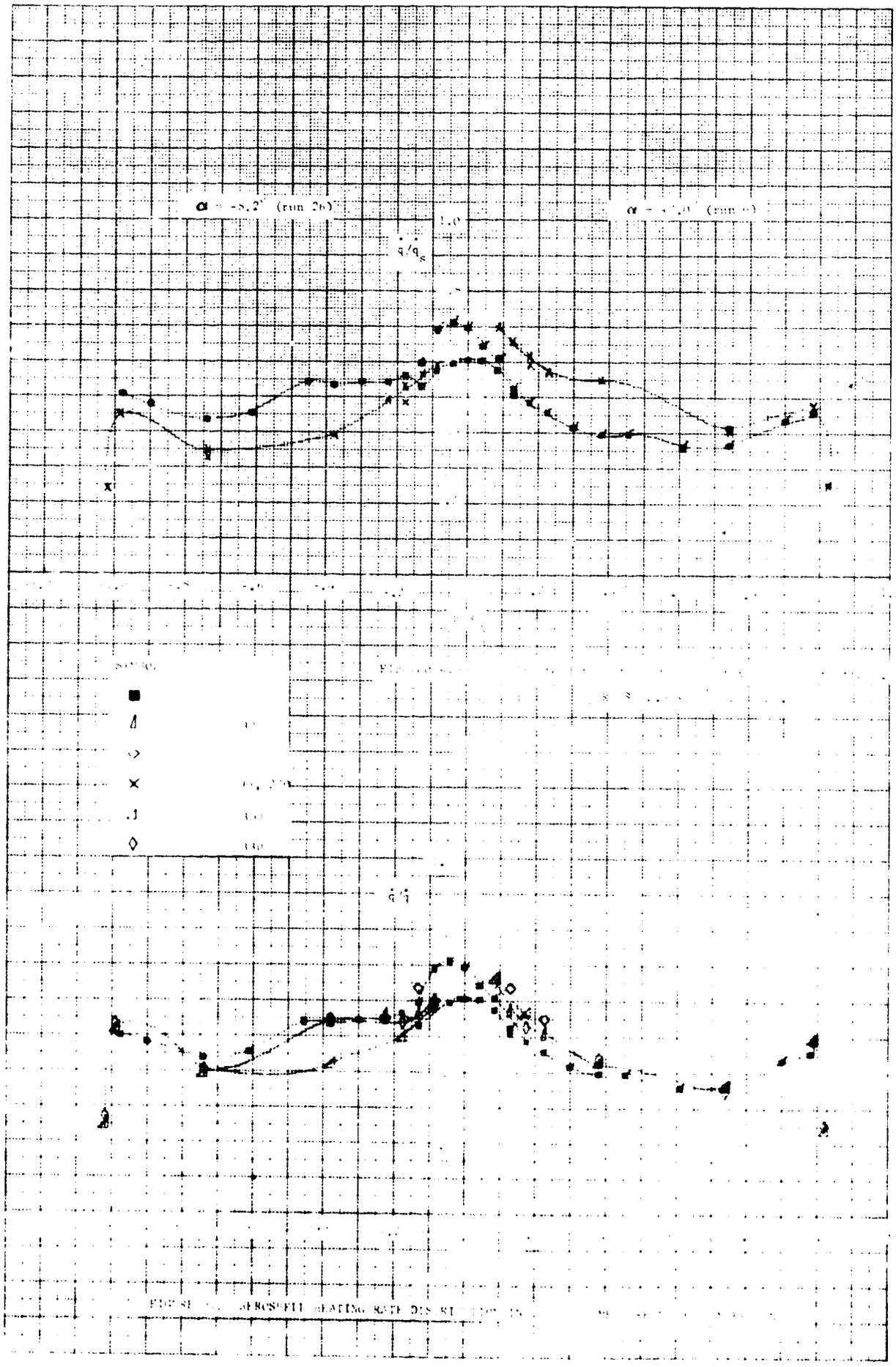

FIGURE [illegible] AEROSHELL HEATING RATE DISTRIBUTION [illegible]

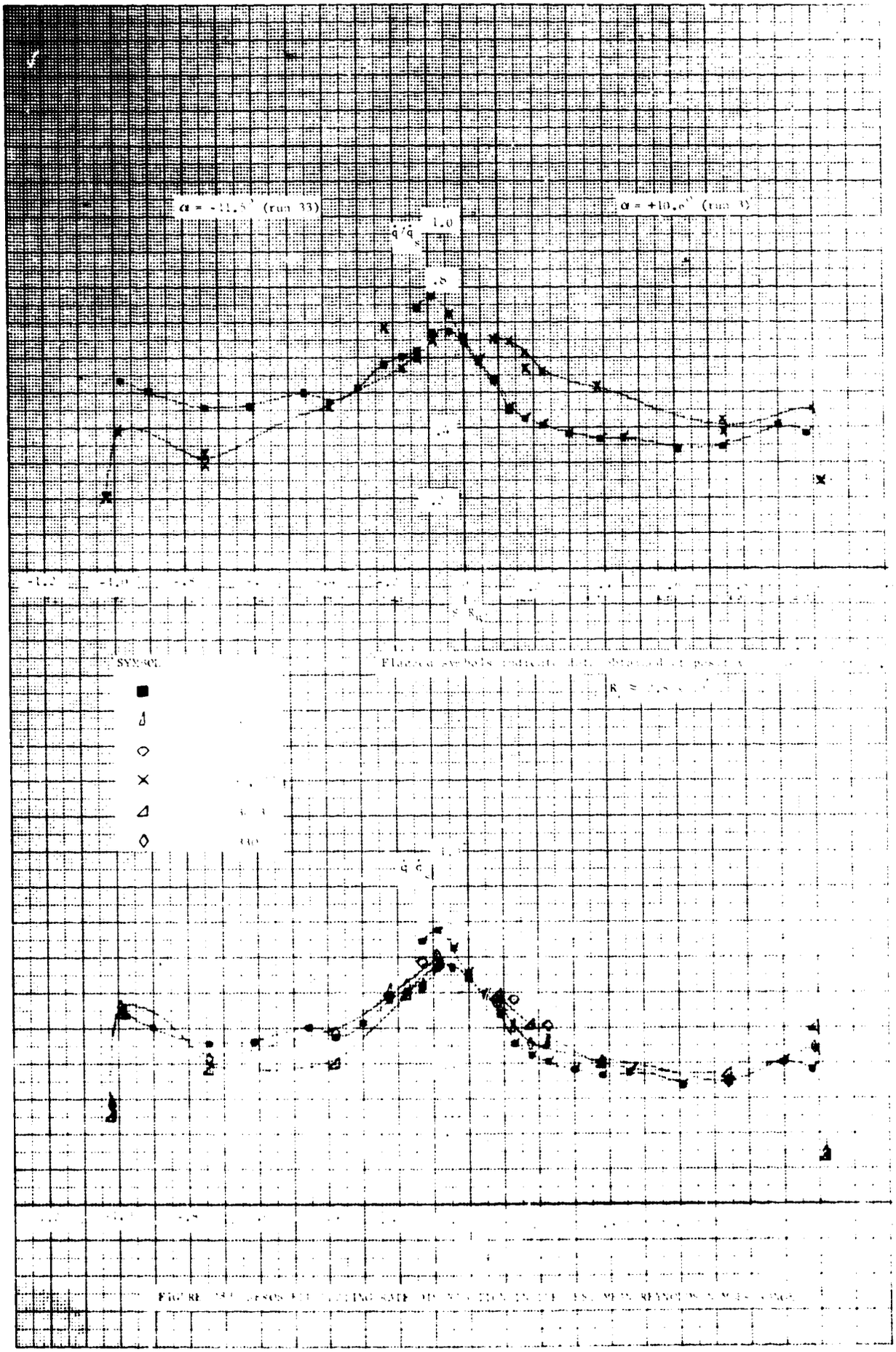

FIGURE [illegible] SEROS [illegible] RATE [illegible] MEAN REYNOLDS [illegible]

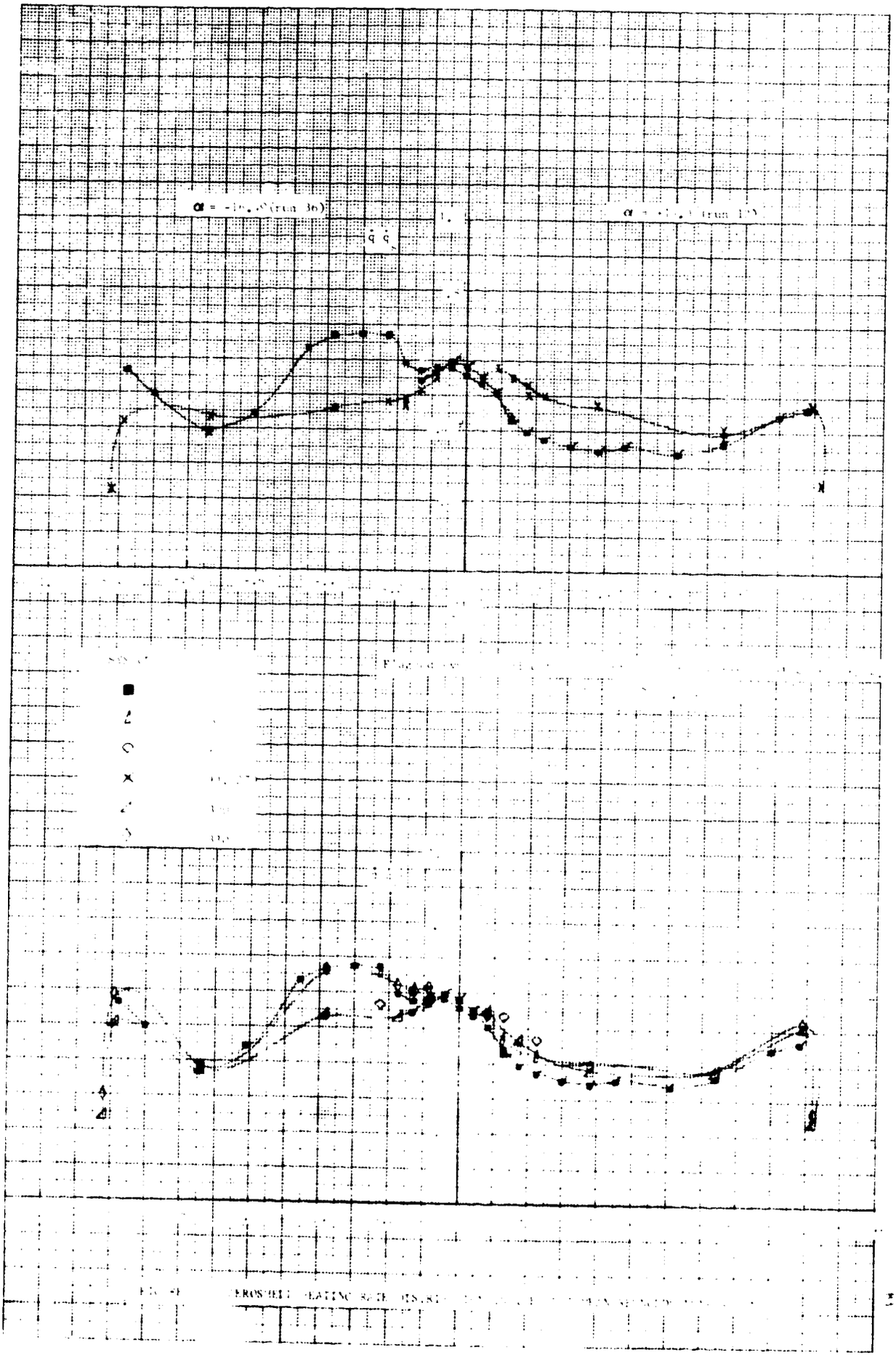

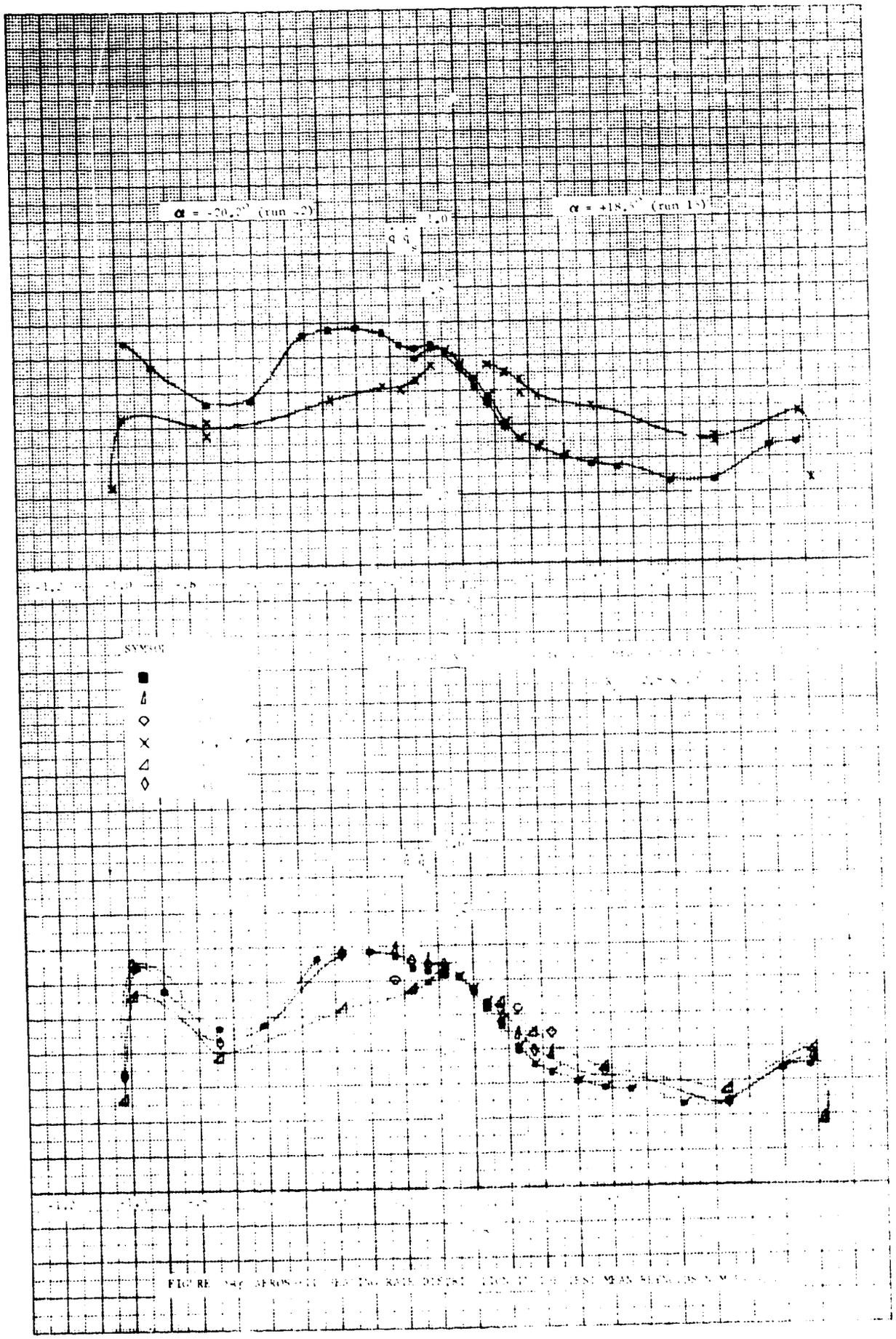
SYMBOL

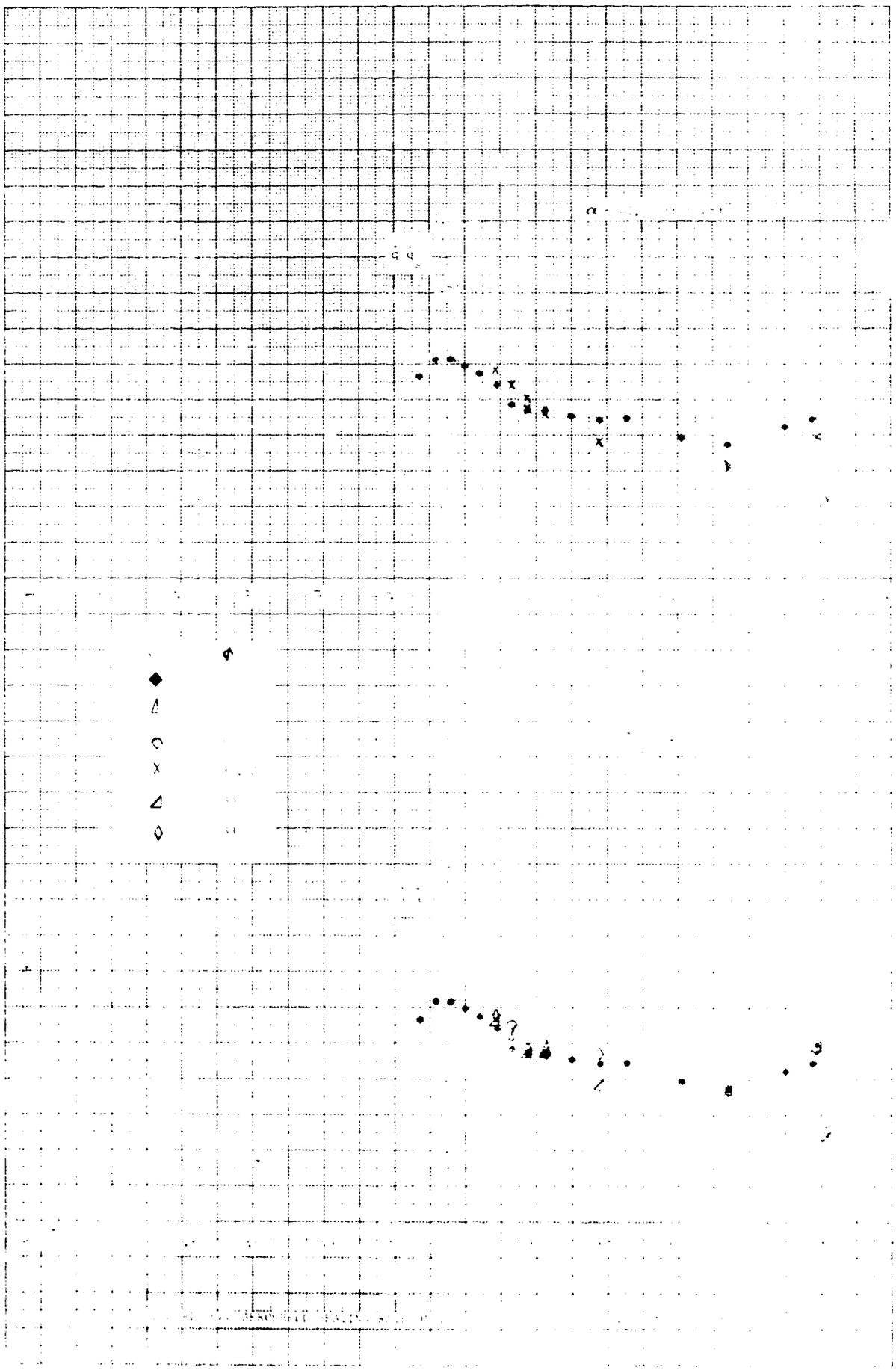

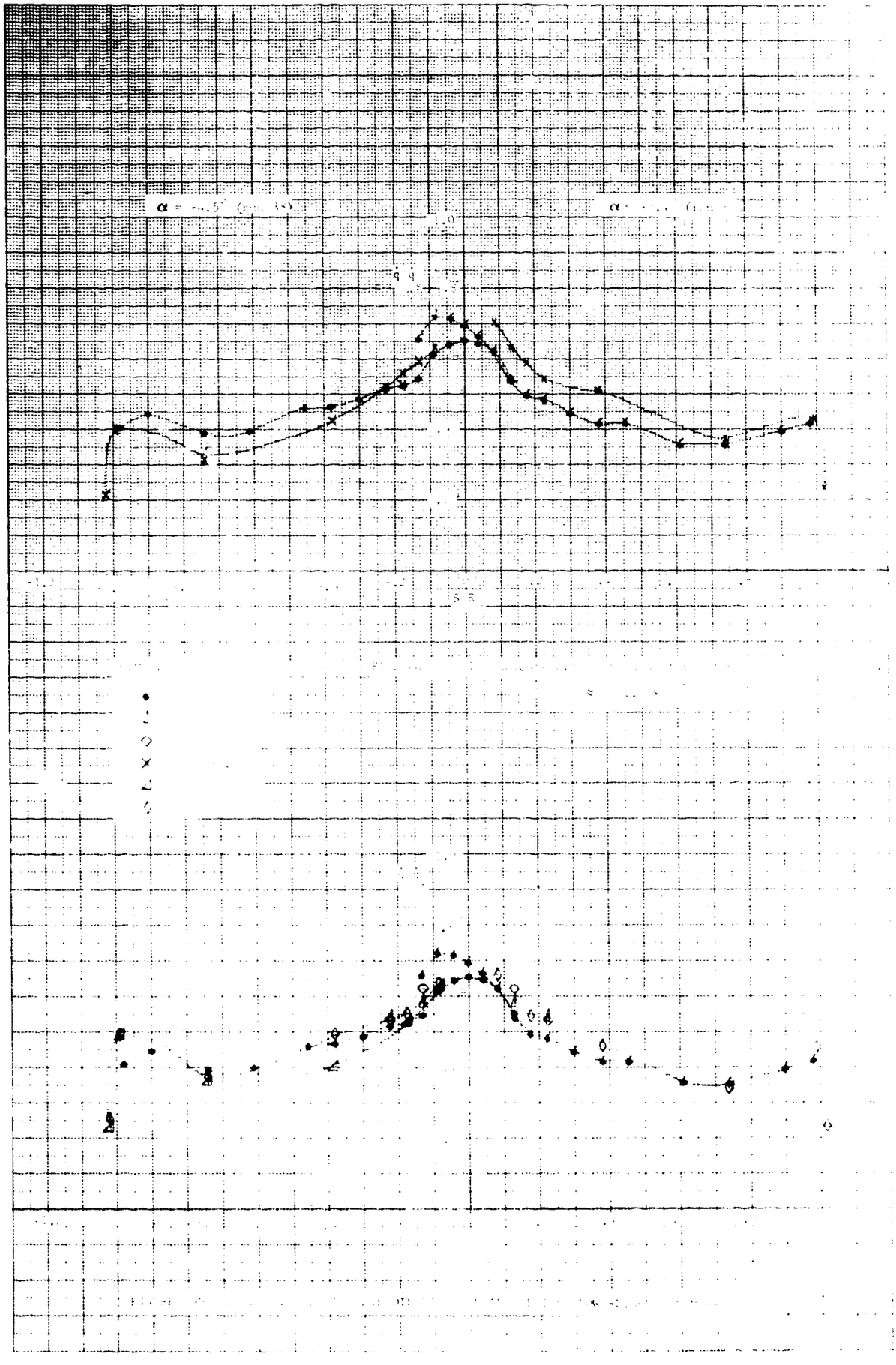

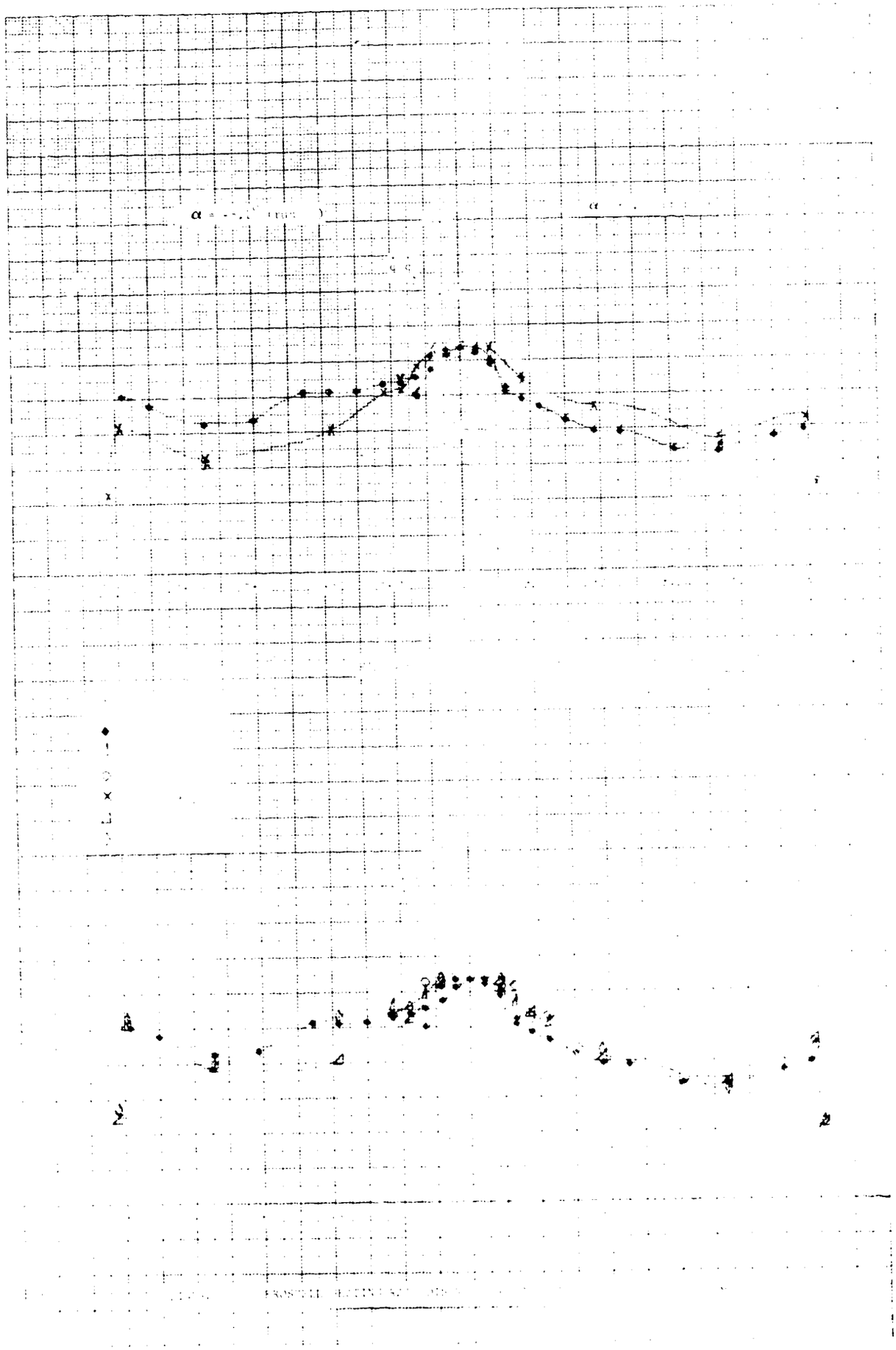

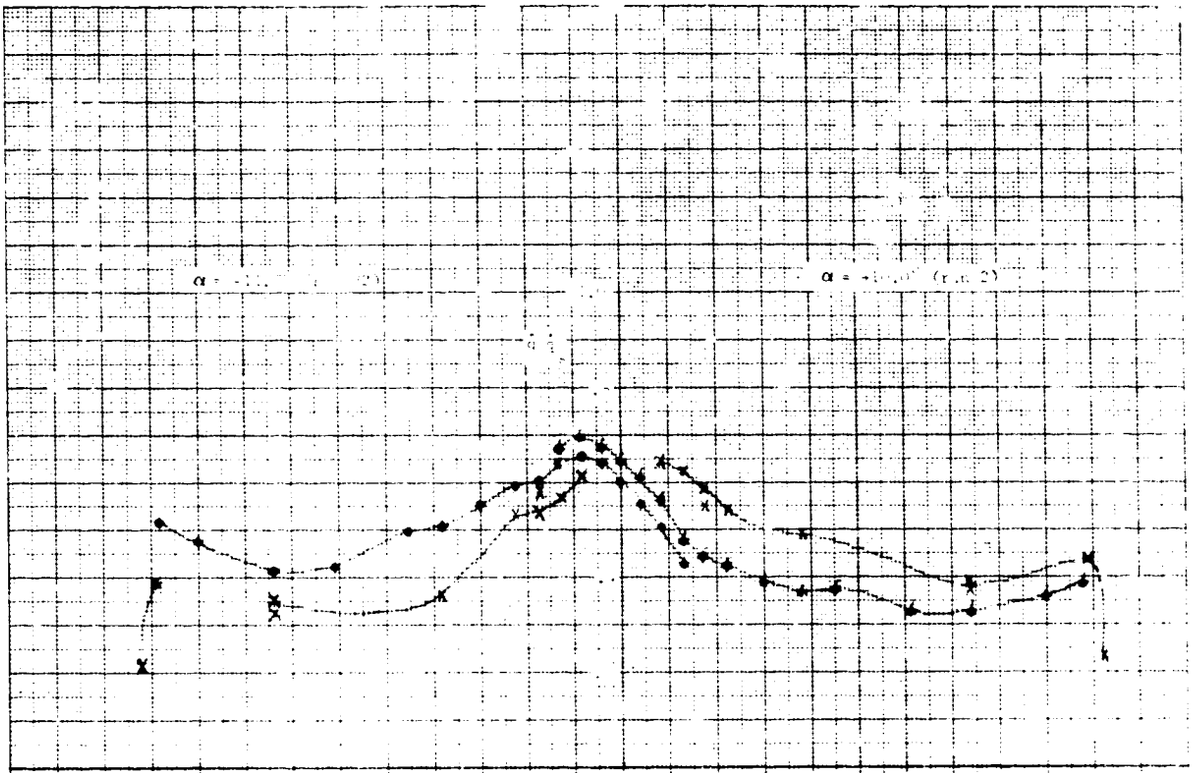

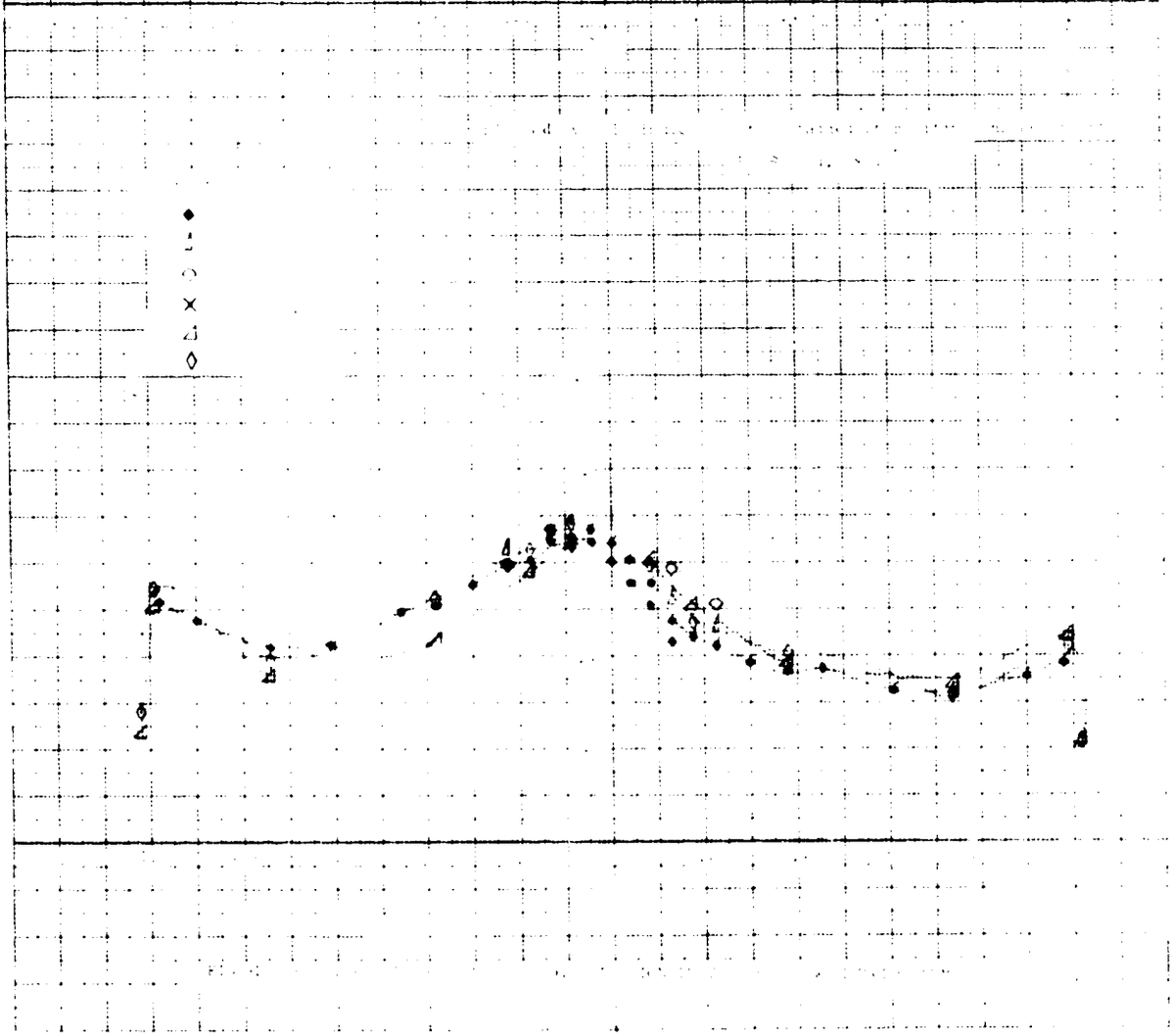

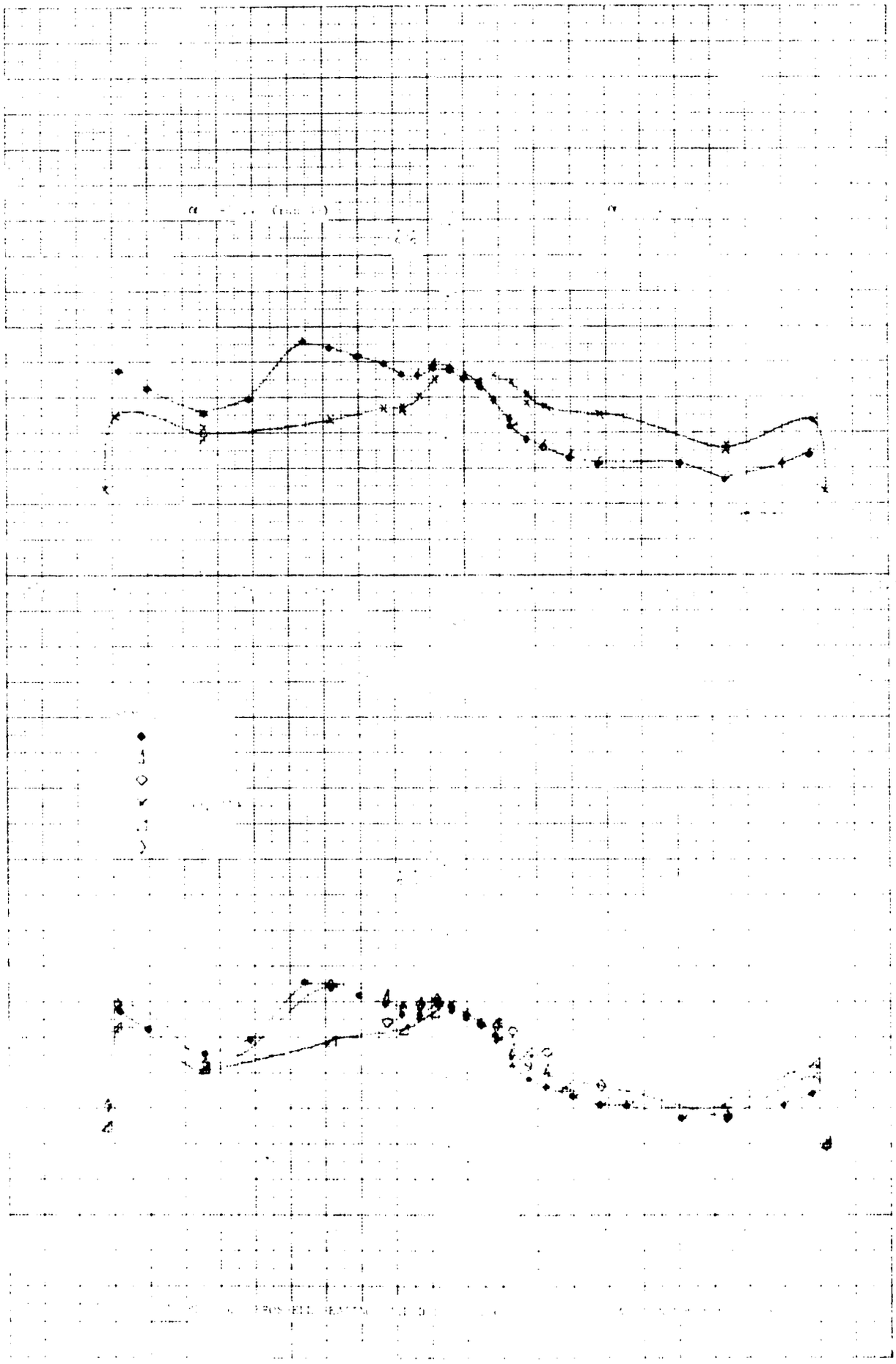

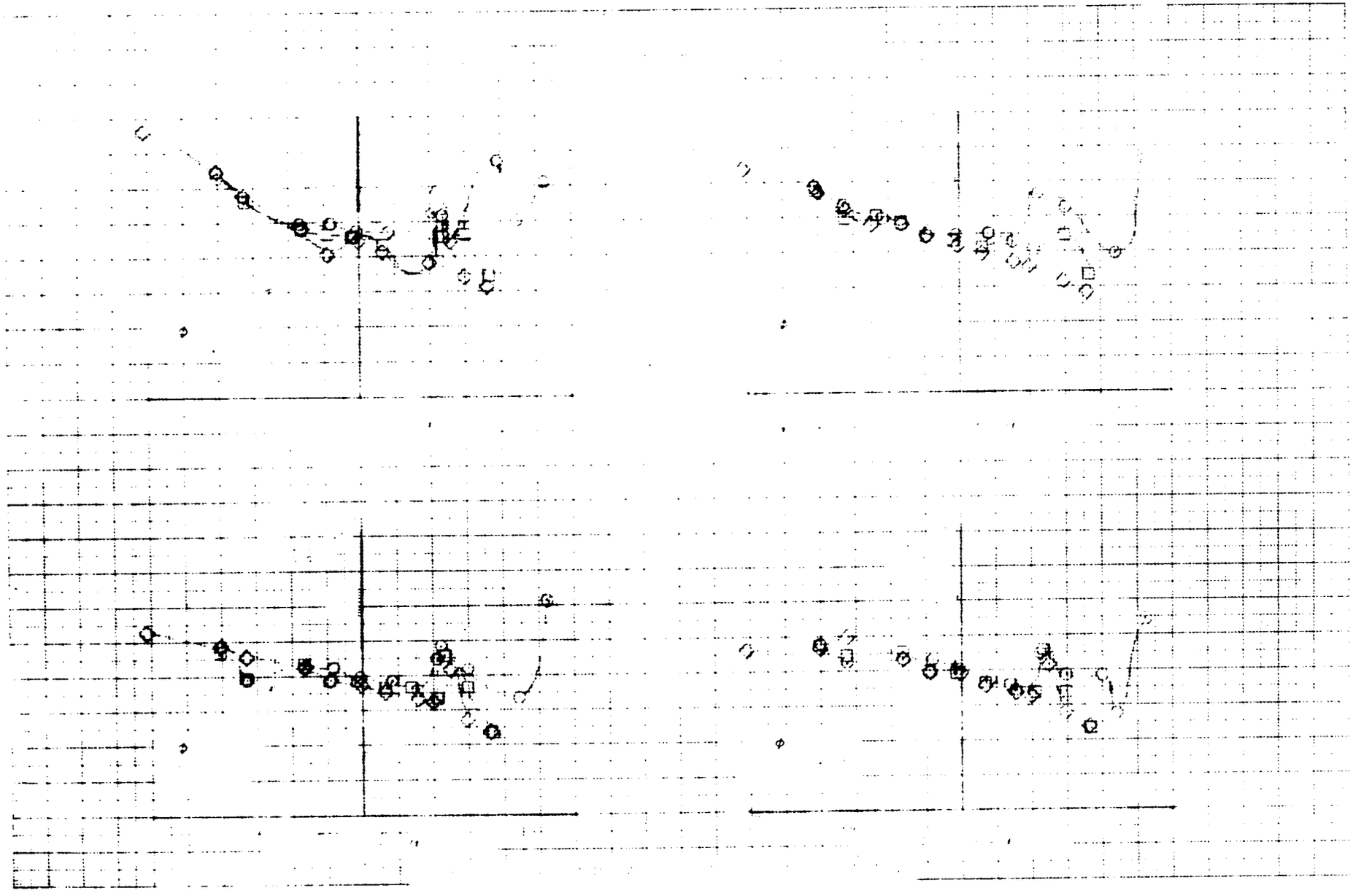

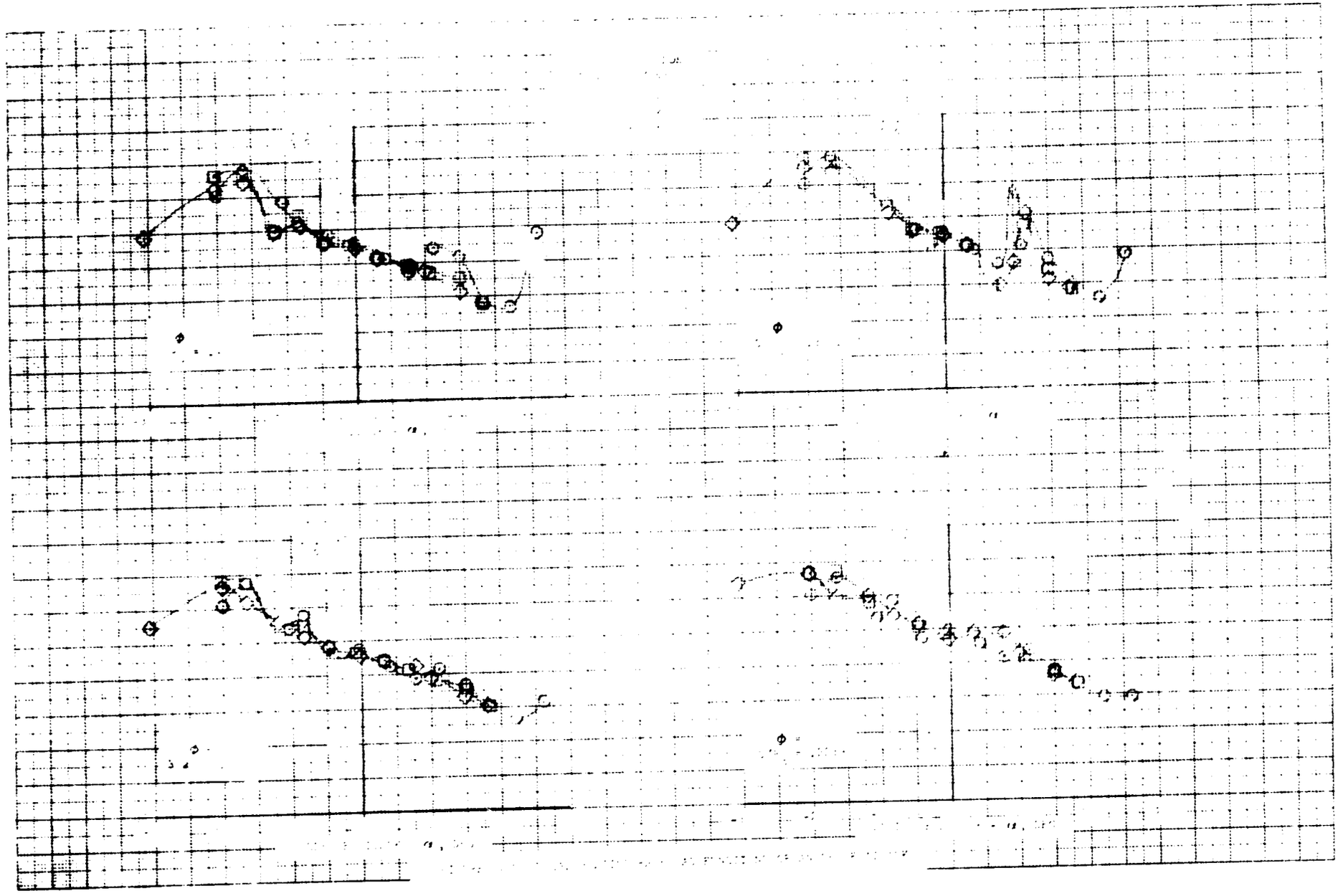

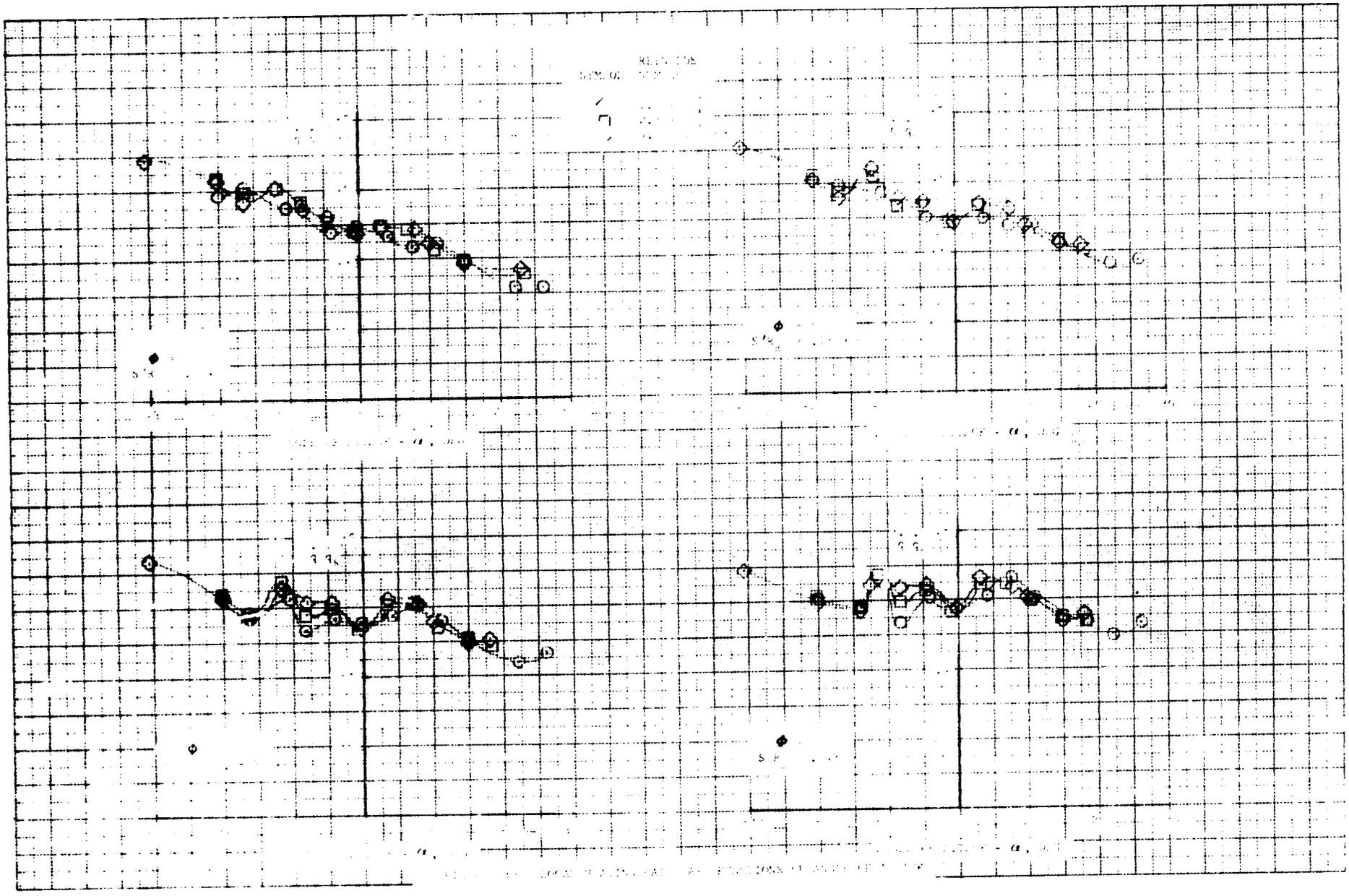

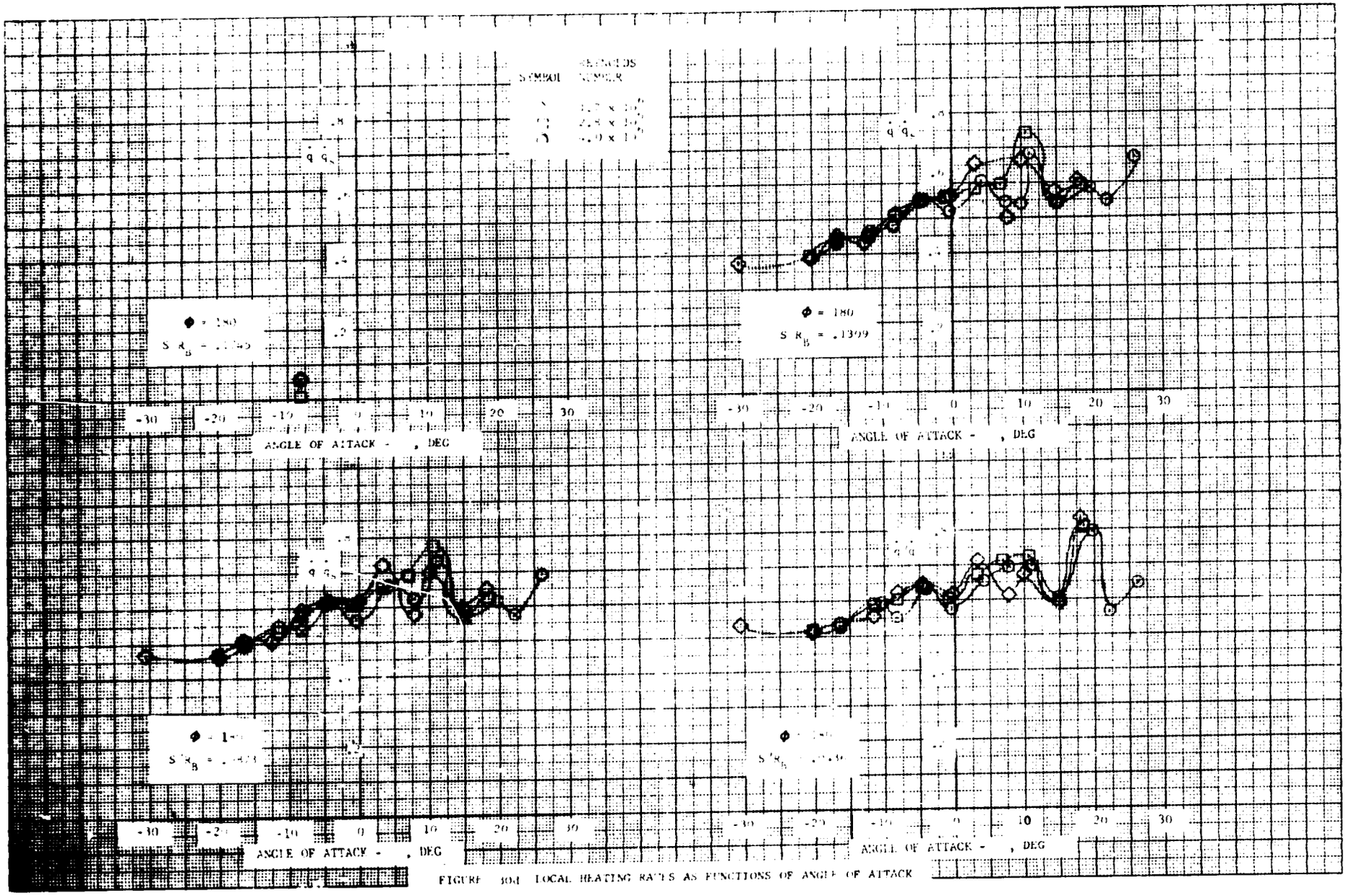

FIGURE 30d LOCAL HEATING RATES AS FUNCTIONS OF ANGLE OF ATTACK

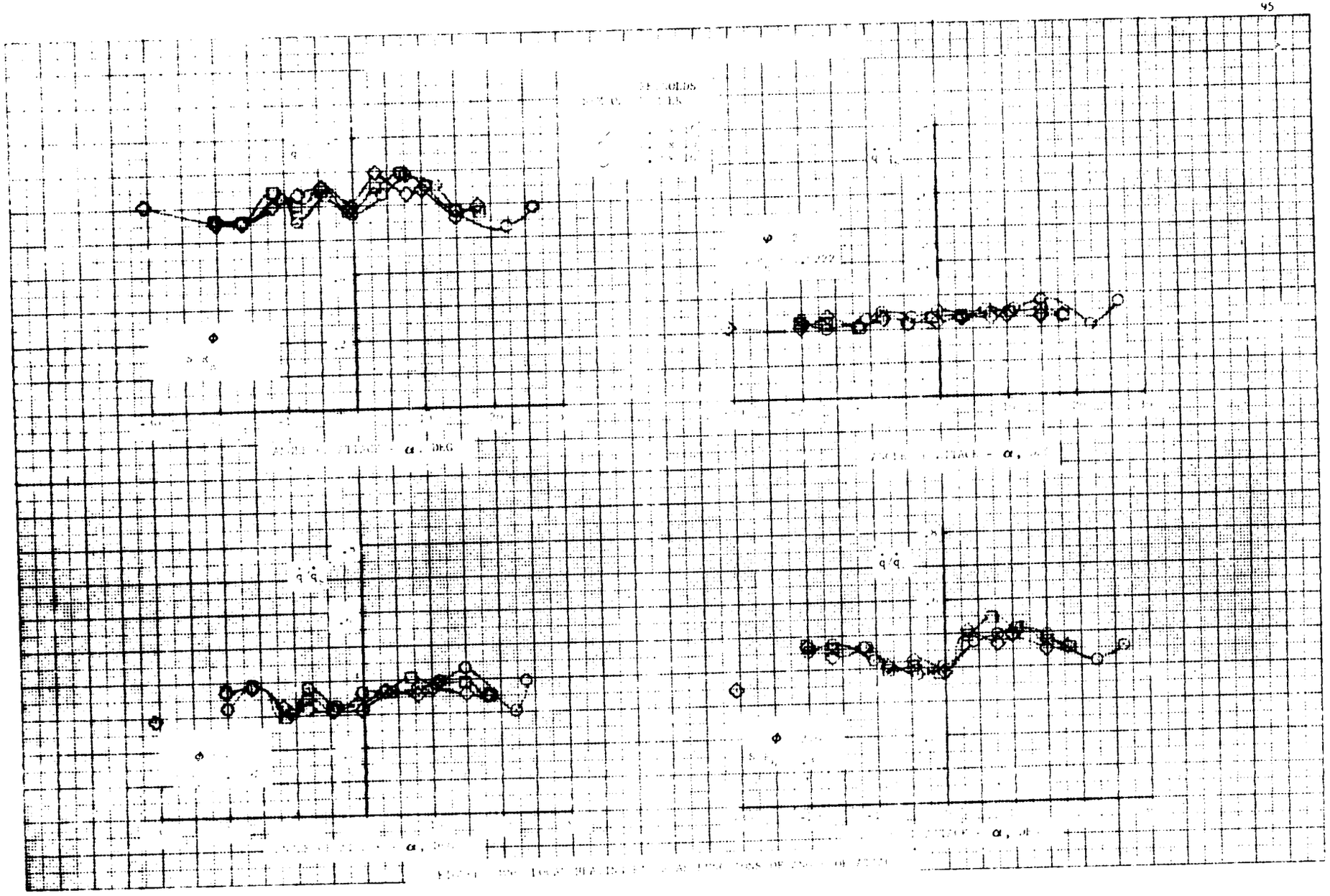

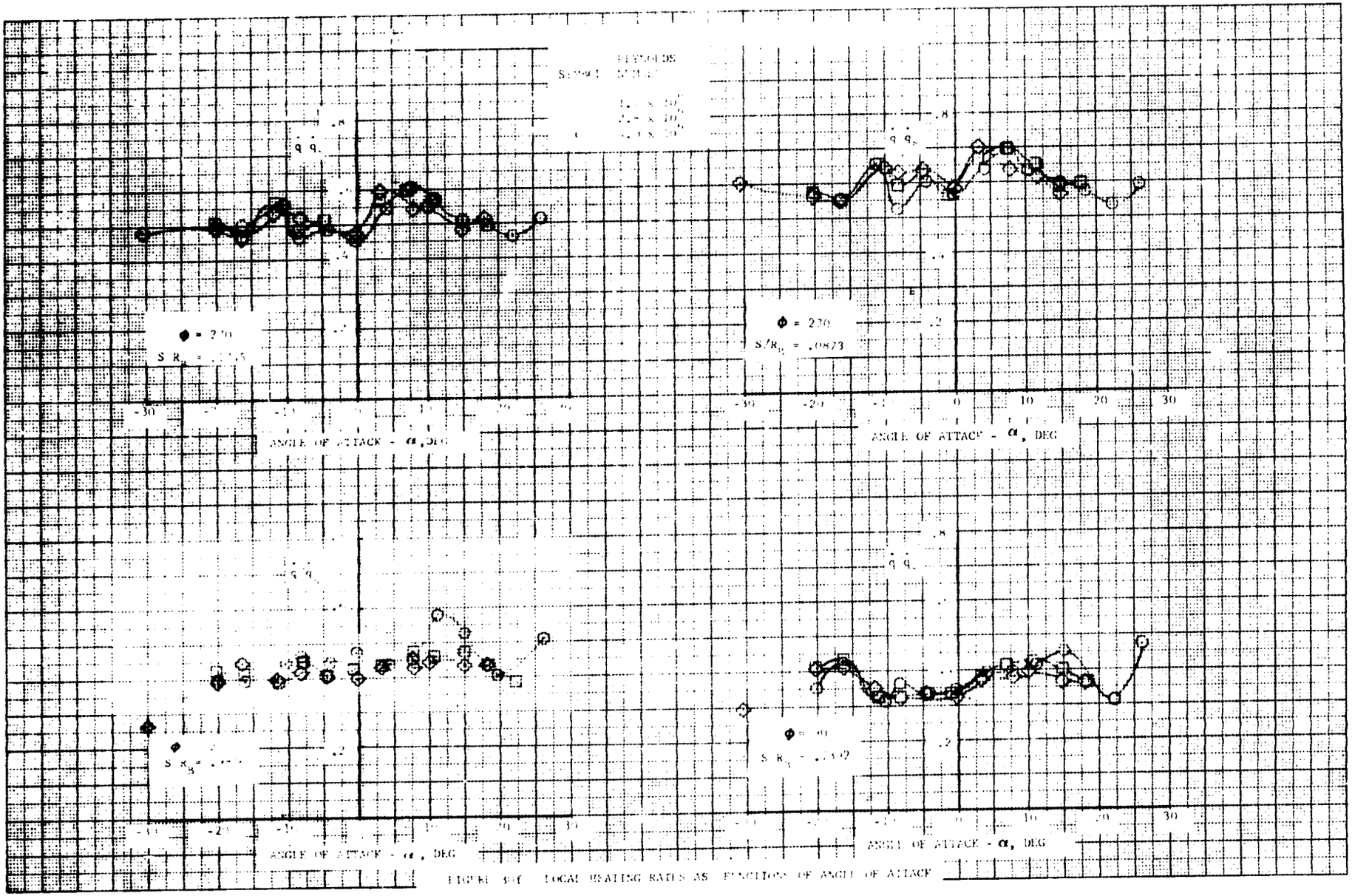

FIGURE 30f LOCAL HEATING RATES AS FUNCTIONS OF ANGLE OF ATTACK

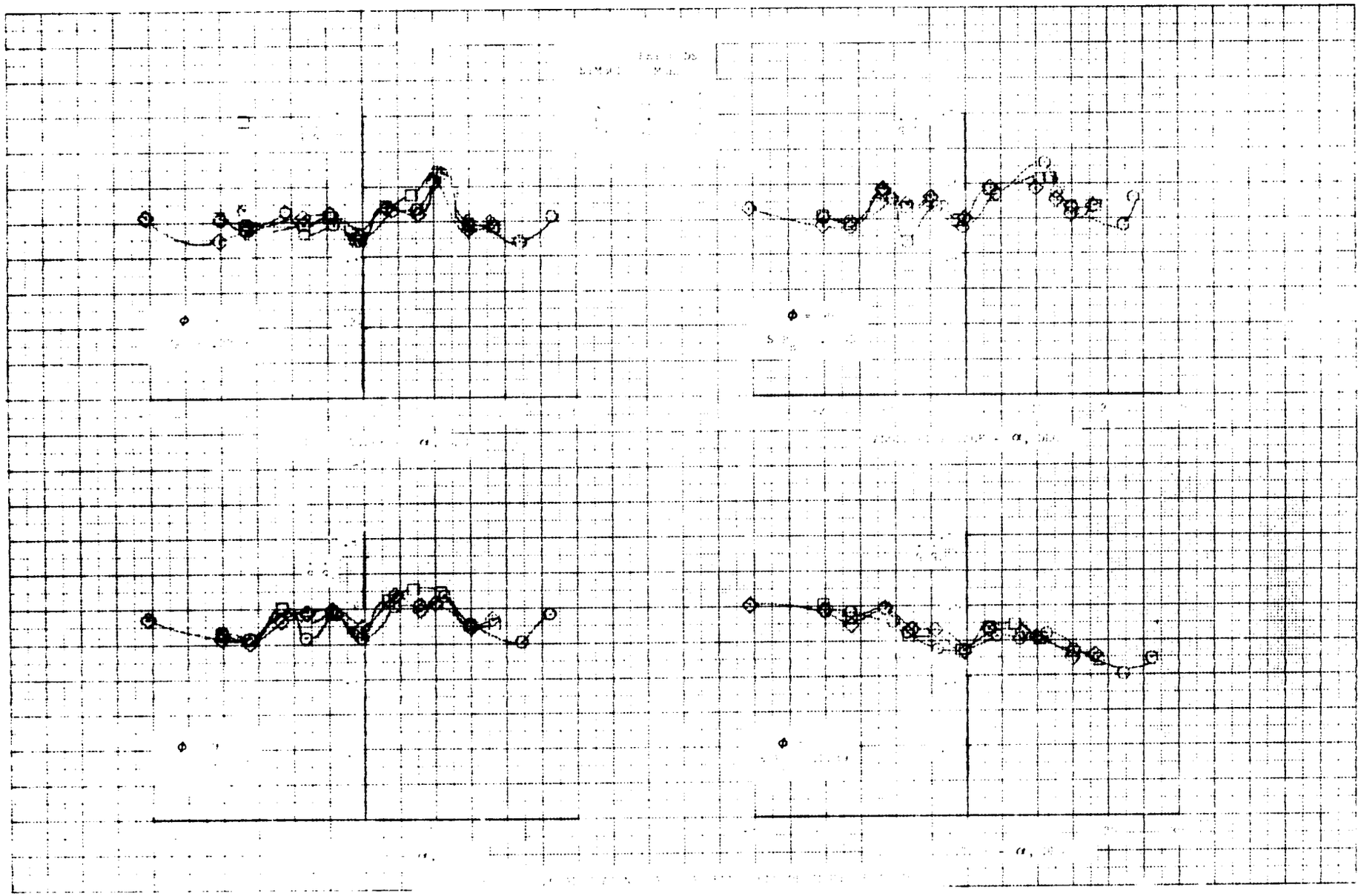

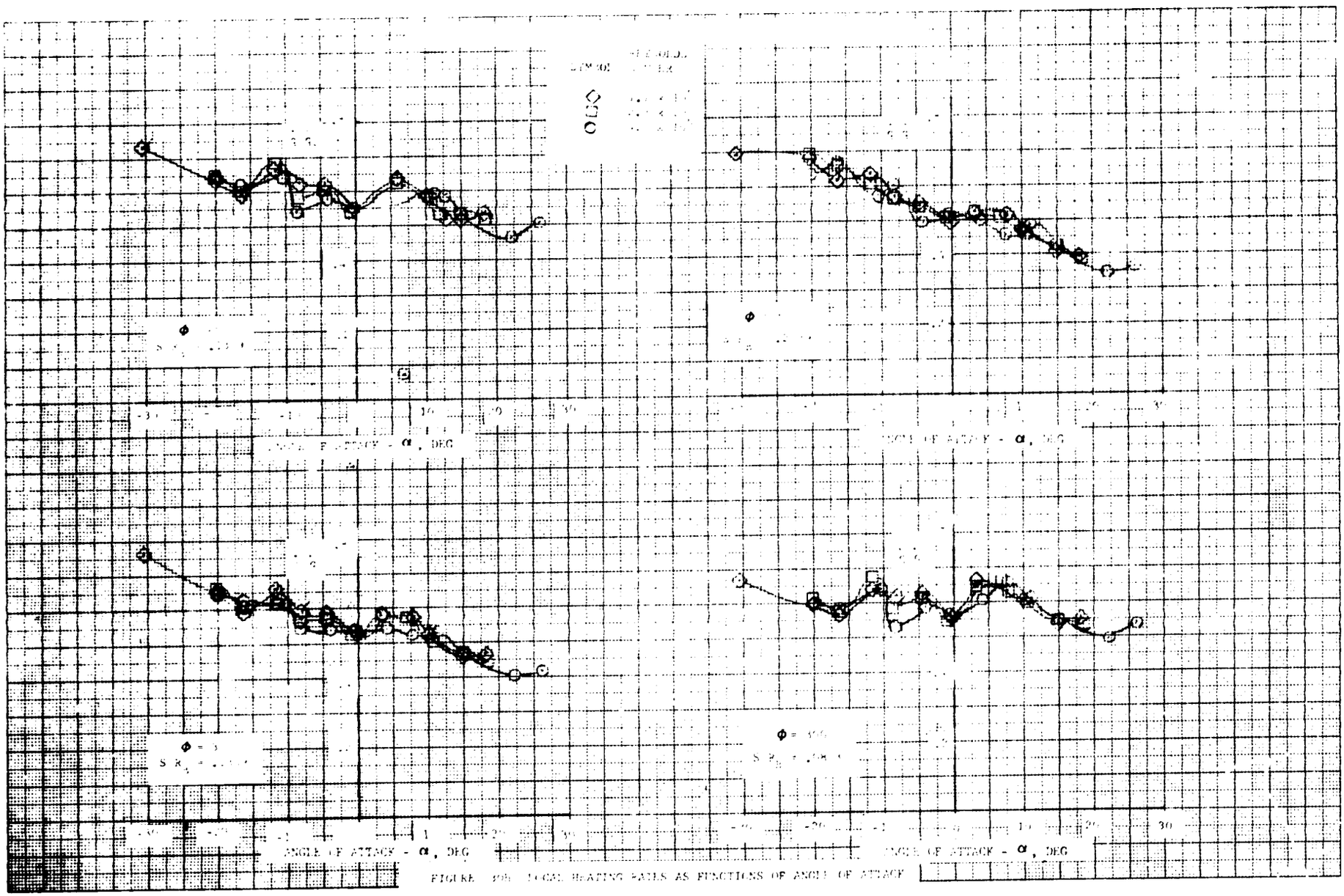

FIGURE [illegible] LOCAL HEATING RATES AS FUNCTIONS OF ANGLE OF ATTACK

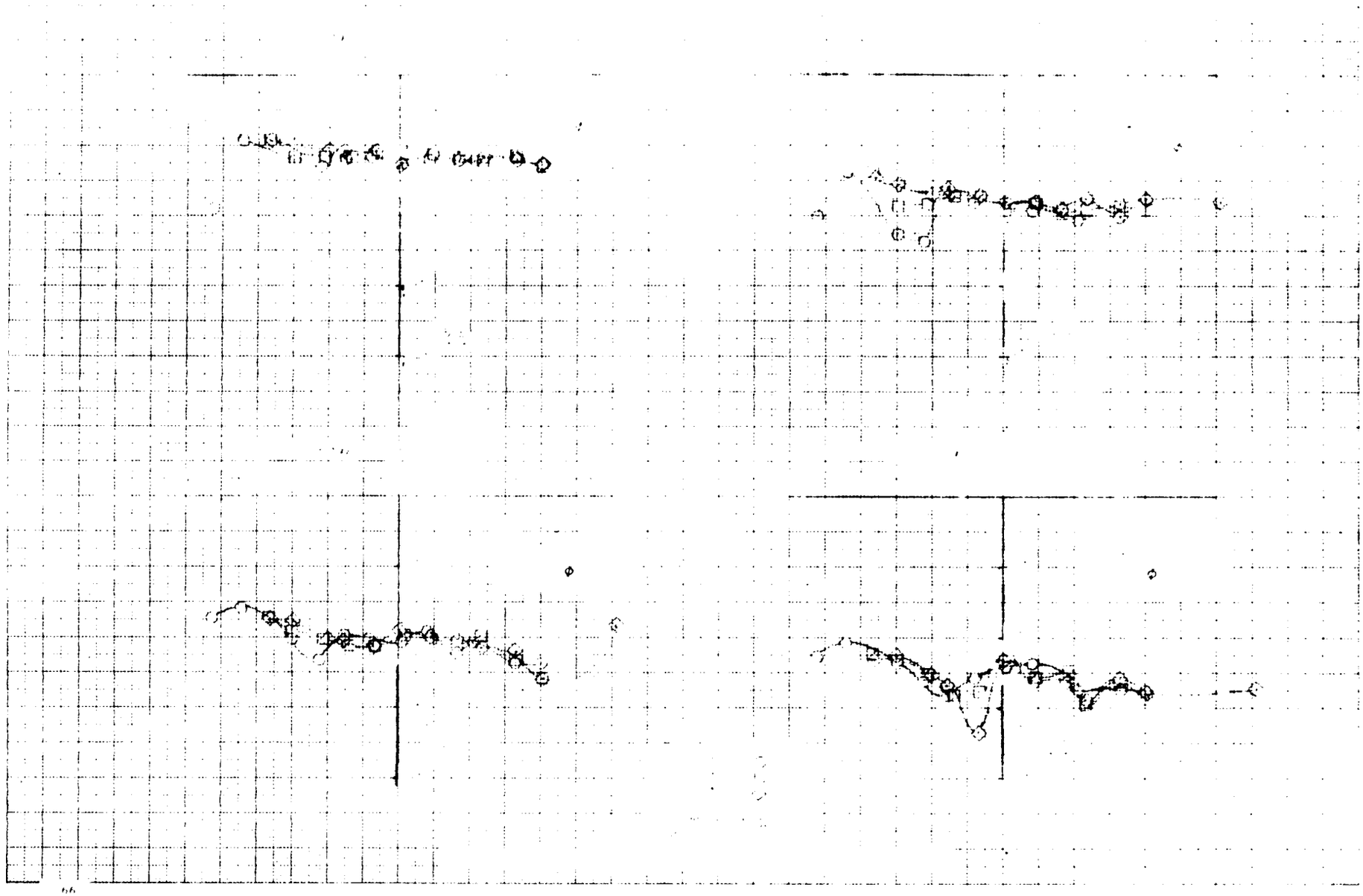

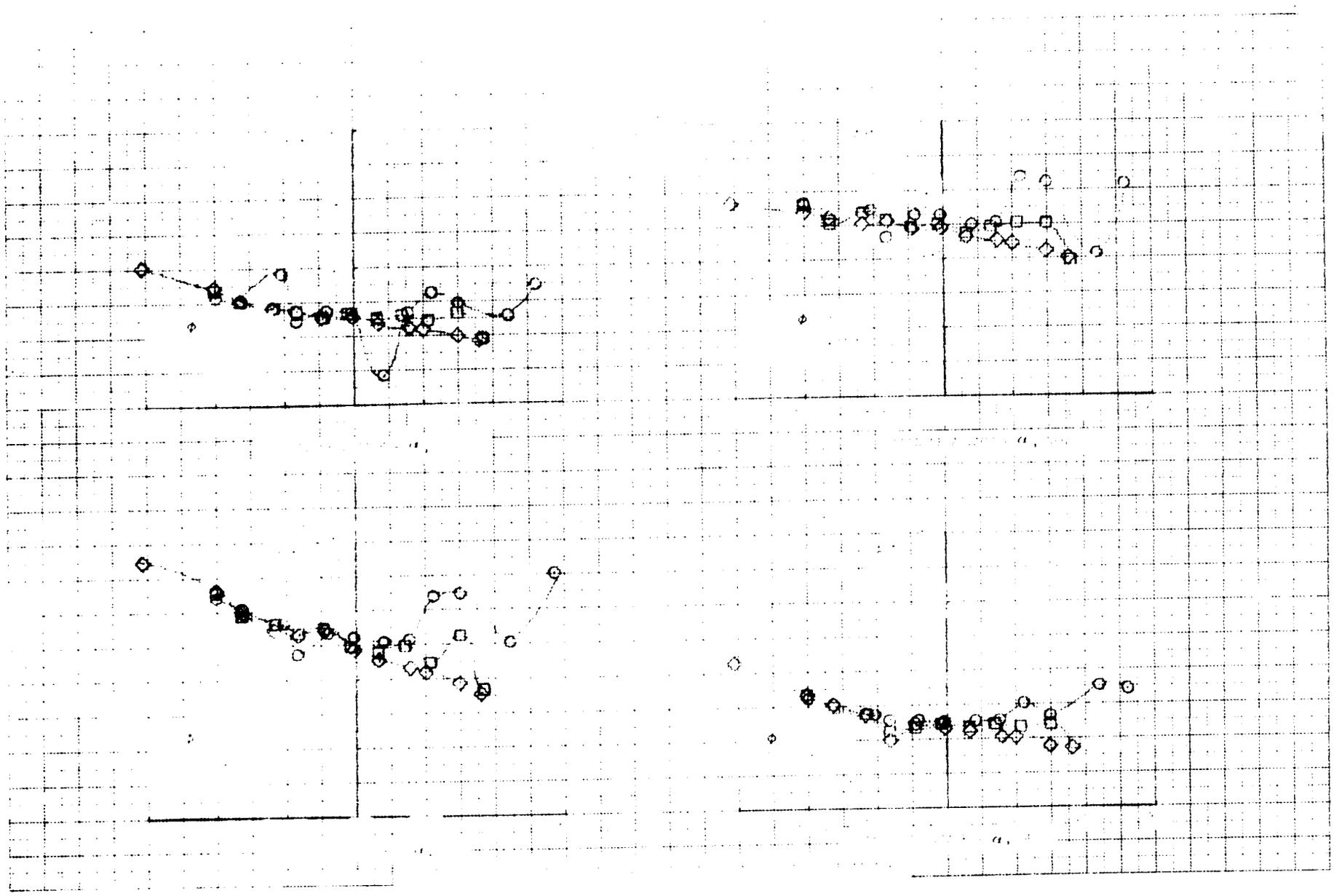

FIGURE 30 LOCAL HEATING RATES AS FUNCTIONS OF ANGLE OF ATTACK

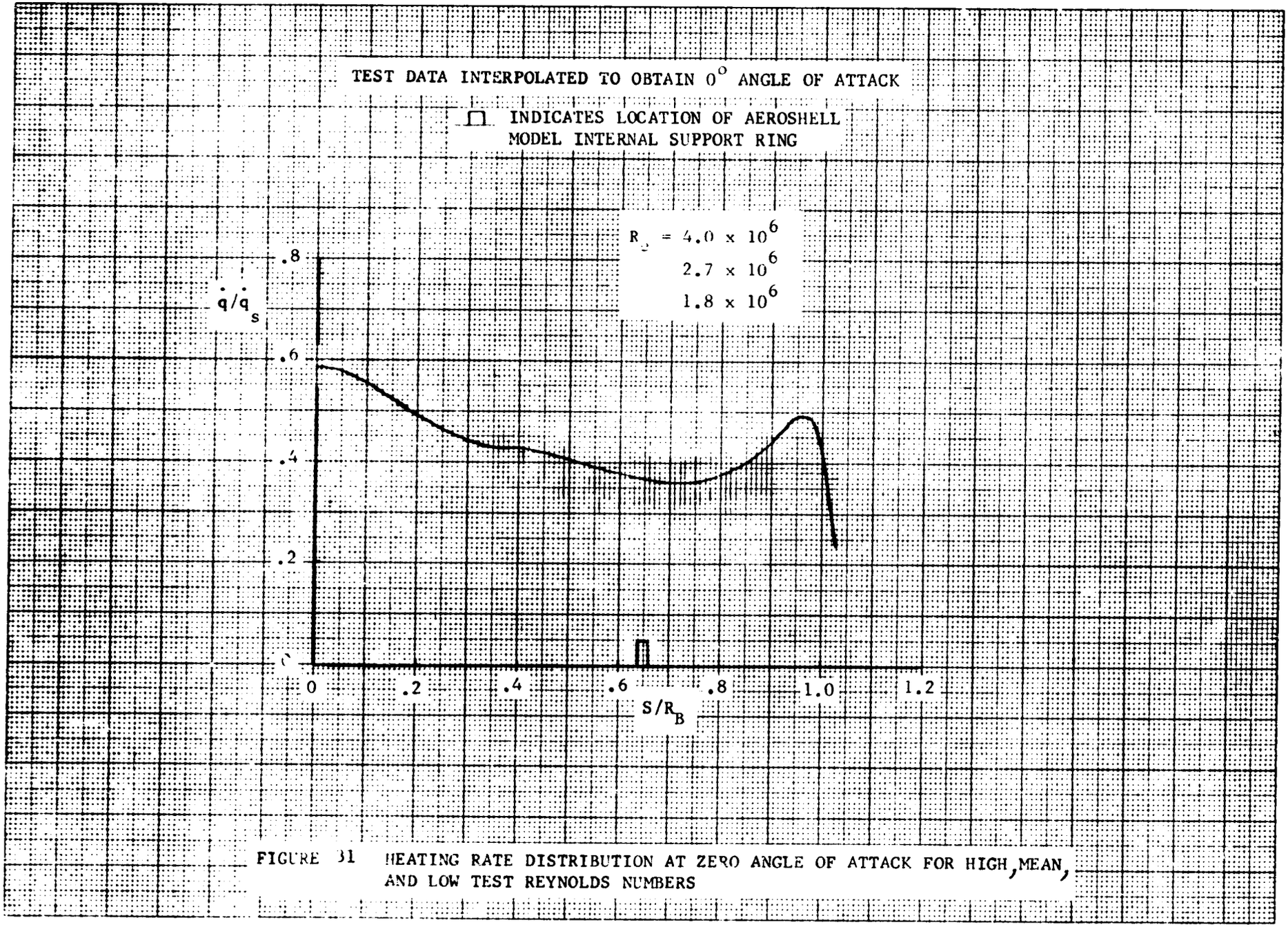

FIGURE 31 HEATING RATE DISTRIBUTION AT ZERO ANGLE OF ATTACK FOR HIGH, MEAN, AND LOW TEST REYNOLDS NUMBERS

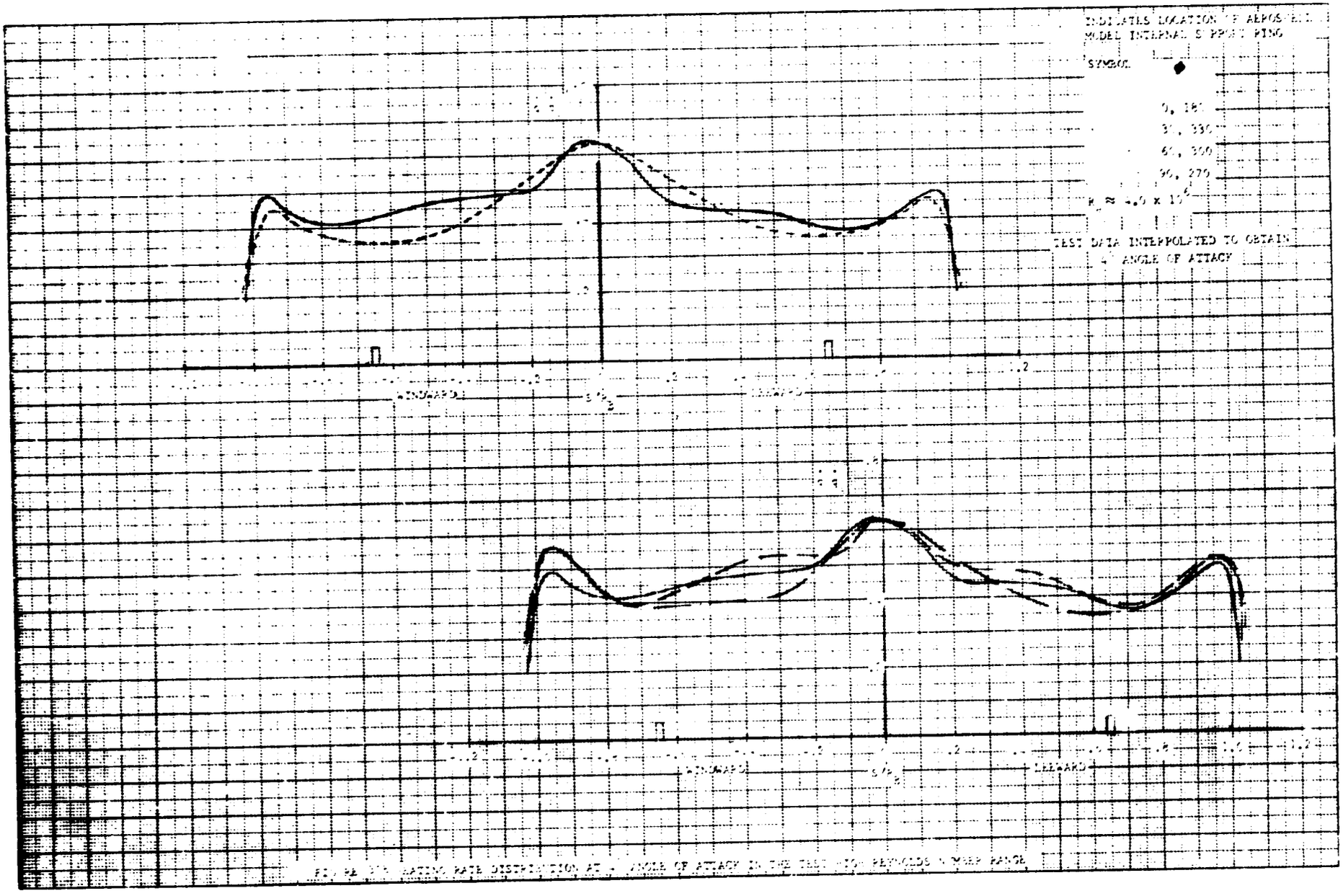
INDICATES LOCATION OF AEROS
MODEL INTERNAL S PROBE RING
SYMBOL
0, 180
30, 330
60, 300
90, 270
TEST DATA INTERPOLATED TO OBTAIN
ANGLE OF ATTACK
INBOARD
LEEWARD

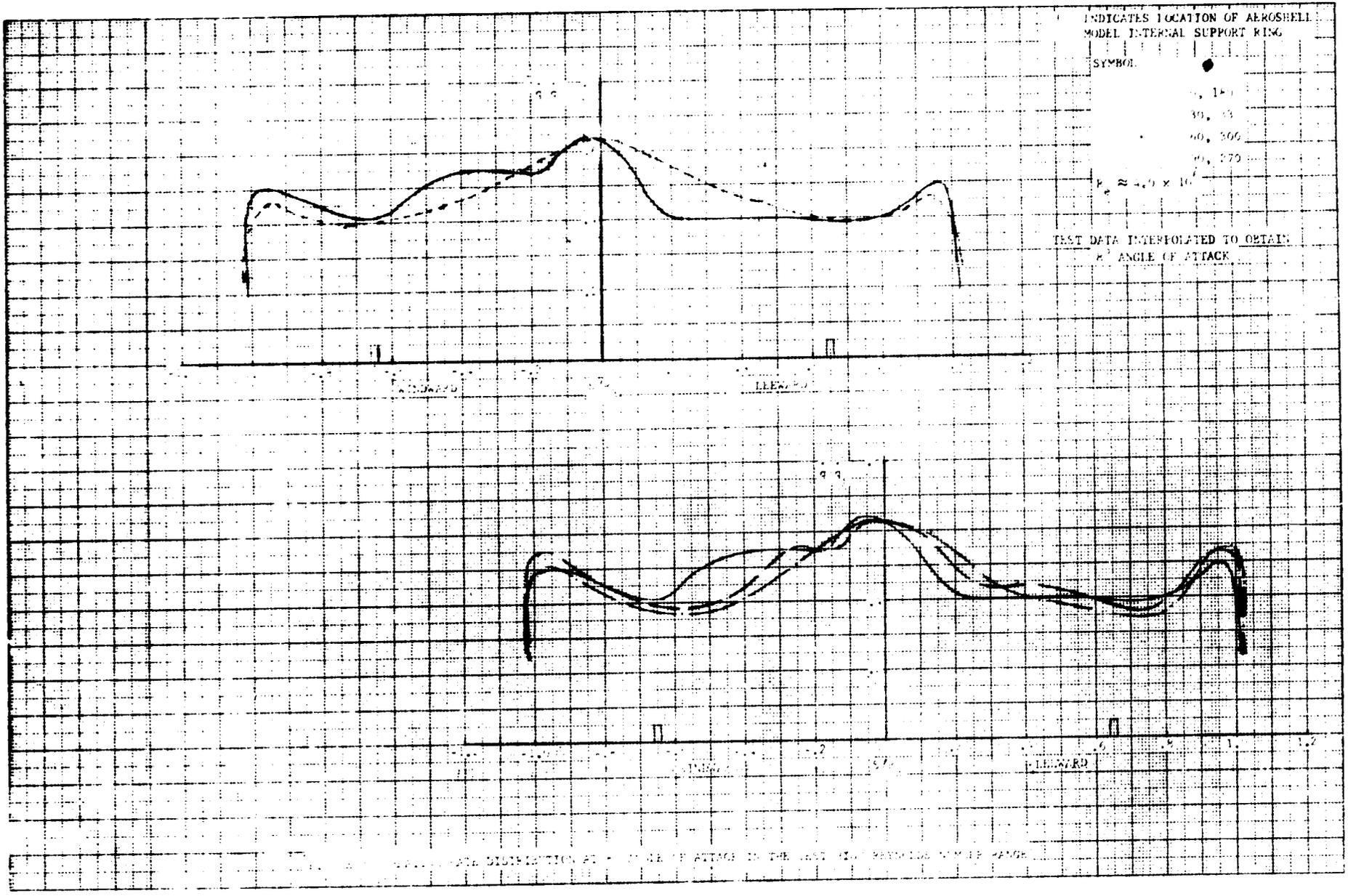
INDICATES LOCATION OF AEROSHELL MODEL INTERNAL SUPPORT RING
SYMBOL
60, 300
90, 270
TEST DATA INTERPOLATED TO OBTAIN ANGLE OF ATTACK
LEEWARD
LEEWARD

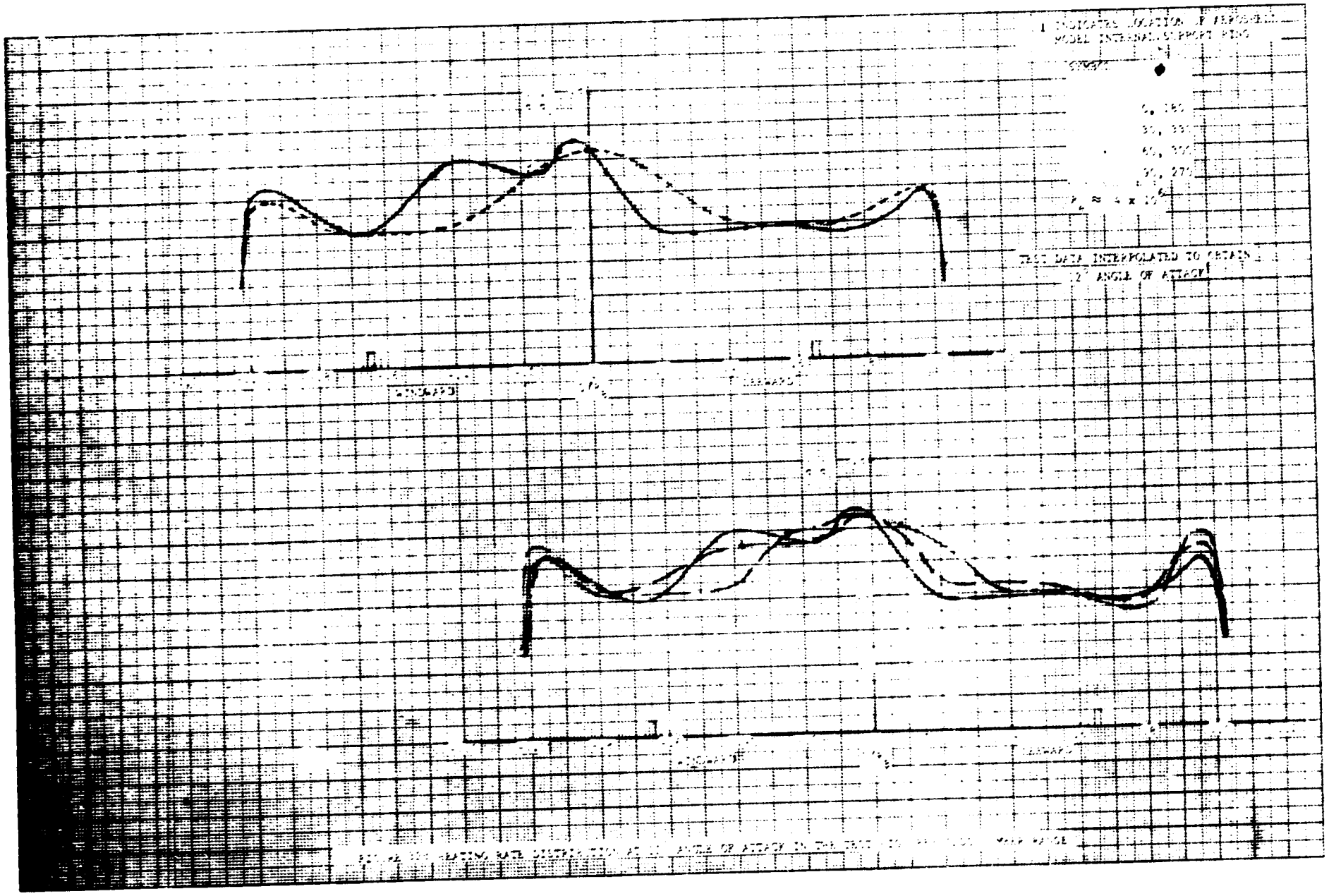

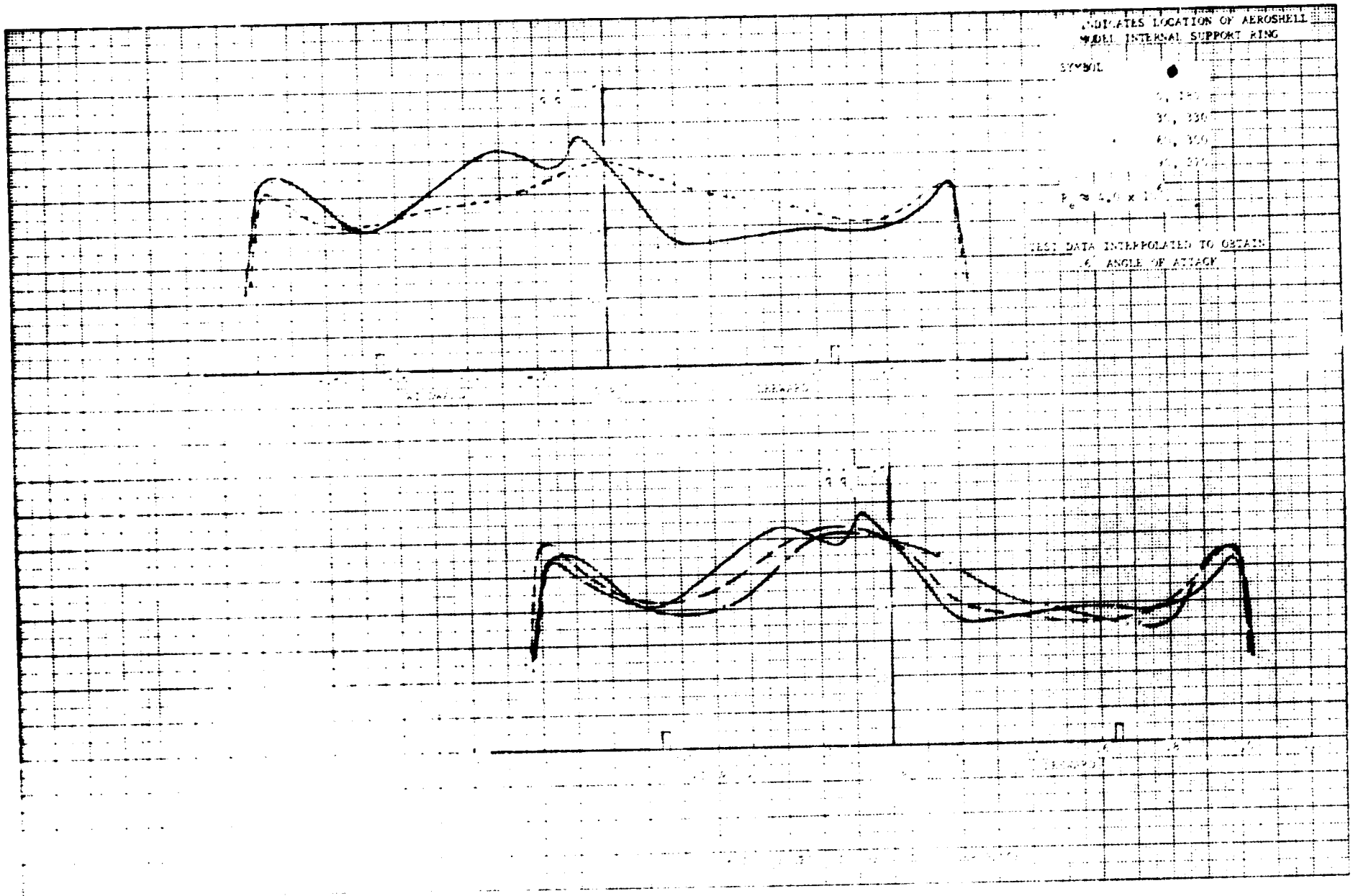
INDICATES LOCATION OF AEROSHELL
MODEL INTERNAL SUPPORT RING
SYMBOL
TEST DATA INTERPOLATED TO OBTAIN
ANGLE OF ATTACK

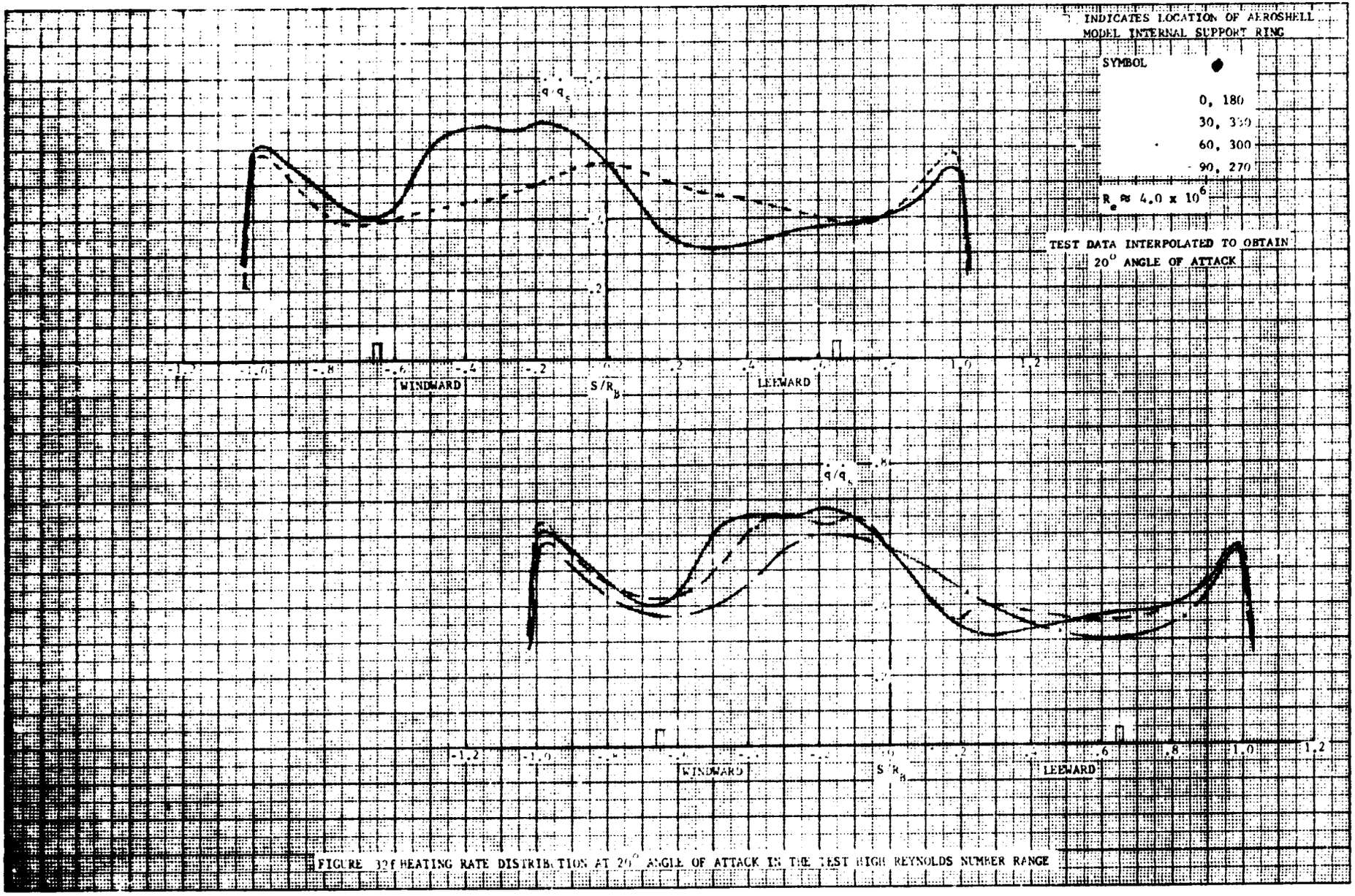

FIGURE 32f HEATING RATE DISTRIBUTION AT 20° ANGLE OF ATTACK IN THE TEST HIGH REYNOLDS NUMBER RANGE

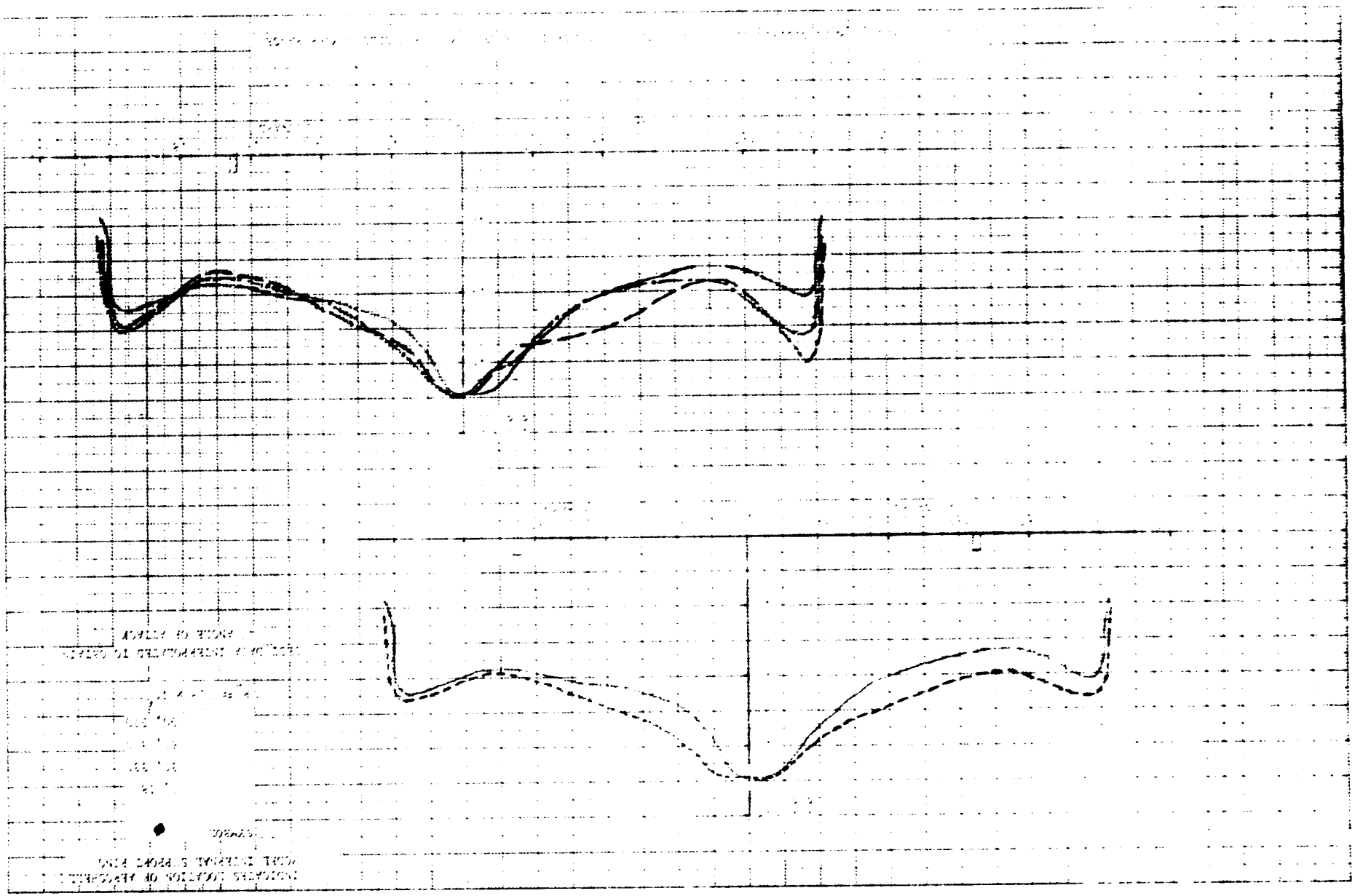

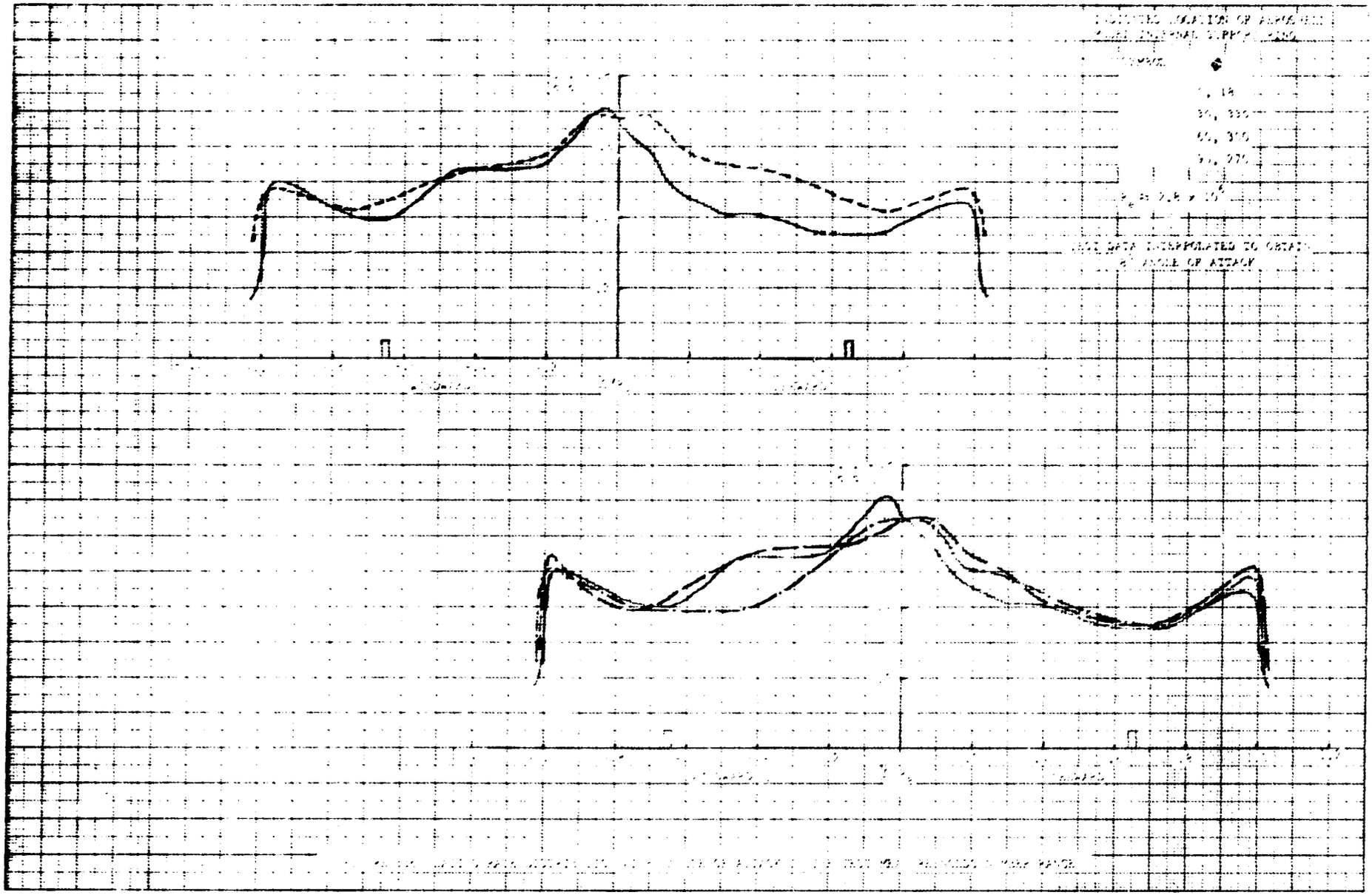

PRESSURE DISTRIBUTION AT 12° ANGLE OF ATTACK IN THE TEST SECTION REYNOLDS NUMBER RANGE

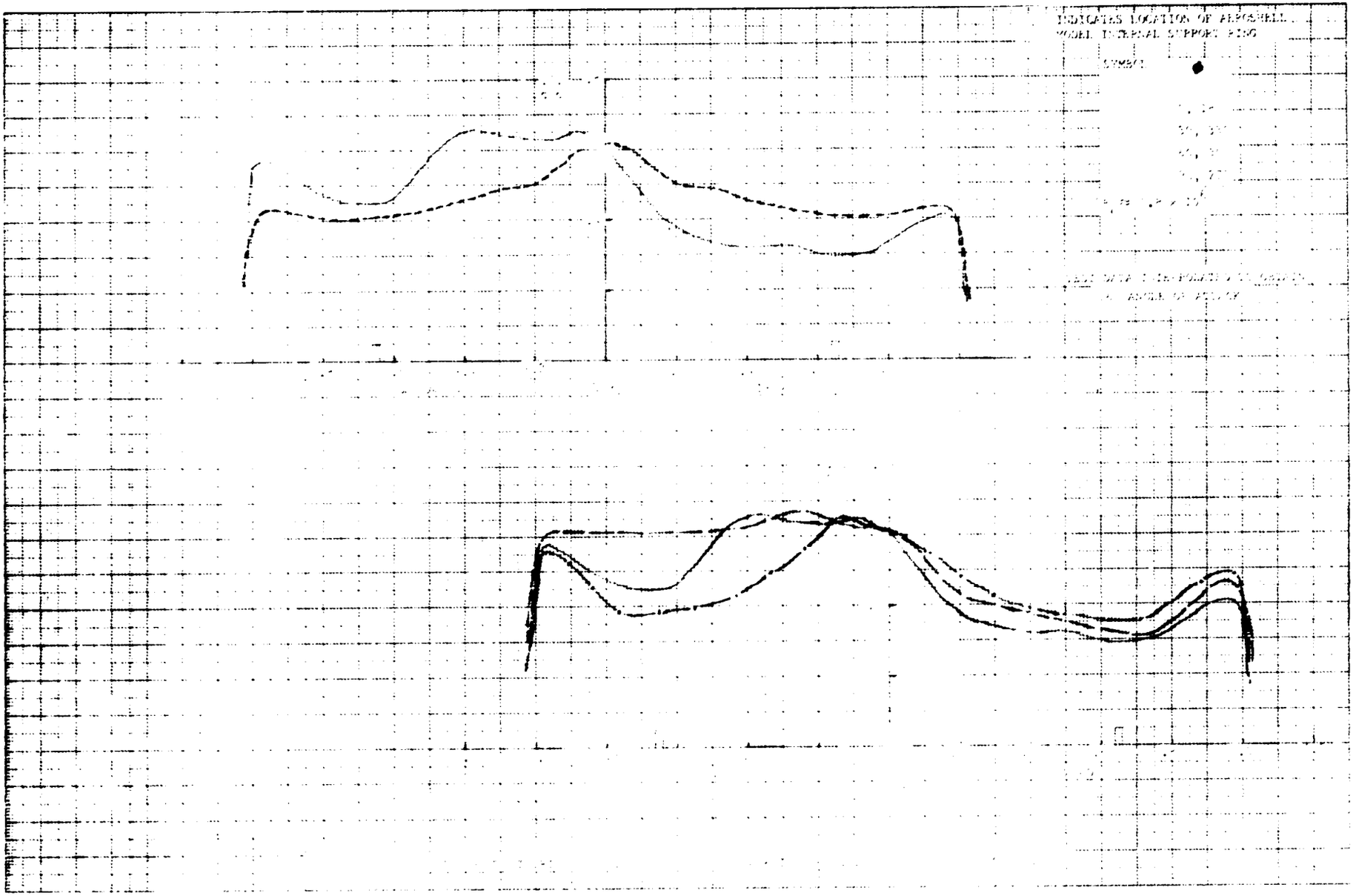
INDICATES LOCATION OF AEROSHELL
MODEL INTERNAL SUPPORT ROD

FIGURE 44 HEATING RATE DISTRIBUTION AT 20° ANGLE OF ATTACK IN THE TEST MACH REYNOLDS NUMBER RANGE

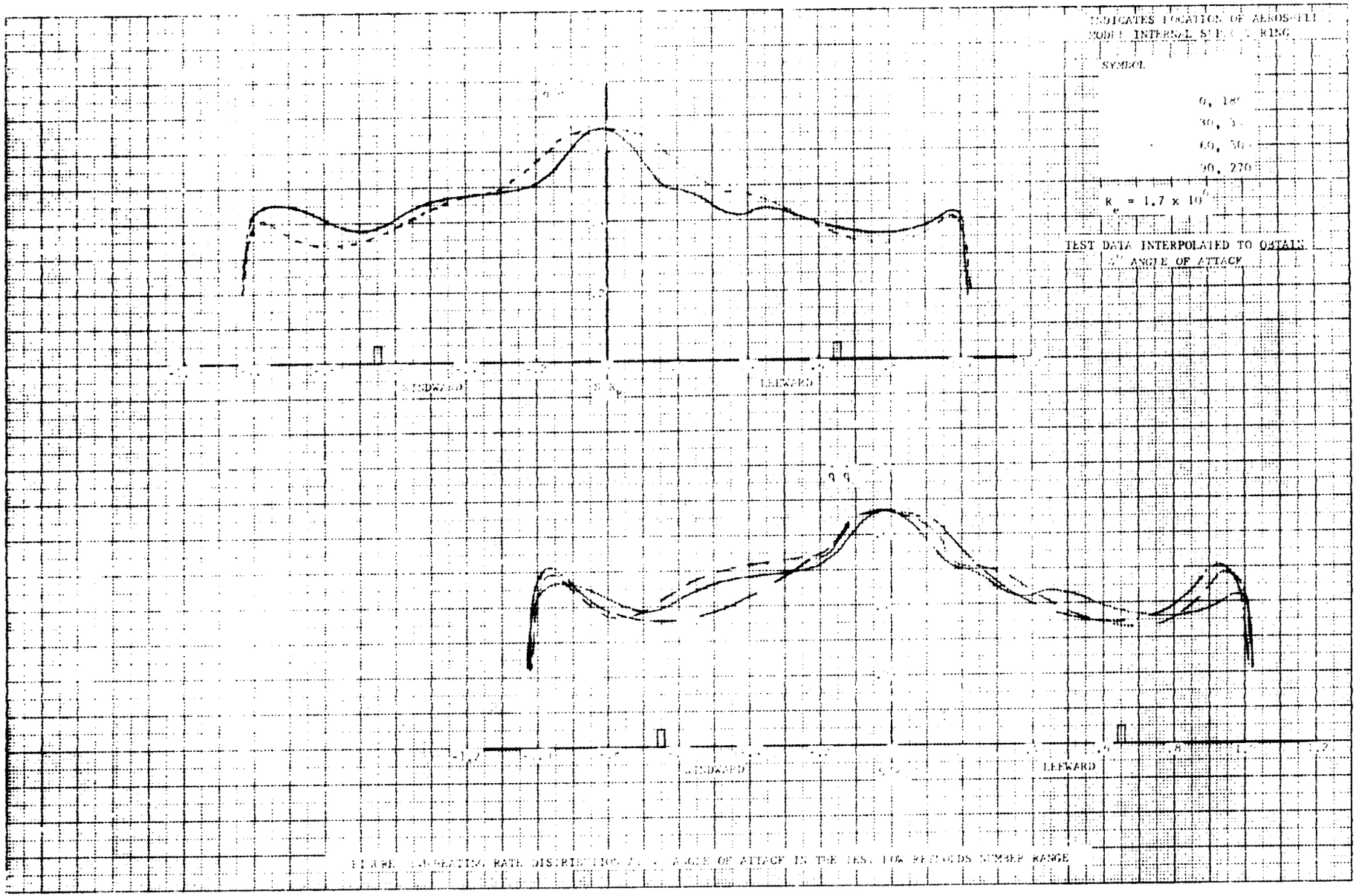

FIGURE [illegible] HEATING RATE DISTRIBUTION [illegible] ANGLE OF ATTACK IN THE TEST LOW REYNOLDS NUMBER RANGE

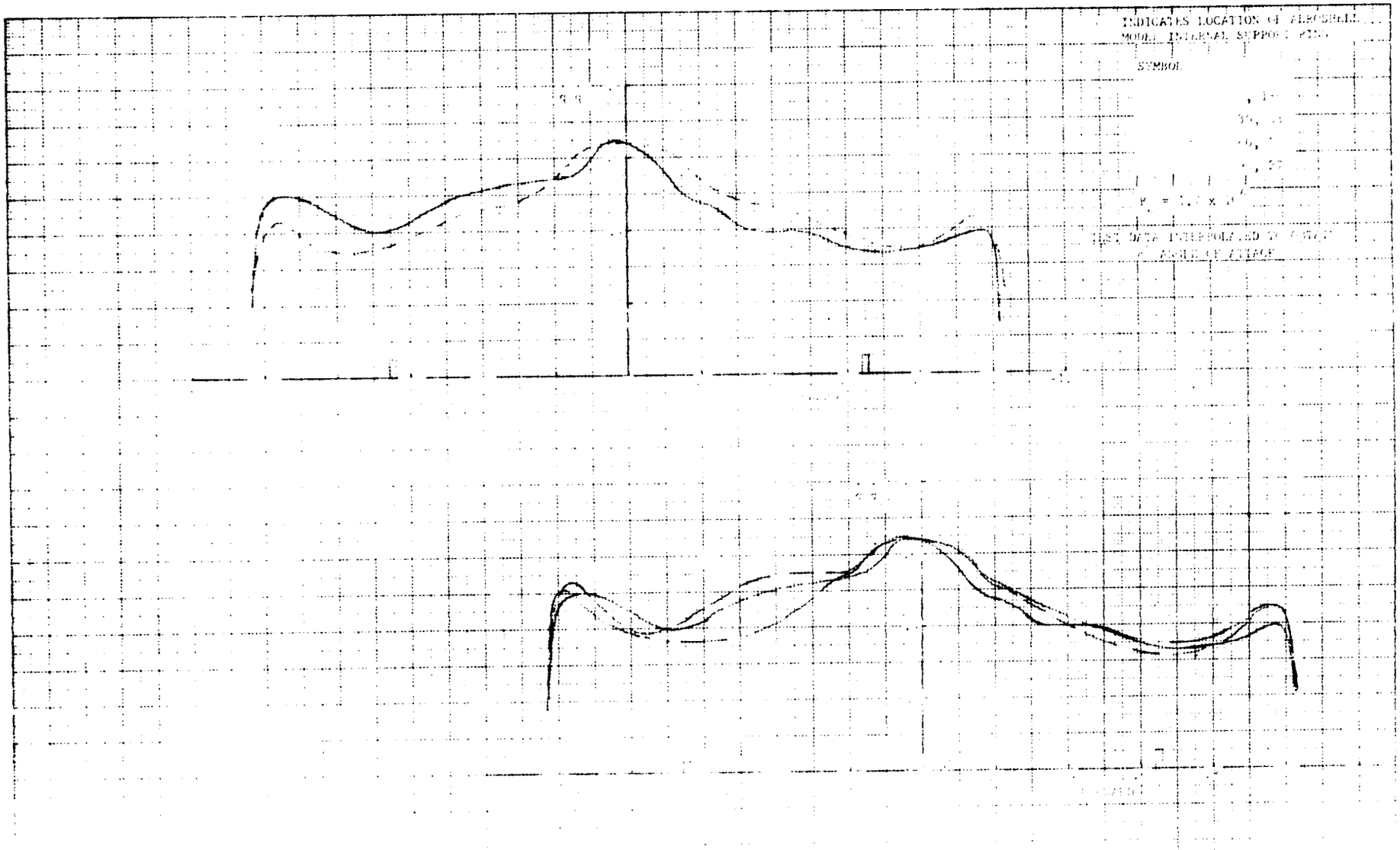
INDICATES LOCATION OF AEROBALL
SYMBOL

FIGURE [illegible] HEATING RATE DISTRIBUTION AT 12° ANGLE OF ATTACK IN THE TEST LOW REYNOLDS NUMBER RANGE

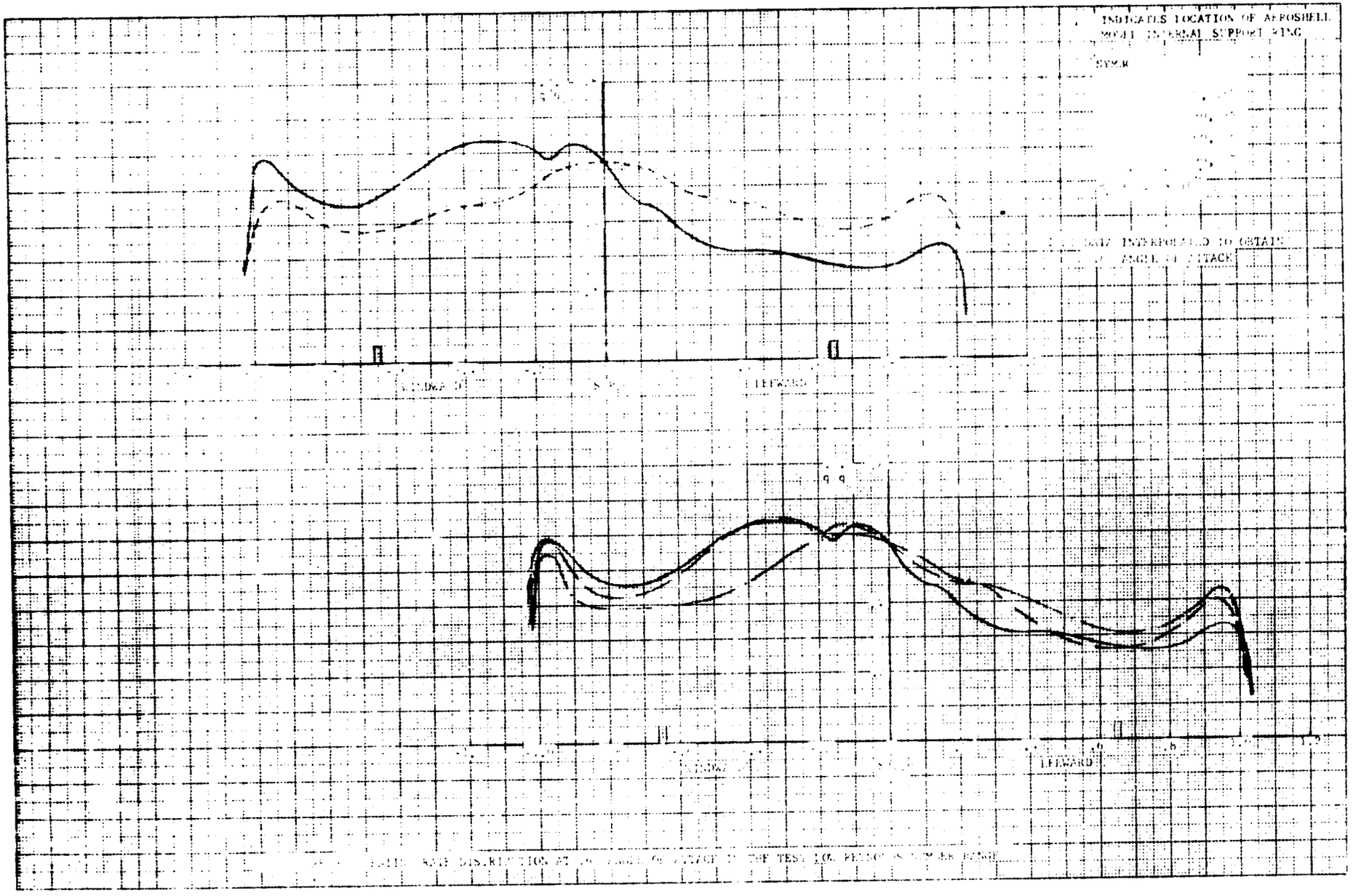

[illegible] RATE DISTRIBUTION AT [illegible] ANGLE OF ATTACK IN THE TEST LOW REYNOLDS NUMBER RANGE

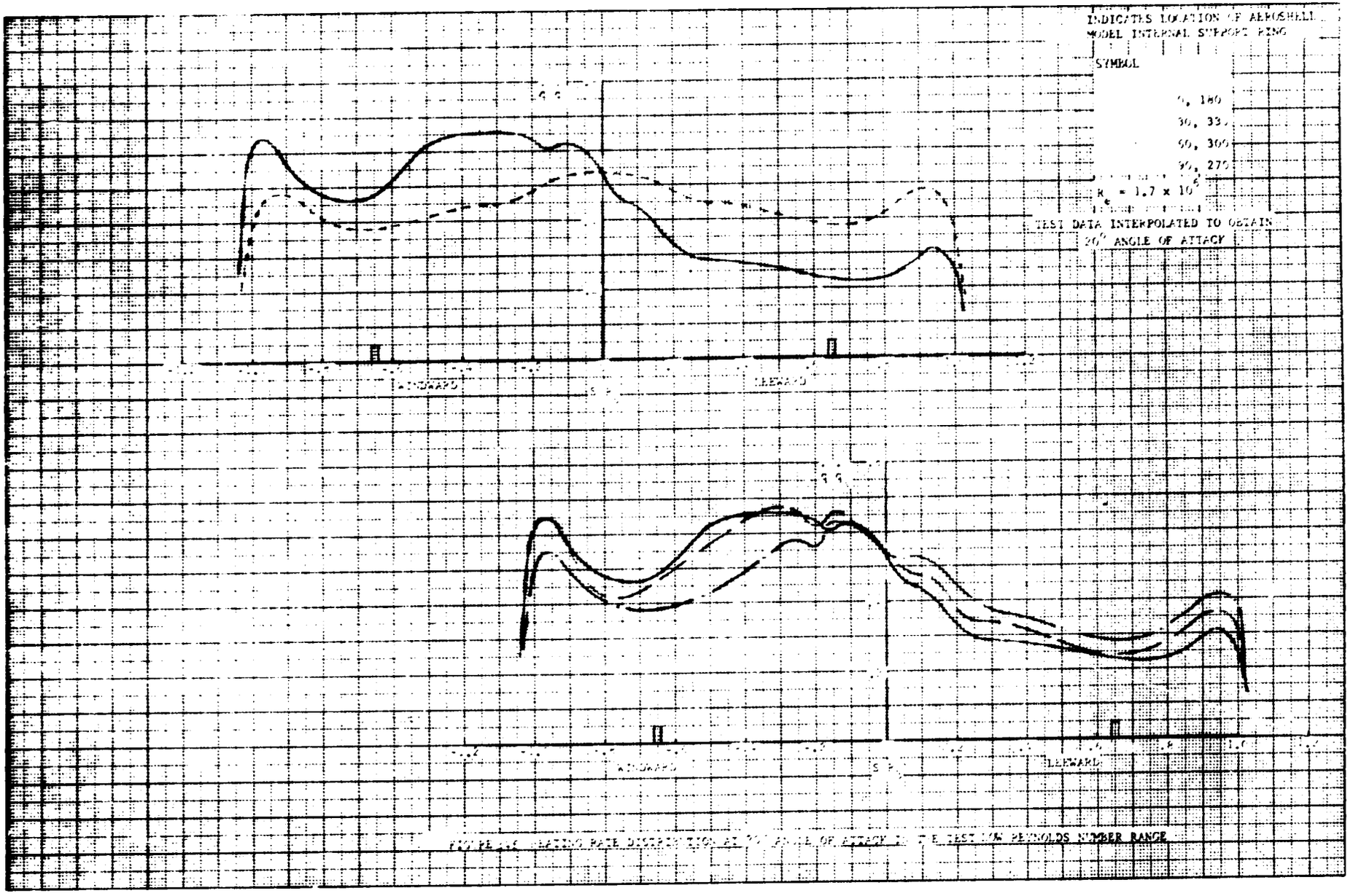

FIGURE [illegible] HEATING RATE DISTRIBUTION AT 20° ANGLE OF ATTACK [illegible] TEST [illegible] REYNOLDS NUMBER RANGE

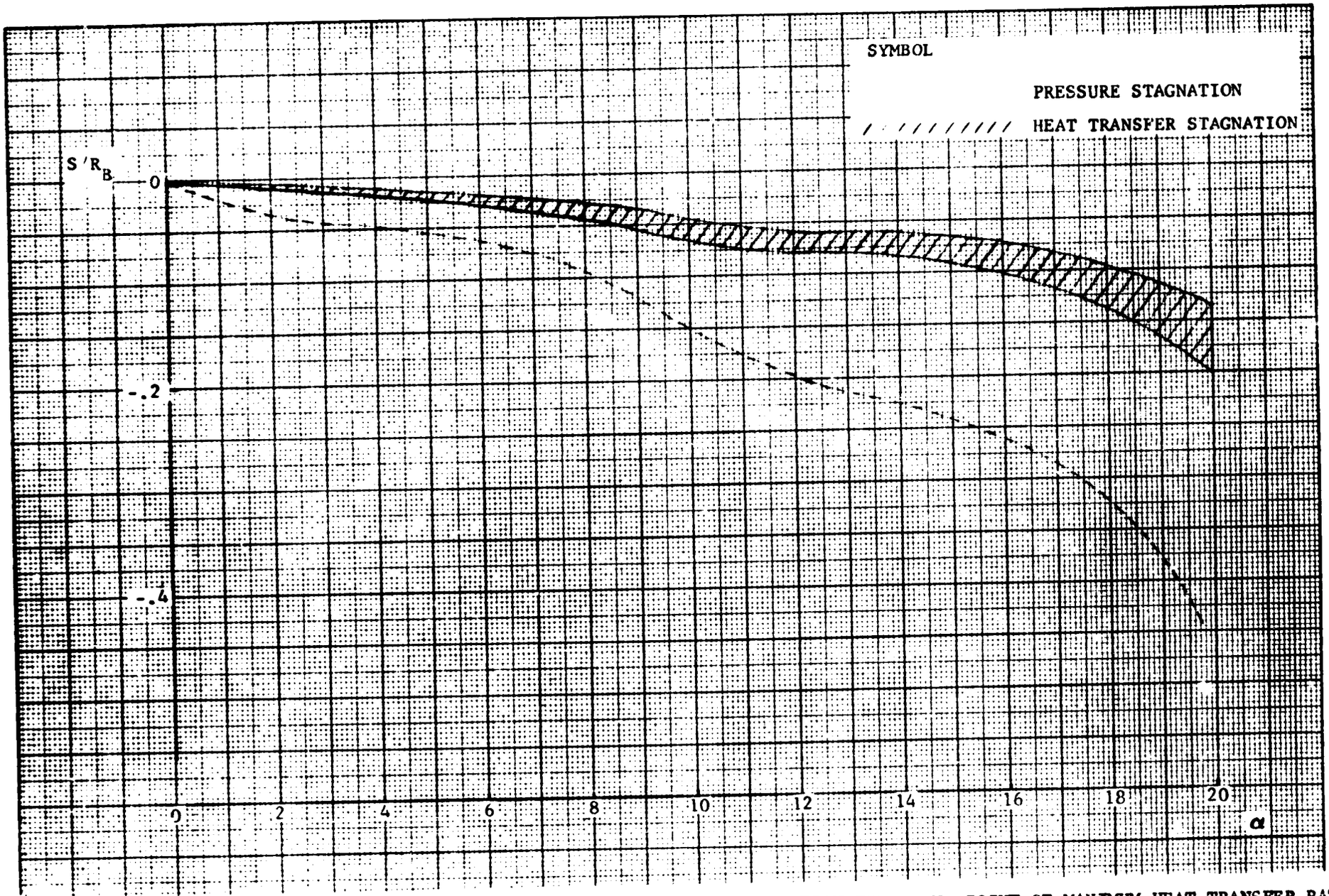

FIGURE 35 COMPARISON OF RADIAL SHIFTS IN PRESSURE STAGNATION POINT AND POINT OF MAXIMUM HEAT TRANSFER RATE FOR EQUIVALENT VARIATION IN α

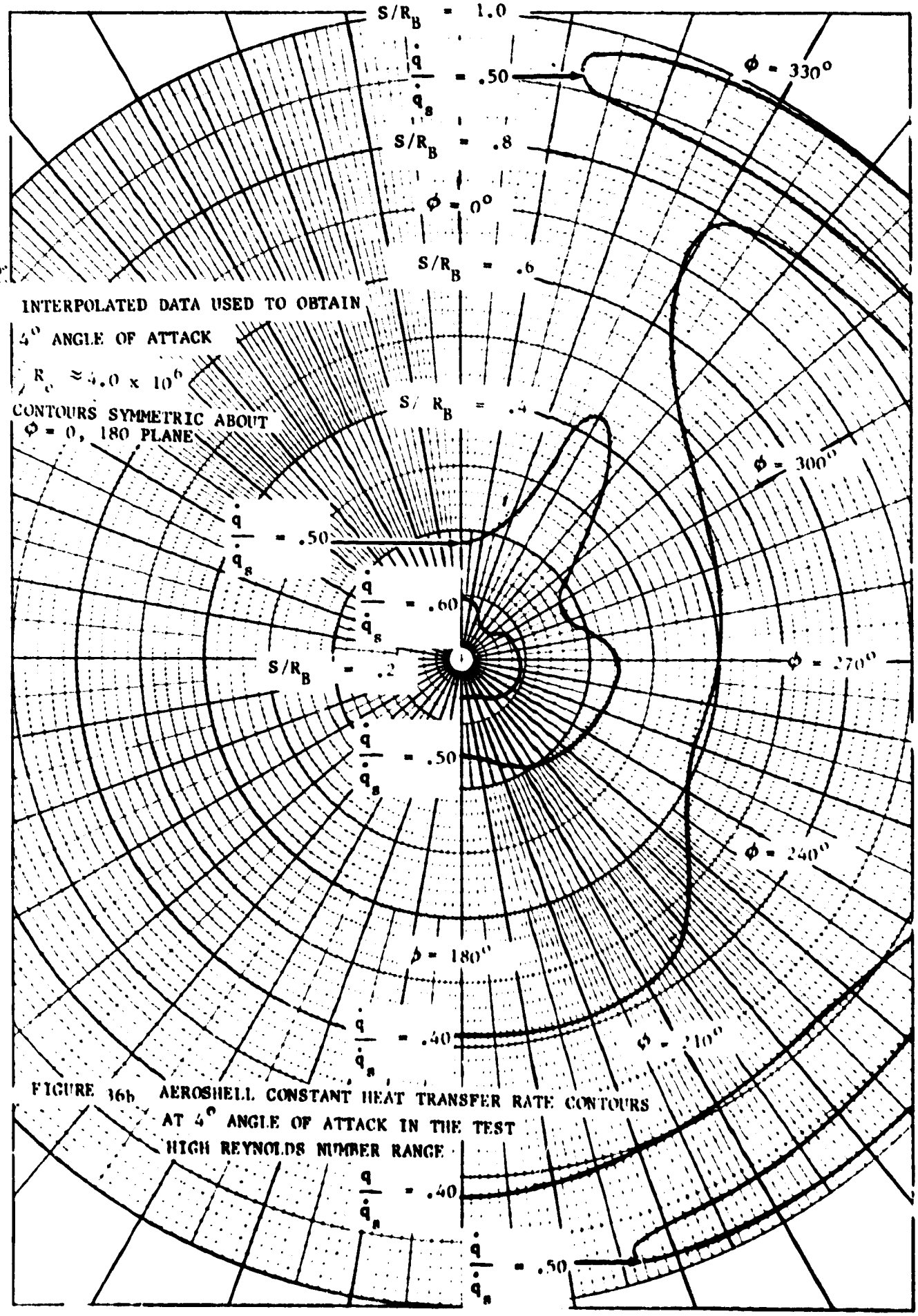

FIGURE 36b AEROSHELL CONSTANT HEAT TRANSFER RATE CONTOURS AT 4° ANGLE OF ATTACK IN THE TEST HIGH REYNOLDS NUMBER RANGE

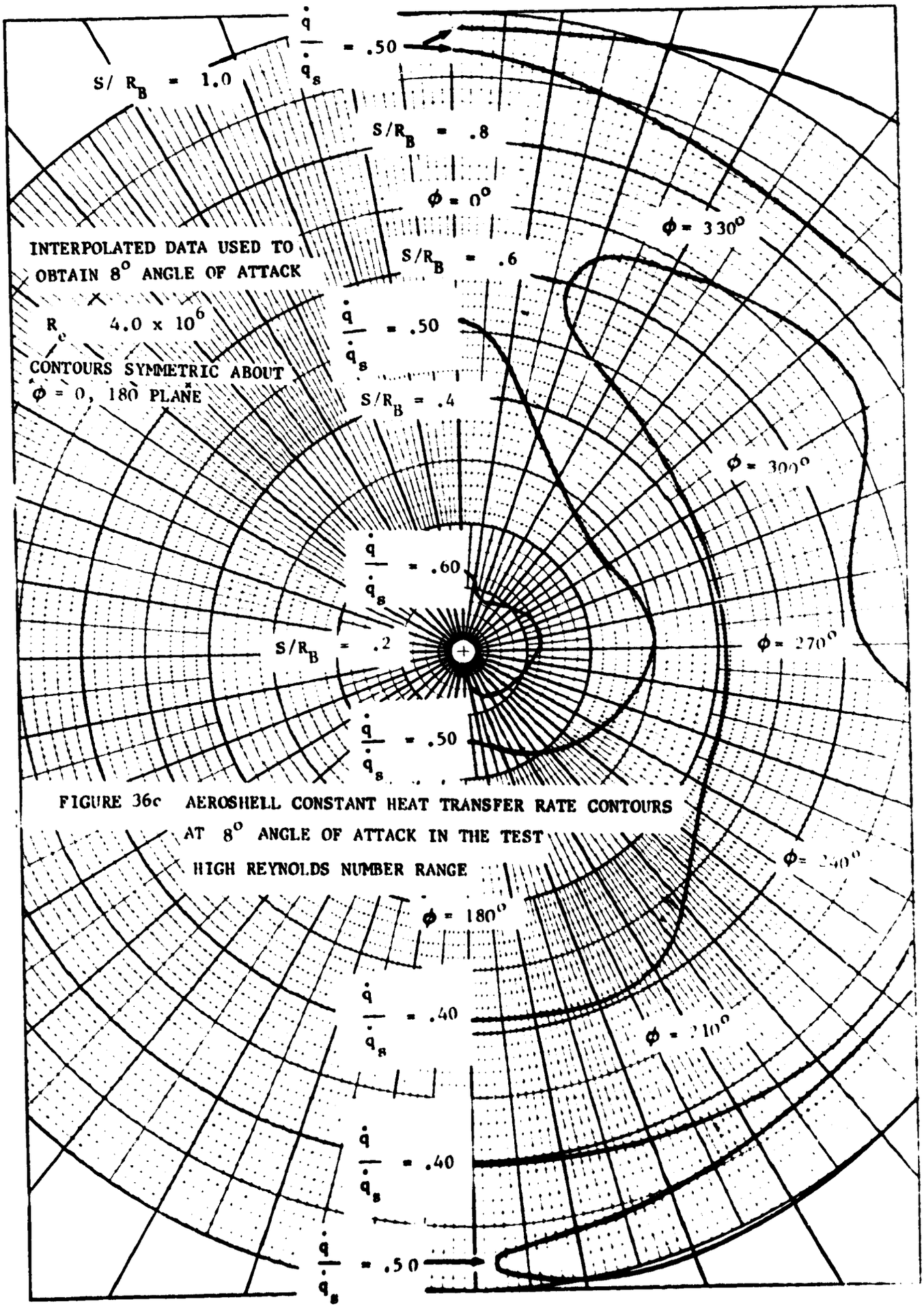

FIGURE 36c AEROSHELL CONSTANT HEAT TRANSFER RATE CONTOURS AT 8° ANGLE OF ATTACK IN THE TEST HIGH REYNOLDS NUMBER RANGE

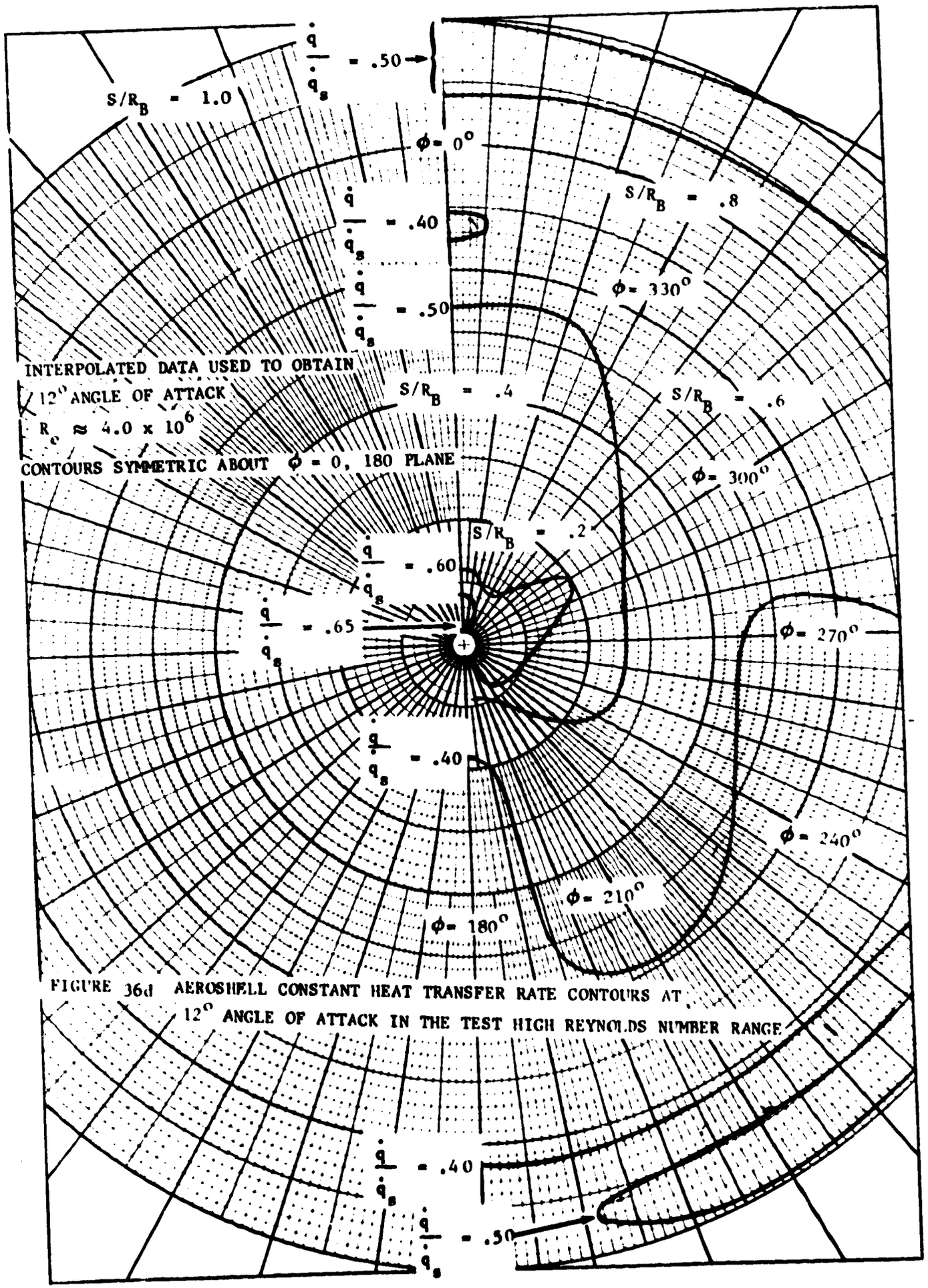

FIGURE 36d AEROSHELL CONSTANT HEAT TRANSFER RATE CONTOURS AT 12° ANGLE OF ATTACK IN THE TEST HIGH REYNOLDS NUMBER RANGE

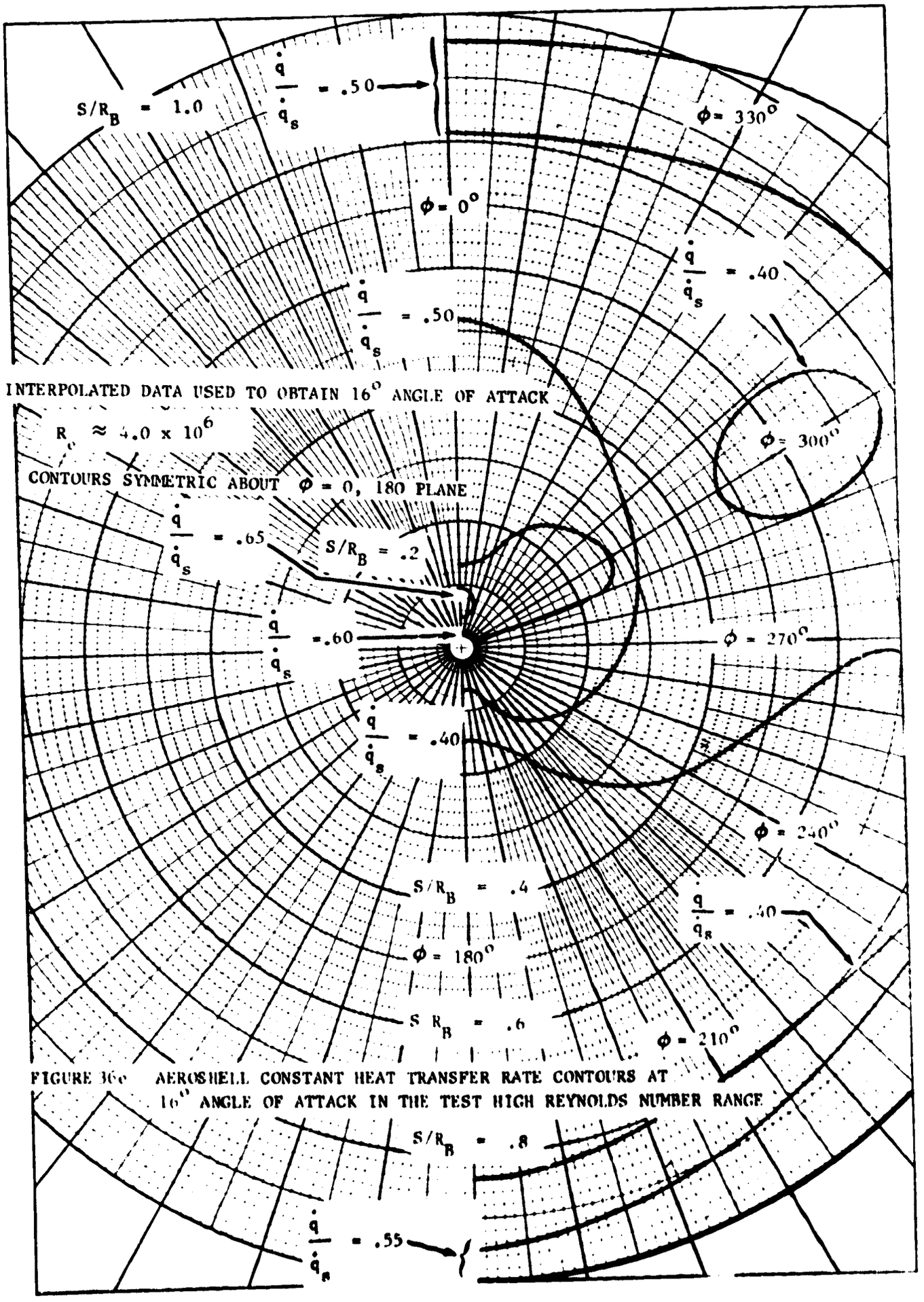

FIGURE 36c AEROSHELL CONSTANT HEAT TRANSFER RATE CONTOURS AT 16° ANGLE OF ATTACK IN THE TEST HIGH REYNOLDS NUMBER RANGE

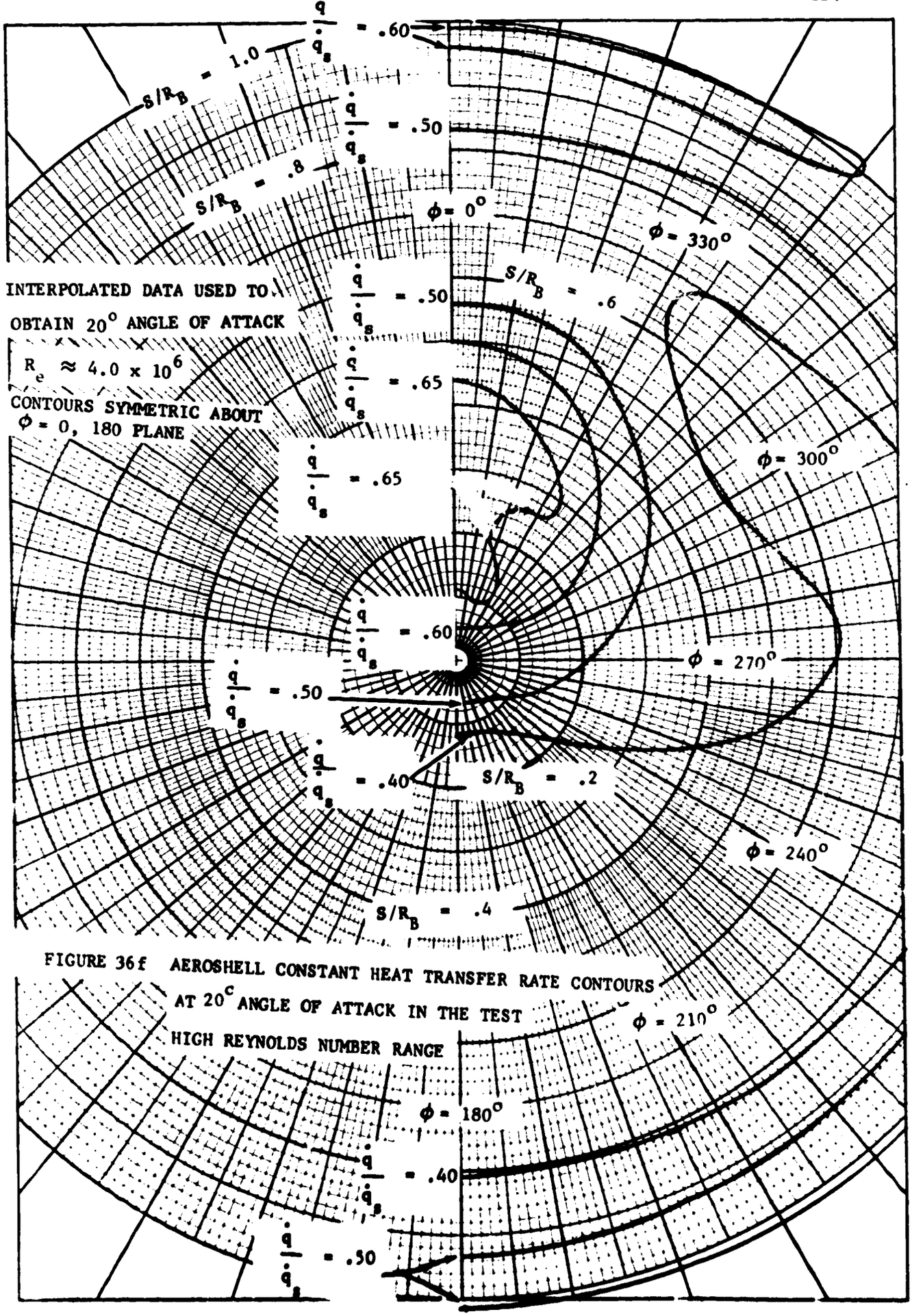

FIGURE 36f AEROSHELL CONSTANT HEAT TRANSFER RATE CONTOURS AT 20° ANGLE OF ATTACK IN THE TEST HIGH REYNOLDS NUMBER RANGE

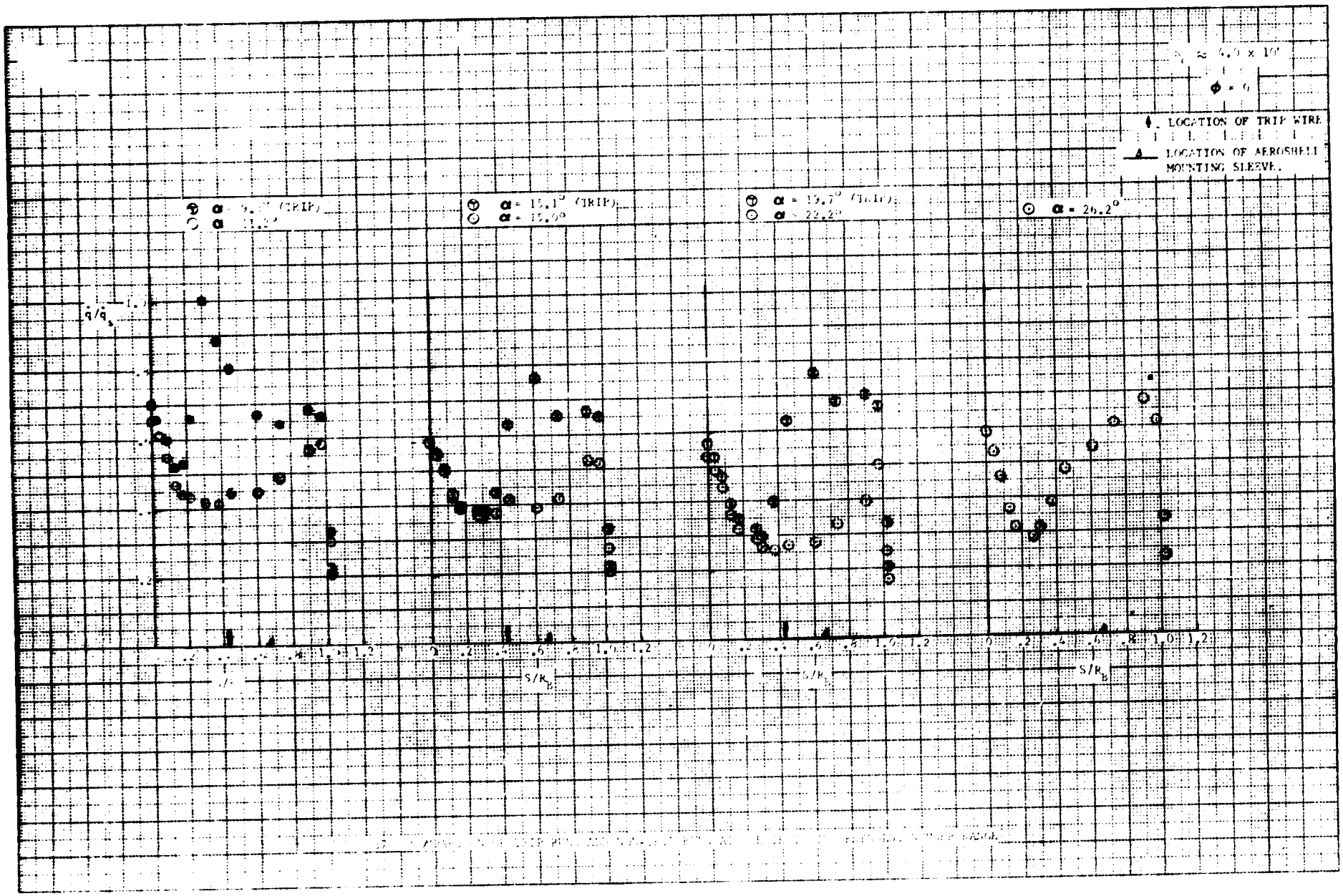
LOCATION OF TRIP WIRE
LOCATION OF AEROSHELL MOUNTING SLEEVE.
α = 15.1° (TRIP)
α = 15.9°
α = 19.7° (TRIP)
α = 22.2°
α = 26.2°
q/q_s
S/R_B
S/R_B
S/R_B

FOLDOUT FRAME

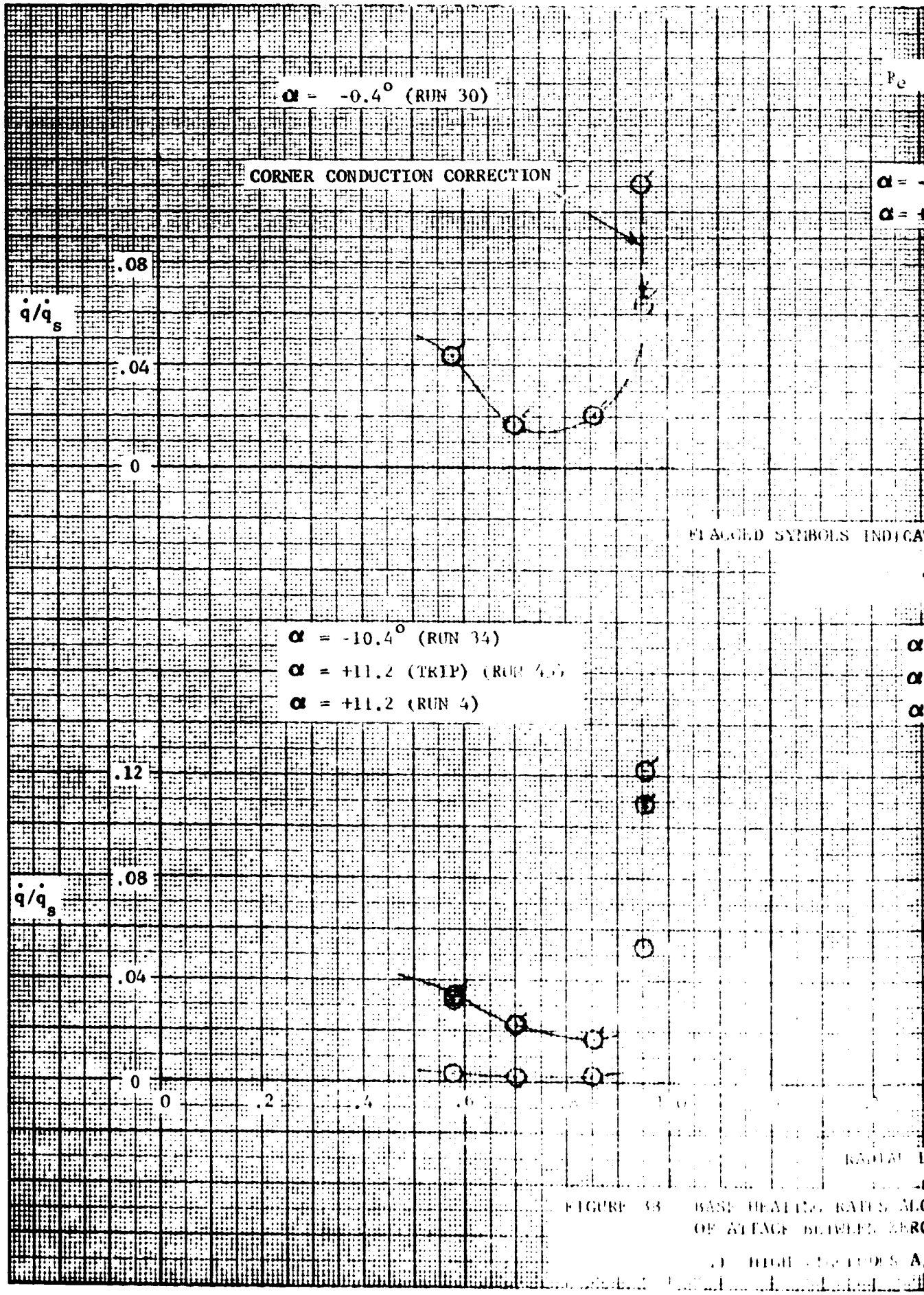

FLAGGED SYMBOLS INDICA

FIGURE 38 BASE HEATING RATES AL
OF ATTAC

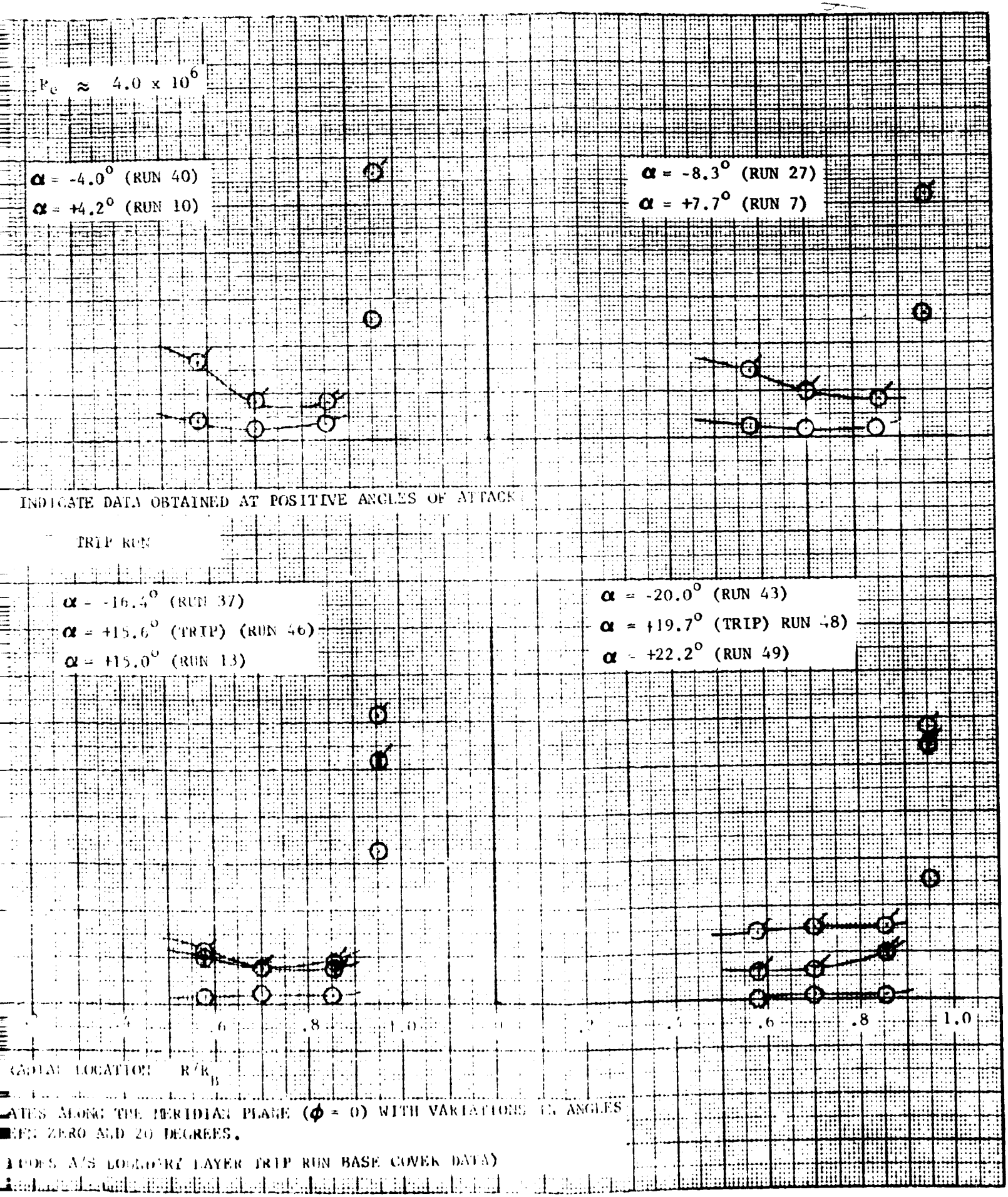
$R_e \approx 4.0 \times 10^6$
$\alpha = -4.0^\circ$ (RUN 40)
$\alpha = +4.2^\circ$ (RUN 10)
$\alpha = -8.3^\circ$ (RUN 27)
$\alpha = +7.7^\circ$ (RUN 7)
INDICATE DATA OBTAINED AT POSITIVE ANGLES OF ATTACK
TRIP RUN
$\alpha = -16.4^\circ$ (RUN 37)
$\alpha = +15.6^\circ$ (TRIP) (RUN 46)
$\alpha = +15.0^\circ$ (RUN 13)
$\alpha = -20.0^\circ$ (RUN 43)
$\alpha = +19.7^\circ$ (TRIP) RUN 48)
$\alpha = +22.2^\circ$ (RUN 49)
.6
.8
1.0
RADIAL LOCATION R/R_B
ATES ALONG THE MERIDIAN PLANE ($\phi = 0$) WITH VARIATIONS IN ANGLES
EN ZERO AND 20 DEGREES.
DOES A/S BOUNDARY LAYER TRIP RUN BASE COVER DATA)

FOLDOUT FRAME

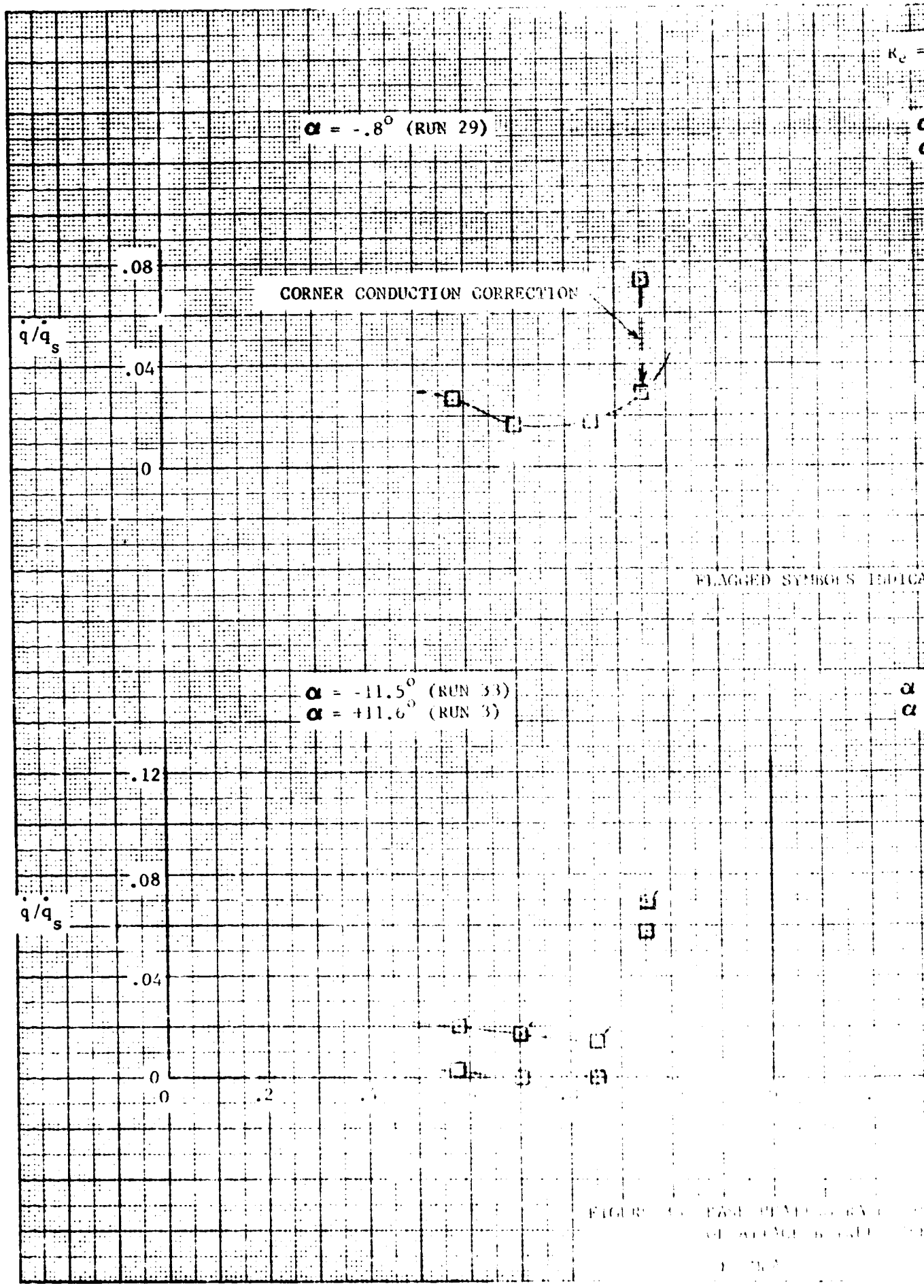

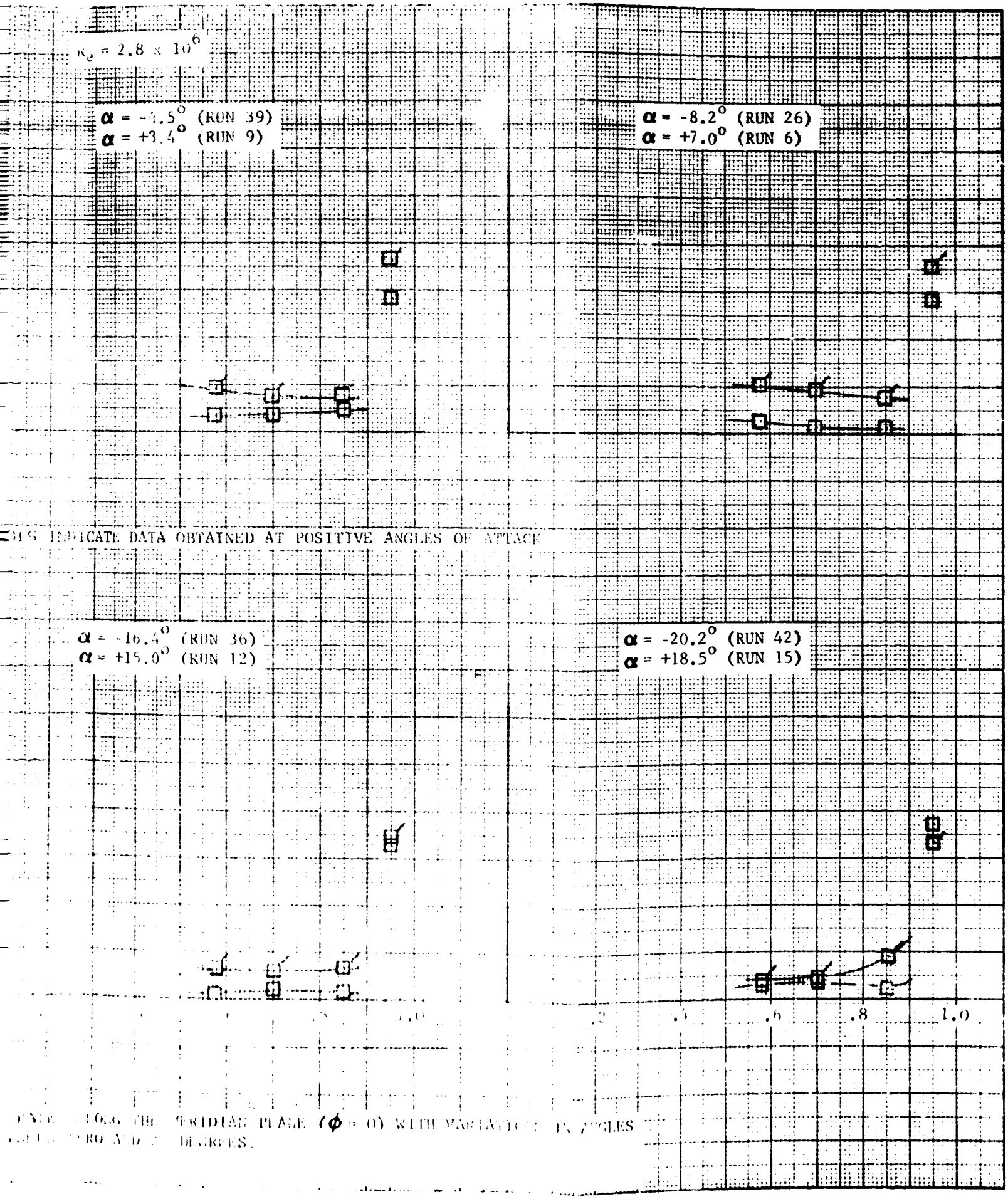

DICATE DATA OBTAINED AT POSITIVE ANGLES OF ATTACK

...ERIDIAN PLANE ($\phi = 0$) WITH VARIATION IN ANGLES ... AND ... DEGREES.

FOLDOUT FRAME

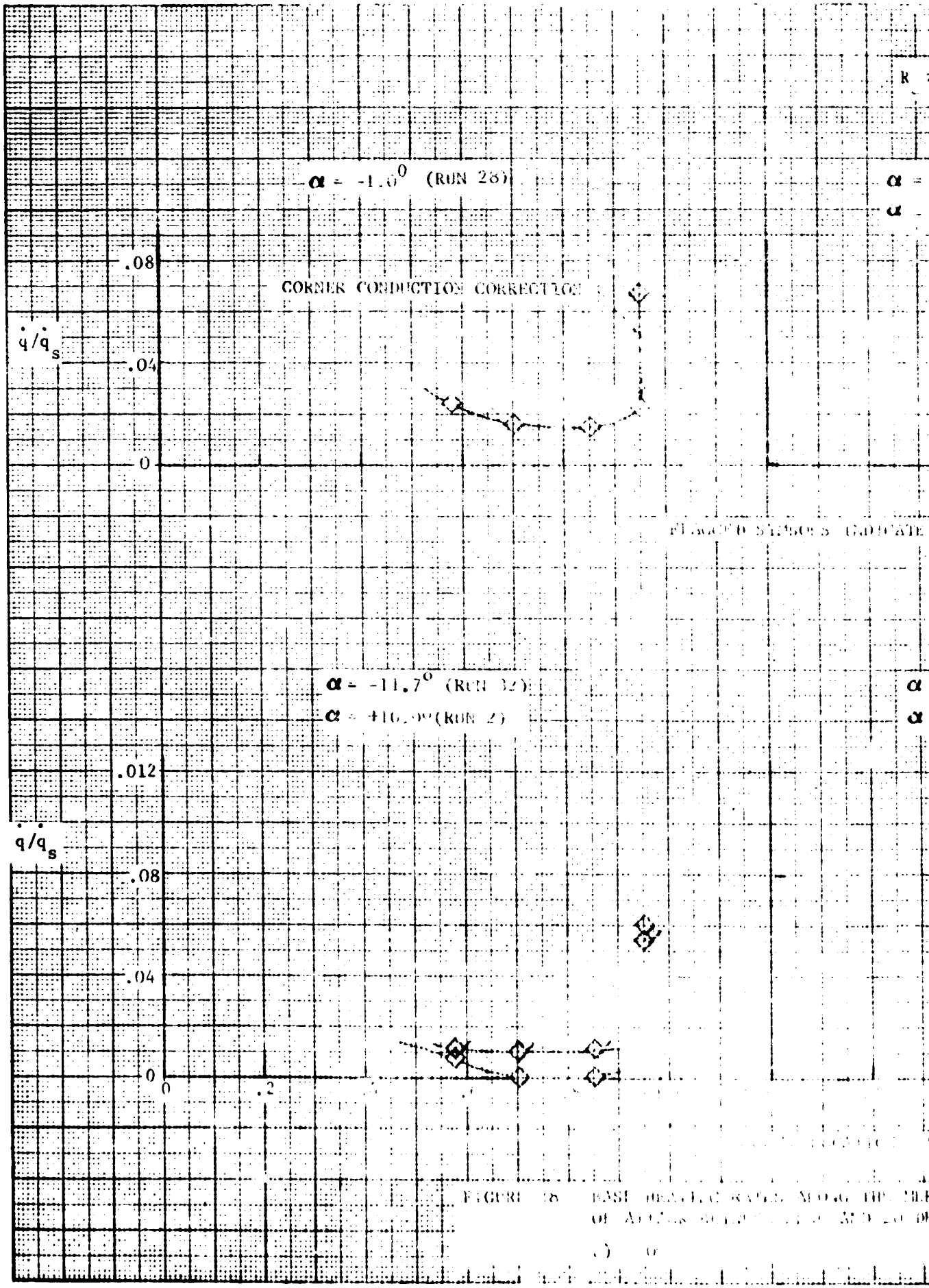

$R_c \approx 1.7 \times 10^6$

$\alpha = -4.5^\circ$ (RUN 38)

$\alpha = +7.4^\circ$ (RUN 5)

$\alpha = -8.1^\circ$ (RUN 25)

$\alpha = +7.8^\circ$ (RUN 5)

...DINATE DATA OBTAINED AT POSITIVE ANGLES OF ATTACK

$\alpha = -16.4^\circ$ (RUN 35)

$\alpha = +14.9^\circ$ (RUN 11)

$\alpha = -20.2^\circ$ (RUN 41)

$\alpha = +18.1^\circ$ (RUN 14)

.4 .6 .8 1.0

...R R_B

...THE MERIDIAN PLANE ($\phi = 0$) WITH VARIATIONS IN ANGLES
...D 20 DEGREES

FOLDOUT FRAME

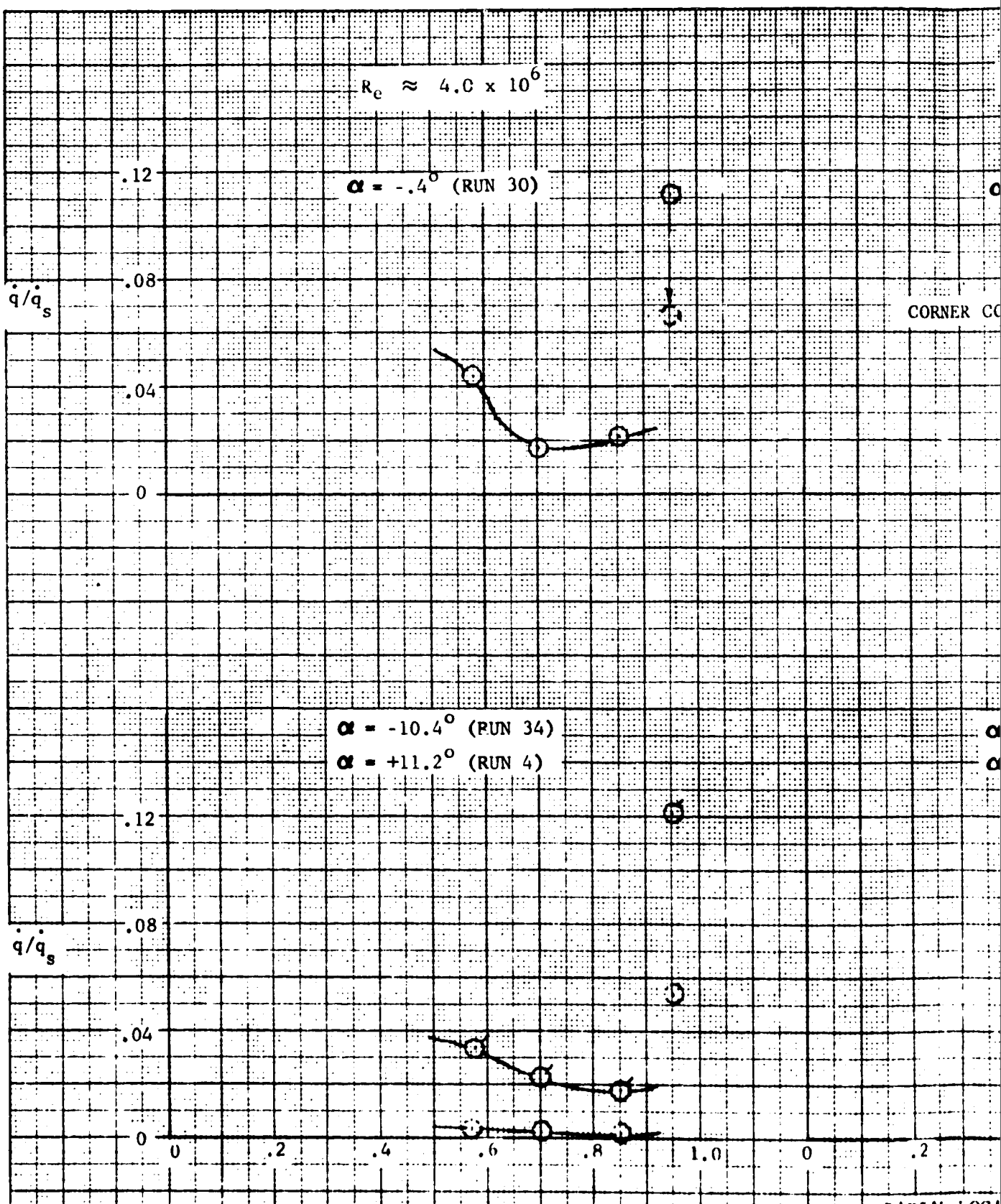

FIGURE 39 BASE HEATING RATES ALONG
ANGLES OF ATTACK 0 AND 1

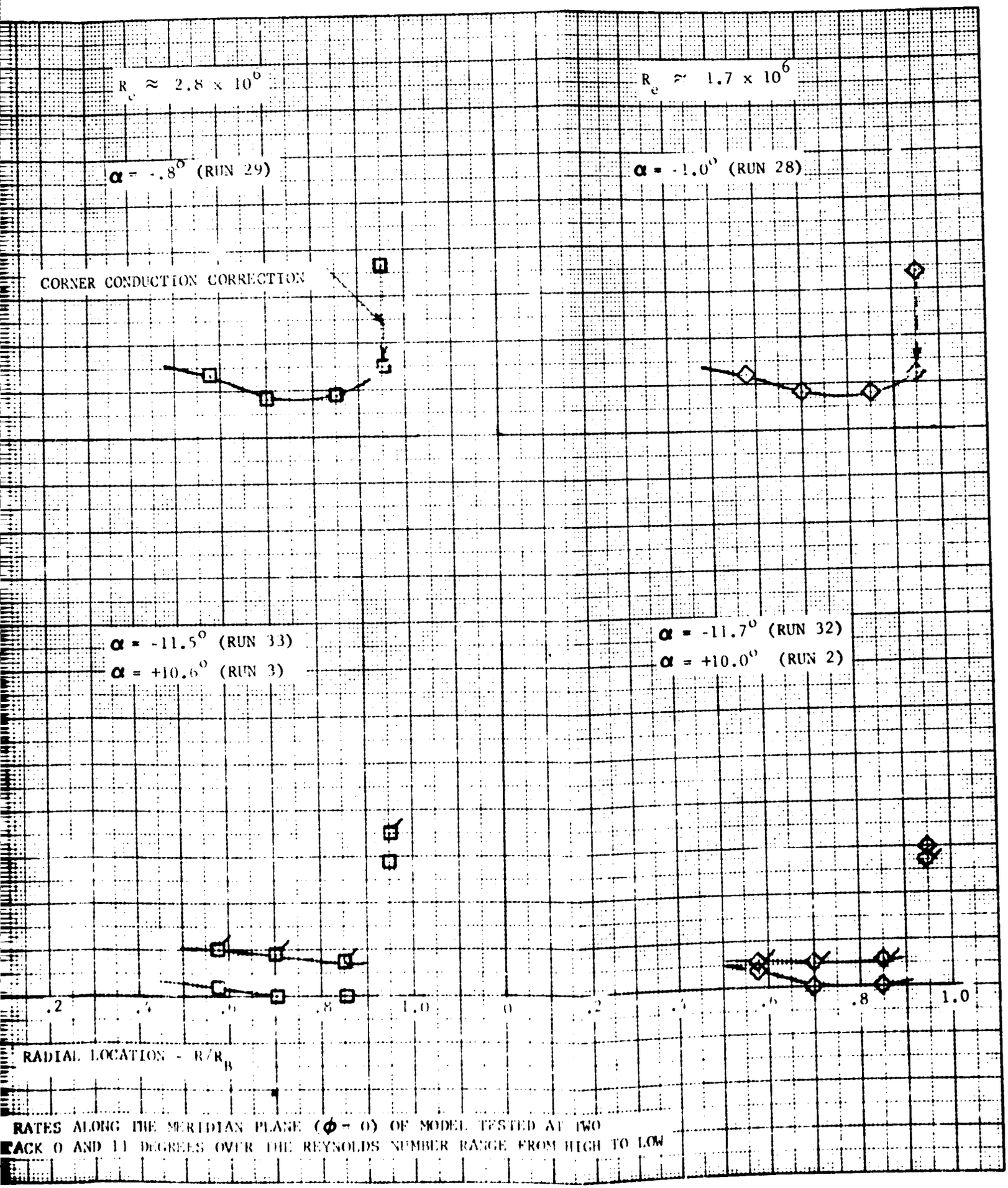

RATES ALONG THE MERIDIAN PLANE ($\phi = 0$) OF MODEL TESTED AT TWO
ACK 0 AND 11 DEGREES OVER THE REYNOLDS NUMBER RANGE FROM HIGH TO LOW

BLOWOUT FRAME

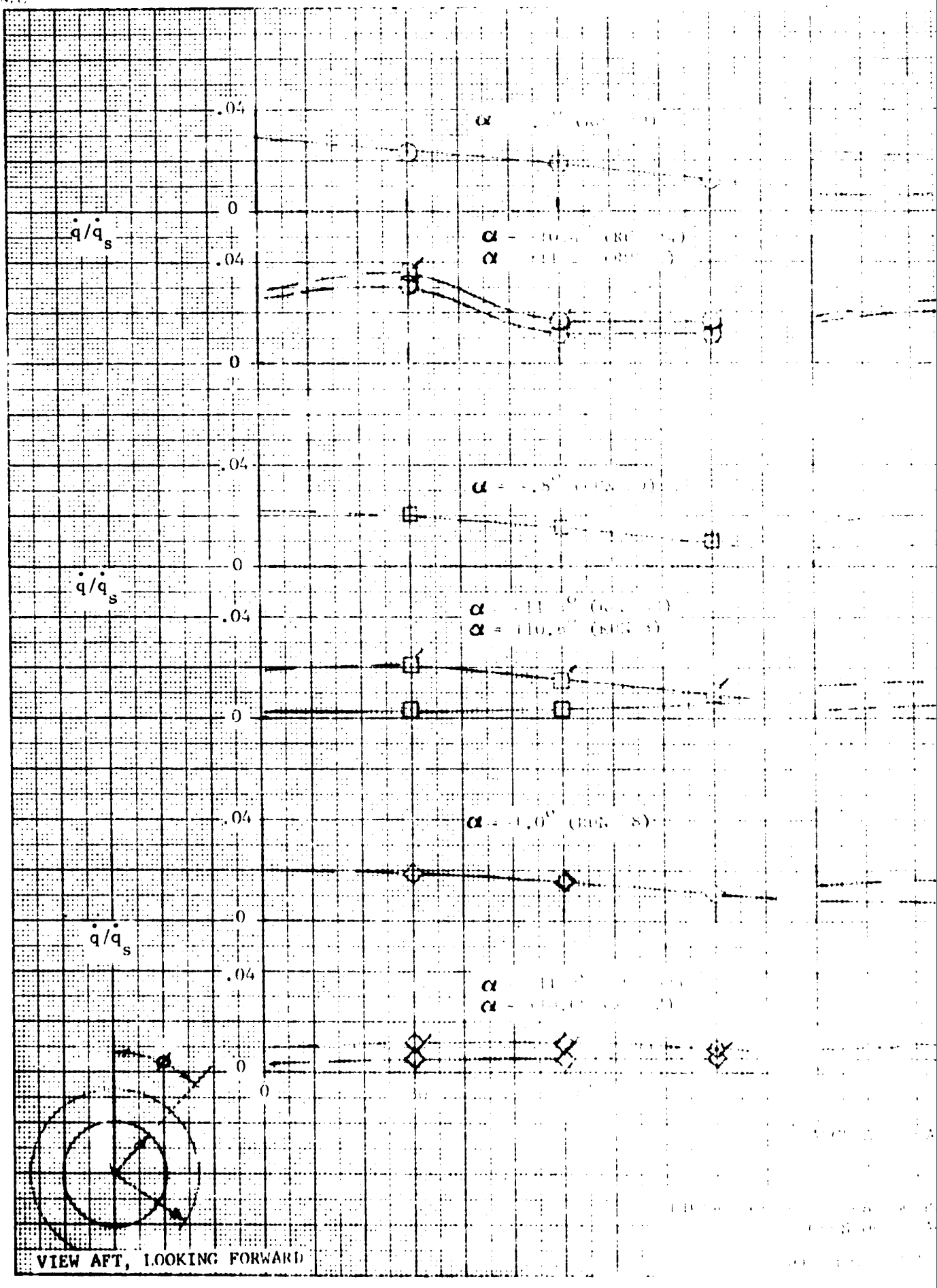

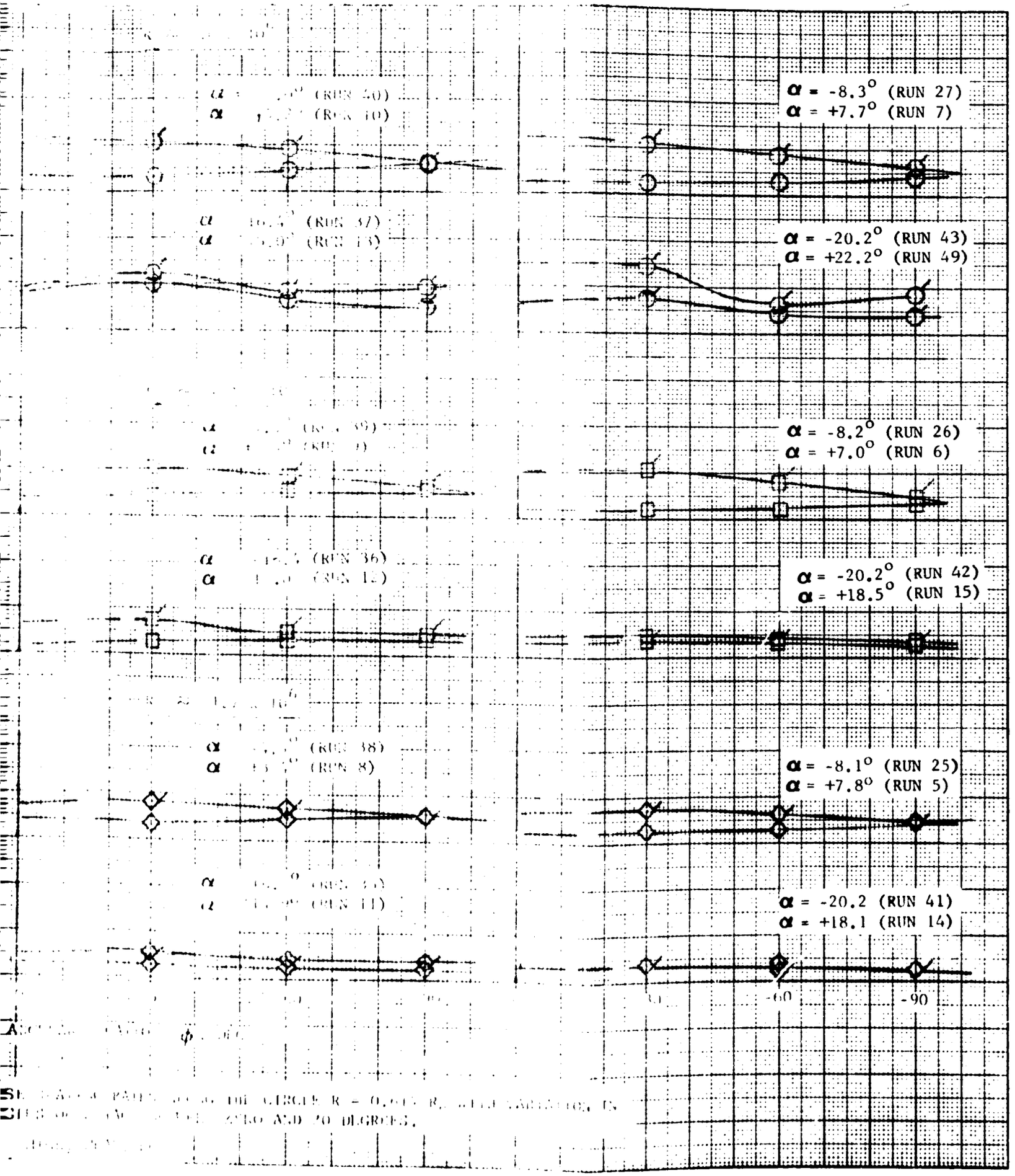
α = -8.3° (RUN 27)
α = +7.7° (RUN 7)
α = -20.2° (RUN 43)
α = +22.2° (RUN 49)
α = -8.2° (RUN 26)
α = +7.0° (RUN 6)
α = -20.2° (RUN 42)
α = +18.5° (RUN 15)
α = -8.1° (RUN 25)
α = +7.8° (RUN 5)
α = -20.2 (RUN 41)
α = +18.1 (RUN 14)
-60
-90

FOLDOUT FRAME

/

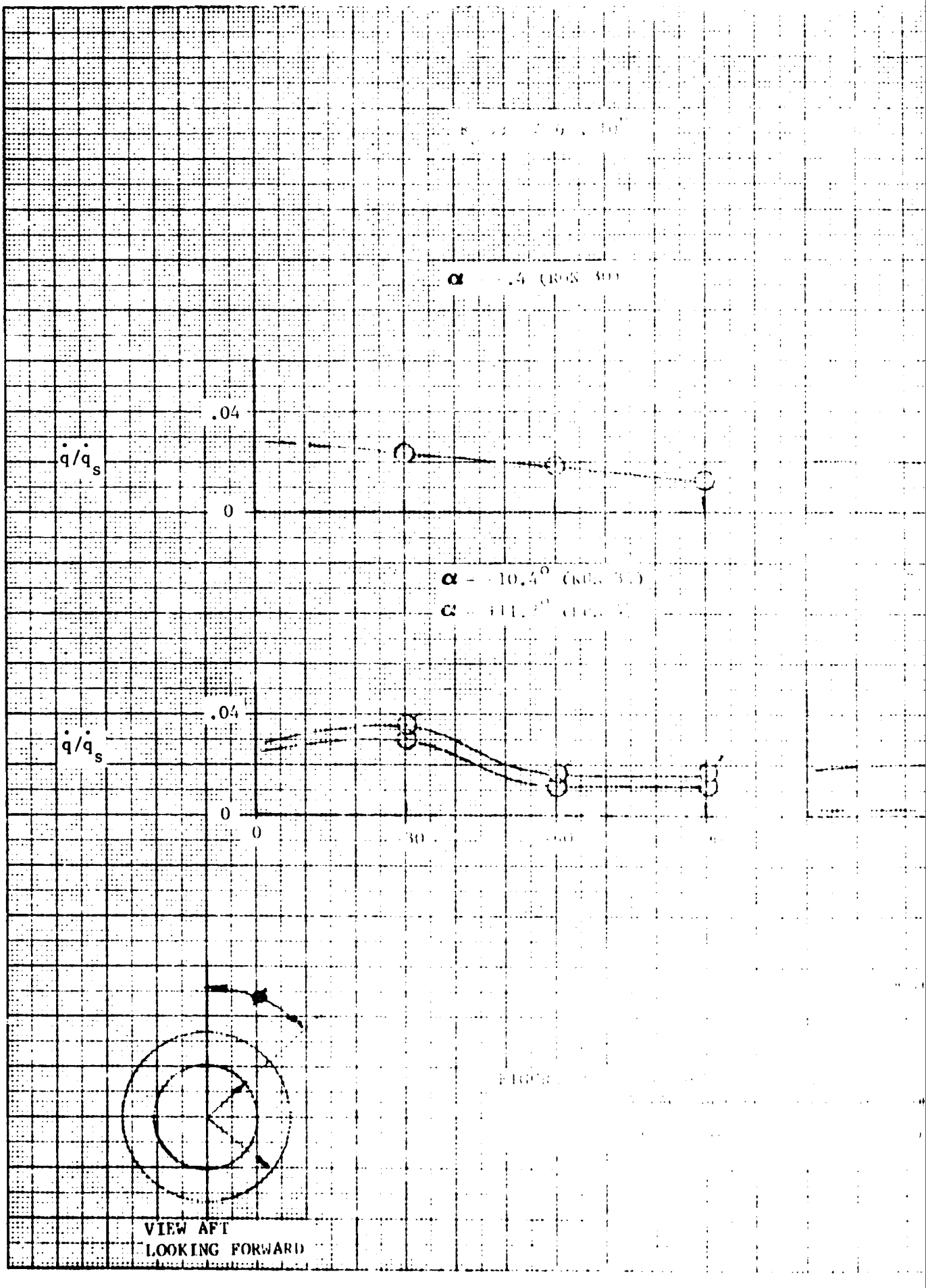

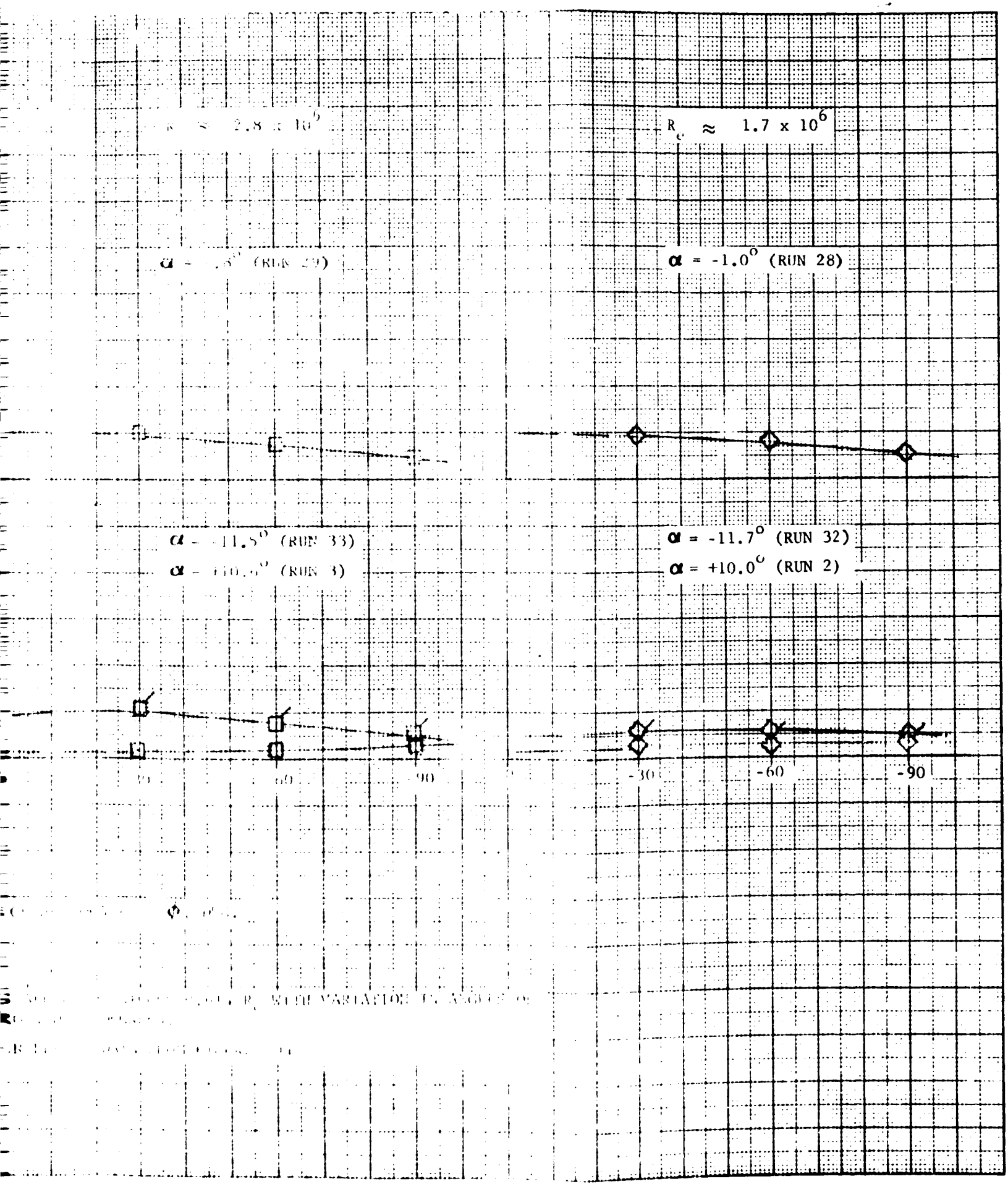
$R_e \approx 1.7 \times 10^6$
α = -1.0° (RUN 28)
α = -11.7° (RUN 32)
α = +10.0° (RUN 2)
-30
-60
-90

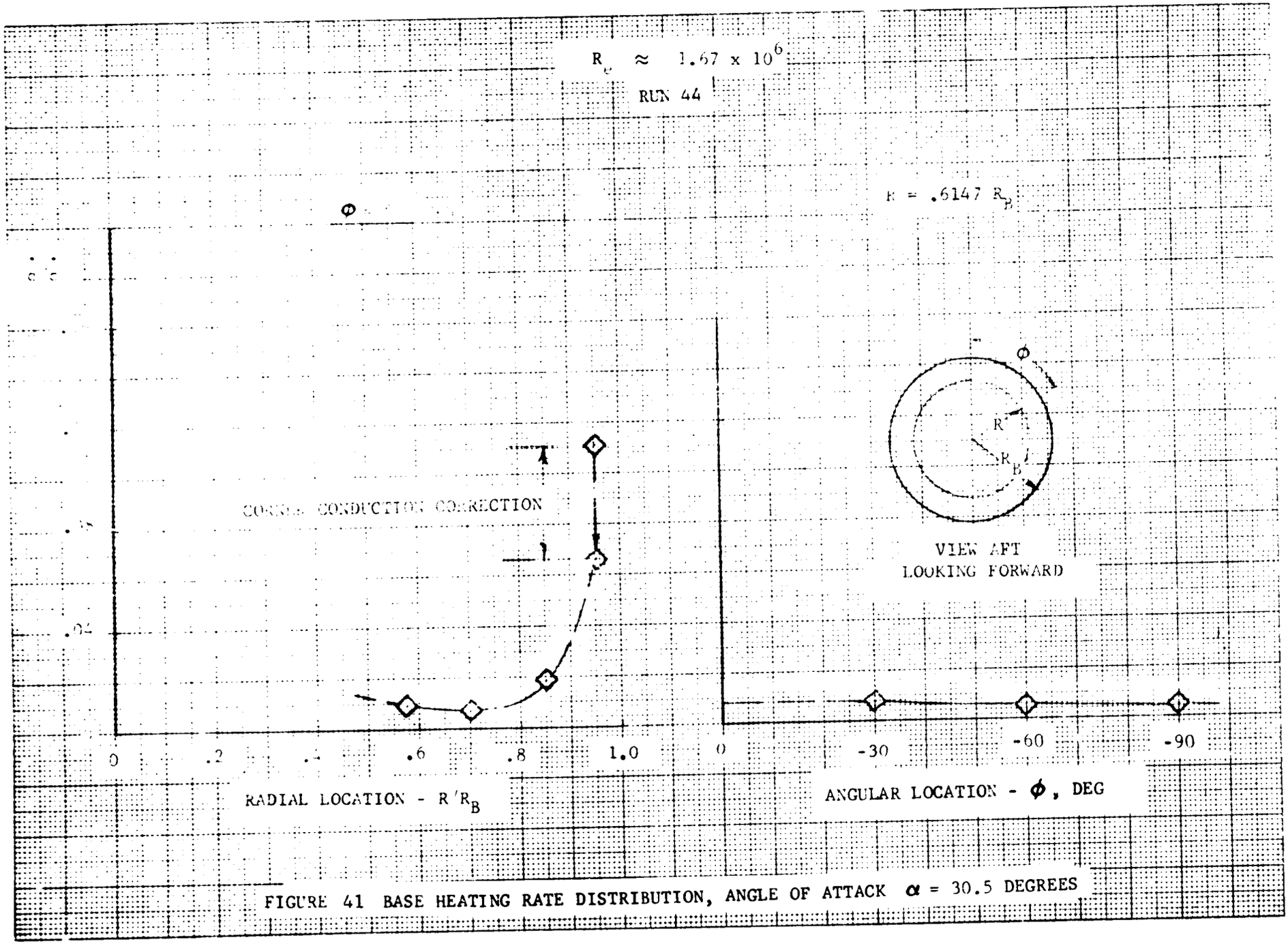

FIGURE 41 BASE HEATING RATE DISTRIBUTION, ANGLE OF ATTACK α = 30.5 DEGREES

APPENDIX I

A. Heat Conduction Corrections

The validity of the assumption of zero conduction in the skin (see equations 1-2) was investigated by evaluating the radial heat-conduction terms at the A/S model nose and peripheral corner.

1. Aeroshell Nose

The relaxation method for conduction problems, Reference 8, was used for the nose thermocouple locations as shown in Sketch 1.

The A/S nose is simulated by a simple control volume where the heat flow to the stagnation point 0 is

$$\Delta Q = (T_4 + T_{25} + T_{31} + T_{33} - 4T_o) \text{ in (Btu/sec).}$$

k is the thermal conductivity and the temperature subscripts denote the five thermocouple points involved.

Choosing a specific High-R_e, zero α run condition, Run 30, the conduction increment becomes:

$$\Delta Q = \frac{10.4}{3600} \quad \frac{\text{Btu}}{\text{Ft-sec-}^oF} \quad \text{x} \quad (0.00275) \quad (\text{FT})$$

$$\text{x} \ (253.5 + 252.7 + 253.0 + 249.0 - 4\ (2720)) \quad (^oF)$$

$$\Delta Q = -0.00067 \text{ Btu/sec}$$

This small negative quantity indicates that negligible heat is conducted from the stagnation point 0 to the surrounding thermocouple points.

2. Aeroshell Corner

Maximum temperature gradients exists around the A/S cone-edge from Sta #13 (front) to Sta #15 (back side).

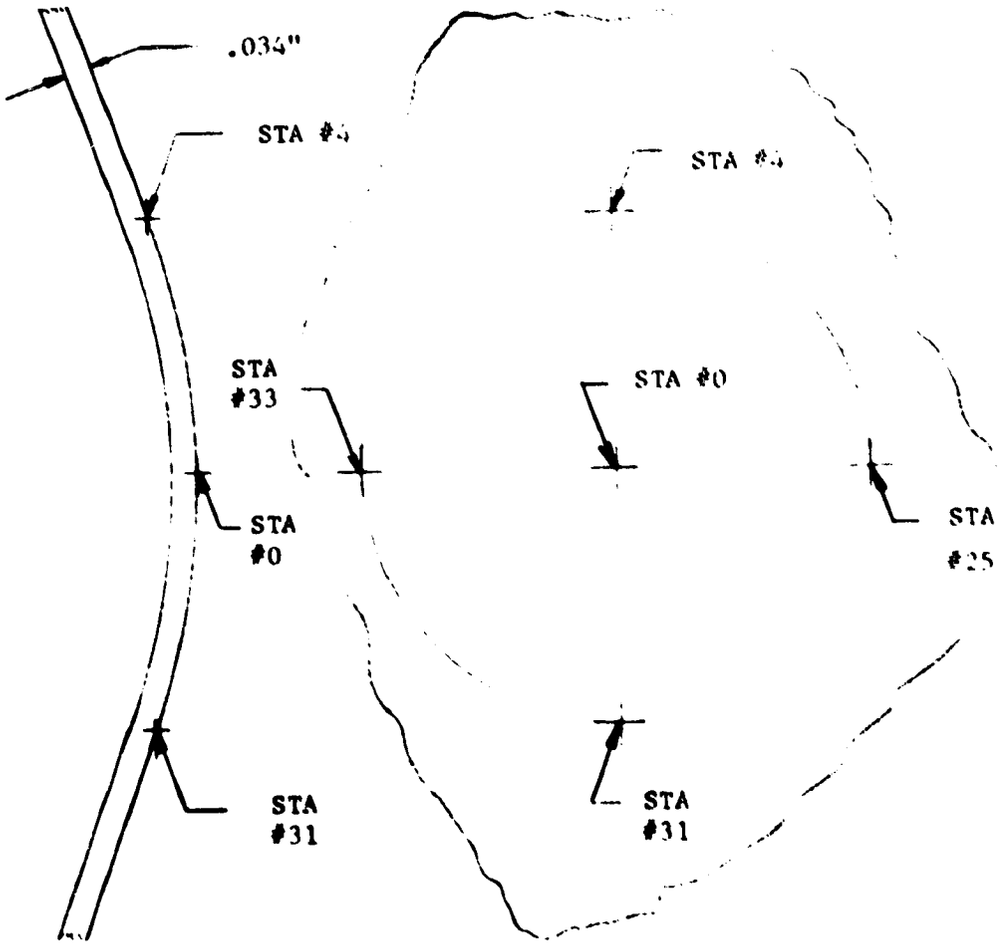

SKETCH 1

Assuming the total heat conduction around the same region to be:

$$\Delta Q = k\,(2\pi R_B\,(\Delta\sigma))\,\frac{\partial T}{\partial s}$$

and basing the temperature gradient term $\partial T/\partial s$ on a general BC temperature level taken at Sta. 18, the conduction term for run 30 at High-R_e and zero-α becomes: $\Delta Q = 0.051$

To compare this conduction quantity with the stagnation heat transfer rate for run #30 of

$$\dot{q}_s = 40 \text{ Btu ft}^{-2}\text{-sec},$$

a reference area, A, is assigned as that part of the A S corner surface extending beyond Sta #13 as shown in Sketch 2.

A practical length of the model flange, or rim, may be the peripheral dimension $2\pi R_B$. Hence,

$$\Delta A = 2\pi R_B \times \Delta\ell'$$

Consequently, the ratio of the conduction heat transfer to the stagnation heat transfer becomes

$$\frac{\Delta Q_c}{Q_s} = \frac{\Delta Q_c}{\dot{q}_s \cdot (\Delta A)} = \frac{k\,(2\pi R_B)\,(\Delta\sigma)\,\frac{\partial T}{\partial s}}{\dot{q}_s\,(2\pi R_B) \times \Delta\ell'} = \frac{k \cdot (\Delta\sigma)\,\frac{\partial T}{\partial s}}{\dot{q} \cdot (\Delta\ell')} = 0.045$$

This quantity indicates that the BC heat transfer rate ratios ($\dot{q}_t/\dot{q}_s$) pertaining to Sta #15 in Figures 39 and 40 should be reduced by $\Delta(\dot{q}/\dot{q}_s) = 0.045$

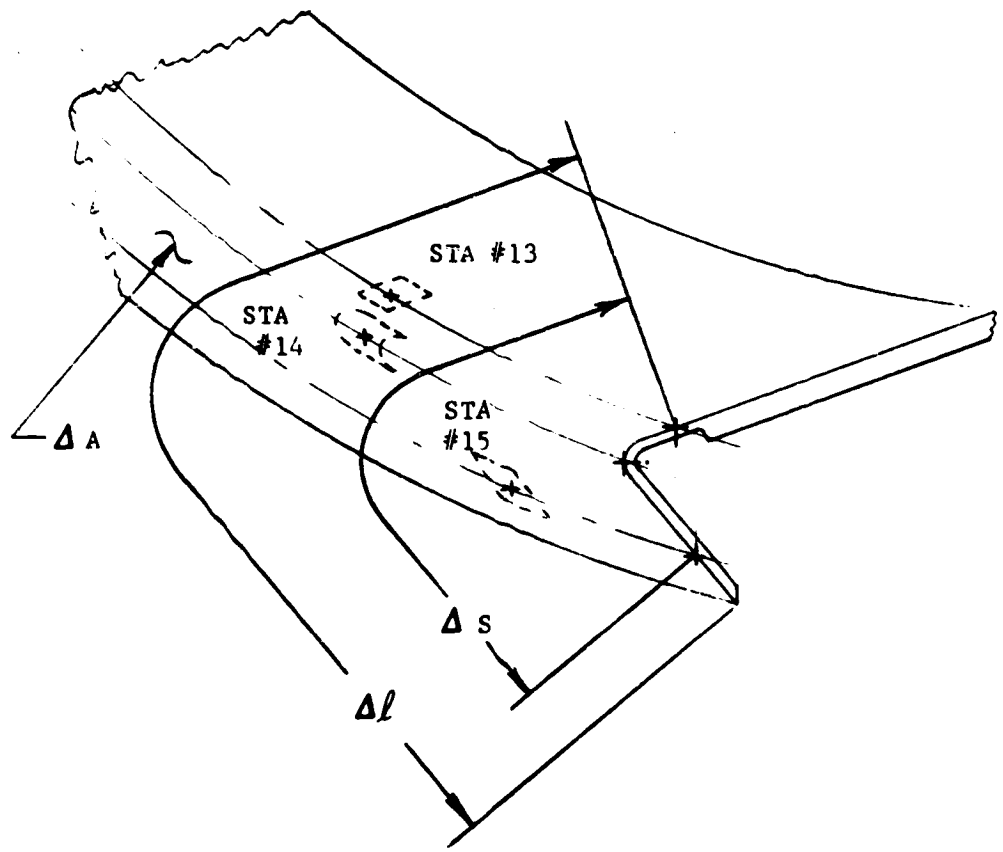

STA.	SYMBOL	DISTANCE IN INCHES
13 TO EDGE	$\Delta\ell$	.332
13 TO 15	Δ_S	.241
SURFACE AREA Ξ $2\pi R_B \cdot \Delta\ell$		

SKETCH 2

B. Surface Roughness

Regarding the no-trip, high-α (α_T = 26.2 deg) boundary-layer-induced increase in $\dot{q}$, the question raised as to possible effects of model surface roughness remains unanswered.

The following measurements are listed for reference only and are not intended for use directly in accuracy analyses of heating rate data.

An attempt was made to measure the model post-test roughness from surface photographs (not shown). From that of a pretest article complying with the 30 micro-inch surface finish the model A/S had suffered a degradation by exposure to tunnel particle abrasion discerned in localized areas as pits and dimples ranging in diameter between 10^{-4} and 10^{-2} in. For comparison only, at High R_e test conditions the leeward boundary layer momentum thickness, θ, and Reynolds number based on leeward boundary layer momentum thickness, R_{e_θ}, were 0 (10^{-3}) inch and about 200 respectively.

APPENDIX II

VLC NEAR-WAKE TEMPERATURE SURVEY

During the week of July 16 through 21, 1972, VLC model near-wake temperature surveys were made in the LRC M-8 VDHT for α = -11.2 deg.

The temperature probe as shown in Figure IIa was developed by LRC. A simple chromel alumel thermocouple probe was installed at the end of a curved narrow sting suspended from the tunnel ceiling. The thermocouple junction was made up of 0.005 in. diameter wires and suspended between two 0.010 in. diameter thermocouple wires about 0.10 in. apart.

The probe coordinates X-Y are denoted in Figure IIb. The X-coordinate is measured aft in the axial direction normal to the plane through the peripheral corner. The probe was oriented successively at three near-wake distances assigned within the given dimension from the plane through the VLC corner to the base cover circular base plate. The Y-coordinate of each probe setting reaches from the base cover frustum.

The Low-R_e (X-Low R_e) run conditions were investigated. Again, the duration of each model run exposure to tunnel flow was about five seconds. Before each run, the probe setting was approximated relative to the model, but the exact probe location was assessed from schlieren pictures.

From simultaneous measurements of probe temperature, tunnel adiabatic recovery temperature, and model base wall temperature, the temperature ratio:

$$\theta = \frac{T-T_w}{T_a-T_w}$$

was plotted as shown in Figure IIb. The θ ratio appears constant within the base recirculation flow region which is bounded by the boundary layer

flow field undergoing the turning expansion around the edge. In the shock layer - or shear layer - prevailing beyond this boundary the θ-ratio increases with the Y coordinate and should, if monitored out to the bow-shock boundary, approach one asymptotically. Sufficient test data were obtained to identify the boundary between the constant-θ and the increasing-θ regions. The distances to these boundaries, Y_{SL}, from the base cover reference points were used as reference parameters in normalized θ plots, Figure IIc.

Finally, isolines of constant θ-ratio were plotted as shown in Figure IId. As already indicated in Figure IIb the θ-ratios increase with R_e. Figure IId also suggests the occurrence of a recirculation bubble in the vicinity of the aft 62-deg. frustum.

The VLC Low-R_e near-wake temperature survey in the LRC M-8 VDHT air medium facility will be used as reference during the forthcoming VLC near-wake temperature survey to be conducted in the LRC M-6 CF_4 tunnel.

FOLDOUT FRAME

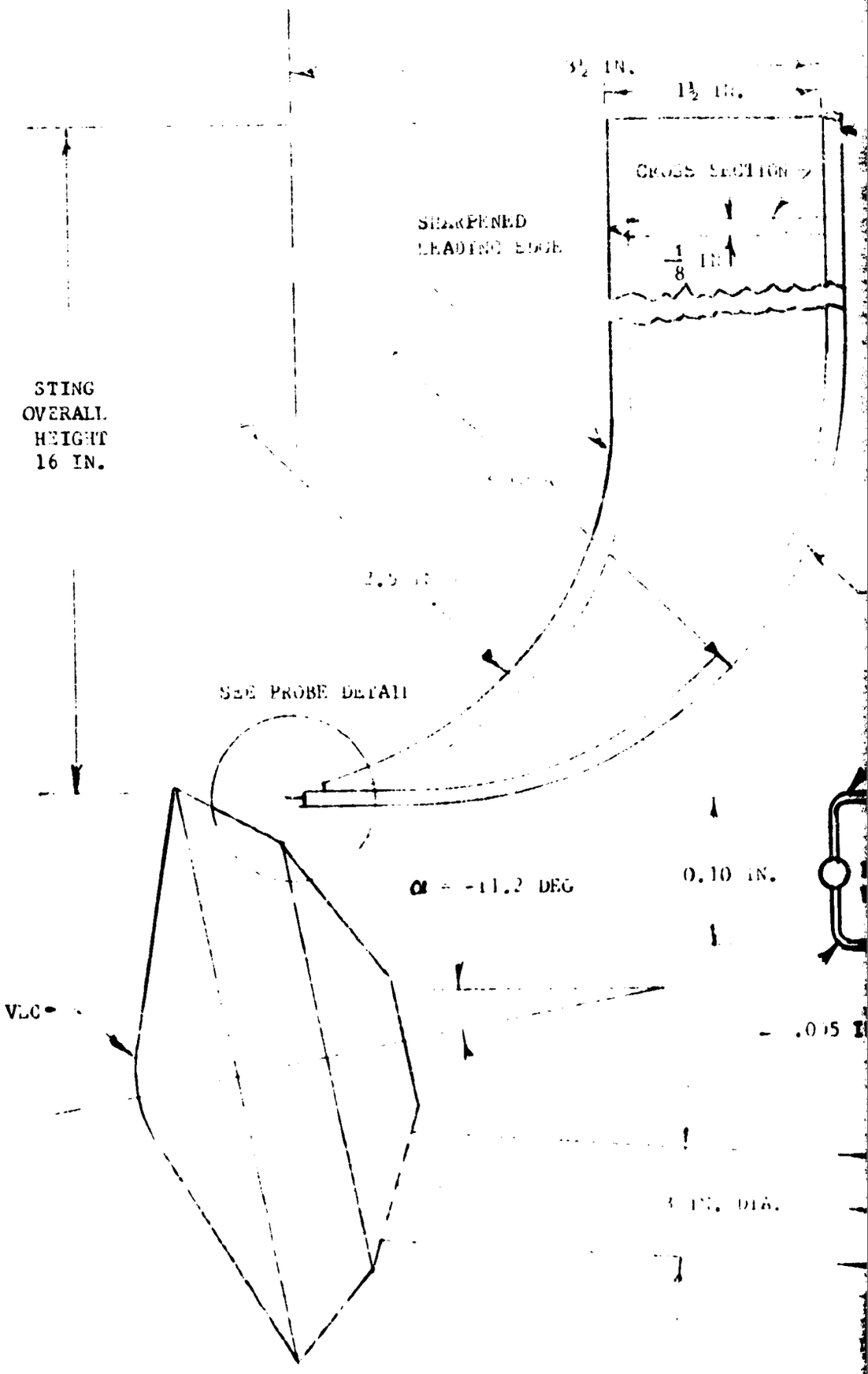

FIGURE 11a VLC MODEL REAR-WALL TEM

FOLDOUT FRAME 2

1/8 IN. DIA. TUBING

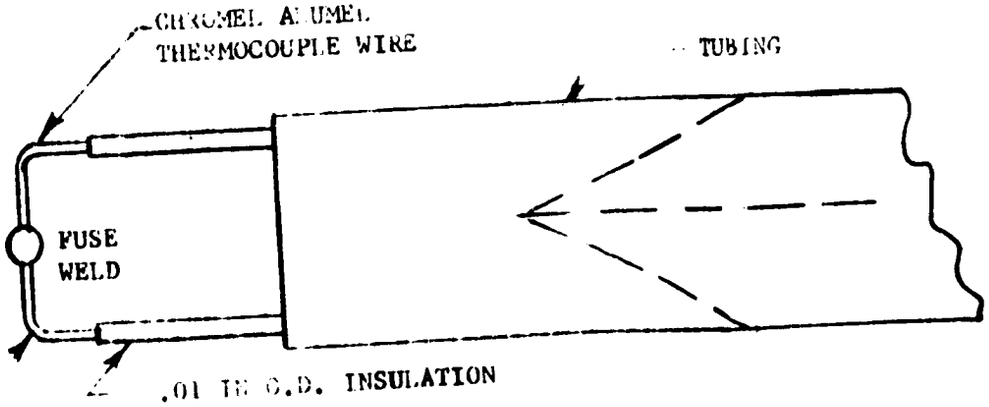

PROBE DETAIL - 10 SCALE

TOP VIEW

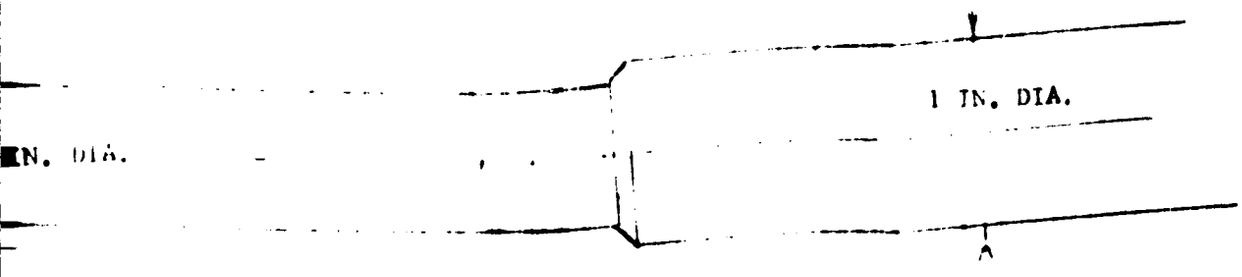

NEAR-WAKE TEMPERATURE PROBE INSTALLATION

FOLDOUT FRAME

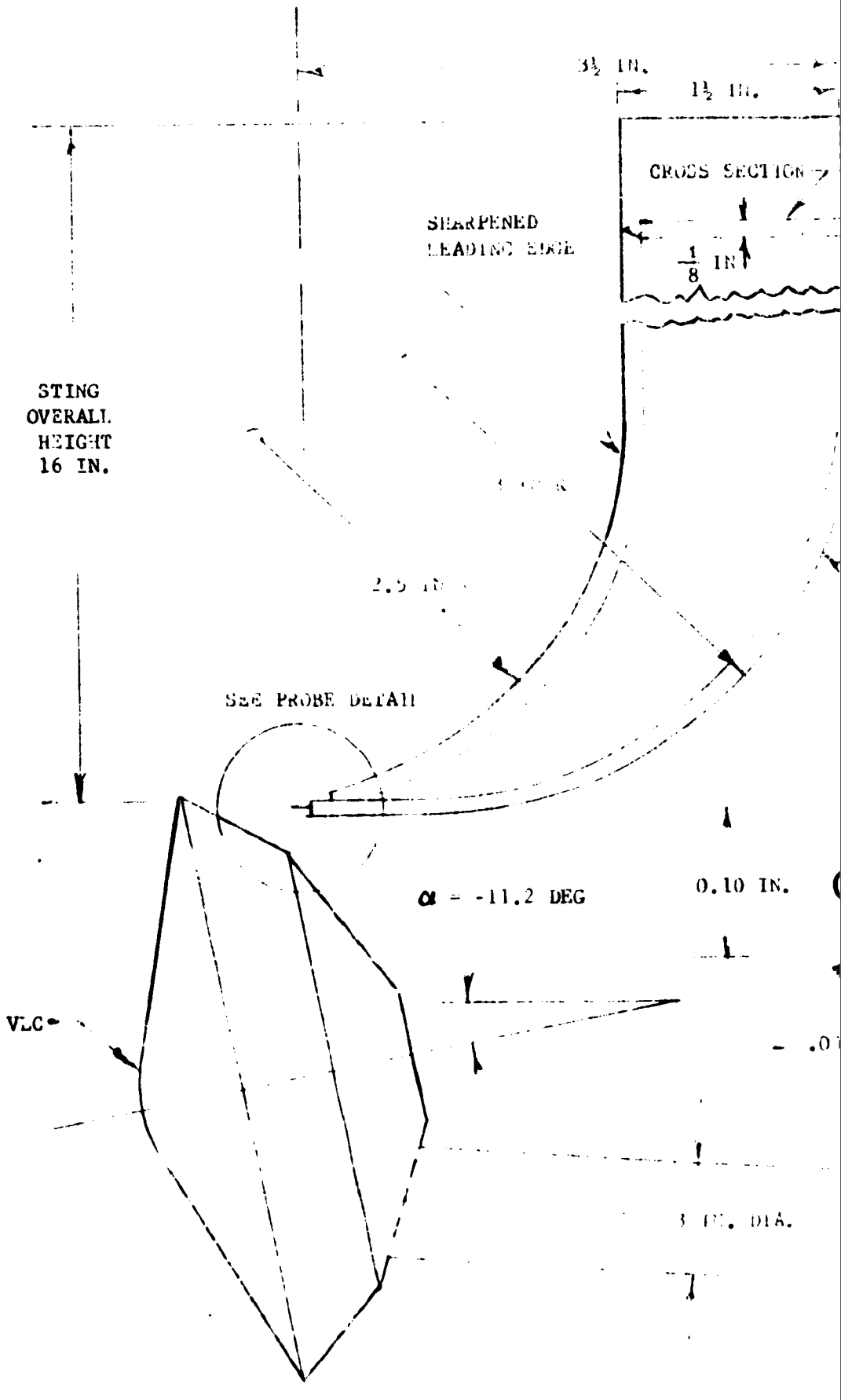

FIGURE 11a VLC MODEL NEAR-WAKE TH

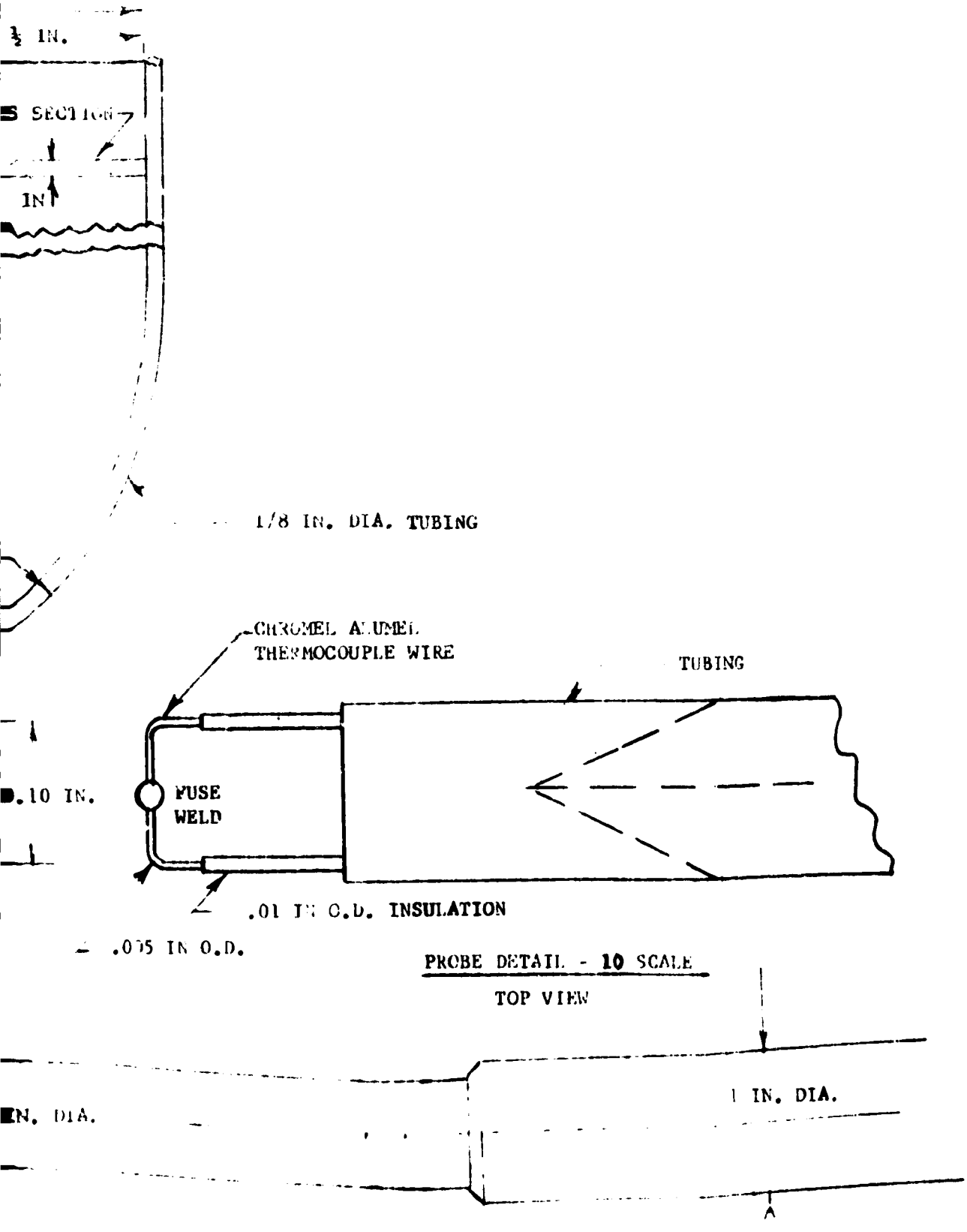

EAR-WAKE TEMPERATURE PROBE INSTALLATION

FOLDOUT FRAME

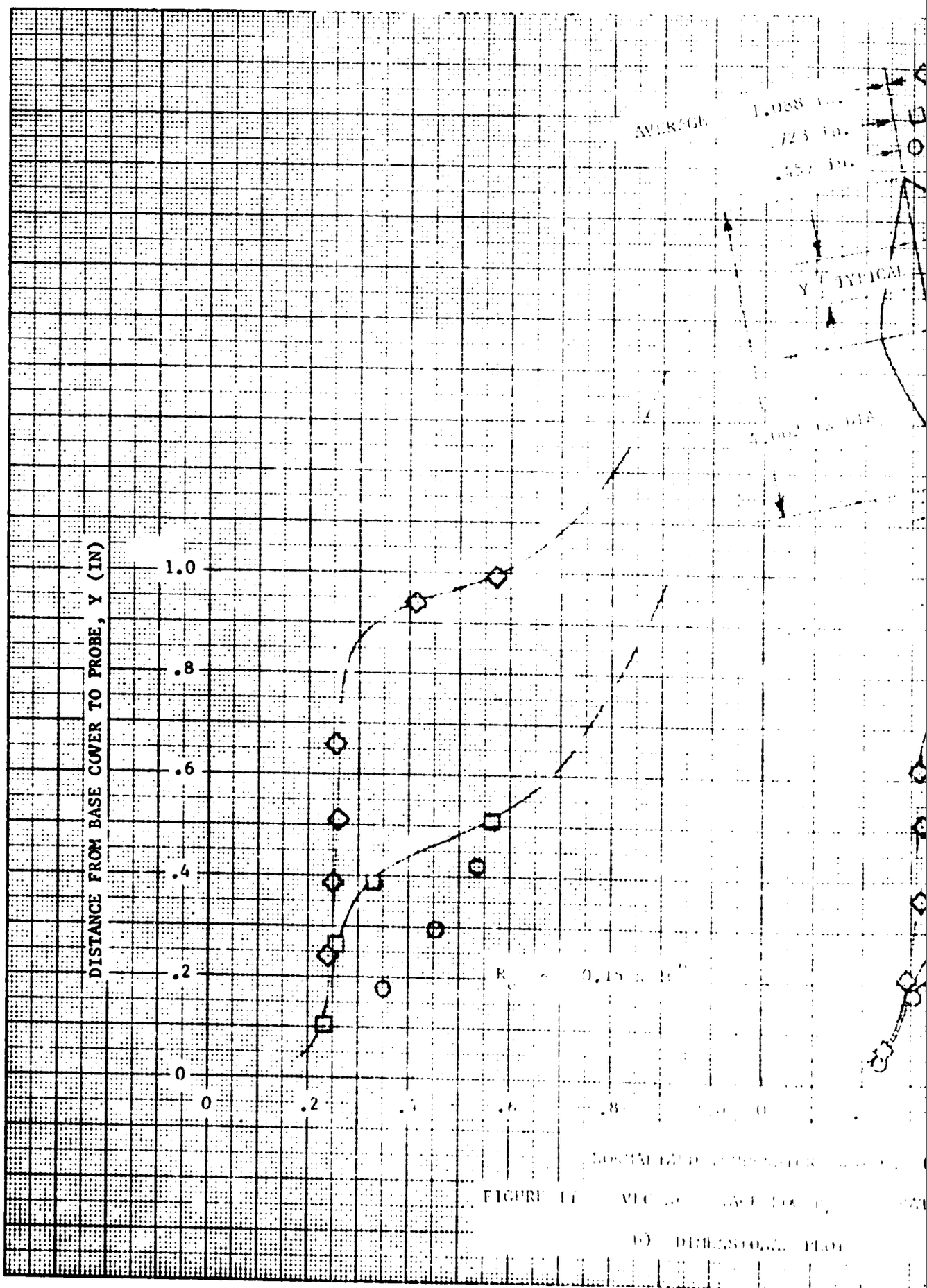

FIGURE 11 [illegible]

b) DIMENSIONAL PLOT

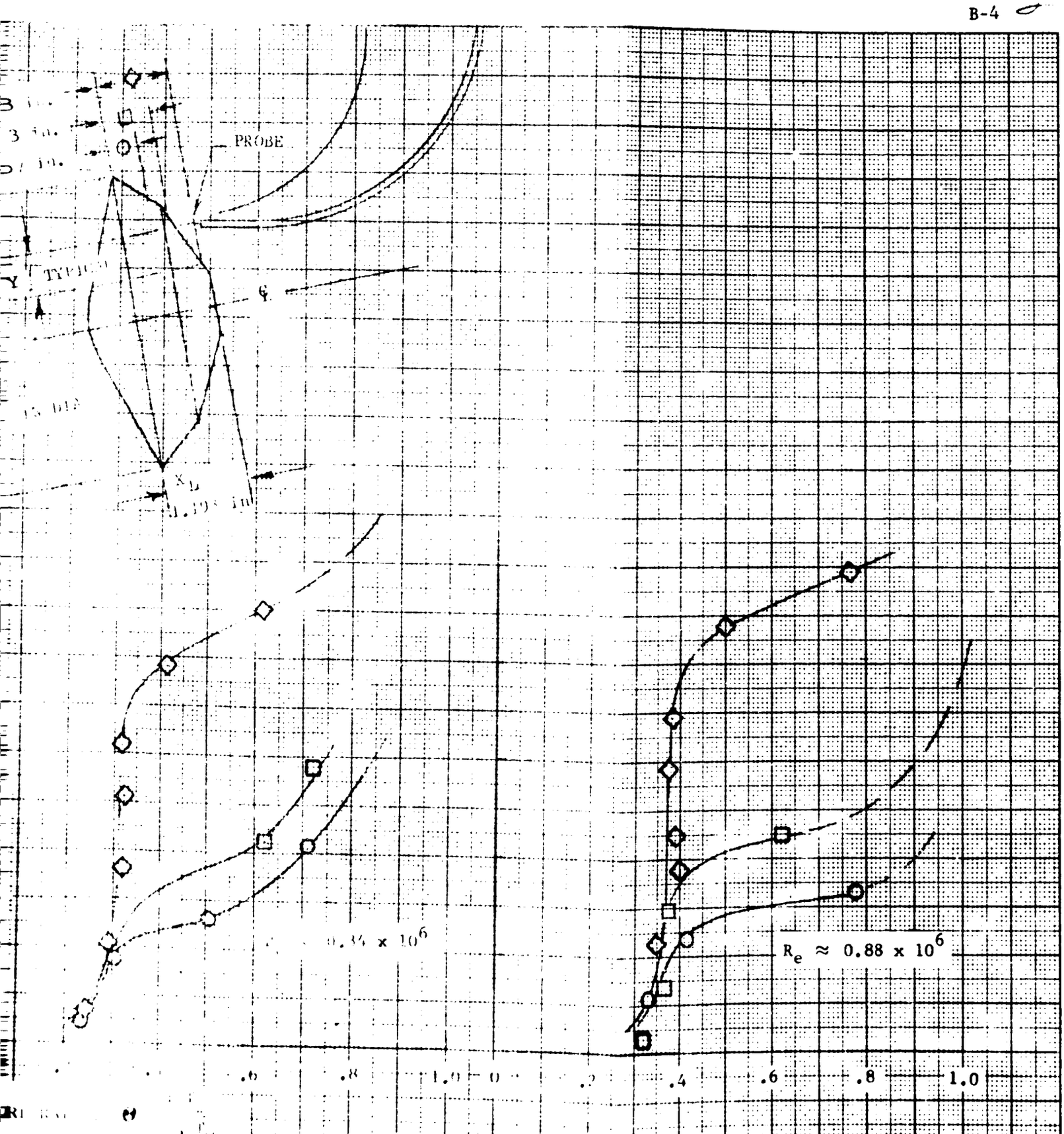

PLOT

FOLDOUT FRAME

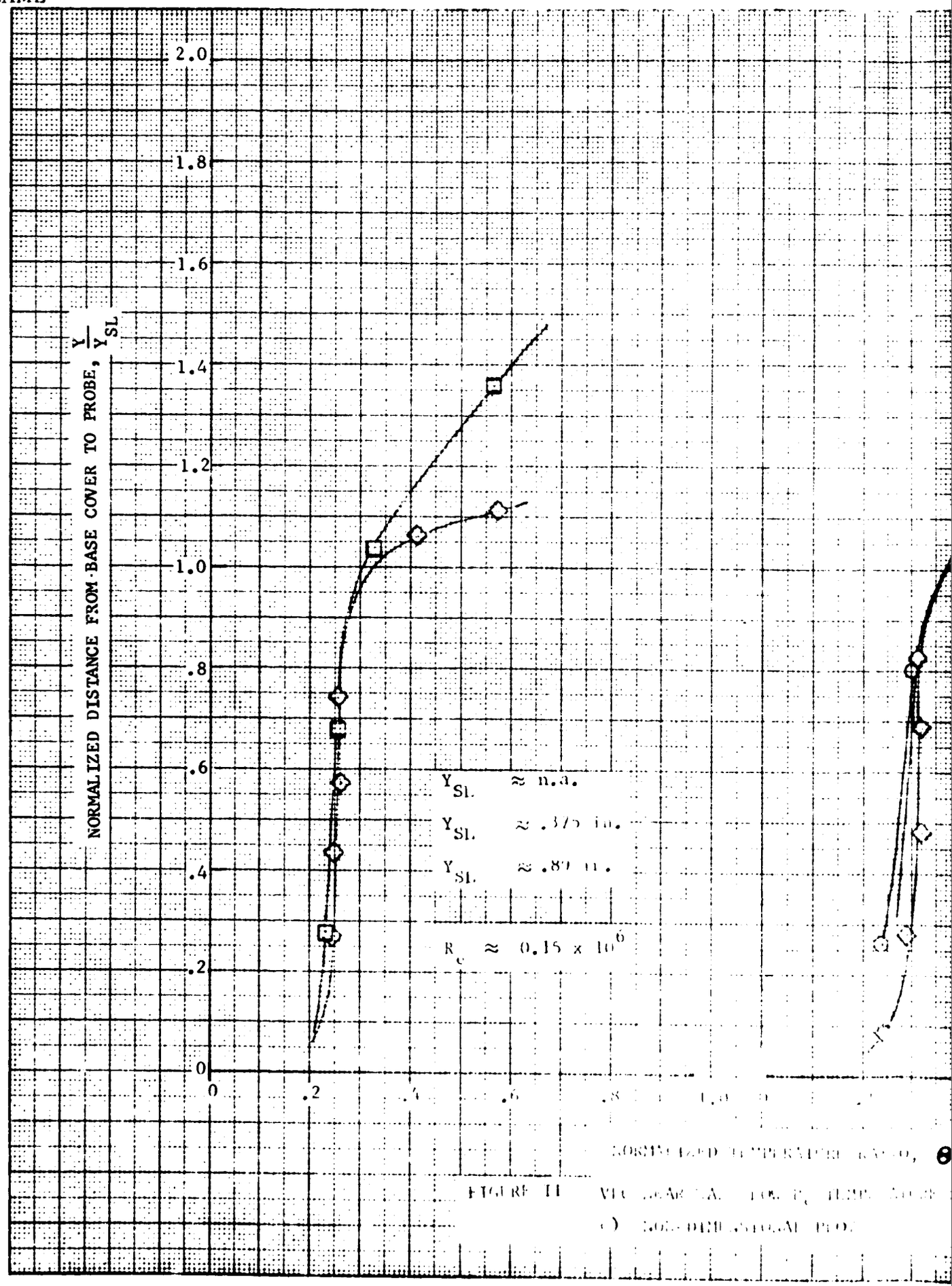

FIGURE 11 [illegible]

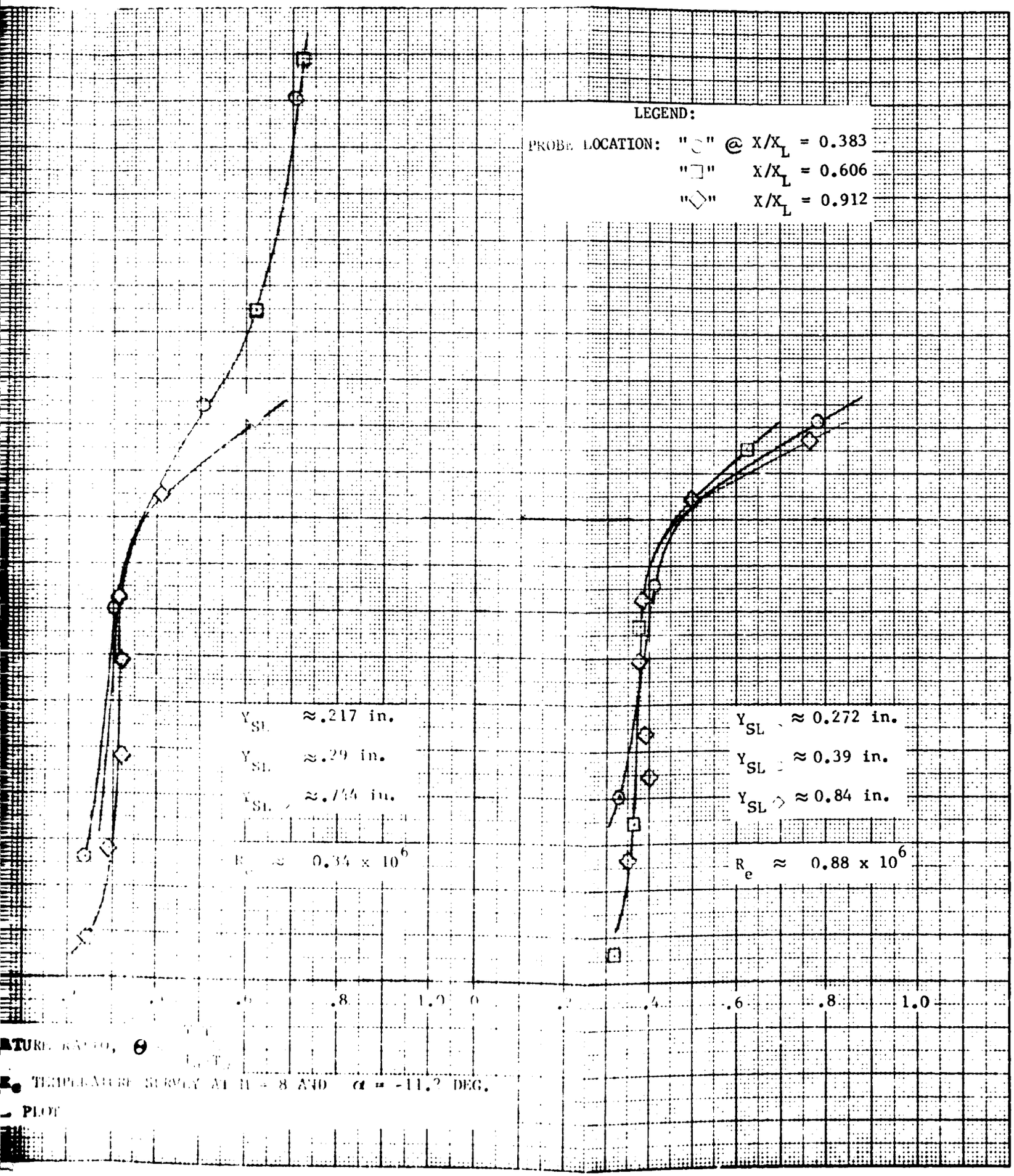

ATURE RATIO, θ

T_t

R_e TEMPERATURE SURVEY AT R = 8 AND α = -11.2 DEG.

PLOT

FOLDOUT FRAME

$R_e = 0.15 \times 10^6$

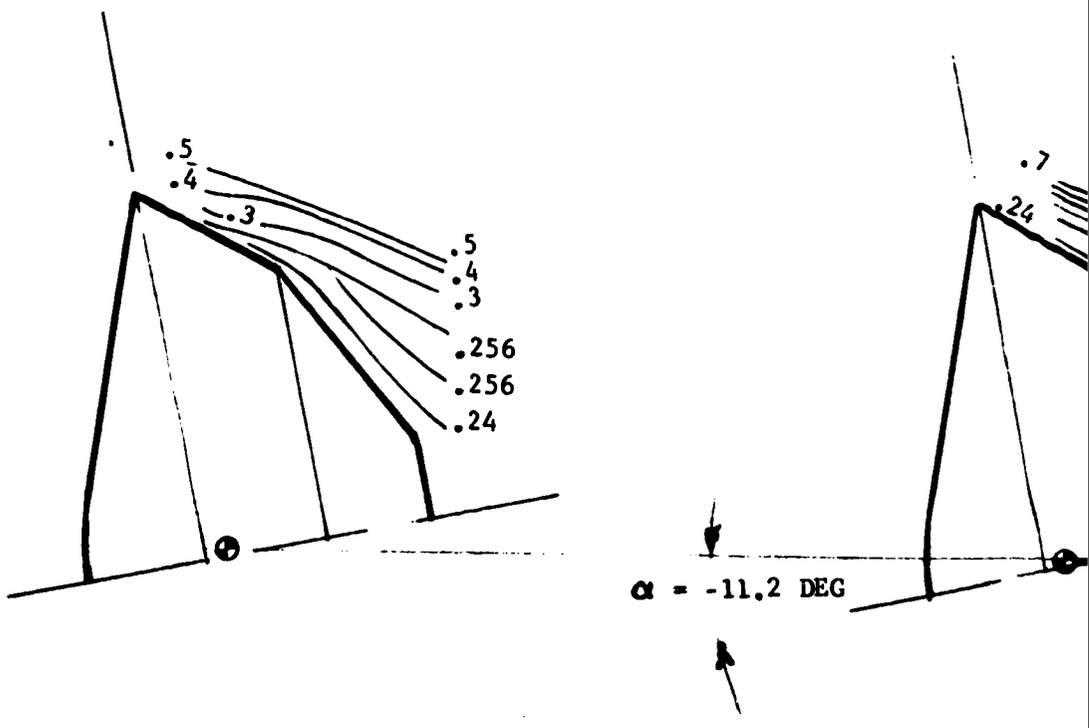

FIGURE II VLC NEAR-WAKE LOW-R_e TEMPERATURE

d) ISOLINES ARE SHOWN AT CONSTA

$R_e = 0.34 \times 10^6$

$R_e = 0.88 \times 10^6$

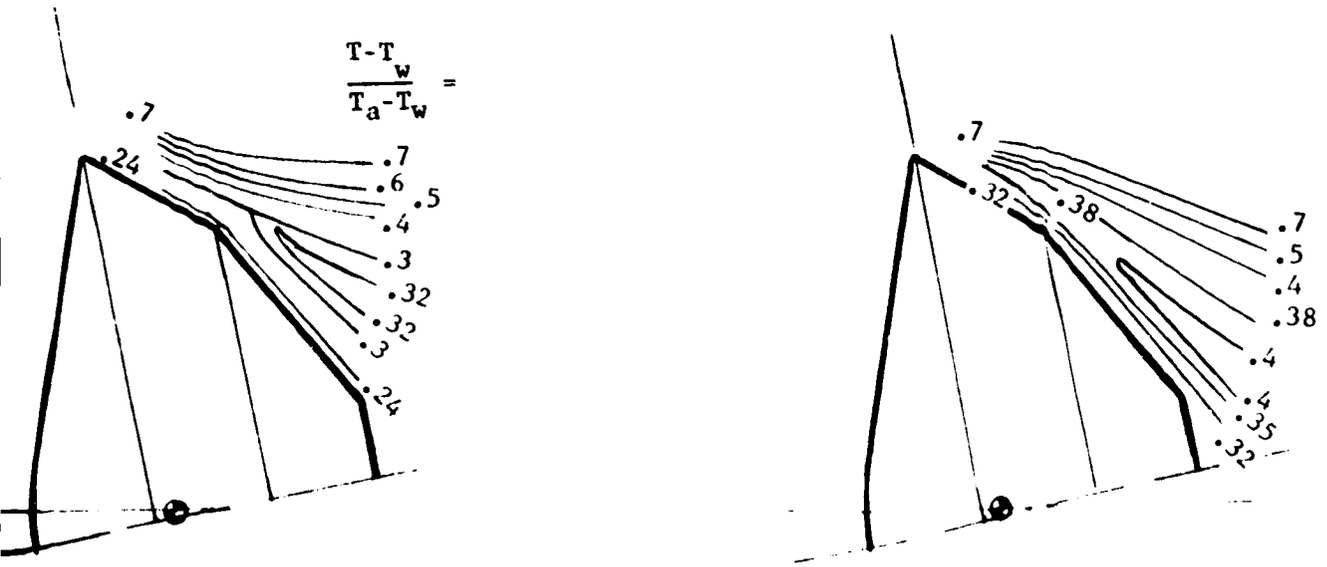

TEMPERATURE SURVEY AT M = 8 AND α = -11.2 DEG.
WN AT CONSTANT TEMPERATURE RATIOS, $\theta = \frac{T-T_w}{T_a-T_w}$